



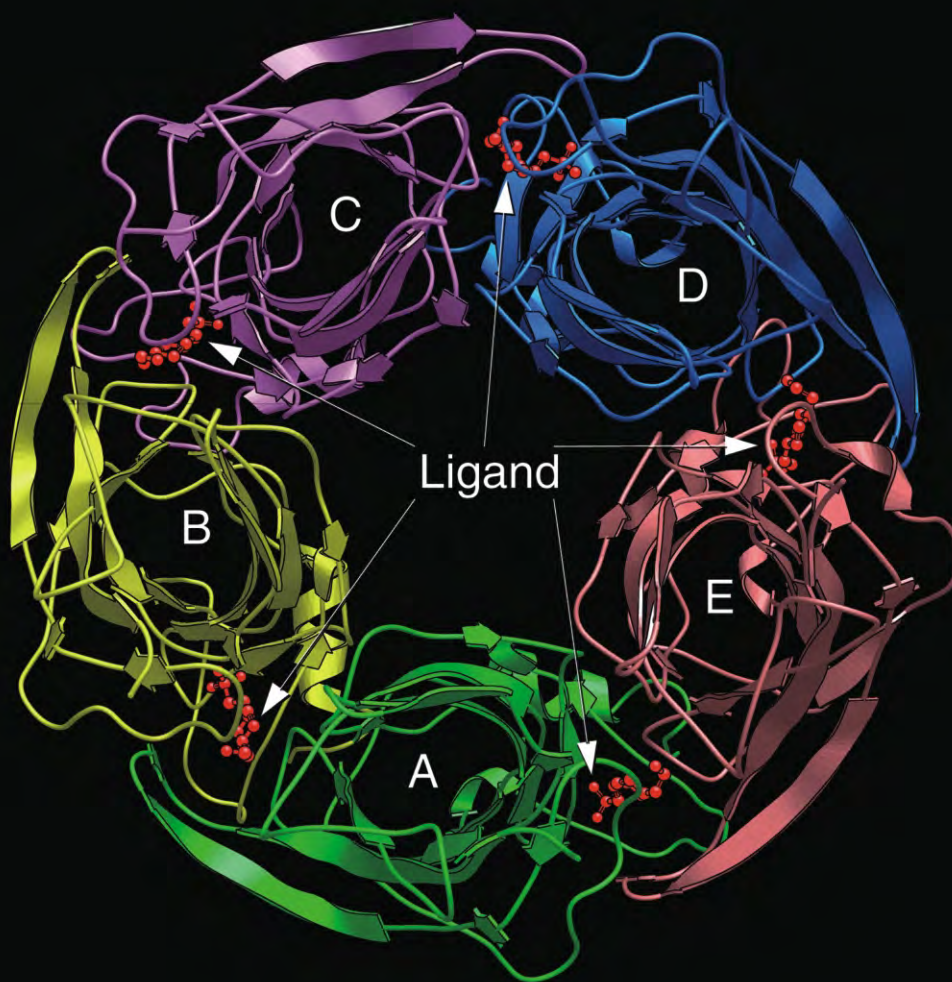
Scientific  
Research

# JBise

ISSN: 1937-6871

Volume 2 Number 6 October 2009

**J**ournal of **B**iomedical **S**cience and **E**ngineering



# Journal Editorial Board

ISSN 1937-6871 (Print) ISSN 1937-688X (Online)

<http://www.scirp.org/journal/jbise>

---

## Editor-in-Chief

**Prof. Kuo-Chen Chou**

Gordon Life Science Institute, San Diego, California, USA

## Editorial Board (According to Alphabet)

<b>Prof. Hugo R. Arias</b>	Midwestern University, USA
<b>Prof. Christopher J. Branford-White</b>	London Metropolitan University, UK
<b>Prof. Thomas Casavant</b>	University of Iowa, USA
<b>Prof. Ji Chen</b>	University of Houston, USA
<b>Dr. Aparup Das</b>	National Institute of Malaria Research (ICMR), India
<b>Dr. Sridharan Devarajan</b>	Stanford University, USA
<b>Prof. Fu-Chu He</b>	Chinese Academy of Science, China
<b>Prof. Zeng-Jian Hu</b>	Howard University, USA
<b>Prof. Wolfgang Kainz</b>	Food and Drug Administration, USA
<b>Prof. Sami Khuri</b>	San Jose State University, USA
<b>Prof. Takeshi Kikuchi</b>	Ritsumeikan University, Japan
<b>Prof. Lukasz Kurgan</b>	University of Alberta, Canada
<b>Prof. Zhi-Pei Liang</b>	University of Illinois, USA
<b>Prof. Juan Liu</b>	Wuhan University, China
<b>Prof. Gert Lubec</b>	Medical University of Vienna, Australia
<b>Dr. Patrick Ma</b>	Hong Kong Polytechnic University, Hong Kong (China)
<b>Prof. Kenta Nakai</b>	The University of Tokyo, Japan
<b>Prof. Eddie Ng</b>	Technological University, Singapore
<b>Prof. Gajendra P. S. Raghava</b>	Head Bioinformatics Centre, India
<b>Prof. Qiu-Shi Ren</b>	Shanghai Jiao-Tong University, China
<b>Prof. Mingui Sun</b>	University of Pittsburgh, USA
<b>Prof. Hong-Bin Shen</b>	Shanghai Jiaotong University, China
<b>Prof. Yanmei Tie</b>	Harvard Medical School, USA
<b>Dr. Elif Derya Ubeyli</b>	TOBB University of Economics and Technology, Turkey
<b>Prof. Ching-Sung Wang</b>	Oriental Institute Technology, Taiwan (China)
<b>Dr. Longhui Wang</b>	Huazhong University of Science and Technology, China
<b>Prof. Dong-Qing Wei</b>	Shanghai Jiaotong University, China
<b>Prof. Zhizhou Zhang</b>	Tianjin University of Science and Technology, China
<b>Prof. Jun Zhang</b>	University of Kentucky, USA

## Editorial Assistants

**Feng Liu**

Scientific Research Publishing, USA. Email: [fengliu@scirp.org](mailto:fengliu@scirp.org)

**Shirley Song**

Scientific Research Publishing, USA. Email: [jbise@scirp.org](mailto:jbise@scirp.org)

---

## Guest Reviewers(According to Alphabet)

André E. Aubert	Siwen Jiang	Zoltan Lukacs	Costantino Salerno
Amparo Alonso-Betanzos	Myungjoo Kang	Bohdana Marvalova	José Nélío S SALES
Marwa Chendeb	Waltraud Klepal	Francesco Migliavacca	Hiroshi Sugiki
Oliver G. Ernst	Dmitry Knorre	Vivek Nigam	Yoko Takahashi
Manuela Ferrario	Detlef.Kuhl	Myriam Passamano	Erica Werner
John Garibaldi	Jeremy Li	Czabanski Robert	Shu-Lan Yeh
Hernâni Gonçalves			Keiko Yoshioka

**TABLE OF CONTENTS**  
**Volume 2, Number 6, October 2009**

<b>Analysis and prediction of exon, intron, intergenic region and splice sites for <i>A. thaliana</i> and <i>C. elegans</i> genomes</b>	
H. Lin, Q. Z. Li, C. X. Chen.....	367
<b>Directly immobilized DNA sensor for label-free detection of herpes virus</b>	
P. D. Tam, M. A. Tuan, N. D. Chien.....	374
<b>Development of a low cost fetal heart sound monitoring system for home care application</b>	
A. K. Mitra, N. K. Choudhari.....	380
<b>Classification with binary gene expressions</b>	
S. Tuna, M. Niranjana.....	390
<b>Study of blood fat concentration based on serum ultraviolet absorption spectra and neural network</b>	
W. H. Zhu, Z. M. Zhao, X. Guo, L. X. Wang, H. Chen.....	400
<b>ECG arrhythmia classification based on logistic model tree</b>	
V. Mahesh, A. Kandaswamy, C. Vimal, B. Sathish.....	405
<b>A MCMC strategy for group-specific 16S rRNA probe design</b>	
Y. B. Wu, L. R. Yan, H. Liu, H. C. Sun, H. W. Xie.....	412
<b>Inhomogeneous material property assignment and orientation definition of transverse isotropy of femur</b>	
H. S. Yang, T. T. Guo, J. H. Wu, X. Ma.....	419
<b>Unsupervised human height estimation from a single image</b>	
Y. P. Guan.....	425
<b>Design of occlusion pressure testing system for infusion pump</b>	
P. Zhang, S. Y. Wang, C. Y. Yu, M. Y. Zhang.....	431
<b>Design and development of a new biomedical / open surgical instrument</b>	
Z. Li.....	435
<b>Wavelet based detection of ventricular arrhythmias with neural network classifier</b>	
A. S. Subramanian, G. Gurusamy, G. Selvakumar.....	439
<b>Contrast enhancement methods in sodium MR Imaging: a new emerging technique</b>	
R. Sharma, A. Sharma, S. Kwon, R. Booth.....	445
<b>Trends in global warming and evolution of polymerase basic protein 2 family from influenza A virus</b>	
S. M. Yan, G. Wu.....	458
<b>Diabetic diagnose test based on PPG signal and identification system</b>	
H. Karimipour, H. T. Shandiz, E. Zahedi.....	465

---

The figure on the front cover shows the computed structure of  $\alpha 7$  nicotinic acetylcholine receptor (nAChR) homopentamer. (Courtesy of Kuo-Chen Chou.)

# Journal of Biomedical Science and Engineering (JBiSE)

## SUBSCRIPTIONS

The *Journal of Biomedical Science and Engineering* (Online at Scientific Research Publishing, [www.scirp.org](http://www.scirp.org)) is published monthly by Scientific Research Publishing, Inc., USA.

E-mail: [service@scirp.org](mailto:service@scirp.org)

**Subscription Rates:** Volume 2 2009

Printed: \$50 per copy.

Electronic: freely available at [www.scirp.org](http://www.scirp.org).

To subscribe, please contact Journals Subscriptions Department at [service@scirp.org](mailto:service@scirp.org).

**Sample Copies:** If you are interested in obtaining a free sample copy, please contact Scientific Research Publishing, Inc at [service@scirp.org](mailto:service@scirp.org).

## SERVICES

### Advertisements

Contact the Advertisement Sales Department at [service@scirp.org](mailto:service@scirp.org).

### Reprints (a minimum of 100 copies per order)

Contact the Reprints Co-ordinator, Scientific Research Publishing, Inc., USA.

E-mail: [service@scirp.org](mailto:service@scirp.org)

## COPYRIGHT

Copyright © 2009 Scientific Research Publishing, Inc.

All Rights Reserved. No part of this publication may be reproduced, stored in a retrieval system, or transmitted, in any form or by any means, electronic, mechanical, photocopying, recording, scanning or otherwise, except as described below, without the permission in writing of the Publisher.

Copying of articles is not permitted except for personal and internal use, to the extent permitted by national copyright law, or under the terms of a license issued by the national Reproduction Rights Organization.

Requests for permission for other kinds of copying, such as copying for general distribution, advertising or promotional purposes, for creating new collective works or for resale, and other enquiries should be addressed to the Publisher.

Statements and opinions expressed in the articles and communications are those of the individual contributors and not the statements and opinion of Scientific Research Publishing, Inc. We assume no responsibility or liability for any damage or injury to persons or property arising out of the use of any materials, instructions, methods or ideas contained herein. We expressly disclaim any implied warranties of merchantability or fitness for a particular purpose. If expert assistance is required, the services of a competent professional person should be sought.

## PRODUCTION INFORMATION

For manuscripts that have been accepted for publication, please contact:

E-mail: [jbiase@scirp.org](mailto:jbiase@scirp.org)



# Analysis and prediction of exon, intron, intergenic region and splice sites for *A. thaliana* and *C. elegans* genomes

Hao Lin<sup>1,2\*</sup>, Qian-Zhong Li<sup>1</sup>, Cui-Xia Chen<sup>1,3</sup>

<sup>1</sup>Laboratory of Theoretical Biophysics, Department of Physics, College of Sciences and Technology, Inner Mongolia University, Hohhot, China; <sup>2</sup>Center of Bioinformatics, School of Life Science and Technology, University of Electronic Science and Technology of China, Chengdu, China; <sup>3</sup>CapitalBio Corporation, Beijing, China; \*Correspondence should be addressed to Hao Lin.  
Email: [hlin@uestc.edu.cn](mailto:hlin@uestc.edu.cn)

Received 18 June 2008; revised 31 May 2009; accepted 8 June 2009.

## ABSTRACT

Although a great deal of research has been undertaken in the area of the annotation of gene structure, predictive techniques are still not fully developed. In this paper, based on the characteristics of base composition of sequences and conservative of nucleotides at exon/intron splicing site, a least increment of diversity algorithm (LIDA) is developed for studying and predicting three kinds of coding exons, introns and intergenic regions. At first, by selecting the 64 trinucleotides composition and 120 position parameters of the four bases as informational parameters, coding exon, intron and intergenic sequence are predicted. The results show that overall predicted accuracies are 91.1% and 88.4%, respectively for *A. thaliana* and *C. elegans* genome. Subsequently, based on the position frequencies of four kinds of bases in regions near intron/coding exon boundary, initiation and termination site of translation, 12 position parameters are selected as diversity source. And three kinds of the coding exons are predicted by use of the LIDA. The predicted successful rates are higher than 80%. These results can be used in sequence annotation.

**Keywords:** Exon; Intron; Intergenic Region; Splice Site; Increment of Diversity

## 1. INTRODUCTION

With the completion of the genomes sequencing, more and more efforts were being put into understanding the functional elements encoded in a genome [1,2,3,4,5,6]. Annotation of gene structure in eukaryotic genomes currently involves both computational and experimental

approaches [7,8,9,10]. Driven by this explosion of genome data and a need to analyze draft data quickly, genefinding programs have also proliferated, particularly those that were designed for specific organisms [11,12,13,14,15]. However, the accuracy was still far from satisfaction [16].

Gene prediction methods can be generally classified as composition-based and similarity-based methods. Composition-based methods, also called *ab initio* gene-finding method, contain two important aspects: type of information and the algorithm. Most types of information measure either codon usage bias, base compositional bias between codon positions or splice site as well as periodicity in base occurrence. Several sophisticated algorithms that deduce the presence of a gene feature using signals and content information have been devised including GenScan [17], Fgenes [18], Genie [19] and MZEF [20]. Although some satisfactory results were obtained by using above software, a considerable proportion of missing or incorrect exon and over predictions were found by using an experimentally validated dataset of some genomic sequences [21]. On the other hand, most *ab initio* gene prediction programs performed prediction based on large parameters. For example, 12,288 parameters were needed by GeneMark [22]. It will deduce unreliable prediction results for small genome [23]. Similarity-based methods such as Genewise [24] and Procrustes [25] predicted a gene relied on homolog sequences. These methods showed a high sensitivity and specificity for predicting genes whose sequence is closely related to the known input sequence. But some species-specific genes are likely to be missed [7]. In order to improve prediction, the programs of combining protein sequence similarity with *ab initio* gene-finding algorithms such as GenomeScan [26] were proposed. Despite great progress, the experiment highlighted errors

with the various predictions and indicated that both types of gene prediction programs are currently unable to determine whole gene structures consistently [27].

Although programs for splice site and gene structure recognition have reached a high level of performance on internal coding exons, standard splice sites might not be sufficient for defining introns in the genomes [28]. And prediction of splice sites in non-coding regions of genes is one of the most challenging aspects of gene structure recognition. The distinguishing intergenic region from intron should be very useful to understand the features of the noncoding and regulatory regions. In addition, finding first exons still remains a challenge, except where the true full-length mRNA sequences are available. Unfortunately, most of the available mRNA sequences are incomplete at their 5' ends and do not provide information about first exons. Apparently, the recognition of exon, intron and intergenic DNA at the meanwhile is very helpful for gene recognition. Specially, it is difficulty to distinguish intron from intergenic sequence in past algorithm.

In this paper, our goal is to provide a new computational method to predict gene structure base on least increment of diversity algorithm (LIDA). The diversity measure was first introduced and employed in biological classification [29]. It is a kind of information description on state space and a measure of whole uncertainty and total information of a system derived from information theory. To compare the similarity of two sources, one defines the increment of diversity (ID) by the difference of the total diversity measure of two systems and the diversity measure of the mixed system. It can be proved that the higher the similarity of two sources, the smaller the ID. So, the increment of diversity of two sources is essentially a measure of their similarity level.

Here, according to the theory of diversity, we firstly predict coding exons, introns and intergenic sequences of *A. thaliana* and *C. elegans* based on the analysis of the compositional differences in near splice sites and conserved sequence segments of the three kinds of sequences (exons, introns and intergenic sequences) in the complete genome of these two model organisms. Subsequently, three kinds of coding exons (first coding exons, internal coding exons and last coding exons) are predicted by use of the least increment of diversity algorithm. It may be useful for improving the prediction of splice sites.

## 2. EXPERIMENTAL

### 2.1. Data Sample

The *A. thaliana* and *C. elegans* genomic DNA sequences are obtained from Genbank. The coding exons, introns and intergenic sequences are respectively extracted from

the above genomes. According to the length distribution, we divide all sequences of one chromosome into three types of subsets. The ranges of three subsets are respectively (30-200bp), (200-500bp) and ( $\geq 500$ bp) for exon and intron sequences, (30-2000bp), (2000-5000bp) and ( $\geq 5000$ bp) for intergenic sequences.

The 15609 first coding exons, 67408 internal coding exons and 15791 last coding exons are extracted from *A. thaliana* complete genome. The 10904 first coding exons, 87743 internal coding exons and 11035 last coding exons are extracted from *C. elegans* complete genome. The subsequences with 9 bases length flanking 5' boundary sites (from  $-5^{\text{th}}$  site to  $+4^{\text{th}}$  site) and 3' boundary sites (from  $-4^{\text{th}}$  site to  $+5^{\text{th}}$  site) are meanwhile extracted respectively from above genome sequences.

### 2.2. Least Increment of Diversity Algorithm (LIDA)

Due to increment of diversity (ID) can measure increment of whole uncertainty (or information) between two data sources, it has been widely applied in bioinformatics investigation, such as protein structural class prediction [30], subcellular location of apoptosis protein [31] and secretory protein prediction [32]. For the purpose of improving prediction capability, ID combined with other predictive model was applied in exon/introns splice site prediction [33], human PolII promoter prediction [34] and protein predictions [35,36,37,38,39,40,41,42]. For reader's conveniences, the theory of diversity is introduced as follows.

Definition 1. For a state space  $X\{n_1, n_2, \dots, n_s\}$  consisting of  $s$  information symbols, if  $n_i$  indicates the numbers of the  $i$ -th state, then the diversity for diversity source  $X: [n_1, n_2, \dots, n_s]$  is defined as [30],

$$D(X) = D(n_1, n_2, \dots, n_s) = N \log N - \sum_{i=1}^s n_i \log n_i \quad (1)$$

here  $N = \sum_{i=1}^s n_i$ . It is easily proved that the diversity equals  $N$  fold of information entropy [43].

Definition 2. If there are two sources of diversity in the same space of  $s$  dimension,  $X: [n_1, n_2, \dots, n_s]$  and  $Y: [m_1, m_2, \dots, m_s]$ , we may define the increment of diversity as

$$\Delta(X, Y) = D(X + Y) - D(X) - D(Y) \quad (2)$$

where  $D(X+Y)$  is the measure of diversity of the mixed source  $X+Y: [n_1 + m_1, n_2 + m_2, \dots, n_s + m_s]$ . Note that  $\Delta(X, Y)$  is a function of two sources. It is easily proved that the increment of diversity [Eq.(2)] is nonnegative and symmetry. Therefore,  $\Delta(X, Y)$  is regarded as a quantitative measure of the similarity level of two independence systems.

### 2.3. Prediction of Exon, Intron and Intergenic Sequence

One DNA sequence can be represented by a diversity source:  $X: [S_i, N_{jk}, M_{lk}]$ , where  $S_i$  means the absolute frequency of the  $i$ -th trinucleotide in the sequence ( $i=1,2,\dots,4^3$ );  $N_{jk}$  means the absolute frequency of base  $k$  at the  $j$ -th position from the beginning of 5' boundary ( $j=1, 2, \dots, 15$ ),  $M_{lk}$  means the absolute frequency of bases  $k$  at the  $l$ -th position from the end of 3' boundary, ( $l=-1, -2, \dots, -15$ ). By calculating above 180 ( $4^3+15\times4+15\times4$ ) parameters of exons, introns and intergenic sequences in standard sets (training sets), we deduce three standard sources of diversity  $X_\xi: [n_1^\xi, n_2^\xi, \dots, n_{184}^\xi]$  in the state space of 184 dimensions. (here  $\xi = e, i, g$  indicates respectively the exon, intron and intergenic sequence.) Three standard measures of diversity can be deduced by use of similar equations as **Eq.(1)**, namely

$$D(X_\xi) = N_\xi \log N_\xi - \sum_{k=1}^{184} n_k^\xi \log n_k^\xi \quad (3)$$

where  $N_\xi = \sum_{k=1}^{184} n_k^\xi$  ( $k=1, 2, \dots, 184$ ), ( $\xi = e, i, g$ ).

Suppose that  $X$  is a DNA sequence whose class is to be predicted. In the same state space, the measure of diversity of sequence  $X$  can be expressed as:

$$D(X) = M \log M - \sum_{k=1}^{184} m_k \log m_k \quad (4)$$

where  $M = \sum_{k=1}^{184} m_k$  ( $k=1, 2, \dots, 184$ ).

The increments of diversity between the diversity source  $X: [m_1, m_2, \dots, m_{184}]$  and the three standard diversity sources  $X_\xi: [n_1^\xi, n_2^\xi, \dots, n_{184}^\xi]$ , (here  $\xi = e, i, g$ ) are

$$\Delta(X, X_\xi) = D(X + X_\xi) - D(X) - D(X_\xi) \quad (\xi = e, i, g) \quad (5)$$

Sequence  $X$  can be predicted to be the class for which the corresponding increment of diversity has the minimum value, and can be formulated as follows.

$$\Delta(X_\xi, X) = \text{Min}\{\Delta(X_e, X), \Delta(X_i, X), \Delta(X_g, X)\} \quad (6)$$

where  $\xi$  can be  $e, i$  or  $g$  and the operator **Min** means taking the minimum value among those in the parentheses, then the  $\xi$  in **Eq.(6)** will give the sequence class to which the predicted sequence  $X$  should belong.

### 2.4. Prediction of Three Kinds of Coding Exons

For each coding exon, the following three kinds of codon positions are investigated to select optimal parameters.

1) The three bases before the 5' boundary sites of exons (acceptor sites) and after the 3' boundary sites of

exons (donor sites) are chosen as information parameters of diversity source.

AGA GCA↑ATG G.....A TGC↑GTA AGA

2) The three bases after the 5' boundary sites of exons (acceptor sites) and before the 3' boundary sites of exons (donor sites) are chosen as information parameters of diversity source.

AGA GCA↑ATG G.....A TGC↑GTA AGA

3) The six bases flanking the 5' boundary sites of exons (acceptor sites) and the 3' boundary sites of exons (donor sites) are chosen as information parameters of diversity source.

AGA GCA↑ATG G.....A TGC↑GTA AGA

(where↑indicates the 5' or 3' exon boundary sites)

By calculating the absolute frequencies of four bases in above positions near splice sites of first coding exons, internal coding exons and last coding exons, we deduce three standard sources of diversity  $X_\xi: \{N_{ja}^\xi \mid j=1,2,3; a=A,C,G,T\}$  in the state space of 12 dimensions (here  $\xi = f, i, l$  corresponding to first coding exon, internal coding exon and last coding exon, respectively). Then, three standard measures of diversity for three coding exons can be calculated by **Eq.(1)**, namely:

$$D(X_\xi) = N_\xi \log N_\xi - \sum_{k=1}^{12} n_k^\xi \log n_k^\xi \quad (7)$$

where  $N_\xi = \sum_{k=1}^{12} n_k^\xi$  ( $k=1, 2, \dots, 12$ ).

Suppose that  $S$  is an exon whose class is to be predicted. In the same state space, the measure of diversity can be expressed as:

$$D(S) = M \log M - \sum_{k=1}^{12} m_k \log m_k \quad (8)$$

According to **Eq.(2)**, the increments of diversity between source  $S$  and three standard sets are

$$\Delta(S, X_\xi) = D(S + X_\xi) - D(S) - D(X_\xi) \quad (\xi = f, i, l) \quad (9)$$

Exon ( $S$ ) can be predicted to be the class for which the corresponding increment of diversity has the minimum value, can be formulated as follows

$$\Delta(X_\xi, S) = \text{Min}\{\Delta(X_f, S), \Delta(X_i, S), \Delta(X_l, S)\} \quad (10)$$

where  $\xi$  can be  $f, i$  or  $l$  and the operator **Min** means taking the minimum value among those in the parentheses, then the  $\xi$  in **Eq.(9)** will give the class to which the predicted coding exon  $S$  should belong.

## 3. RESULTS

### 3.1. Evaluating Predicted Performance of Proposed Method

In order to evaluate the correct prediction rate and reliability of a predictive method, the sensitivity ( $S_n$ ), speci-

ficity ( $S_p$ ) and correlation coefficient ( $CC$ ) are defined by

$$S_n = TP / (TP + FN)$$

$$S_p = TP / (TP + FP)$$

$$CC = \frac{(TP \times TN) - (FP \times FN)}{\sqrt{(TP + FP) \times (TN + FN) \times (TP + FN) \times (TN + FP)}}$$

For a given sequence class  $\xi$ ,  $TP$  denotes the number of the sequences correctly predicted to be in  $\xi$  class sequences (true positive),  $FP$  denotes the number of the sequences incorrectly predicted to be in  $\xi$  class sequences (false positive),  $TN$  denotes the number of the sequences correctly predicted to be in non- $\xi$  class sequences (true negatives),  $FN$  denotes the number of the sequences incorrectly predicted to be in non- $\xi$  class sequences (false negative). Sensitivity shows the rate of correct prediction. Specificity shows the confidence level for predictive method. The correlation coefficient ( $CC$ ) affects the entirely performance of the prediction algorithm.

### 3.2. The Prediction of Exon, Intron and Intergenic Sequence

Approximate 1/2 sequences of standard sets (training sets) and 1/2 testing sets are randomly chosen by computer programs from the corresponding subset. In order to eliminate the dependence of the predictive results on the training dataset, the standard set (training set) are randomly selected 10 times. The numbers of the known coding exons, introns and intergenic sequences are shown in **Table 1**.

Based on the **Eq.(6)**, the three classes of sequences are predicted by use of the 184 information parameters. In order to compare prediction quality of different information parameters, we perform our algorithm to predict exons, introns and intergenic sequences using 64 trinucleotides. The contrast results of test sets between 64 and 184 signals parameters for *A. thaliana* (A) and *C. elegans* (C) are shown in **Table 2**.

**Table 1.** The length-distribution of three kinds of sequences in the chromosomes of the two model species.

Genome	class	Standard set				Test set			
		1 <sup>st</sup> subset	2 <sup>nd</sup> subset	3 <sup>rd</sup> subset	total	1 <sup>st</sup> subset	2 <sup>nd</sup> subset	3 <sup>rd</sup> subset	total
<i>A.thaliana</i> Chr1~4	Exon	15229	4723	2126	22728	14982	4868	2417	22267
	Intron	16130	3183	919	20329	16181	3405	870	20456
	Intergenic	6109	2525	1109	9747	6742	2490	1105	10337
<i>C.elegans</i> Chr1~6	Exon	10507	4896	1002	16739	12214	4809	1034	18057
	Intron	12181	2859	2283	17354	13217	2935	2317	18469
	Intergenic	5023	1446	1109	7617	5483	1598	1086	8167

**Table2.** The results for test set with 64 and 184 signals of *A. thaliana* and *C. elegans*.

No. of signals	Class of exon	<i>A. thaliana</i>			<i>C. elegans</i>		
		$S_n$ (%)	$S_p$ (%)	$CC$ (%)	$S_n$ (%)	$S_p$ (%)	$CC$ (%)
64	Exon	85 (95, 98)	94 (96, 95)	83 (92, 93)	73 (78, 88)	89 (95, 95)	70 (74, 89)
	Intron	85 (81, 73)	89 (91, 83)	78 (80, 73)	92 (75, 67)	87 (78, 87)	81 (66, 57)
	Intergenic	86 (92, 83)	65 (78, 80)	69 (79, 75)	66 (65, 78)	53 (41,50)	50 (39,47)
184	Exon	84 (91, 94)	96 (98, 98)	84 (90,91)	73 (76,84)	92 (98, 98)	73 (76, 88)
	Intron	98 (98, 99)	88 (87, 79)	88 (88, 85)	99 (99,100)	90 (85,93)	91 (88, 92)
	Intergenic	88 (90, 84)	89 (94,95)	86 (90, 86)	79 (85, 87)	65 (63,90)	65 (67, 85)

The number outside the bracket denotes the predicted results for the 1<sup>st</sup> subset. Two numbers in bracket, respectively, denotes the predicted results for the 2<sup>nd</sup> subset and the 3<sup>rd</sup> subset.

**Table 3.** The results of prediction for three kinds of exons in *A. thaliana* and *C. elegans* genomes.

Methods	Class of exon	<i>A. thaliana</i>			<i>C. elegans</i>		
		<i>Sn</i> (%)	<i>Sp</i> (%)	<i>CC</i> (%)	<i>Sn</i> (%)	<i>Sp</i> (%)	<i>CC</i> (%)
First choosing method	First coding exon	86	74	76	86	70	75
	Internal coding exon	93	93	77	96	97	81
	Last coding exon	82	96	87	87	98	89
Second choosing method	First coding exon	90	54	63	82	33	45
	Internal coding exon	68	95	55	62	96	38
	Last coding exon	89	56	64	87	34	48
Third choosing method	First coding exon	86	57	64	86	40	52
	Internal coding exon	74	94	58	74	96	50
	Last coding exon	88	62	69	88	49	61

### 3.3. The Prediction of Three Kinds of Coding Exons

For predicting three types of coding exons, a total of 1000 first coding exons, 1000 internal coding exons and 1000 last coding exons are randomly selected as training sets from gene sequences of *A. thaliana* and *C. elegans*. The remained sequences are regarded as the test sets. In order to eliminate the dependence of the predictive results on the training dataset, this selected procession repeat 10 times.

According to Eq.(10), three types of coding exons using different information parameters are predicted. The results are shown in Table 3. As seen from Table 3, the first parameter-chosen method achieve best results among three kinds of parameters.

## 4. DISCUSSION

The recognition results of the exon, intron and intergenic sequence show that the  $S_n$ ,  $S_p$  and  $CC$  values with 184 parameters are higher than the results with 64 signals. For *A. thaliana* (*A*) and *C. elegans* (*C*), the average correct prediction rates of standard sets are 88.6% and 88.2%, the average correct prediction rates of testing sets are 93.6% and 88.4%, respectively. Overall correct prediction rates are 91.1% and 88.4%, respectively.

For evaluating performance of proposed method, exons, introns and intergenic sequences of *D. melanogaster*s and *S. cerevisiae* were predicted using 184 parameters. The overall accuracies of 92.28% and 94.88% were achieved for *D. melanogaster*s and *S. cerevisiae*, respectively. We also performed LIDA to predict coding regions and intergenic sequences of *E. coli*. The overall accuracy of 92.88% was achieved.

Despite great progress, however, gene prediction entirely based on DNA analysis is still far from perfect. In the recent comparison of gene-prediction programs, the best algorithms in two well-annotated regions could achieve sensitivities (a measure of the ability to detect true positives) and specificities (a measure of the ability to discriminate against false positives) of less than 95% and 90% for different genomes, respectively [44,45].

In our method, three kinds of sequences (exons, introns and intergenic sequences) are simultaneously predicted. If considering the random effect, the correct prediction rate for three kinds of sequences is only 2/3 of the correct prediction rate for two kinds of sequences (exons and introns). That is to say, if two types of sequences are simultaneously predicted, the random correction rate is 1/2; if three types of sequences are simultaneously predicted, the random correction rate is 1/3. Such as, 90% correct prediction rate for predicting two types of sequences is only same as 60% for predicting three types of sequences. So, same correct prediction rate in our result is higher than the correct prediction rate of two kinds of sequences in any other methods.

The results of the prediction for the three types of coding exons indicate that the sensitivity ( $S_n$ ), specificity ( $S_p$ ) and correlation coefficient ( $CC$ ) are the best by use of three bases before the 5' boundary sites of exons and after the 3' boundary sites of exons in three selections. Especially, the correlation coefficient ( $CC$ ) is apparently higher in first choosing method than that in second and third methods. It is consistent with the highly conserved sequences near the ends of introns and the conserved GT-AG rule. The three kinds of coding exons have not been studied in other methods.

In addition, according to the statistical analysis of se-



quences in the region near splicing sites, we find there are some special preferences for certain bases. The results show that the sequence of the near splice site region is strongly conserved. Except the GT-AG rule, there is a strong bias of base G in the -4th site from the 3' term of introns for *A. thaliana* genome, but the base T is biased in the same site for *C. elegans* genome. The stop codons of the two model species bias TAA, and the bases GT and AT are biased in the two sites after the stop codon for *A. thaliana* and *C. elegans* genomes, respectively. It may be a possible signal for stopping translation. The base A is biased at positions -4, -2 and -1 before translation start sites. And the bases G and A are respectively biased in the 4-th site after translation start sites (TSS). These biases may be relative to the translation start signals. In addition, the base bias of the 1-st sites of the 5' term within internal coding exons and last coding exons is different for *A. thaliana* from *C. elegans* genomes. The base G is biased by the *A. thaliana*, base A is biased by *C. elegans*.

By the further statistics of the base pairs in the boundary region of exons, the first coding exons and internal coding exons in *A. thaliana* and *C. elegans* genomes are generally ended by AG. The internal coding exons and last coding exons in *A. thaliana* genome are generally started by GT, but the two exons in *C. elegans* genome are generally started by AT. It is possible additional information for splice sites. These results may be very useful to improve correct prediction rate of splice sites.

## 5. CONCLUSIONS

This paper proposed a novel algorithm-increment of diversity for gene structure prediction. This algorithm may be deduced from information entropy. It is well known that the mutual information can describe how to extract information regarding b from source a if the conditional probability  $p(b|a)$  is known [33]. But ID is different from mutual information. It can describe increment of complication between two informational sources. Our prediction results also exhibit that ID is a promising method.

## 6. ACKNOWLEDGEMENTS

The authors thank Professor C. J. Benham and Dr. H.Q. Wang in UC Davis for helpful discussions. The work was supported by National Science Foundation of China, No. 30560039.

## REFERENCES

- [1] J. L. Ashurst and J. E. Collins, (2003) Gene annotation: Prediction and testing, *Annu. Rev. Genomics Hum Genet.*, **4**, 69–88.
- [2] M. Nowrousian, C. Würtz, S. Pöggeler, and U. Kück, (2004) Comparative sequence analysis of *Sordaria macrospora* and *Neurospora crassa* as a means to improve genome annotation, *Fungal Genetics and Biology*, **41**, 285–292.
- [3] E. Eden and S. Brunak, (2004) Analysis and recognition of 5'UTR intron splice sites in human Pre-mRNA, *Nucleic Acids Res.*, **32**, 1131–1142.
- [4] M. Kozak, (2006) Rethinking some mechanisms invoked to explain translational regulation in eukaryotes, *Gene*, **382**, 1–11.
- [5] H. A. Meijer and A. A. M. Thomas, (2002) Control of eukaryotic protein synthesis by upstream open reading frames in the 5'-untranslated region of an mRNA, *Biochem. J.*, **367**, 1–11.
- [6] F. B. Guo and X. J. Yu, (2007) Re-prediction of protein-coding genes in the genome of *Amsacta moorei* entomopoxvirus, *Journal of Virological Methods*, **146**, 389–392.
- [7] F. B. Guo and C. T. Zhang, (2006) ZCURVE\_V: A new self-training system for recognizing protein-coding genes in viral and phage genomes, *BMC Bioinformatics*, **7**, 9.
- [8] Y. H. Qiao, J. L. Liu, C. G. Zhang, X. H. Xu, and Y. J. Zeng, (2005) SVM classification of human intergenic and gene sequences, *Mathematical Biosciences*, **195**, 168–178.
- [9] V. Brendal, L. Xing, and W. Zhu, (2004) Gene structure prediction from consensus spliced alignment of multiple ESTs matching the same genomic locus, *Bioinformatics*, **20**, 1157–1169.
- [10] S. Karlin, J. Mrázek, and A. J. Gentles, (2003) Genome comparisons and analysis, *Current Opinion in Structural Biology*, **13**, 344–352.
- [11] S. Gopal, G. A. M. Cross, and T. Gaasterland, (2003) An organism-specific method to rank predicted coding regions in *Trypanosoma brucei*, *Nucleic. Acids Res.*, **31**, 5877–5885.
- [12] S. D. Schlueter, Q. Dong, and V. Brendel, (2003) Gene-Seqer@PlantGDB: Gene structure prediction in plant genomes, *Nucleic. Acids Res.*, **31**, 3597–3600.
- [13] J. E. Moore and J. A. Lake, (2003) Gene structure prediction in syntenic DNA segments, *Nucleic. Acids Res.*, **31**, 7271–7279.
- [14] J. Wang, *et al.*, (2003) Vertebrate gene predictions and problem of large genes, *Nature Reviews Genetics*, **4**, 741–749.
- [15] F. Gao and C. T. Zhang, (2004) Comparison of various algorithms for recognizing short coding sequences of human genes, *Bioinformatics*, **20**, 673–681.
- [16] M. Q. Zhang, (2002) Computational prediction of eukaryotic protein-coding genes, *Nature Reviews Genetics*, **3**, 698–709.
- [17] Burge, C. and Karlin, S. (1997) Prediction of complete gene structures in human genomic DNA, *J. Mol. Biol.*, **268**, 78–94.
- [18] V. V. Solovyev, A. A. Salamov, and C. B. Lawrence, (1995) Identification of human gene structure using linear discriminant functions and dynamic programming, *Proc. Int. Conf. Intell. Syst. Mol. Biol.*, **3**, 367–375.
- [19] M. G. Reese, D. Kulp, H. Tammana, and D. Haussler, (2000) Genie-Gene finding in *Drosophila melanogaster*, *Genome. Res.*, **10**, 529–538.
- [20] S. Rogic, A. K. Mackworth, and F. B. Ouellette, (2001) Evaluation of gene-finding programs on mammalian sequences, *Genome. Res.*, **11**, 817–832.
- [21] M. Q. Zhang, (1997) Identification of protein coding regions in human genome by quadratic discriminant ana-

- lysis, *Proc. Natl. Acad. Sci., USA*, **94**, 565–568.
- [22] J. Besemer, A. Lomsadze, and M. Borodovsky, (2001) GeneMarkS: A self-training method for prediction of gene starts in microbial genomes, implications for finding sequence motifs in regulatory regions, *Nucleic Acids. Res.*, **29**, 2607–2618.
- [23] F. B. Guo, H. Y. Ou, and C. T. Zhang, (2003) ZCURVE: a new system for recognizing protein-coding genes in bacterial and archaeal genomes, *Nucleic. Acids. Res.*, **31**, 1780–1789.
- [24] E. Birney and R. Durbin, (2000) Using GeneWise in the *Drosophila* annotation experiment, *Genome. Res.*, **10**, 547–548.
- [25] M. S. Gelfand, *et al.*, (1996) Gene recognition via spliced sequence alignment, *Proc. Natl. Acad. Sci., USA*, **93**, 9061–9066.
- [26] R. F. Yeh, L. P. Lim, and C. B. Burge, (2001) Computational inference of homologous gene structures in the human genome, *Genome. Res.*, **11**, 803–816.
- [27] I. M. Meyer and R. Durbin, (2004) Gene structure conservation aids similarity based gene prediction, *Nucleic Acids. Res.*, **32**, 776–783.
- [28] L. P. Lim and C. B. Burge, (2001) A computational analysis of sequence features involved in recognition of short introns, *Proc. Natl. Acad. Sci., USA*, **98**, 11193–11198.
- [29] R. R. Laxton, (1978) The measure of diversity, *J. Theor. Biol.*, **70**, 51–67.
- [30] Li, Q. Z. and Lu, Z. Q., (2001) The prediction of the structural class of protein: Application of the measure of diversity, *J. Theor. Biol.*, **213**, 493–502.
- [31] Chen, Y. L. and Li, Q. Z., (2007) Prediction of the subcellular location of apoptosis proteins, *J. Theor. Biol.*, **245**, 775–783.
- [32] Y. C. Zuo and Q. Z. L., (2009) Using K-minimum increment of diversity to predict secretory proteins of malaria parasite based on groupings of amino acids, *Amino Acids*, DOI 10.1007/s00726-009-0292-1.
- [33] L. R. Zhang and L. F. Luo, (2003) Splice site prediction with quadratic discriminant analysis using diversity measure, *Nucleic. Acids. Res.*, **31**, 6214–6220.
- [34] J. Lu and L. F. Luo, (2005) Human polII promoter prediction, *Prog. Biochem. Biophys.*, **32**, 1185–1191.
- [35] H. Lin and Q. Z. Li, (2007) Predicting conotoxin superfamily and family by using pseudo amino acid composition and modified Mahalanobis discriminant, *Biochem. Biophys. Res. Commun.*, **354**, 548–551.
- [36] H. Lin, and Q. Z. Li, (2007) Using pseudo amino acid composition to predict protein structural class: Approached by incorporating 400 dipeptide components, *J. Comput. Chem.*, **28**, 1463–1466.
- [37] F. M. Li and Q. Z. Li, (2008) Using pseudo amino acid composition to predict protein subnuclear location with improved hybrid approach, *Amino Acids*, **34**, 119–125.
- [38] X. Z. Hu and Q. Z. Li, (2008) Prediction of the  $\beta$ -Hairpins in proteins using support vector machine, *Protein J.*, **27**, 115–122.
- [39] H. Lin, (2008) The modified Mahalanobis Discriminant for predicting outer membrane proteins by using chou's pseudo amino acid composition, *J. Theor. Biol.*, **252**, 350–356.
- [40] X. Z. Hu, Q. Z. Li, and C. L. Wang, (2009) Recognition of beta-hairpin motifs in proteins by using the composite vector, *Amino Acids*, DOI 10.1007/s00726-009-0299-7.
- [41] W. Chen and L. Luo, (2009) Classification of antimicrobial peptide using diversity measure with quadratic discriminant analysis, *J. Microbiol Methods*, DOI: 10.1016/j.mimet.2009.03.013.
- [42] Y. Feng and L. Luo, (2008) Use of tetrapeptide signals for protein secondary-structure prediction, *Amino Acids*, **35**, 607–614.
- [43] L. Luo, (2006) Information biology: Hypotheses on coding information quantity, *Acta Scientiarum Naturalium Universitatis NeiMongol*, **37**, 285–294.
- [44] Z. Wang, Y. Z. Chen, and Y. X. Li, (2004) A brief review of computational gene prediction methods, *Geno. Prot. Bioinfo.*, **2**, 216–221.
- [45] L. Stein, (2001) Genome annotation: From sequence to biology, *Nature Rev. Genet.*, **2**, 493–503.

# Directly immobilized DNA sensor for label-free detection of herpes virus

Phuong Dinh Tam<sup>1,2</sup>, Mai Anh Tuan<sup>2</sup>, Nguyen Duc Chien<sup>3</sup>

<sup>1</sup>Hanoi Advanced School of Science and Technology, Hanoi University of Technology, Hanoi, Vietnam; <sup>2</sup>International Training Institute for Materials Science, Hanoi University of Technology, Hanoi, Vietnam; <sup>3</sup>Institute of Engineering Physics, Hanoi University of Technology, Hanoi, Vietnam.

Email: [tampd-hast@mail.hut.edu.vn](mailto:tampd-hast@mail.hut.edu.vn)

Received 24 March 2008; revised 12 May 2009; accepted 29 June 2009.

## ABSTRACT

This paper reports the direct immobilization of deoxyribonucleic acid (DNA) sequences of Herpes simplex virus (5'-AT CAC CGA CCC GGA GAG GGA C-3') on the surface of DNA sensor by using the cyclic voltammetric method with the presence of pyrrole. The potential was scanned from -0.7 volt to + 0.6 volt, the scanning rate was at 100mV/s. This kind of DNA sensor was developed to detect Herpes virus DNA in real samples. The FTIR was applied to verify specific binding of DNA sequence and conducting polymer, the morphology of conducting polymer doped with DNA strands was investigated by using a field emission scanning electron microscope (FE-SEM). The results showed that output signal given by co-immobilized DNA/PPy membrane sensor was better than that given by APTS immobilized membrane sensors. The sensor can detect as low as 2 nM of DNA target in real samples.

**Keywords:** DNA Sensor; Hybridization; APTS

## 1. INTRODUCTION

The detection of specific DNA/RNA sequences is of great importance in numerous applications of modern life science, including identification of medical research and clinical diagnosis [1,2], controlling the food quality [3,4], environmental analysis [5,6]. Many methods have been used for this purpose such as polymerase chain reaction (PCR) [7,8,9], quartz crystal micro-balance (QCM) [10,11], fluorescence [12], surface plasmon resonance [13], microfluidic system [14], cell culture and real-time PCR, etc. These methods are precise, and allow a wide, dynamic range of detection. However, they are complex, costly and time consuming. In addition, it is impossible to carry the on-site/in-field tests. Thus,

development of a cheap, reliable device allowing rapid detection is always the challenge for scientists and engineers. In this context, DNA sensor based on electrochemical detection is one of the feasible and promising tools.

We reported, in this paper, the direct co-immobilization of DNA sequence of Herpes simplex virus and polypyrrole onto the surface of a sensor by cyclic voltammetry to determine the herpes DNA target sequence in the sample. The herpes simplex virus (HSV) is an enveloped double-stranded DNA virus. There are two distinct forms of HSV, serotype 1 and serotype 2 (HSV-1 and HSV-2). HSV-2 is the most common cause of genital herpes, whereas HSV-1 is the most common cause of facial herpes or cold sores. HSV-1 is transmitted through contact with oral secretions. Diseases caused by Herpes virus are commonly found in patients in Vietnam.

## 2. EXPERIMENTS

### 2.1. Chemical Reagents

DNA sequences used in this work (Table 1) were supplied by Invitrogen Life Technologies Company through National Institute of Hygiene and Epidemiology of Vietnam. Pyrrole was purchased from Merck. Other chemicals are of analytical grade.

### 2.2. Sensor Fabrication

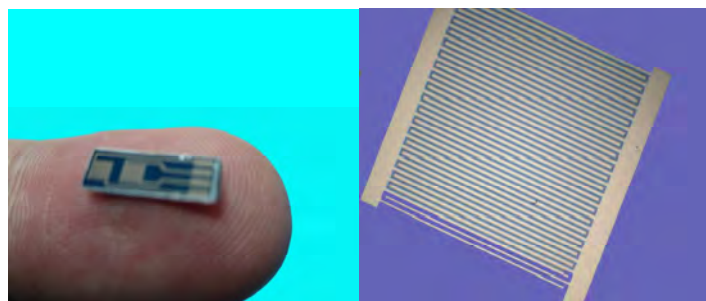
The microelectrode based DNA sensor was designed and fabricated at clean room of ITIMS. The sensor consists of pairs of microelectrodes on the surface of silicon substrate, one of which acts as working sensor and the other as a reference electrode. The dimension of the inter-electrodes was 20  $\mu\text{m}$  x 20  $\mu\text{m}$  (Figure 1). The detailed fabrication process was discussed in [15].

### 2.3. Cyclic Voltammetry Electropolymerization

Electropolymerization was carried out by using IM6EX

**Table 1.** DNA sequences used in this work.

Types	DNA sequences
Probe	5'-AT CAC CGA CCC GGA GAG GGA C-3'
Non-complementary	5'-AT CAC CGA CCC GGA GAG GGA C-3'
Target	3'-TA GTG GCT GGG CCT CTC CCT G-5'
Mis/1	3'-TA GTG <u>G</u> GT GGG CCT CTC CCT G-5'
Mis/2	3'-TA GTG <u>G</u> GT GGG <u>A</u> AT CTC CCT G-5'

**Figure 1.** 20  $\mu\text{m}$  x 20  $\mu\text{m}$  microelectrode sensor was fabricated at ITIMS.

(Germany) impedance analyzer at room temperature in which the micro-sensor acted as working electrode while auxiliary electrode was a platinum wire. Reference electrode is Ag/AgCl in saturated KCl.

The sensor was first surface cleaned by  $\text{KCr}_2\text{O}_7$  in  $\text{H}_2\text{SO}_4$  98% followed by cyclic voltammograms (swept potential from  $-1.5\text{V}$  to  $+2.1\text{V}$ , scan rate:  $25\text{mV/s}$ ) in  $0.5\text{M}$   $\text{H}_2\text{SO}_4$  to activate the surface of the sensors. Finally, the potential was swept on the working electrode from  $-0.7$  volt to  $0.6$  volt versus standard counter electrode (SCE). The scanning rate was  $100\text{mV/s}$ .

## 2.4. Measurement

Differential measurements were realized to determine the changes in conductance of DNA membrane. An AC reference signals (10 KHz,  $100\text{mV}$  sine wave), generated by the generator of Lock-in Amplifier SR830, and was applied on two identical micro-electrodes of DNA sensor. The output signal was acquired by measuring the voltage drop on two  $1\text{K}\Omega$  resistances by the A and B channels of the Lock-in Amplifier and processed by a PC through RS 232 interface. All measurements were performed at room temperature. In this experiment, five DNA sensors were used to test the hybridization of DNA sequences.

## 3. RESULTS AND DISCUSSION

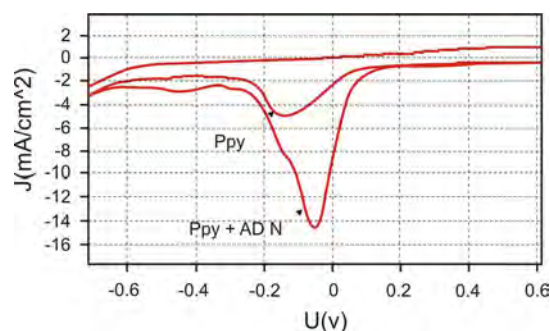
### 3.1. The Polymerization of PPy/DNA

Normally, pyrrole is polymerized with the presence of an anionic dopant which contributes to film conductivity. Variety of anions can be used as dopant for polypyrrole

(PPy) polymerization such as  $\text{Cl}^-$ ,  $\text{NO}_3^-$ . In this work  $\text{ClO}_4^-$  and DNA sequence were used.

According to Wang *et al* [16], DNA can be considered as sole counter anion in the electropolymerization process at the working electrode. This allowed maximum possible incorporation of DNA in the conductive polymer throughout the film thickness and full contribution of oligonucleotides charged phosphates to the polymer conductivity.

The cyclic voltammograms of synthesized Ppy and Ppy/DNA film is shown in **Figure 2** where the oxidation of pyrrole monomer leads to the formation of radical cation, subsequent oxidation of the dimer and coupling will result in the formation of an insoluble polymer, positively charged on the surface. This electrochemical procedure allowed the formation of a copolymer which

**Figure 2.** Cyclic voltammograms of  $0.5\text{mM}$  Ppy doped  $0.05\mu\text{M}$  DNA probe sequence in  $\text{LiClO}_4$  solution. Swept potential from  $-0.7\text{V}$  to  $0.6\text{V}$ , scanning rate is at  $100\text{mV/s}$ .



is a mixture of polypyrrole and an oligonucleotides that shows an increasing current along with conducting film growth which corresponds to incorporation of oligo into the Ppy film. The film was rinsed and used for detection of DNA hybridization.

### 3.2. FTIR Spectrum of Ppy and DNA/Ppy

In this work, the FTIR spectroscopy was used to verify the existence of polypyrrole and DNA sequence on the microelectrode surface after the polymerization process. The infrared spectrum of the DNA/Ppy complexes and pure Ppy were performed on Nicolet 6700 FT-IR machine with the effective range from  $400\text{ cm}^{-1}$  to  $4000\text{ cm}^{-1}$  at room temperature. As shown in **Figure 3**, the absorption band at  $1889\text{ cm}^{-1}$ – $1629\text{ cm}^{-1}$  vibration plane implied G-C and A-T base pairs while the backbone phosphate group at  $1095\text{ cm}^{-1}$  was perturbed upon Ppy interaction [17,18].

The absorption band at  $1254\text{ cm}^{-1}$  was assigned to the bipolaronic species formed in the over oxidation pro-

cess of Ppy [19]. The C-H and N-H bonds were also observed at  $735\text{ cm}^{-1}$  (for DNA/Ppy film);  $734\text{ cm}^{-1}$  for Ppy film;  $894\text{ cm}^{-1}$  for DNA/Ppy and  $897\text{ cm}^{-1}$  for Ppy membrane, respectively. These results show very good agreement with earlier reported work [20].

### 3.3. Morphology of Conducting Polymer Film

The morphology of sensor surface coated with Ppy film was studied by FE-SEM. **Figure 4** indicated micrographs of polypyrrole doped with  $\text{LiClO}_4$  (4a) and with both  $0.1\text{ M LiClO}_4$  and  $0.05\text{ }\mu\text{M}$  DNA sequence (4b) membrane given by direct electropolymerization method.

In **Figure 4(a)**, the pure PPy doped with  $\text{LiClO}_4$  was cauliflower structure matching other works [21]. This structure is related to the dopant intercalation in the polymeric chain. As in **Figure 4(b)** the DNA strands was observed as white dots in host polymer membrane. Good distribution of DNA in PPy membrane makes it advantage for hybridization process of the probe in target solution.

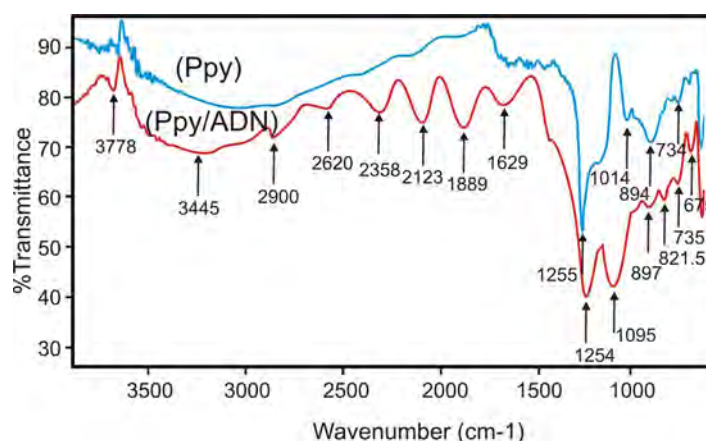


**Figure 3.** The FTIR spectra of Ppy/DNA and Ppy (upper curve: Ppy/dopant, lower curve: Ppy/dopant/DNA).

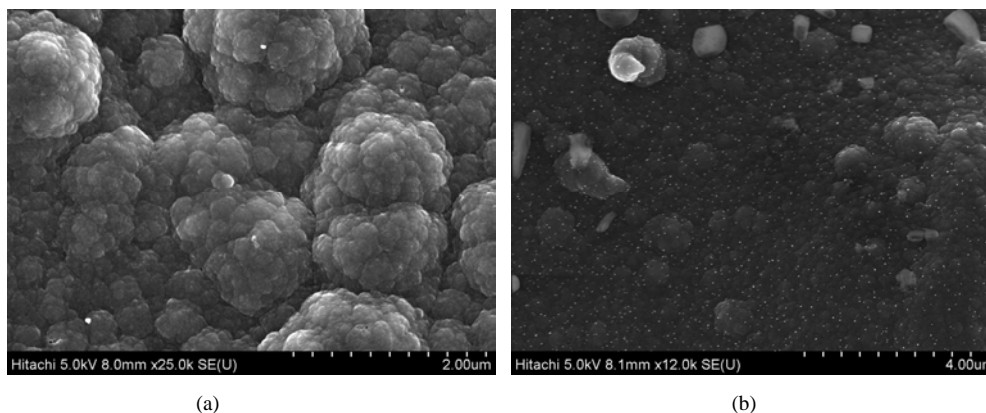


**Figure 4.** The FE-SEM of Ppy and Ppy–DNA coated onto microelectrode surface. a) Ppy doped  $\text{LiClO}_4$ ; b) © Ppy doped  $\text{LiClO}_4$  and DNA.



### 3.4. The Hybridization of DNA Sensor

As above-mentioned, the probe-attached sensor is commonly soaked into solution containing target DNA. A DNA helix sequence is formed on the surface of the sensor when target/immobilized DNA matching occurred.

Such hybridization is detected by changes in the conductance of the conductive membrane on the surface of sensors leading to the change in output signal of the system. In **Figure 5**, the hybridization illustrated by linear curve that described the relation between the target DNA concentration and output signal of the DNA sensor. For both APTS and Ppy/DNA attachment method, the sensor can detect as low as 2 nM of target DNA. However, the intensity of the output signal found to be better when direct immobilization was used than that given by APTS. This is explained by the contribution of Ppy and dopant which improve the conductivity of the membrane namely enhancing the electric charge transfer within the film.

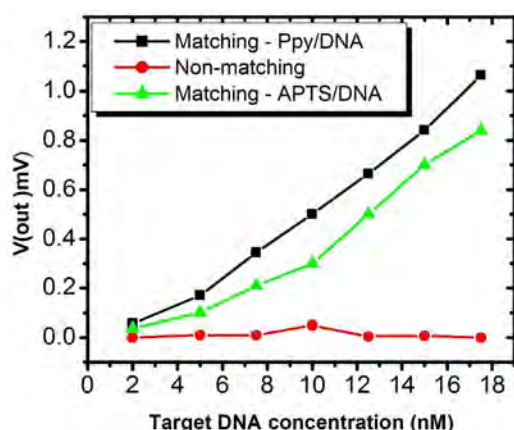


**Figure 5.** DNA sequence hybridization curve at room temperature, 0.05  $\mu$ M probe DNA.

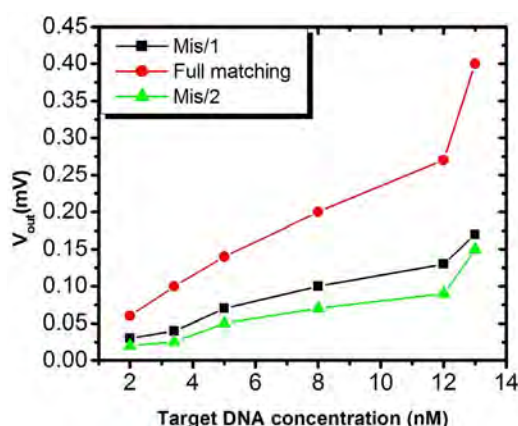


**Figure 6.** The detection mismatch DNA sequence at room temperature, 0.05  $\mu$ M probe DNA.

### 3.5. Detection of Mismatches DNA Sequence Using the DNA Sensor

Mismatch detection is our first trial step for sensor selectivity investigation. In this work, we used two different mismatched sequences of Herpes virus (**Table 1**), and then compared their hybridization signals with those of fully complementary targets to investigate the effects of the base pair mismatches. As presented in **Figure 6**, a much stronger signal of DNA hybridization containing fully matched DNA compares to system containing mismatched DNA was clearly found. This study is still in progress for statistic conclusion.

The influence of the mismatch positions was investigated by change of the DNA single base pair mismatch (mis/1) possessed a C (Cytosine) instead of a G (Guanine) at the 7<sup>th</sup> oligo and the three base pair mismatch sequence (mis/2) additionally contained CC instead of AA at 12<sup>th</sup> and 13<sup>th</sup> position close to the 5' end of the DNA molecule. **Figure 6** presents the evident decrease of signal was observed when probe DNA was hybridized with two mismatches. It also can be seen that, the signal reduction of mis/2 was stronger than mis/1. From these results, it can be deduced that the electrochemical DNA sensor has enough high sensitivity to detect a single base pair mismatch DNA at some of positions within the sequence.

### 3.6. Hybridization with PCR Amplified Sample

The DNA sequence of herpes virus in real sample was used in our work. Firstly, the DNA sequences of herpes virus were amplified by PCR method (20  $\mu$ g/ $\mu$ l) and then divided into 2 parts: 10  $\mu$ g/ $\mu$ l DNA sequence for gel electrophoresis; 10  $\mu$ g/ $\mu$ l DNA sequence for DNA hybridization detection using the DNA sensor. The **Figure 7** showed results of 92 base pairs fragment-amplified by PCR method in which lane M indicates the Marker,

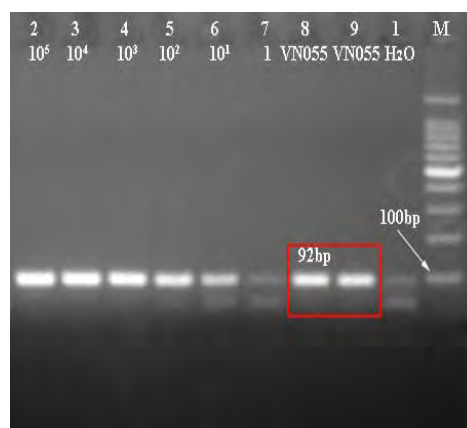


**Figure 7.** Agarose gel electrophoresis of the PCR products amplified in the thermal cyclor.

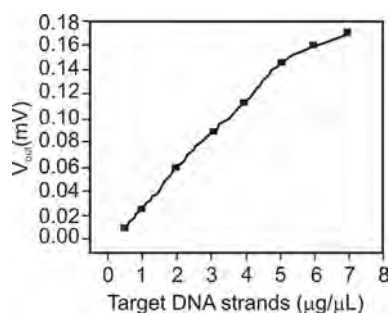


**Figure 8.** PCR amplified DNA sequence detected by DNA sensor.

lane 1: PCR performed in H<sub>2</sub>O Enppendorf tubes, lanes 2÷7: the DNA template with various DNA concentrations, and lanes 8, 9 are for the Herpes virus PCR products with 92 base pairs.

Note that, the PCR amplified sample was double strands, thus, before the performance of DNA sequence detection, the sample was thermally denatured at 98°C for 5 minutes and then was quickly decreased to 50°C to obtain the single DNA strand. Afterwards, our DNA sensors were immersed into the cell containing the sample to detect the target. **Figure 8** described the relation between target DNA concentration and output signal of DNA sensor at room temperature, phosphate buffer solution with 0.5 μM probe DNA. It can be seen that, output signal of DNA sensor is linear with target DNA concentration. This result went well that given by PCR method and matched our purpose to develop the DNA sensor as pre-diagnostic device.

## 4. CONCLUSIONS

This paper described the direct immobilization of DNA strand on the surface of sensor by electrochemical method. The DNA sensor was used to determine the Herpes simplex virus DNA in the sample. The results showed that, the DNA sensor can detect as small as 2 nM of herpes virus DNA concentration at room temperature and the intensity of the output signal is better than by using APTS attachment method. The influence of mismatch DNA was determined with decrease of 50% signal (mis/1) and 75% signal (mis/2) compares to full matching at 12 nM target DNA concentration. We still keep doing further research to verify selectivity and sensitivity of the sensors at different measuring conditions.

## 5. ACKNOWLEDGEMENTS

The work has been supported by Ministry of Education and Training under research project code B2008-01-175

## REFERENCES

[1] K. Jalava, S. Nikkari, J. Jalava, E. Eerola, M. Skurnik, O.

- Meurman, O. Ruuskanen, A. Alanen, E. Kotilainen, P. Toivanen, and P. Kotilainen, (2000) Direct amplification of rRNA genes in diagnosis of bacterial infections, *J. of Clinical Microbiology*, **38**, 32–39.
- [2] J. Wang, G. Rivas, C. Parrado, X. Cai, and M. N. Flair, (1997) Electrochemical biosensor for detecting DNA sequences from the pathogenic protozoan *Cryptosporidium parvum*, *Talanta*, **44**, 2003–2010.
- [3] M. Passamano and M. Pighini, (2006) QCM DNA-sensor for GMOs detection, *Sensors and Actuators B*, **118**, 177–181.
- [4] A. Rang, B. Linke, and B. Jansen, (2005) Detection of RNA variants transcribed from the transgene in Roundup ready soybean, *Eur. Food Res. Tech.*, **220**, 438–443.
- [5] J. Wang, G. Rivas, X. Cai, E. Palecek, P. Nielsen, H. Shiraishi, N. Dontha, D. Luo, C. Parrado, M. Chicharro, P. A. M. Farias, F. S. Valera, D. H. Grant, M. Ozsoz, and M. N. Flair, (1997) DNA electrochemical biosensors for environmental monitoring, *Analytical Chemical Act.*, **347**, 1–8.
- [6] Y. Lu, J. Liu, J. Li, P. J. Bruesehoff, C. M. B. Pavot, and A. K. Brown, (2003) New highly sensitive and selective catalytic DNA biosensors for metal ions, *Biosensors and Bioelectronics*, **18**, 529–540.
- [7] P. Rossmanith, M. Krassnig, M. Wagner, and I. Hein, (2006) Detection of *Listeria monocytogenes* in food using a combined enrichment/real-time PCR method targeting the *prfA* gene, *Research in Microbiology*, **157**, 763–771.
- [8] K. E. Yoder and R. Fishel, (2006) PCR-based detection is unable to consistently distinguish HIV 1LTR circles, *Journal of Virological Methods*, **138**, 201–206.
- [9] B. D. Rio, A. G. Binetti, M. C. Martín, M. Fernández, A. H. Magadán, and M. A. Alvarez, (2007) Multiplex PCR for the detection and identification of dairy bacteriophages in milk, *Food Microbiology*, **24**, 75–81.
- [10] I. Mannelli, M. Minunni, S. Tombelli, and M. Mascini, (2003) Quartz crystal microbalance (QCM) affinity biosensor for genetically modified organisms (GMOs) detection, *Biosensor and Bioelectronics*, **18**, 129–140.
- [11] X. D. Zhou, L. J. Liu, M. Hu, L. L. Wang, and J. M. Hu, (2002) Detection of hepatitis B virus by piezoelectric biosensor, *J. Pharm. and Biomed. Anal.*, **27**, 341–345.
- [12] R. Epstein, I. Biran, and D. R. Walt, (2002) Fluorescence-based nucleic acid detection and micro arrays, *Anal. Chimica Acta.*, **469**, 3–36.
- [13] T. Jiang, M. Minunni, P. Wilson, J. Zhang, A. P. F. Turner, and M. Mascini, (2005) Detection of TP53 mutation using a portable surface plasmon resonance DNA-based biosensor, *Biosensors and Bioelectronics*, **20**, 1939–1945.
- [14] K. Yamashita, Y. Yamaguchi, M. Miyazaki, H. Nakamura, H. Shimizu, and H. Maeda, (2004) Microfluidic system for DNA sequence detection, *Chem. Eng. Journal*, **101**, 157–161.
- [15] P. D. Thanh, M. A. Tuan, N. D. Chien, and C. Jean-Marc, (2004) Investigation on interferences of conductometric biosensor using tyrosinase enzyme, in *Proc. 7th Vietnamese-German Seminar on Physics and Engineering*, Vietnam, 158–161.
- [16] J. Wang, M. Jiang, A. Fortes, and B. Mukherjee, (1999) New label-free DNA recognition based on doping nu-

- cleic-acid probes within conducting polymer films, *Anal. Chim. Acta*, **402**, 7–12.
- [17] H. A. Tajmir-Riahi, (2006) An overview of protein-DNA and protein-RNA interactions, *J. of the Iranian Chem. Soc.*, **3**, 297–304.
- [18] Y. Zhou and Y. Li, (2004) Studies of interaction between poly (allylamine hydrochloride) and double helix DNA by spectral methods, *Biophysical Chemistry*, **107**, 273–281.
- [19] L. S. Andréa and O. A. S. Maria, (2007) Electrodeposition of polypyrrole films on aluminum from tartrate aqueous solution, *J. Braz. Chem. Soc.*, **18**, 143–152.
- [20] M. Omastová, J. Pionteck, and S. Koina, (1996) Preparation and characterization of electrically conductive polypropylene/polypyrrole composites, *Eur. Polym. J.*, **32**, 681–689.
- [21] H. N. Cong, K. E. Abbassi, J. L. Gautier, and P. Chartier, (2005) Oxygen reduction on oxide/polypyrrole composite electrodes: effect of doping anions, *Electrochimica Acta.*, **50**, 136–1376.

# Development of a low cost fetal heart sound monitoring system for home care application

Arun Kumar Mittra<sup>1</sup>, Nitin K. Choudhari<sup>2</sup>

<sup>1</sup>MIET, Gondia: Department of Electronics Engineering, Manoharbhair Patel Institute of Engineering and Technology, Gondia (MS), India; <sup>2</sup>Smt. Bhugwati College of Engineering, Nagpur, India.  
Email: [akmittra@gmail.com](mailto:akmittra@gmail.com)

Received 6 January 2008; revised 26 April 2009; accepted 26 June 2009.

## ABSTRACT

**Variations in fetal heart rate (FHR) is a potential indicator of stress on unborn in the womb of mother. In hospitals, FHR surveillance is performed by ultrasound based Doppler equipments. However, recent studies show that frequent exposure to ultrasound radiations is not recommended for the fetal well-being. Because of this and many other reasons, these instruments are not recommended for prolonged home monitoring applications. This work is focused around development of a prototype system for fetal home monitoring application. Presented system can record the abnormal FHR and alert the pregnant women to report to a physician. Recorded data is then processed by a novel methodology for deriving results of diagnostic importance. The instrument has been tested on pregnant women in the clinical environment and has gone through an extensive clinical trial at local hospitals. The results show that the technique is suitable and effective for long-term FHR home monitoring application.**

**Keywords:** Ambulatory Monitoring; Phonocardiography; Cardiography; Simulation; Signal Processing

## 1. INTRODUCTION

To diagnose pre-term labor, ambulatory monitoring for abnormal FHR has proven to be an effective method [1]. Abnormality in fetal heart rate (FHR) is an indicator of pre-maturity and miscarriage. It is very important to monitor, such abnormalities in pregnant women, which are at high risk, with history of miscarriage. These abnormalities are unpredictable and may occur at any time, especially in the case of pre-term labor. The pathogenesis of pre-term labor is still poorly understood, however, the unusual occurrence of pre-maturity and miscarriage can be largely prevented by the timely diagnosis of

pre-term labor and its arrest with tocolytic medication. If the unborn heart rate increases very high or drops to a very low, it calls for urgent attention. In both the cases, it is obvious that the baby is in stress and special urgent medical attention is needed. For this reason, the electronic monitoring of the FHR has become one of the most familiar methods used in the antenatal period [2,3]. The ultrasound based Doppler instruments are widely used for this purpose in hospitals, but for varied reasons, they are not suitable for home monitoring application and long-term surveillance of unborn [4,5]. It is imperative to note that these instruments are also invasive in nature.

There is still a gap between existing technologies and the user requirement for safe, convenient, and reliable fetal monitoring [6,7]. In view of these considerations, a strong need is felt for the development of a FHR monitoring machine which will be non-invasive, cost effective, simple to operate and which can be used by a pregnant woman for prolonged home monitoring application [8]. Preliminary experiments in this regard have been conducted [9,10] and a cost effective prototype is developed for at home long term FHR recording and monitoring. This instrument can record fetal heart sound for hours in a standard MP3 format. In case of abnormal symptoms, the subject visits the physician where the recorded data can be analyzed with the help of associated software and computer. The audiovisual display of fetal heart sound will provide valuable additional information to the physician for diagnosis and treatment.

The basic technique used in the presented instrument is called fetal Phonocardiography (fPCG) [11,12]. In this technique a specially designed microphone is placed on the abdomen of the subject, which primarily detects and records the fetal heart sound. However, phonocardiography is extremely susceptible to ambient noise [13,14, 15]. Unfortunately, the fetal heart activity produces much less acoustic energy and moreover it is surrounded by highly noisy environment. This noise has a direct consequence on the signal that often changes remarkably from one beat to next, with the additional characteristic

of poor signal to noise ratio (SNR). These unwanted disturbance signals contribute an additional difficulty in the detection of the principal fetal heart sounds (S1 and S2). Hence it is necessary to develop and evaluate signal-processing technique to improve SNR before obtaining reliable time references of the fetal heart sound signal [16]. In order to improve SNR, and accomplish an optimal external noise cancellation performance, phonocardiographic devices need a very superior and advanced noise reducer in the preprocessing stage of the instrument. In this work a very effective noise reducer is designed and used in the presented prototype system. The design is implemented with help of Matlab Simulink and intensive tests are carried out in order to evaluate the performance of resultant method. The instrument has been found effective from 30<sup>th</sup> week to final term of gestation with satisfactory level of sensitivity.

The paper is organized as follows: The next section discusses the hardware of the presented system, used for the detection and recording of fetal heart sound and ambient noise. The following section, describes software and different signal processing techniques used by the system. The article then presents a comprehensive computer simulation. The last section deals with experimental and clinical trial results with conclusions.

## 2. SYSTEM DESCRIPTION

The Fetal heart sound monitoring system presented in this study, primarily comprises of two main modules:

- 1) Detection and Recording Module (DRM).
- 2) Processing and Display Module (PDM).

The DRM is a small hardware, which is placed on the subject's abdomen for detection and recording of the fetus heart sound signal. This module records the abnormal FHR and alerts pregnant woman, that it is time to seek some medical attention.

The PDM is software, developed for physician's personal computer. When the subject approaches the physician along with DRM, recorded data is down loaded and then processed with the use of PDM, to generate the results of diagnostic importance.

### 2.1. Detection and Recording Module (DRM)

It is a small low cost hardware comprising of a specifically designed acoustic cone, piezoelectric sensor, pre-amplifiers, power amplifiers, filters and a USB compatible MP3 voice recorder. The basic functions of this module are as follows:

- 1) Fetal heart sound detection from maternal abdomen and recording of the same on one of two channels in MP3 voice recorder (Abdominal Channel).
- 2) External noise detection through an open-air microphone and recording on another channel (Noise Channel).
- 3) Generation of audiovisual indications from fetal heart sound signal.

Block diagram of DRM with all necessary details is shown in the **Figure 1**. It can be seen that the complete

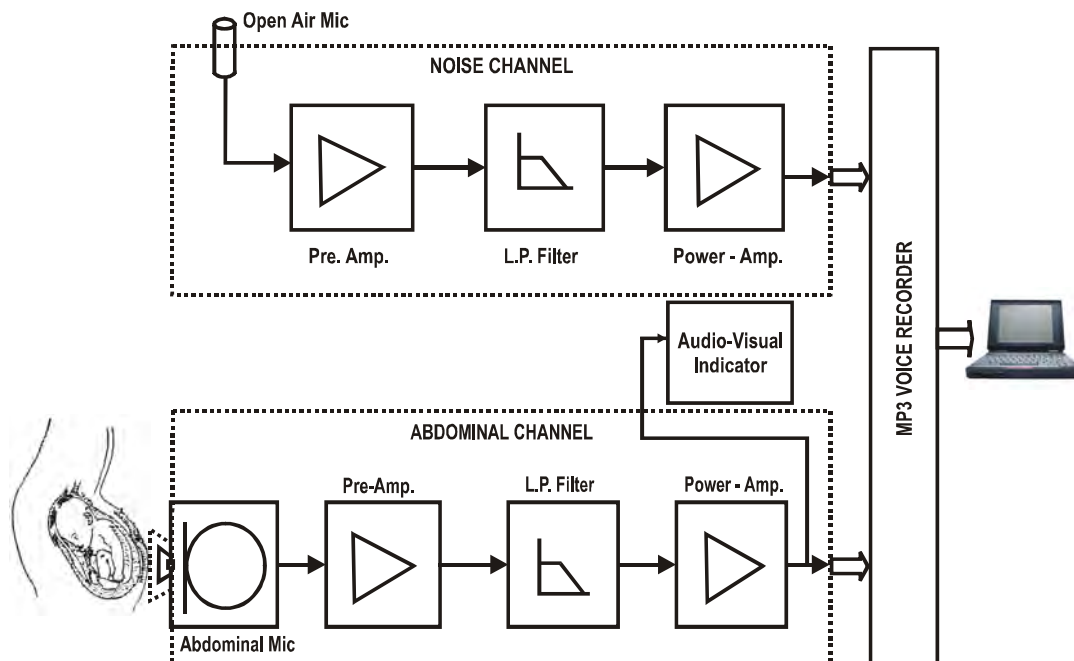


**Figure 1.** Block diagram of DRM hardware.



system is divided in two basic sections: a) Abdominal Channel b) Noise Channel.

a) Abdominal Channel: Fetal phonocardiography requires the conversion of mechanical vibration on subject's abdomen to electrical signal by microphone. Fetus heart sound is extremely weak hence it cannot be sensed properly by putting a sensor immediately on the subject's abdomen. To overcome this problem a particular acoustic cone is developed which is a direct extension of the chest piece of standard stethoscope. The air enclosed in the cone acts as a transmission media between the membrane and electro-mechanical transducer device. The output of the sensor is fed to pre-amplifier for high amplification and better noise rejection. IC LM 381 is used here for this particular purpose, which raises the signal from the transducer level to the line level.

It is essential to keep ambient noise as low as possible; this is carried out by an active low pass filter with cut-off frequency of 200 Hz. This value of cut off frequency is selected, because most of the fetus heart sound spectrum lies below this frequency limit. Active filter is implemented using an easily available operational amplifier IC 741 along with suitable resistor capacitor network. IC TBA810 based power amplifier further strengthens the output signal from filter, and provides audible fetus heart sound. It is then recorded on any one channel of MP3 voice-recorder. This amplifier further provides driving power to audio-visual indicator of the DRM device.

b) Noise Channel: In fetal phonocardiographic measurement, ambient noise creates major problem at signal processing stage [17,18]. To overcome this problem, special signal processing techniques are used in this study, which require a primary sample of the noise, creating disturbance in the signal of interest. To facilitate this, ambient noise is detected through an independent open-air microphone. After pre-amplification and filter-

ing, noise signals are recorded on another channel of the memory device.

It is important to note that abdominal channel microphone detects the sound primarily originating from the maternal abdomen, but these signals get mixed with a damped version of the external noise. The open air Noise Channel microphone detects only the ambient noise and does not contain any traces of fetal heart sound signal. Photographs of prototype experimental model are shown in the **Figures 2(a) & 2(b)**.

## 2.2. Processing and Display Module (PDM)

The PDM is the software part of presented system, made available in the physician's personal computer. When pregnant woman feels some abnormality and the DRM alerts her, she may go to the hospital with the DRM. Stored data within the device is used for further processing and investigation through PDM. Block diagram of PDM with all necessary signal flow details is shown in the **Figure 3**.

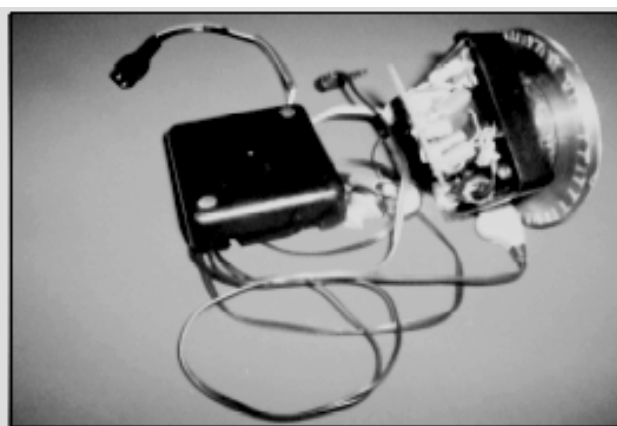
A brief description of each signal-processing module incorporated in the block diagram is given below:

a) Data Acquisition: The output of the MP3 voice recorder is directly fed to the Line-in of the multimedia card, which contains on board signal conditioning, analog to digital conversion and digital signal processing hardware. Matlab data acquisition toolbox is used to download both channels of MP3 voice recorder and to store it in two separate \*.wav files. These files carry noised fetal heart sound signal and external noise separately.

b) Adaptive Filter: Adaptive filters track the dynamic nature of a system and allow elimination of unwanted part of the signal. In this study adaptive filters are used for external noise cancellation i.e. removal of external unwanted background sound signal from the fetal heart



(a)



(b)

**Figure 2.** Photographs of prototype.

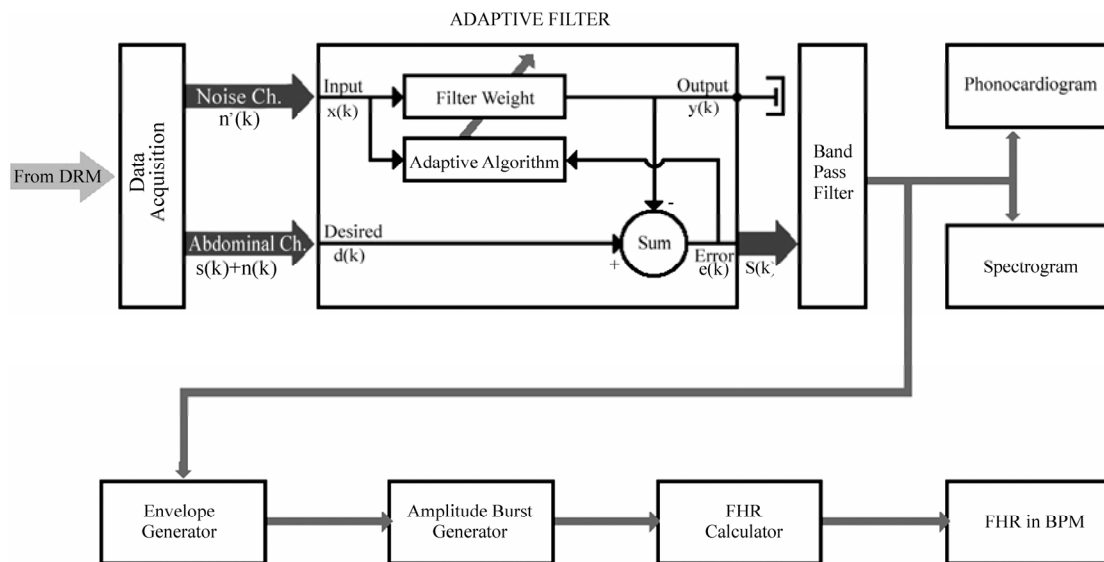


**Figure 3.** Block diagram of PDM.

sound signal. As shown in **Figure 3**, desired signal  $d(k)$ , the one to clean up, comes from abdominal channel, carries noise  $n(k)$  and wanted signal  $s(k)$ . The Noise Channel carries only background noise  $n'(k)$ , is applied as input signal  $x(k)$  of the filter. As long as the input noise to the filter  $n'(k)$  remains correlated to the unwanted noise  $n(k)$ , the adaptive filter adjusts its weights  $w(k)$  to reduce the value of the difference between  $y(k)$  and  $d(k)$ , this results in elimination of external noise and a clean fetal heart signal  $s(k)$  will appear on the error port. The generalized mathematical relationship between different signals and filter weights can be depicted as:

$$\begin{aligned}
 d(k) &= s(k) + n(k) \\
 y(k) &= \text{Filter}\{x(k), w(k)\} \\
 \text{or } y(k) &= w(k) \cdot n'(k) \\
 e(k) &= d(k) - y(k) \\
 &= s(k) + n(k) - w(k) \cdot n'(k) \\
 &\cong s(k) \\
 w(k+1) &= w(k) + e(k) \cdot x(k)
 \end{aligned}$$

Notice that in this implementation, the error signal actually converges to the input data signal, rather than converging to zero.

c) Band Pass Filter: Adaptive filtering of recorded signal removes only the external noise from the composite abdominal signal. A band pass digital filter is designed to limit the signal in  $35 \text{ Hz} < f < 200 \text{ Hz}$  frequency band. The selection of lower frequency limit is based on the experimental result, that a considerable part of the disturbing maternal heart and digestive sound lies below this border, while the fetal heart sounds are not dominantly present there any more. Upper limit is set to remove maternal respiratory sound and remaining traces

of external noise signals.

d) Phonocardiogram: Fetal Phonocardiograph is a time versus amplitude plot of fetal heart sound and is considered as the primary time domain characteristic of the fetal heart sound signal. It is a graphical representation of vibration or sound signal detected from the maternal abdominal wall, caused by the contractile activity of the fetal heart. The general fPCG wave pattern of the signal over cardiac cycles may be readily appreciated by visual inspection and can be used as a potential indicator of few congenital diseases.

e) Spectrogram: fPCG signals possess multiple resonance frequencies. This leads towards the need to describe the fPCG signals, not only in terms of time but also in terms of frequency domain, also known as spectrogram. It provides distribution of the signal's energy or power over a wide band of frequencies.

f) Envelop Generation: In order to find out exact periodicity of heartbeat, it is proposed to use envelope of the fetal heart sound signal. This envelope encompasses and traces the peaks of signal under consideration. In this application it is derived by the method of squaring and low pass filtering [19]. The resultant envelope signal reflects the amplitude dynamics of signal on the same time scale as of the original signal.

g) Burst Generator: After the process of envelope generation, exact positioning of amplitude burst is carried out by the method of thresholding and relaying. Whenever amplitude of signal envelopes goes above a pre-defined limit it is relayed over as a maximum value otherwise it is taken as zero. This process results in a series of discrete pulses representing occurrences, and duration of fetal heartbeats.

h) FHR Calculation: The last element of the signal-processing block is for the FHR determination. This is carried out by counting numbers of discrete pulses in the signal for a pre-defined time interval.

### 3. SYSTEM SIMULATION

Processing and Display Module (PDM) described above is simulated using the Simulink modeling tool of Matlab version 7. The model is built by interconnecting requisite blocks, which are available in the software library and their parameters are entered while designing them for simulation. The inputs of the simulating system are the recorded signals of DRM module, where as the outputs are Phonocardiogram, Spectrogram and record of FHR in Beats Per Minutes (BPM). System simulation of developed PDM module is shown in **Figure 4**.

After data acquisition, signals are de-noised with the help of adaptive filter. Fetal heart sound signals, detected from mother's abdomen are fetched from corresponding \*.wav file and applied to the desired port of the filter block. This signal carries fetal heart sound and a damped version of the external noise. The unwanted external noise is available in another \*.wav file and is applied to the input port of the filter. De-noised signal comes out

through the error port of the filter block. It should be noted that the output port is not used in the simulation process; however this port provides internal feedback for error calculation in the filter block.

Adaptive filtering eliminates only the external noise. For suppressing remaining artifacts, digital band pass filter is used in the simulation. This block allows signals of the specified range only, while signals of all other frequencies are attenuated. After the band pass filtering signals are relatively less distorted and applied to the time scope block of the module. This block provides the time-domain response of the fetal heart signal, which is also called as phonocardiogram. The frequency domain response i.e. cardio-spectrogram of de-noised signal is produced through periodogram and vector scope block icons. The periodogram block computes a non-parametric estimate of the spectrum. The block averages the squared magnitude of the FFT computed over windowed sections of the input and normalizes the spectral average by the square of the sum of the window samples. The vector scope block is a comprehensive display tool similar to a digital oscilloscope. It is used here to plot frequency-domain response of the de-noised fetal heart sound signal.

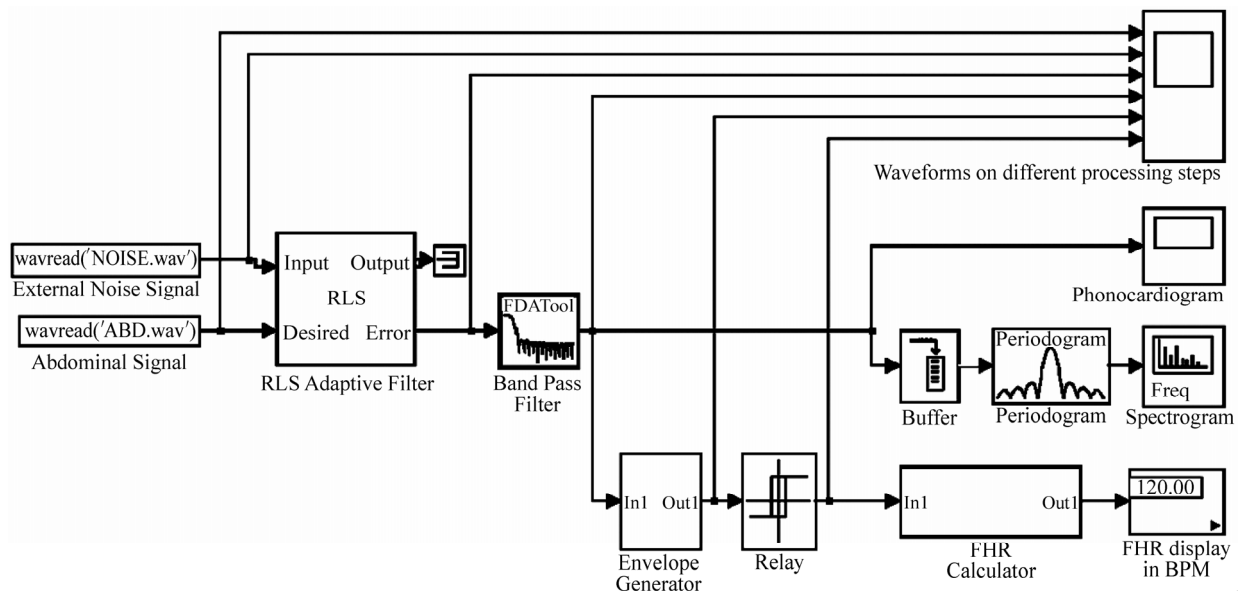


**Figure 4.** System simulation of PDM.

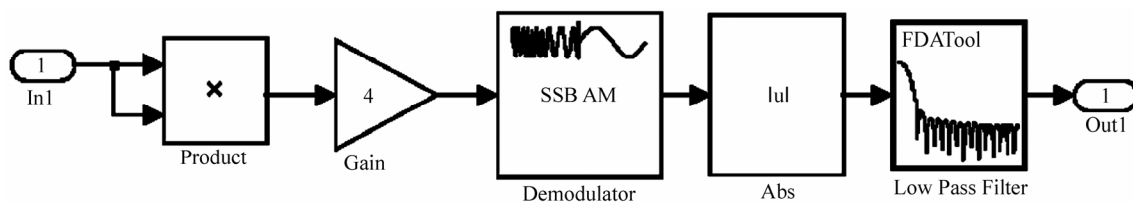


**Figure 5.** Sub-system for envelop generation.

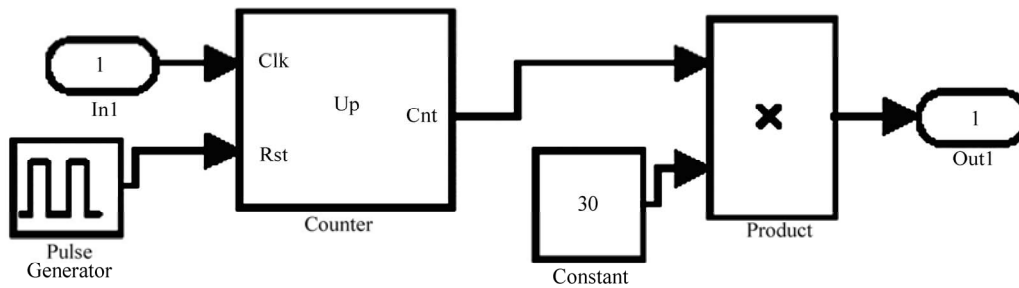


**Figure 6.** FHR calculator sub-system.

The simulation block diagram showing the bottom-most blocks (refer **Figure 4**) are related with the FHR calculation. The first block is for envelope generation and it is a simulink subsystem as shown in **Figure 5**.

This sub system is based on the concept of squaring and low pass filtering. The input signal is first multiplied by itself. Squaring the signal effectively modulate the input by using itself as the carrier wave. This means half the energy of the signal is pushed towards higher frequencies and half is shifted towards DC. The envelope can then be obtained by keeping all the DC low frequency energy and eliminating the high frequency energy. In this sub-system, a simple minimum-phase low pass filter is used to get rid of the high frequency energy.

Output of envelope generator is connected to the relay block (refer **Figure 4**). This block allows its output to switch between two threshold values. Once the relay is ON, it remains ON until the input drops below the value of the switch-off point parameter and when the relay is OFF, it remains OFF until the input exceeds the value of the switch-on point parameter. This block converts the envelope signal into a series of discrete pulses. These pulses are fed to FHR Calculator sub-subsystem. Details of this sub-system are shown in **Figure 6**, in which the Counter block increments an internal counter each time it receives a trigger at the click (Clk) port. A trigger signal at the reset (Rst) port brings the counter to its initial state.

Counter output is converted to Beats Per Minute (BPM) and is then finally displayed on the output device.

#### 4. EXPERIMENTAL TESTING AND RESULTS

Experimental testing is necessary to verify the reliability and performance of any system under a developmental stage. An artificial womb, which give simulated testing conditions for fetal monitoring system is very appropriate and useful for initial testing in comparison to actual clinical testing on pregnant women. In this work, an artificial womb is prepared for simulated performance testing of monitoring systems under study. Through Matlab signal processing toolbox, simulated signals are generated for fetal heart sound, maternal heart sound, maternal

respiratory sound and for external noise. After amplification these signals are applied to different speakers placed underneath a rubber balloon filled with water. DRM hardware under test is placed on the opposite side of the balloon. This arrangement simulates a fetal heart-beat passing through amniotic fluid to the wall of the mother's abdomen. For providing external support, the complete assembly is housed in a solid wooden tub. It is then placed in a thick glass envelop for elimination of outside noise interference. Presented system was initially tested on above-mentioned artificial womb. This was a totally subjective test, performed only to check viability of the instrument.

After satisfactory performance with artificial womb, system has been tested on the pregnant women in clinical environment. More than 15-fetal heart sound recorded samples were taken from different women, who were between 36 to 40<sup>th</sup> week of singleton pregnancy. Recorded data was transferred to personal computer in \*.wav file through multimedia card. Matlab Simulation discussed above was used to process and display the recorded sound from wave files. **Figure 7** shows signal waveforms at various stages of the simulation, obtained from abdominal recording of a pregnant woman at 39 weeks of gestation (Subject No. 1). In these graphs, X-axis represents the time in seconds whereas Y-axis represents amplitude of signal in volts. Uppermost waveform (Graph a) represents 2 seconds time span of representative sample of fetal heart sound, practically recorded through the abdominal microphone.

Second waveform (Graph b) is the corresponding external noise, recorded through external microphone. It may be noted that noise level is very high, which contaminates the fetal heart sound to a larger extent. This representative sample of noise is used as a reference input for adaptive filters in signal processing stage of simulation. Third waveform (Graph c) describes the de-noised signal coming out from the adaptive filter. It can be observed that external noise is considerably reduced and amplitude burst are distinctly visible in the waveform. In order to further increase the signal to noise ratio, band pass filters are used. Fourth waveform (Graph d) is the signal after band pass filtering and this

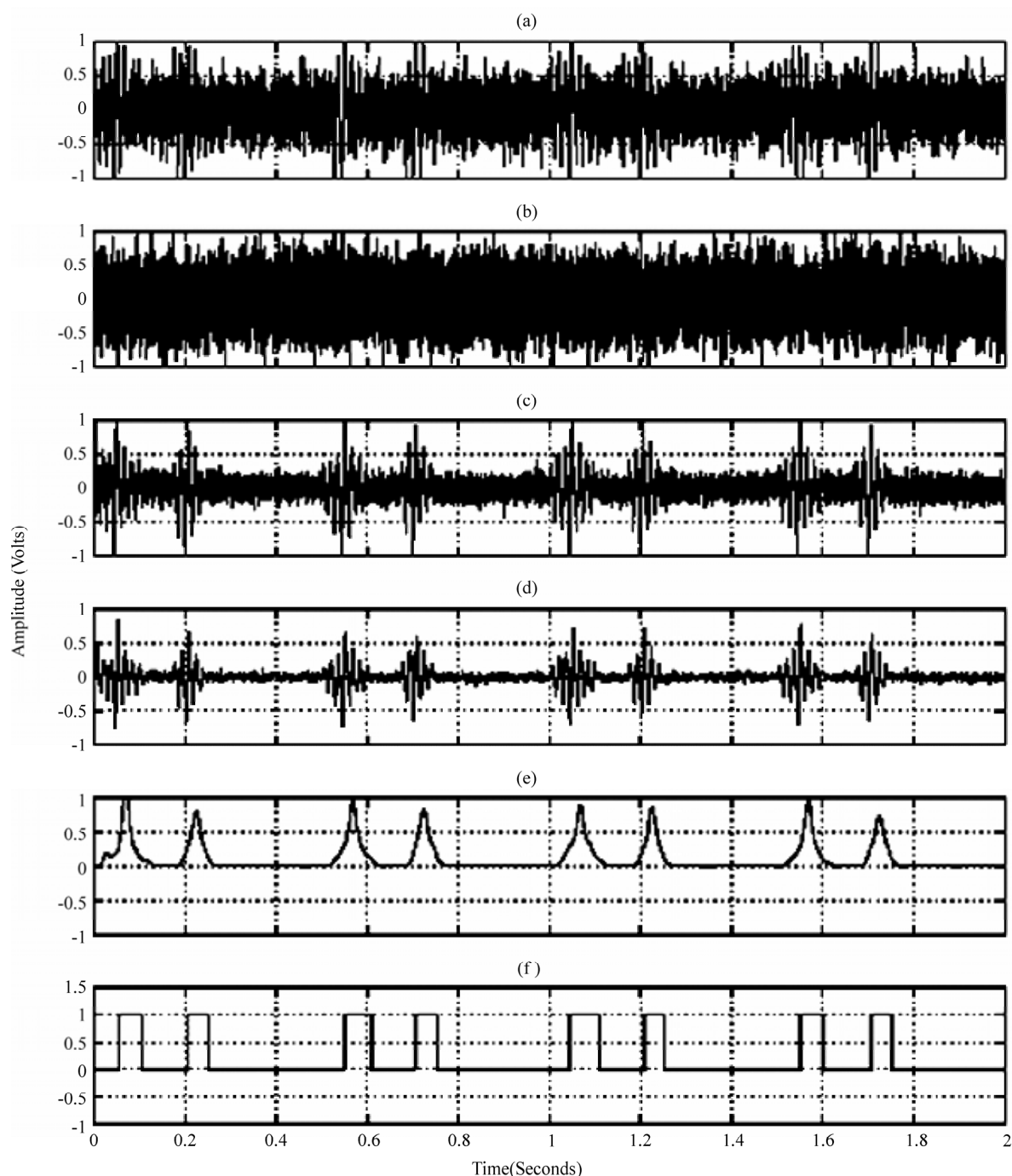


**Figure 7.** Simulation output (a) Signals from abdominal channel (b) Signals from external channel (c) Signal after adaptive filtering (d) Signal after band pass filtering (e) Signal after envelope generator (f) Signal after thresh holding.

is the final phonocardiographic signal, which the instrument provides. Fifth waveform (Graph e) is signal envelope provided by the complex process of envelope generation. This envelope is then passed through an amplitude thresholding process that in turn converts amplitude burst of the envelope signal into discrete pulses. The last waveform (Graph f) indicates the final processed signal,

used for the FHR calculation.

It is believed that a more precise examination of phonocardiographic signal may be useful for pre-detection of intra uterine growth retardation and other abnormalities of fetal. To facilitate this, a separate time scope block is provided in the simulation. This block provides a zoomed-in version of signal for any specified period of



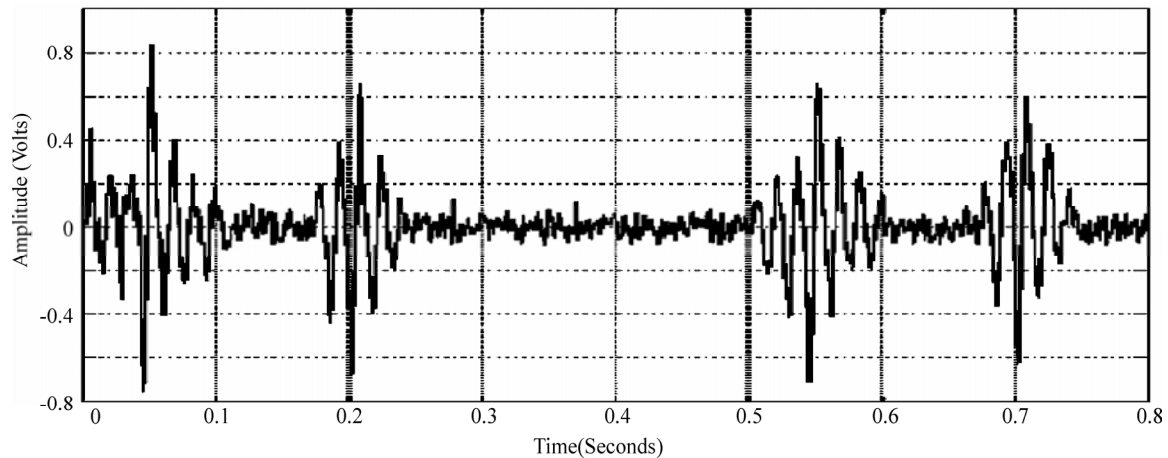


**Figure 8.** Fetal phonocardiogram.

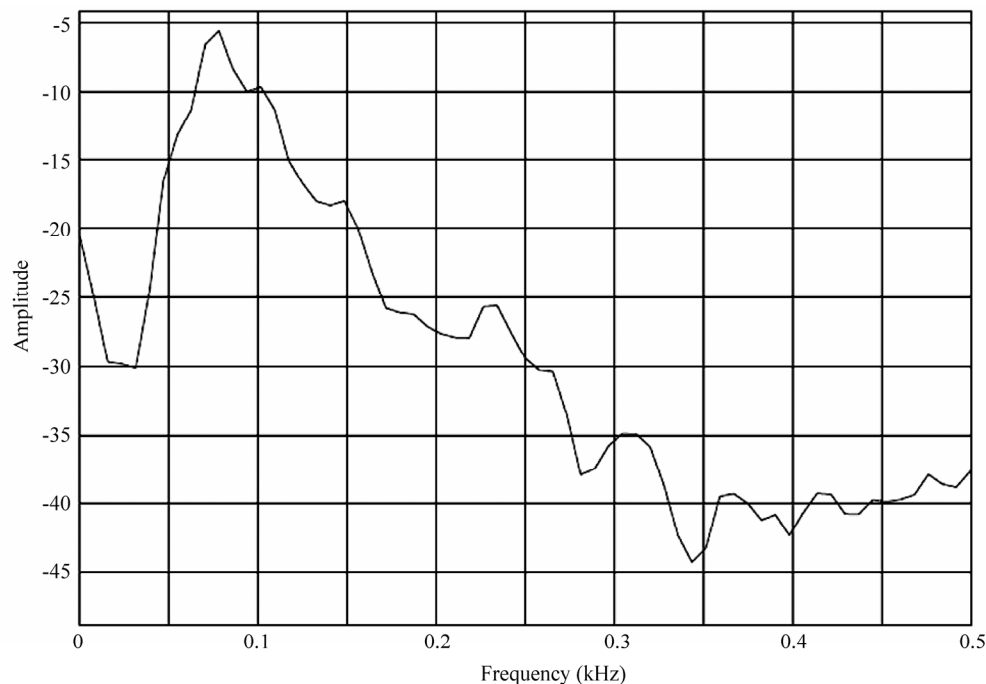


**Figure 9.** Fetal spectrogram.

time. **Figure 8** shows such display for a time interval of 0.8 seconds.

Phonocardiogram is the time domain response of the fetal heart sound signal. Presented system is in addition; capable of providing frequency domain response of the signal, called Spectrogram. It represents the contribution of every frequency of the spectrum to the power of overall signal. Spectrogram of fetal heart sound for a small time window around 0.55 sec instant of previous illustration is shown in the **Figure 9**.

In order to support the performance of developed system, phonocardiogram signals recorded through proto-

type were compared with signals of simultaneously used ultrasound Doppler based instrument (Model: Coddle-Graph-L of Maestros Mediline Systems). In this comparative experimentation following parameters were measured:

$N'$  = Total number of amplitude bursts detected by prototype.

$N$  = Total number of amplitude bursts detected by reference instrument.

$M$  = Total number of missed bursts by the prototype.

$F$  = Total number of false bursts detected by the prototype.

**Table 1.** Outcome of comparative measurement.

Subject No	Number of Amplitude Burst from Prototype	Number of Amplitude Burst from Reference Instrument	Number of Missed Amplitude Burst	Number of False Amplitude Burst	Performance Index %
1	260	270	10	0	96.30
2	290	286	0	4	98.60
3	274	280	6	0	97.86
4	278	284	6	0	97.89
5	310	302	0	8	97.35
6	294	298	4	0	98.66
7	290	296	0	6	97.97
8	318	324	0	6	98.15
9	292	290	2	0	99.31
10	312	302	10	0	96.69
11	266	280	0	14	95.00
12	302	306	0	4	98.69
13	286	288	0	2	99.31
14	298	304	0	6	98.03
15	314	310	4	0	98.71
16	304	308	0	4	98.70

From these data, performance of the instrument [20] can be derived with the help of formula:

$$\text{Performance Index} = \frac{N - (M + F)}{N} \times 100$$

This comparative measurement is performed on 16 pregnant women between 36<sup>th</sup> to 40<sup>th</sup> week of gestation age, and average recording duration was stayed limiting to one minute. It is observed that in most of the cases, phonocardiographic-based prototype signal quality is almost at par with the ultrasound Doppler based signals. **Table 1** shows result of these measurements and calculation of corresponding performance indices.

In light of these recorded values, the overall Performance Index of the system is found around 97% in correlation of ultrasound based Doppler instrument. This performance value is fairly good for a prototype model and will certainly improve in commercially advanced system.

## 5. CONCLUSIONS

This work presents development of a very powerful, non-invasive, portable and low cost battery operated standalone fetal heart sound recording and monitoring system that can be used in prevailing home environment. The hardware of prototype model is of the size 9 X 8 X 4.4 cm and of the weighs 205 grams with 9 V alkaline

battery. Signal recorded through this prototype model are digitally processed and analyzed on a personal computer. Using enhanced adaptive and band pass filtering techniques, a remarkable improvement in signal to noise ratio is achieved by the system. Processed signals are finally used to produce impressive results of significant diagnostic and clinical importance. Instrument has been tested on pregnant women with varied gestational period and also validated by simultaneous measurement with a standard ultrasonic Doppler device. From the results it can be concluded that the presented system is viable and can effectively be used in the development of commercial phonocardiographic-based fetal home care monitoring system.

## 6. ACKNOWLEDGEMENTS

The fetal heart sound recordings were done at district government women hospital and at Ratnaparkhi Nursing Home Gondia (M.S.). The authors of this paper would also like to thank Dr. Shrish Ratnaparkhi (Gynecologist), Dr. (Mrs.) Megha Ratnaparkhi (Obstetrician), Prof. Vijay Chourasia and Prof. (Mrs.) Vijaya Rahangdale for their kind support in carrying out observations with the help of developed prototype instrument. Pregnant women who volunteered to participate in clinical test are also appreciated for their kind gesture.

## REFERENCES

- [1] M. Godinez, *et al.*, (2003) On-line fetal heart rate monitor by phonocardiography, Proceedings of 25th annual

- international conference-IEEE, Cancun Mexico, 3141–3144.
- [2] M. Moghavvemi, *et al.*, (2003) A non-invasive PC based measurement of fetal phonocardiography, *Journal of Sensors and Actuators*, **1**(107), 96–103.
  - [3] A. K. Mittra, *et al.*, (2007) Fetal heart rate detection and monitoring techniques: A comparative analysis and literature review, *Proceedings of National Conference-INVENT-2007*, M. P. Institute of Engineering and Technology, Gondia (M. S.), 124–140.
  - [4] F. Javed, *et al.*, (2006) A signal-processing module for the analysis of heart sounds and heart murmurs, *Proceedings of International MEMS Conference*, Singapore, **34**, 1098–1105.
  - [5] B. H. Tan, *et al.*, (2000) Real time analysis of fetal phonocardiography, *Proceedings of IEEE International Conference-TENCON-2000*, Kuala Lumpur, **2**(2000), 135–140.
  - [6] A. K. Mittra, *et al.*, (2006) Design & development of PC-Based fetal heart sound monitoring system, *The Indian Journal of Information Science & Technology*, **1**(2), 1–8.
  - [7] A. K. Mittra, *et al.*, (2004) Function analysis of sensors used in cardiotocograph: A trans-abdominal fetal heart rate and uterine contraction monitoring machine, *National Conference on Sensors Technology-Gwalior*, 28–31.
  - [8] A. K. Mittra, *et al.*, (2006) Functional analysis of fetus heart sound and uterous contraction monitoring machine using quality function deployment, *I-Manager: Journal of Engineering and Technology*, **2**(2).
  - [9] A. K. Mittra, *et al.*, (2006) Development of non-invasive portable fetus heart sound monitoring machine: An experimental approach, *The Journal of Lab Experiments*, **6**(2), 104–110.
  - [10] A. K. Mittra, *et al.*, (2005) Improvisation in technique for trans abdominal monitoring of fetal heart rate and uterus contraction, *Proceedings of national conference-BIOCON-2005*, Bharati Vidyapeeth Deemed University Pune, 25–28.
  - [11] V. Nigam, *et al.*, (2004) Cardiac sound separation, *Proceedings of IEEE International Conference on Computers in Cardiology*, Chicago, 497–500.
  - [12] C. Horvath, B. Uveges, F. Kovacs, and G. Hosszu, (2007) Application of the matching pursuit method in a fetal phonocardiographic telemedicine system, *29th Annual International Conference of the IEEE Engineering in Medicine and Biology Society*, EMBS, 1892–1895.
  - [13] A. Jimenez-Gonzalez and C. J. James, (2008) Blind source separation to extract foetal heart sounds from noisy abdominal phonograms: A single channel method, *4th IET International Conference on Advances in Medical, Signal and Information Processing*, MEDSIP, 1–4.
  - [14] K. K. Spyridou and L. J. Hadjileontiadis, (2007) Analysis of fetal heart rate in healthy and pathological pregnancies using wavelet-based features, *29th Annual International Conference of the IEEE-Engineering in Medicine and Biology Society EMBS*, 1908–1911.
  - [15] F. Kovacs, *et al.*, (2000) A rule based phonocardiographic method for long term fetal heart rate monitoring, *IEEE Transactions on biomedical engineering*, **47**(1), 124–130.
  - [16] M. Brusco, *et al.*, (2004) Digital phonocardiography: A PDA-based approach, *Proceedings of the 26<sup>th</sup> Annual International Conference of the IEEE EMBS*, San Francisco California, **1**, 2299–2302.
  - [17] Y. M. Lee, *et al.*, (2002) Remote heart rate monitoring system based on phonocardiography, *Proceedings of Student Conference on Research and Development-IEEE*, Shah Alam Malaysia, 27–30.
  - [18] P. Varady, (2001) Wavelet-based adaptive de-noising of phonocardiographic records, *Proceedings of IEEE-23 Annual EMBS International Conference*, Istanbul Turkey, **2**, 1846–1849.
  - [19] <http://www.mathworks.com/products/demos/shipping/dspblks/dspenvdet.html>.
  - [20] E. C. Karvounis, M. G. Tsipouras, D. I. Fotiadis, and, K. K. Naka, (2007) An automated methodology for fetal heart rate extraction from the abdominal electrocardiogram, *IEEE Transactions on Information Technology in Biomedicine*, **11**(6), 628–638.

# Classification with binary gene expressions

Salih Tuna, Mahesan Niranjan<sup>1</sup>

<sup>1</sup>School of Electronics and Computer Science, University of Southampton, Southampton, UK.  
Email: [mn@ecs.soton.ac.uk](mailto:mn@ecs.soton.ac.uk)

Received 30 March 2008; revised 25 May 2009; accepted 3 June 2009.

## ABSTRACT

Microarray gene expression measurements are reported, used and archived usually to high numerical precision. However, properties of mRNA molecules, such as their low stability and availability in small copy numbers, and the fact that measurements correspond to a population of cells, rather than a single cell, makes high precision meaningless. Recent work shows that reducing measurement precision leads to very little loss of information, right down to binary levels. In this paper we show how properties of binary spaces can be useful in making inferences from microarray data. In particular, we use the Tanimoto similarity metric for binary vectors, which has been used effectively in the Chemoinformatics literature for retrieving chemical compounds with certain functional properties. This measure, when incorporated in a kernel framework, helps recover any information lost by quantization. By implementing a spectral clustering framework, we further show that a second reason for high performance from the Tanimoto metric can be traced back to a hitherto unnoticed systematic variability in array data: Probe level uncertainties are systematically lower for arrays with large numbers of expressed genes. While we offer no molecular level explanation for this systematic variability, that it could be exploited in a suitable similarity metric is a useful observation in itself. We further show preliminary results that working with binary data considerably reduces variability in the results across choice of algorithms in the pre-processing stages of microarray analysis.

**Keywords:** Microarray Gene Expression; Binary Gene Expressions; High Numerical Precision; mRNA Molecules

## 1. INTRODUCTION

It is anecdotally known and has been formally established recently that gene expression measurements archived in microarray repositories are reported to a far higher numerical precision than is supported by the underlying biology of the measurement environment. Here, precision refers to the difference between representing the mRNA abundance, or relative abundance, of a gene to several decimal places (e.g. 2.4601) and retaining only the binary information as to whether the gene is expressed or not. Shmulevich and Zhang [1] recommend that gene expressions should be quantized to binary precision and Hamming distance between signatures used as distance metric in solving class prediction problems. Their starting point in defining binary expressions is a “notion of similarity used by biologists when comparing gene expressions from different samples... counting the number of genes that show significant differential expression”. From this premise, they give an algorithm for binarizing gene expressions and show that a multi dimensional scaling (MDS) projection of the data separates different types of tumors. More recently, Zilliox and Irizarry [2] introduce the concept of gene expression “barcodes”, which are essentially binary representations of transcriptomes, and present impressive results on predicting tissue types. These authors take a very different approach in that they scan through a very large number of archived datasets of a particular array type to construct barcodes. Genes that are frequently expressed across the whole ensemble are set to be ON and the others set OFF. In our own recent work [3], we showed that progressive quantization of gene expression measurements, right down to binary levels, loses very little information as far as the quality of inference is concerned. We were able to demonstrate this on a range of different inference problems including classification, cluster analysis, determination of genes that are periodically expressed and the analysis of developmental time course data.

Why would we be interested in low precision, or binary, representations? The initial motivation comes from the underlying biology. mRNA is only available in very

small quantities in cells and are extracted from a population of cells rather than from a single cell. Further, the process of microarray hybridization itself is a stochastic one, the effect of which is pronounced when small numbers of molecules are involved. All these reasons put together make one sceptical about high precision representations of the transcriptome, i.e. the signal available may only be reliable to low precision. Critical appraisals of microarray technology, while recognising good reproducibility of technical replicates, often identifies large variations with respect to biological replicates. One such survey by Draghici *et al.* [4] concludes:

“...the existence and direction of gene expression changes can be reliably detected for the majority of genes. However, accurate measurements of absolute expression levels and the reliable detection of low abundance genes are currently beyond the reach of microarray technology.”

Artificially inflated precision can potentially hurt. A plethora of sophisticated inference methods (e.g. Bayesian inference) have been applied to microarray data. Algorithmic complexity of such models is generally derived from how well noise is captured. High precision gives the illusion of complex noise structures leading to the use of such algorithms. If the data were far simpler, one would impose a far higher sense of parsimony in model selection. Simple classification rules offering good performance (e.g. the top scoring pairs of genes approach of Geman *et al.* [5]) on some problems also bears testimony to this point. Motivated by the above, we ask the following research question: If transcriptome can be represented at low precision, binary for instance, can we take advantage of properties of high dimensional binary spaces to achieve increased classification performance? We show that this is indeed the case, by use of a particular similarity metric between high dimensional binary vectors, the so called Tanimoto metric. Following experiences seen in the chemoinformatics literature, we embed this similarity metric in a kernel discriminant framework (support vector machines-SVM) and show that very high classification accuracies are obtainable with binary representation of expression profiles. We offer explanations for why such increased performances can be achieved, and attribute this to two reasons: a) the training of class boundaries that happen in SVMs, and b) a hitherto unnoticed probe level uncertainty in microarray data.

Finally, the analysis of microarray data goes through a number of stages of processing steps: background intensity correction, within array normalization, between array normalization and algorithms for detecting differentially expressed genes. A user has a choice of several algorithms at each of these steps and a very large choice if we consider combinations of available algorithms. A

particular appeal of working with binarized representations, as shown by preliminary results in this paper, is that the algorithmic variability in inference is drastically reduced without compromising the quality of inference.

## 2. RESULTS

### 2.1. Classification

**Table 1** compares classification performances of several classifiers on six microarray class prediction datasets. In all cases the accuracies are averaged over 25 random partitions of the data into training and test sets, and standard deviations in performance across these partitions is also given. In all the different problems we checked to ensure that our implementation of the linear SVM classifier acting on raw data performed as well as the results quoted in the original publication or some other publication that used the dataset, thus confirming the correctness of our implementation. Note that in all the tasks considered, comparing data represented at raw and binary precisions and classifying with linear SVMs, we note that binarising the data has not lost much discrimination. In fact in some of the tasks binarization has actually improved performance. Secondly, in half the tasks considered, the use of Tanimoto kernel SVM improves the results of binarized classification. Where there is not an improvement, the method is at least as good as a linear SVM on binarized data.

Our simulations also show that in all the tasks considered the distance to template methods perform significantly worse than the corresponding kernel methods. This is true both for templates set as centroids and for centroids positioned optimally by genetic search. In two of the four datasets considered, optimization of templates quickly led to overtraining, resulting in classifiers whose performance on test data (entries in **Table 1**) were worse than their initial values (which were the performances with templates at centroids). In the genetic optimization, we also found that the local search by mutation was the dominant contributor, showing that the solution to the optimized distance based classifier was in the vicinity of the centroids. Cross-over operations nearly always produced far worse solutions and were quickly abandoned. To explore this further, in addition to the centroids, we included noisy templates into the search algorithm, but found no improvement.

### 2.2. Clustering

**Figure 1** shows the eigenvector obtained in spectral clustering for the widely studied ALL/AML problem [11], computed in three different ways: raw and binarized data with negative exponential of Euclidean distance as similarity, and binarized data with Tanimoto similarity. The scatter clearly shows cluster separation along the components of the eigenvector. This is also



reflected in the Fisher scores between clusters and the corresponding classification errors which are shown in **Table 2**, (columns 4 and 5), where except in one of the datasets, there is improvement in the cluster tightness when Tanimoto similarity is applied. Similarly, in all but one of the tasks, the resulting classification error rates are also lower for the Tanimoto metric.

The final column in **Table 2** shows classification error rates arising from spectral clustering when the microarray profile consists of a filtered subset of genes. In each task we ranked the genes according to their Fisher scores of discriminating power taken one at a time, precisely

the same way as done by Golub *et al.* [11], and report best performing subsets. The difference between the different distance metrics with subsets of genes is shown in **Figure 2** for four of the tasks. We see that the use of Tanimoto similarity leads to better separated clusters in general. Further the better separated clusters also lead to better discrimination. We emphasize that the clustering here is done without the use of class labels, and it is to verify how good the clusters are that we use this information. Thus as expected note the accuracies much lower than when the problem is formulated as a classification problem in the first place.

**Table 1.** Comparison of classification with different types of kernels for SVM.

Dataset	Data type	Method	Accuracy
West <i>et al.</i> [6]	Raw-Binary	Linear-SVM	0.83 $\pm$ 0.10
	Binary	Linear-SVM	0.86 $\pm$ 0.08
	Binary	Tanimoto-SVM	0.87 $\pm$ 0.08
	Binary	Distance-to-class mean	0.79 $\pm$ 0.08
	Binary	Distance-to-optimized template	0.77 $\pm$ 0.11
Huang <i>et al.</i> [7]	Raw-Binary	Linear-SVM	0.63 $\pm$ 0.12
	Binary	Linear-SVM	0.67 $\pm$ 0.08
	Binary	Tanimoto-SVM	0.67 $\pm$ 0.10
	Binary	Distance-to-class mean	0.60 $\pm$ 0.11
	Binary	Distance-to-optimized template	0.66 $\pm$ 0.11
Gordon <i>et al.</i> [8]	Raw-Binary	Linear-SVM	0.99 $\pm$ 0.01
	Binary	Linear-SVM	0.96 $\pm$ 0.03
	Binary	Tanimoto-SVM	0.99 $\pm$ 0.01
	Binary	Distance-to-class mean	0.88 $\pm$ 0.07
	Binary	Distance-to-optimized template	0.90 $\pm$ 0.07
Brown <i>et al.</i> [9]	Raw-Binary	Linear-SVM	0.99 $\pm$ 0.01
	Binary	Linear-SVM	0.98 $\pm$ 0.01
	Binary	Tanimoto-SVM	0.98 $\pm$ 0.01
	Binary	Distance-to-class mean	0.67 $\pm$ 0.02
	Binary	Distance-to-optimized template	0.75 $\pm$ 0.03
Alon <i>et al.</i> [10]	Raw-Binary	Linear-SVM	0.78 $\pm$ 0.11
	Binary	Linear-SVM	0.82 $\pm$ 0.07
	Binary	Tanimoto-SVM	0.84 $\pm$ 0.03
	Binary	Distance-to-class mean	0.80 $\pm$ 0.07
	Binary	Distance-to-optimized template	0.72 $\pm$ 0.10
Golub <i>et al.</i> [11].	Raw-Binary	Linear-SVM	0.96 $\pm$ 0.05
	Binary	Linear-SVM	0.95 $\pm$ 0.03
	Binary	Tanimoto-SVM	0.96 $\pm$ 0.04
	Binary	Distance-to-class mean	0.94 $\pm$ 0.02
	Binary	Distance-to-optimized template	0.92 $\pm$ 0.09

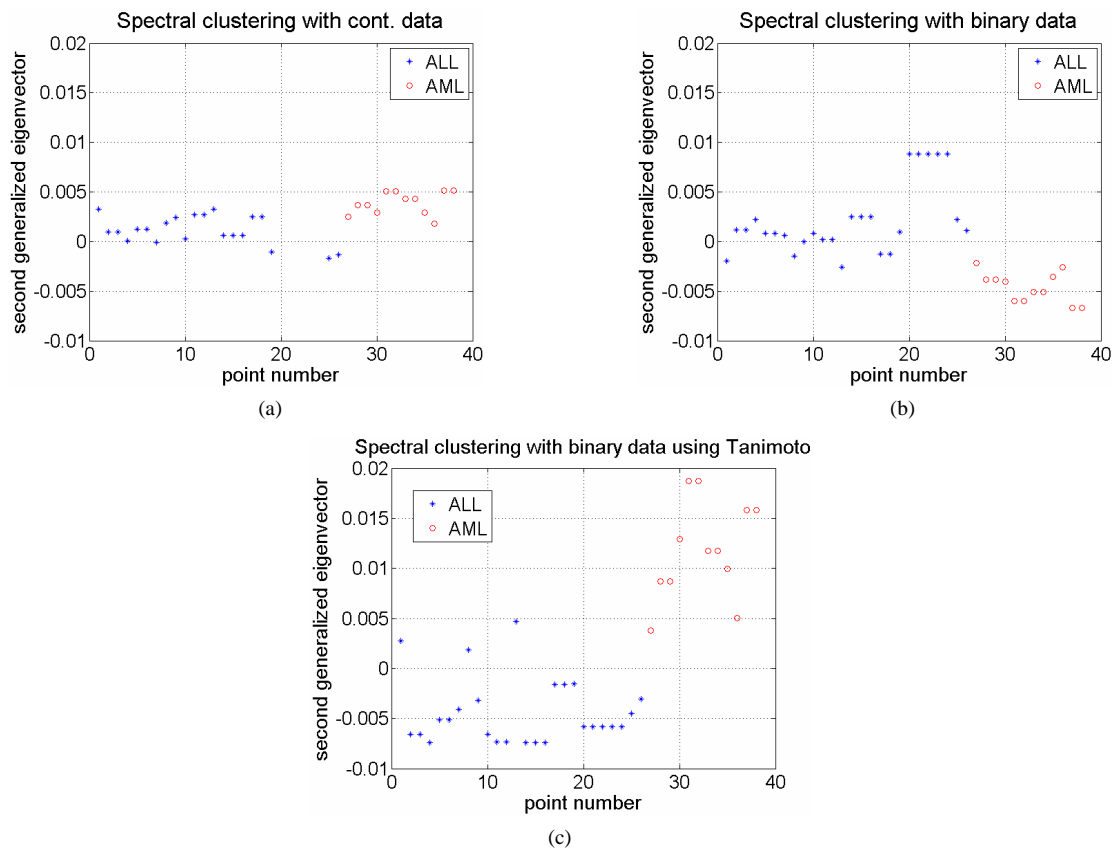


**Figure 1.** Figures showing spectral clustering results for different type of metrics. In (a) spectral clustering is applied to continuous data by using Euclidean distance, in (b) binary data is used with Euclidean distance and in (c) binary data is used with Tanimoto coefficient for spectral clustering. Data from [11].

**Table 2.** Comparison of spectral clustering results by using Tanimoto and Euclidean distance with Fisher score and error rates.

Dataset	Data type	Distance metrics	Fisher score	Error rate	Error rate (best subset of genes)
Simulated data	Raw	Euclidean	$2.47 \pm 0.50$	$0.14 \pm 0.08$	
	Binary	Euclidean	$0.47 \pm 0.49$	$0.33 \pm 0.02$	
	Binary	Tanimoto	$0.66 \pm 0.21$	$0.21 \pm 0.10$	
Golub <i>et al.</i> [11]	Raw	Euclidean	$0.98 \pm 0.41$	$0.32 \pm 0.23$	$0.05 \pm 0.11$
	Binary	Euclidean	$1.01 \pm 0.43$	$0.10 \pm 0.08$	$0.02 \pm 0.04$
	Binary	Tanimoto	$1.49 \pm 0.42$	$0.05 \pm 0.05$	$0.004 \pm 0.02$
Huang <i>et al.</i> [7]	Raw	Euclidean	$0.35 \pm 0.22$	$0.21 \pm 0.05$	$0.04 \pm 0.05$
	Binary	Euclidean	$0.37 \pm 0.18$	$0.22 \pm 0.05$	$0.03 \pm 0.05$
	Binary	Tanimoto	$0.33 \pm 0.17$	$0.21 \pm 0.05$	$0.02 \pm 0.04$
West <i>et al.</i> [6]	Raw	Euclidean	$0.35 \pm 0.04$	$0.45 \pm 0.06$	$0.45 \pm 0.06$
	Binary	Euclidean	$0.30 \pm 0.18$	$0.33 \pm 0.08$	$0.21 \pm 0.15$
	Binary	Tanimoto	$0.35 \pm 0.24$	$0.28 \pm 0.09$	$0.11 \pm 0.07$
Gordon <i>et al.</i> [8]	Raw	Euclidean	$0.21 \pm 0.07$	$0.17 \pm 0.03$	$0.16 \pm 0.03$
	Binary	Euclidean	$0.41 \pm 0.19$	$0.13 \pm 0.02$	$0.09 \pm 0.03$
	Binary	Tanimoto	$0.52 \pm 0.19$	$0.12 \pm 0.02$	$0.08 \pm 0.02$

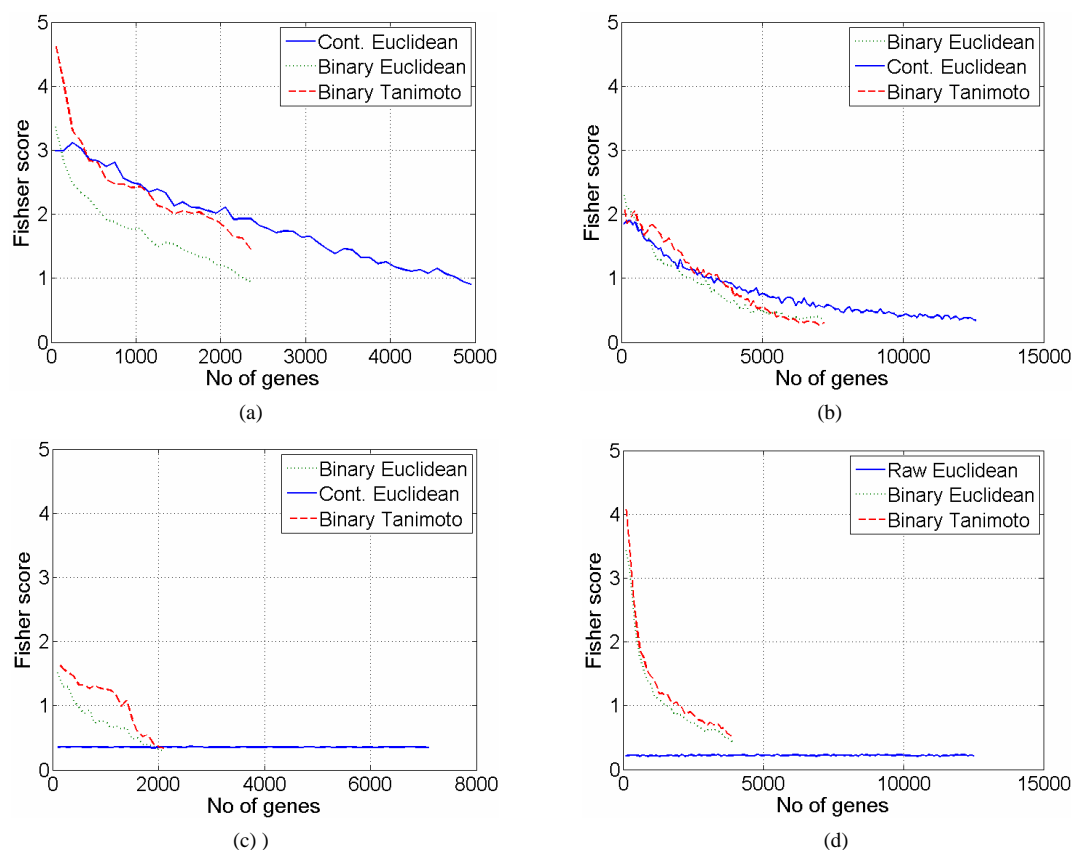


**Figure 2.** Comparison of spectral clustering results for four different datasets at various number of genes selected with Fisher Ratio. (a) is for [11], (b) is for [7], (c) is for [6] and (d) is for [8].

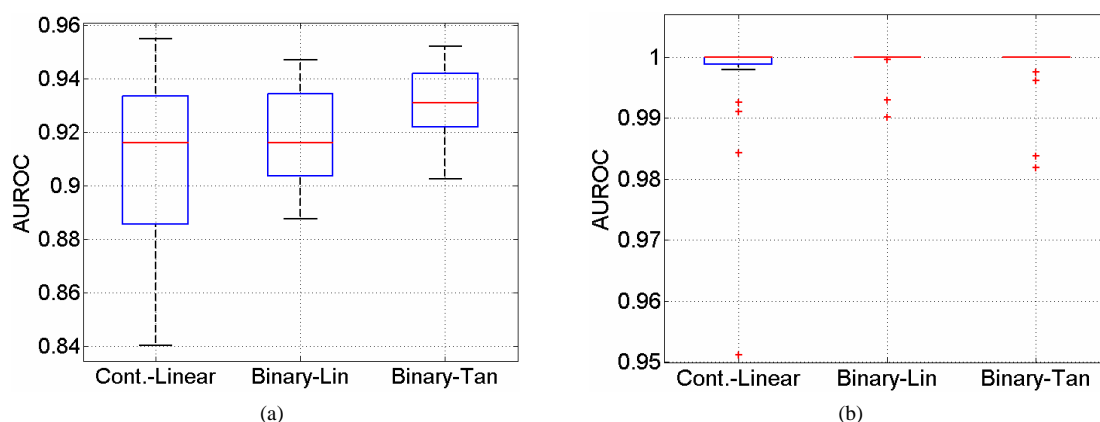


**Figure 3.** Reduction in variability of results due to preprocessing choice of algorithms. randomly chosen 38 combinations of preprocessing the CEL files produce large variations in classification results (leftmost columns). Working with discretized data reduces this variation in the inference. (a) data from [6], and (b) data from GSE2665.

## 2.3. Reduction in Algorithmic Variability

**Figure 3** shows reduction in the variability caused by choice of preprocessing algorithms. Patterns of gene

expression levels change substantially with choice of algorithms, and this has a substantial effect on the resulting inference. A recent careful study (P. Boutros, personal communication<sup>1</sup>) established that this variability is significant. The leftmost columns of **Figures 3(a)** and **(b)** show this as box plots on two datasets. We see

<sup>1</sup>Also presented at the Microarray Gene Expression Society (MGED) meeting, Riva del Garda, Italy, September 2008.

standard deviations in classifier performances, with outliers removed, of 0.032 and 0.134 respectively, and these reduce to 0.017 and 0.009 when the expression levels are binarized. The use of Tanimoto metric (box plots of the last columns of **Figure 3**) improves this even further.

### 3. DATA AND METHODS

#### 3.1. Approach

Our approach was to show that on a sample of classification problems published in literature, classification accuracies reported by the authors do not significantly degrade when the gene expression data is quantized to binary precision (i.e. if the gene is expressed or not). Having achieved this, we implemented a similarity measure suitable for high dimensional binary spaces in a kernel framework to show that any loss of performance is easily recovered. In a number of cases the approach we took indeed produced better accuracies than working with the data at raw precision (see Results).

#### 3.2. Tanimoto Similarity

Tanimoto coefficient ( $T$ ) [12], between two binary vectors, is defined as follow:

$$T = \frac{c}{a + b - c}$$

where

$a$  : the number of expressed points for gene  $x$ ,

$b$  : the number of expressed points in gene  $y$  and

$c$  : the number of common expressed points in two genes.

Tanimoto similarity ranges from 0 (no points in common) to 1 (exact match) [13] and is the rate of the number of common bits on to the total number of bits on two vectors. It focuses on the number of common bits that are on. The denominator of Tanimoto coefficient can be considered as a normalization factor which helps to reduce the bias of the vector size (i.e with larger vectors Tanimoto coefficients work better [14,15]. For this reason Tanimoto coefficient is the preferred similarity measure in chemoinformatics as all the vectors are long and there are only few bits on.

Tanimoto kernel can be defined as [16]:

$$K_{Tan}(x, z) = \frac{x^T z}{x^T x + z^T z - x^T z}$$

where  $a = x^T x$ ,  $b = z^T z$  and  $c = x^T z$ . It follows from the work of Trotter [16] that this similarity metric satisfies Mercer conditions to be useful as a valid kernel: i.e. kernel computations in the space of the given binary vectors map onto inner products in a higher dimensional space so that SVM type optimizations for large margin class boundaries is possible.

Alternate ways of classification of binarized data can

be considered. Motivated by the distance to barcode classifier built by Zilliox and Irizarry [2] we implemented similar classifiers. An obvious choice in these circumstances is to set two templates, one to represent each class, and position them at the centroids of the two class profiles. This is a distance to mean classifier in standard statistical pattern recognition terminology. A particular limitation of this strategy is discussed later. The barcodes designed by Zilliox and Irizarry [2], however, are not positioned at the centroids because they are evaluated by analysing a large number of archived experiments. We also built such discriminant templates, by doing a stochastic search starting from the centroids as initial condition. Such an optimization achieves templates that are better positioned in the input space than centroids for distance-based discrimination.

Clustering is the most popular tool in the analysis of microarray data. In order to conform whether the use of Tanimoto distance metric is useful in clustering, we applied the method of spectral clustering to the classification problems considered above. Without knowledge of the class labels, we clustered each of the datasets into two clusters using spectral clustering. Subsequently, using knowledge of the class labels we looked to see how well separated the clusters formed were, and how accurately the data was allocated to the right clusters. To measure cluster compactness we used the Fisher ratio as performance metric:

$$\text{Fisher Score} = \frac{\text{abs}(\mu_1 - \mu_2)}{\sigma_1 + \sigma_2}$$

Checking if the examples were consistently associated with the right clusters, we computed percentage classification errors. The choice of classification problems to evaluate cluster compactness offers a far better setting than clustering genes into functions. This is because cluster analysis, when the data has large numbers of clusters in them, is notoriously unstable. With data taken from classification problems, we could expect well defined cluster formations (e.g. cancer versus non-cancer), in which we can compare the role of different distance metrics.

#### 3.3. Datasets

We give a short description of the datasets used in our study.

- **Yeast dataset** compiled and first used in Brown *et al.* [9] for predicting yeast gene functions. cDNA arrays, in which the task is to classify 121 ribosomal genes from the remaining 2346 using 79 features. The features are hybridization conditions during cell cycle progression under different synchronization methods.
- Widely used **Leukemia dataset** (Golub *et al.*, [11]); there are 5000 genes with 38 samples (27

ALL, 11 AML), being the test subset of the full dataset.

- **Colon dataset** (Alon *et al.*, [10]), 2000 genes with 62 samples (20 normal and 42 tumour samples).
- Two **Breast cancer datasets**, first one from (West *et al.*, [6]) 7129 genes and 49 samples, (25 ER+ and 24 ER-) and the other Huang *et al.* [7] 12625 genes with 89 samples (depending on LN status).
- **Lung cancer dataset**, (Gordon *et al.*, [8]), 12533 genes and 181 samples (31 malignant pleural mesothelioma (MPM) and 150 adenocarcinoma (ADCA)).
- 53 randomly selected datasets from ArrayExpress (<http://www.ebi.ac.uk/arrayexpress/>) and Gene Expression Omnibus (GEO) (<http://www.ncbi.nlm.nih.gov/geo/>) for probe level uncertainty analysis analysis. Accession numbers of these datasets are:

**GEO:** GSE5666, GSE7041, GSE8000, GSE8505, GSE6487, GSE6850, GSE8238, GSE2665

**Array Express:** E-GEOD-6783, E-GEOD-6784}, E-MEXP-1403, E-ATMX-30, E-GEOD-6647, E-GEOD-6620, E-ATMX-13, E-MEXP-1443, E-GEOD-2450, E-GEOD-2535, E-MEXP-914, E-MEXP-268, E-GEOD-2848, E-GEOD-2847, E-MEXP-430, E-GEOD-6321, E-MEXP-70, E-GEOD-1588, E-MEXP-727, E-TABM-291, E-GEOD-3076, E-GEOD-1938, E-GEOD-7763, E-GEOD-3854, E-GEOD-1639, E-TABM-169, E-MAXD-6, E-MEXP-526, E-GEOD-2343, E-GEOD-3846, E-MEXP-26, E-GEOD-1723, E-GEOD-1934, E-MAXD-6, E-MEXP-879, E-GEOD-10262, E-GEOD-10422, E-MEXP-998, E-MEXP-580, E-GEOD-10072, E-GEOD-10627.

#### Web Pages:

<http://yeast.swmed.edu/cgi-bin/dload.cgi>,  
<http://data.genome.duke.edu/west.php>,  
<http://data.genome.duke.edu/lancet.php>,  
<http://chestsurg.org/publications/2002-microarray.aspx>

- Synthetic data was produced following Dettling [17], using R code made available by the authors. Data is produced to follow the statistics (mean and correlation structure) of the leukaemia data [11]. We generated several realizations of 200 samples in 250 dimensions. We explored varying these values over a range, and results reported in this paper correspond to the above figures.

### 3.4. Spectral Clustering

Spectral clustering uses eigenvectors of the pairwise similarity matrix to partition the data. The most widely used distance metric to calculate the similarity matrix is the negative exponential of a scaled Euclidean distance.

$$A_{(i,j)} = \exp \left( -\frac{\|x_i - x_j\|^2}{\sigma^2} \right)$$

where the scale parameter  $\sigma$  is a free tuning parameter. The steps involved in spectral clustering, in which we replace the similarity measure by Tanimoto similarity between binary strings, are summarized as follows:

- Pairwise similarity matrix  $A_{i,j}$  between the genes  $i$  and  $j$  is calculated by using Tanimoto coefficient.
- Following Brewer [18] an exponential is applied:

$$A_{ij}^F = \exp^{-\alpha(A_{ij}-1)^2}$$

- Compute the normalized Laplacian matrix.

$$L = D^{-1/2} \times A^F \times D^{-1/2}$$

- Compute the eigenvalue decomposition of L.

$$(D - L)y_i = \lambda_i D y_i$$

- Select the eigenvector corresponding to the second smallest eigenvalue.

Parameters  $\alpha$  and  $\sigma$  were tuned by searching over a range of feasible values:  $-5.0 \rightarrow 5.0$ .

Uncertainties in results for cluster analysis were evaluated by a bootstrap method. For each of the tasks, 100 datasets of the same size as the original data were created by sampling with replacement before the application of the spectral clustering algorithm. Performances reported are averages and standard deviations across these 100 bootstrap samples.

### 3.5. Optimised Templates

The search to find templates better than class means for a distance-to-template classifier was implemented as a stochastic local search by means of a genetic algorithm. Templates were initialized to class means. At every step in an iterative search, we randomly changed 20% of the elements in the two templates, to derive mutated barcodes in their vicinity. Throughout the search, we retained ten best template pairs at any iteration. Large search steps were implemented by crossover operation between pairs of templates whereby half the bits in the patterns were swapped between pairs, a standard operation in genetic algorithms. We evaluated the accuracy of the resulting classifier and there was an improvement we retained the mutated templates, and discarded them if was no improvement.



### 3.6. Algorithmic Variability

We used the EXPRESSO set of algorithms in package Affy in Bioconductor. For both datasets West *et al.* [6] and GSE2665, we worked from the CEL files and applied a total of 38 different preprocessing combinations from a total of 315 possibilities, randomly chosen.

### 3.7. Other Details

To analyse probe level uncertainties (Milo *et al.* [19]) we used the PUMA package (Propagating Uncertainty in Microarray Analysis), downloaded from the site ([www.bioinf.manchester.ac.uk/resources/puma/](http://www.bioinf.manchester.ac.uk/resources/puma/)). For quantization of microarray data, we used the method developed by Zhou *et al.* [20], which models gene expressions as mixture Gaussian densities. For quantization to binary levels, two Gaussians are used, resulting in two means and standard deviations:  $\mu_1, \mu_2, \sigma_1$  and  $\sigma_2$ . From these a threshold  $\theta$ , is computed as  $\theta = 0.5 \times (\mu_1 + \mu_2 + \sigma_1 - \sigma_2)$ . SVM implementations were done in the MATLAB SVM package described in Gunn [21] (<http://www.isis.ecs.soton.ac.uk/isystems/kernel/>).

## 4. CONCLUSIONS

The results suggest that a binary representation for transcriptomic data is indeed suitable and good classification accuracies can be obtained in this space using suitable similarity metrics cast in a kernel framework. There are two reasons for the superior performance of Tanimoto-SVM based approach over the distance to template approach inspired by the barcode approach.

### 4.1. Distance to Template Classifier

Why did the distance to template method not perform well consistently in classification problems? We suggest this result is largely to be expected. With continuous data, it is a well known result of statistical pattern recognition

that classification by computing distances to a template is optimal only in the case that the distributions of each class is Gaussian, isotropic (i.e. variances of each feature is the same) and these variances are the same for both [22]. When any of these assumptions is violated, a distance to template classifier is no longer optimal. Even under the mild relaxations of the assumption, that of Gaussian densities with identical but nonisotropic covariance matrices, the optimal classifier requires computation of second order statistics in the form of the Mahalanobis distance to class means. In gene expression data isotropic variation cannot be assumed. Under regulation by combinatorial transcription factor activity where each transcription factor may control several genes, correlated expression of groups of genes should be expected. Indeed, the wide use of cluster analysis of microarray data is based on the assumption that correlated expression profiles might suggest co-regulation. Therefore, as uncorrelated features cannot be assumed, optimal classification is unlikely to be achieved by distance to template decision rules.

Does the same difficulty arise in the barcode method proposed by Zilliox and Irizarry (2007)? To verify this we took three datasets, one of which was not included in their analysis. Prediction accuracies for these three, comparing the barcode method to Tanimoto-SVM, are shown in **Table 3**. We note that training and testing on the same database, as we have done with Tanimoto-SVM, achieves consistently better prediction accuracies than the barcode method. But in fairness to the barcode method we remark that their intention is to make predictions on a new dataset based on accumulated historic knowledge, rather than repeat the training/testing process all over again. On this point, while there is impressive performance reported on the datasets Zilliox and Irizarry (2007), worked on, the method can fail badly too, as in the case of the lung cancer prediction task E-GEOD-10072 shown in **Table 3**.

**Table 3.** Comparison of Tanimoto-SVM with [2]'s barcode.

Dataset	Data type	Method	Accuracy
E-GEOD-10072	Binary	Barcode	0.50
Lung	Binary	Tanimoto-SVM	$0.89 \pm 0.03$
Lung tumor vs. normal	Binary	Tanimoto-SVM	$0.99 \pm 0.03$
GSE2665	Binary	Barcode	0.95
Lymph node/tonsil	Binary	Tanimoto-SVM	$0.99 \pm 0.02$
lymph node vs. tonsil	Binary	Tanimoto-SVM	$1.0 \pm 0.0$
GSE2603	Binary	Barcode	0.90
Breast Tumor	Binary	Tanimoto-SVM	$0.99 \pm 0.01$
Breast Tumor vs. normal	Binary	Tanimoto-SVM	$0.99 \pm 0.01$

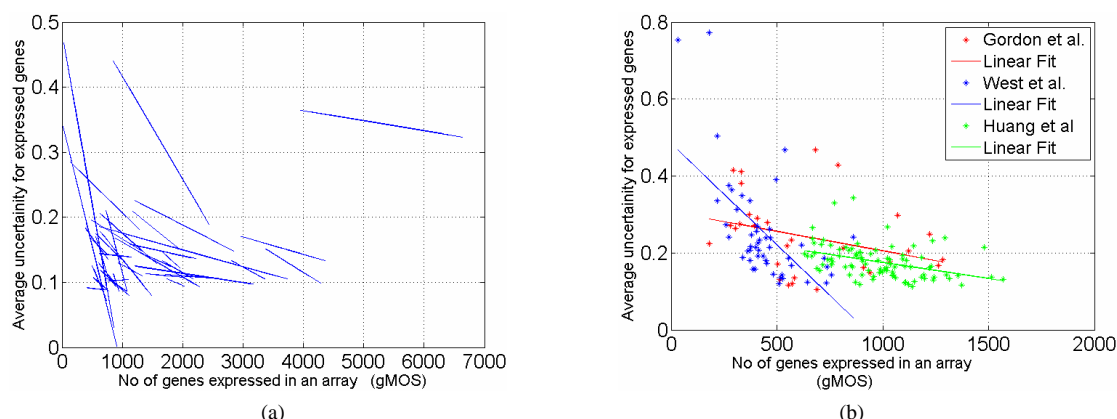


**Figure 4.** A systematic variation in probe level uncertainty of Affymetrix microarray data. (a) On 53 randomly chosen arrays we plot the average uncertainty of determining expression levels against the number of genes detected as present. Only liner regression lines are shown for clarity. (b) Scatter plots of uncertainties against number of expressed genes, and the linear regression lines, for the three datasets analysed in this paper.

## 4.2. Probe Level Uncertainty

The Tanimoto similarity metric attaches higher scores to profiles with large numbers of expressed genes. For example if we consider two pairs of vectors with

$$\begin{bmatrix} 1 & 0 & 0 & 0 & 0 & 0 & 0 \end{bmatrix} \quad \begin{bmatrix} 1 & 1 & 0 & 0 & 0 & 0 & 0 \end{bmatrix}, \\ \begin{bmatrix} 1 & 1 & 0 & 0 & 0 & 0 & 0 \end{bmatrix} \quad \begin{bmatrix} 1 & 1 & 1 & 0 & 0 & 0 & 0 \end{bmatrix}$$

In both cases Hamming distance, thus Euclidean distance, is one. The Tanimoto similarities between these pairs, however, are different: 0.5 for the first pair and 0.66 for the second. We suggest that a reason why such a weighting on the similarity scores translates to improve clustering and class prediction performance comes from the uncertainties associated with microarray measurements. We found a systematic variation in uncertainties in expression levels as function of the numbers of expressed genes in an array. To illustrate this we used a probabilistic model of encapsulating probe level uncertainties introduced in Milo *et al.* (2003) [19], and plotted the average uncertainty in expressed genes as a function of the number of genes marked as expressed under our quantization scheme for several arbitrarily chosen datasets.

**Figure 4** shows the variation in uncertainty with numbers of expressed genes, for three of the datasets on which we report classification results, and for 50 arbitrarily taken datasets from archives. We see that there is a systematic reduction in probe level uncertainty as the number of expressed genes in an array gets larger<sup>2</sup>. We offer no molecular level explanation for this, but the

effect is systematic and its impact on the Tanimoto-SVM is clear. Arrays with larger numbers of expressed genes are being measured with higher levels of confidence. Hence if we were to increase the weighting given to similarities between such profiles we would expect increased performance. Such probe level uncertainty has been of interest to other researchers, too. Rattray *et al.* [23] and Sanguinetti *et al.* [24] show how cluster analysis and visualization in a subspace by principal component projections can be carried out incorporating probe level uncertainty. In general these are errors-in-variables type models. We believe accounting for probe level (and other low level) uncertainties in microarray analysis is an important topic, and the systematic variability we have noted here may well be an aspect that other researchers can exploit in microarray inference.

## REFERENCES

- [1] I. Shmulevich and W. Zhang, (2002) Binary analysis and optimization-based normalization of gene expression data, *Bioinformatics*, **18**(4), 555–565.
- [2] M. J. Zilliox and R. A. Irizarry, (2007) A gene expression bar code for microarray data, *Nature Methods*, **4**(11), 911–913.
- [3] S. Tuna and M. Niranjan, (2009) Inference from low precision transcriptome data representation, *Journal of Signal Processing Systems*, [Online, 22 April 2009], doi: 10.1007/s11265-009-0363-2.
- [4] S. Draghici, P. Khatri, A. C. Eklund, and Z. Szallasi, (2006) Reliability and reproducibility issues in DNA microarray measurements, *Trends in Genetics*, **22**(2), 101–109.
- [5] D. Geman, C. d’Avignon, D. Q. Naiman, and R. L. Winslow, (2004) Classifying gene expression profiles from pairwise mRNA comparisons, *Statistical Applications in Genetics and Molecular Biology*, **3**.
- [6] M. West, C. Blanchette, H. Dressman, E. Huang, S. Ishida, R. Spang, H. Zuzan, J. A. Olson, J. R. Marks, and

<sup>2</sup>We stress that this variation is *not* a consequence of amplifying noise in the data of normalised poor quality arrays; i.e. for an array scanned at low intensity, normalization amplifies noise; the effect of such noise would be to *increase* the average uncertainty when more and more genes are taken as expressed. This is precisely the opposite of what we see in **Figure 4**.

- J. R. Nevins, (2001) Predicting the clinical status of human breast cancer by using gene expression profiles Proceedings of National Academy of Sciences, **98**(20), 11462–11467.
- [7] E. Huang, S. H. Cheng, H. Dressman, J. Pittman, M. Tsou, C. Horng, A. Bild, E. S. Iversen, M. Liao, C. Chen, M. West, J. R. Nevins, and A. T. Huang, (2003) Gene expression predictors of breast cancer outcomes Lancet, **361**, 1590–1596.
- [8] G. J. Gordon, R. V. Jensen, L. Hsiao, S. R. Gullans, J. E. Blumenstock, S. Ramaswamy, W. G. Richards, D. J. Sugarbaker, and R. Bueno, (2002) Translation of microarray data into clinically relevant cancer diagnostic tests using gene expression ratios in lung cancer and mesothelioma, Cancer Research, **62**(17), 4963–4967.
- [9] M. P. S. Brown, W. N. Grundy, D. Lin, N. Cristianini, C. W. Sugnet, T. S. Furey, M. Ares, and D. Haussler, (2000) Knowledge-based analysis of microarray gene expression data by using support vector machines, Proceedings of National Academy of Sciences, **97**(1), 262–267.
- [10] U. Alon, N. Barkai, D. A. Notterman, K. Gish, S. Ybarra, D. Mack, and A. J. Levine, (1999) Broad patterns of gene expression revealed by clustering analysis of tumor and normal colon tissues probed by oligonucleotide arrays, Proceedings of National Academy of Sciences, **96**(12), 6745–6750.
- [11] T. R. Golub, D. K. Slonim, P. Tamayo, C. Huard, M. Gaasenbeek, J. P. Mesirov, H. Coller, M. L. Loh, J. R. Downing, M. A. Caligiuri, C. D. Bloomfield, and E. S. Lander, (1999) Molecular classification of cancer: Class discovery and class prediction by gene expression monitoring, Science, **286**(5439), 531–537.
- [12] T. T. Tanimoto, (1958) “An elementary mathematical theory of classification and prediction,” IBM Internal Report.
- [13] P. Willett, (2006) Similarity-based virtual screening using 2d fingerprints, Drug Discovery Today, **11**(23/24), 1046–1053.
- [14] P. Willett, J. M. Barnard, and G. M. Downs, (1998) Chemical similarity searching, Journal of Chemical Information and Computer Sciences, **38**(6), 983–996.
- [15] J. D. Holliday, N. Salim, M. Whittle, and P. Willett, (2003) Analysis and display of the size dependence of chemical similarity coefficients, Journal of Chemical Information and Computer Sciences, **43**(3), 819–828.
- [16] M. Trotter, (2006) Support vector machines for drug discovery. PhD thesis, University College London, UK.
- [17] M. Dettling, (2004) BagBoosting for tumor classification with gene expression data, Bioinformatics, **20**(18), 3583–3593.
- [18] M. Brewer, (2007) Development of a spectral clustering method for the analysis of molecular data sets, Journal of Chemical Information and Modeling, **47**(5), 1727–1733.
- [19] M. Milo, A. Fazeli, M. Niranjani, and N. D. Lawrence, (2003) A probabilistic model for the extraction of expression levels from oligonucleotide arrays, Biochemical Society Transactions, **31**(6), 1510–1512.
- [20] X. Zhou, X. Wang, and E. R. Dougherty, (2003) Binarization of microarray data on the basis of a mixture model, Molecular Cancer theapeutics, **2**(7), 679–684.
- [21] S. Gunn, (1998) Support vector machines for classification and regression, Tech. Rep., University of Southampton.
- [22] R. O. Duda, P. E. Hart, and D. G. Stork, (2001) Pattern Classification, John Wiley & Sons, USA, ISBN 0-41-05669-3.
- [23] M. Rattray, X. Liu, G. Sanguinetti, M. Milo, and N. Lawrence, (2006) Propagating uncertainty in microarray data analysis, Briefings in Bioinformatics, **7**(1), 37–47.
- [24] G. Sanguinetti, M. Milo, M. Rattray, and N. D. Lawrence, (2005) Accounting for probe-level noise in principal component analysis of microarray data, Bioinformatics, **21**(19), 3748–3754.

# Study of blood fat concentration based on serum ultraviolet absorption spectra and neural network

Wei-Hua Zhu<sup>1,2</sup>, Zhi-Min Zhao<sup>1</sup>, Xin Guo<sup>1</sup>, Le-Xin Wang<sup>1</sup>, Hui Chen<sup>1</sup>

<sup>1</sup>College of Science, Nanjing University of Aeronautics and Astronautics, Nanjing, China; <sup>2</sup>College of Science, Hohai University, Nanjing, China.

Email: [weihua\\_zhu@126.com](mailto:weihua_zhu@126.com); [zhaozhimin@nuaa.edu.cn](mailto:zhaozhimin@nuaa.edu.cn)

Received 11 April 2008; revised 31 May 2009; accepted 9 June 2009.

## ABSTRACT

Blood plays an important role in the clinical diagnosis and treatment, the analysis of blood will be of very important practical significance. The experiment shows that the absorption spectra of blood are of serious noise in the wave band of 200 to 300 nm, which hides the useful spectral characteristics. The effective separation of the noise was achieved by db4 wavelet transform, and the signals of reconstruction have been obviously improved in the noise serious wave band, reflecting some useful information. The absorption peaks of different samples are displaced to some degrees. The correlation between absorbance at 278nm and blood fat concentration is no significant and random. Based on the evident correlation between serum absorption spectrum and blood fat concentration in the wave band of 265 to 282nm, a neural network model was built to forecast the blood fat concentration, bringing a relatively good prediction. This provides a new spectral test method of blood fat concentration.

**Keywords:** Blood Fat Concentration; Ultraviolet Absorption Spectra; Neural Network (NN); Serum; Wavelet Transform

## 1. INTRODUCTION

An organism (especially the human organism) is a complex life system, with important spectral information. Research shows that the spectral features of an abnormal biological tissue will be changed. Swiss scientists found that nerve cell degeneration will lead Alzheimer's disease. Early diagnosis of the disease can be made through the analysis of fluorescence information of degeneration process of tissue [1]. Thus, it is a new challenging research topic to make effective analysis and diagnosis of

disease using the spectrum information of biological tissue, particularly blood analysis technology. Some meaningful research about this have attracted much attention [2,3,4,5,6,7,8,9,10,11,12,13,14,15,16,17,18].

Although a lot of researches about blood spectra have been reported, a deep and general research is still need to be processed. This may be because that little blood sample was used and the samples were not representative. For example, Wang *et al.* [2] have studied the infrared absorption spectra of normal blood sample and abnormal blood sample, the difference of the spectra between normal and abnormal blood samples was obtained, however, there are only three samples were researched, so the reliability of their results should be tested deeper. The actual blood components are very complex, so the absorption spectrum is consist of multiple spectral components, the information of the components can be obtained from the spectrum distribution and spectral characteristics.

Neural network can simulate human learning to handle highly nonlinear problems. This can make it widely applied in complex systems forecast, achieving the effect of nonlinear mappings, which are difficult to achieve by traditional algorithms [19,20,21].

It is known from the early study [22] that the serum with different blood fat concentration presents unlike absorption spectrum, therefore, information such as blood fat in the serum can be obtained by analyzing the absorption spectrum of different concentration blood fat and then be help for diseases diagnosing. This paper studies the relation between the blood fat concentration and the absorption spectrum at 278nm, as well as to establish the BP nerve network model used for predicting blood fat concentration, supplying a new method for spectrum analysis of the blood detection.

## 2. NEURAL NETWORK STRUCTURE AND METHODS

**Figure 1** shows a widely applied BP neural network

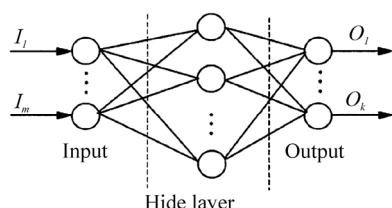


**Figure 1.** Diagram of a BP neural network.

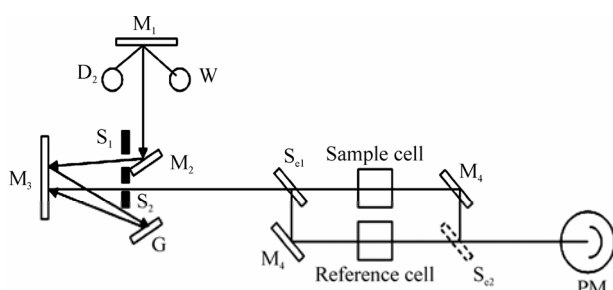


**Figure 2.** Optical pathway diagram of detecting absorption spectra.

structure (this schematic diagram can be obtained in all textbooks about serve network), which is a feed-forward neural network. I is for input and O is for output. The neurons of this network structure only receive one output before the neurons normally. There is no connection between neurons in the same layer. Study shows that three layer feed-forward neural network will be able to approach any continuous function [23].

In this paper, BP neural network was used to determine the blood fat content in the blood, which contains three layers, that is, input layer, hide layer and output layer respectively. There is a node in the output layer, which represents blood fat content (expressed by concentration). The absorbance of 265nm to 282 nm wave band is for Network input. The number of hide layer node was determined by the correlation coefficient between the target and the output. The two transfer function is different. S-type function was used for input layer and hide layer, and specific function here was hyperbolic form. The linear function was used for hide layer and output layer.

In order to improve the efficiency of neural network training, the absorption spectra were pretreatment:

- 1) Normalization will make the treated input and target data appear normal distribution.
- 2) The treated samples data were used for PCA to eliminate redundant data and to reduce the number of data dimension.

In order to increase network capacity of generalization and recognition, “stay ahead” approach was used in training. The samples were divided into training samples collection, validation samples collection and testing samples collection.

### 3. SPECTRAL DETECTION SYSTEM AND EXPERIMENTAL SAMPLES

#### 3.1. Spectral Detection System

The absorption spectra detection system used in the experiment is UV-3600 made by SHIMADZU Corporation. **Figure 2** shows UV-3600 optical pathway diagram of double beam spectrophotometer. A beam of light from lamp-house  $D_2$  or W becomes parallel beam through reflector  $M_1$ , plane reflector  $M_2$ , entrance slit  $S_1$  and collimating mirror  $M_3$ . The parallel beam is dispersed by grating G. Then, through  $M_3$ , enters slit  $S_2$ , sector mirror  $S_{e1}$  and reflector  $M_4$ , the beam alternately enters into the sample cell and the reference cell. At last, the beam alternately passes through  $S_{e2}$  and is finally received by photomultiplier PM. The signal of the beam then displays on the computer.

#### 3.2. Experimental Samples

All the samples come from the Hospital of Nanjing University of Aeronautics and Astronautics. Person, whose blood was collected, are not permitted to have breakfast. 0.2ml blood serum mixes with 2ml distilled water. The mixture of proper volume is injected into quartz cell and spectrometer will be used for detecting the absorption spectra of the samples.

### 4. PROCESSING ANALYZING OF EXPERIMENTAL RESULTS

#### 4.1. The Reconstruction of Absorption Spectra

**Figure 3** shows the original signal, reconstruction signal

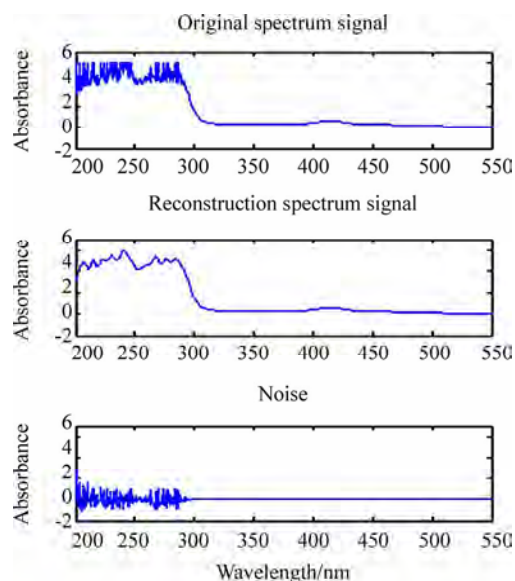


**Figure 3.** Original signal, reconstruction signal and the noise.



and the noise of a sample by db4 wavelet transform (the signal filtering threshold was selected based on both rigorsure rules and the principle of stein unbiased likelihood estimate). It is discovered from **Figure 3** that there is serious noise in the wave band from 200nm to 300 nm in the original spectrum signal, which has an influence on analyzing useful information in the spectrum. The reconstruction signal between 200nm and 300nm becomes clear, and some absorption peaks (such as 278nm) appear. **Figure 3** shows that the noises mainly concentrate on the wave band from 200nm to 300nm, and the values of the noises evenly distribute near zero, which is usually the characteristic of the noise. There is no noise in the wave band after 300nm, and it accords with the original spectrum.

**Figure 4** shows the reconstruction signals of part different samples in the wave band from 200nm to 300nm. It can be known from the **Figure 4** that absorption spectrum is of the following characteristics in the wave band from 200nm to 300 nm: 1) The shape of the absorption spectrum is complex. There is more absorption peak, showing that there is a complex absorption phenomenon in blood group macromolecules. 2) The curve shapes of absorption spectra are similar to different samples, due to that the spectrum is synthesis of some group macromolecules absorption spectrum. Therefore, the spectral distribution contains information such as the blood fat content. 3) The absorption peak of different samples displace to some degree.

#### 4.2. Relationship between Absorbance of 278nm and Blood Fat Concentration

Zhao *et al.* [22] have reported the ultraviolet absorption spectrum of normal and abnormal serum respectively,

they found that the absorbance of these two different kinds serum are obvious different at 278nm, however, there are only three samples are studied, so none exact conclusions are obtained. Our paper will research the relation between absorbance and concentration of 45 samples at 278nm. The relationship is shown in **Figure 5**. The abscissa is blood fat content, and longitudinal coordinates is absorbance.

We can see from **Figure 5** that the correlation between the absorbance and blood fat content is not obvious but random. It indicates the absorbance at 278 nm is synthesis of absorption of all kinds of components. When the blood fat content is in 0.5-1.0 mmol.L<sup>-1</sup>, many samples have the larger absorbance, mostly due to that other constituent's absorbance is relatively larger. Therefore, for the actual blood, whether abnormal blood fat level can not be used to determine only considered the absorbance of some peaks (such as 278 nm) usually.

#### 4.3 Neural Network Prediction Fat Content

As noted above, the absorbance is the synthesis of absorbance of all kinds of components. There is information of many elements at any wavelength. Therefore, the spectral distribution contains much information such as the blood fat content. In this paper, the neural network model based on a certain absorption spectra was used to obtain information of the blood fat contents. When the range of wavelength variation is changed, the correlation coefficient between the predictive value and target value for the blood concentration will vary. Therefore, we can choose suitable model based on the correlation coefficient. It is known from the calculation that a good network forecast model can be found when the spectrum data of 265 to 282 nm is used for network input.

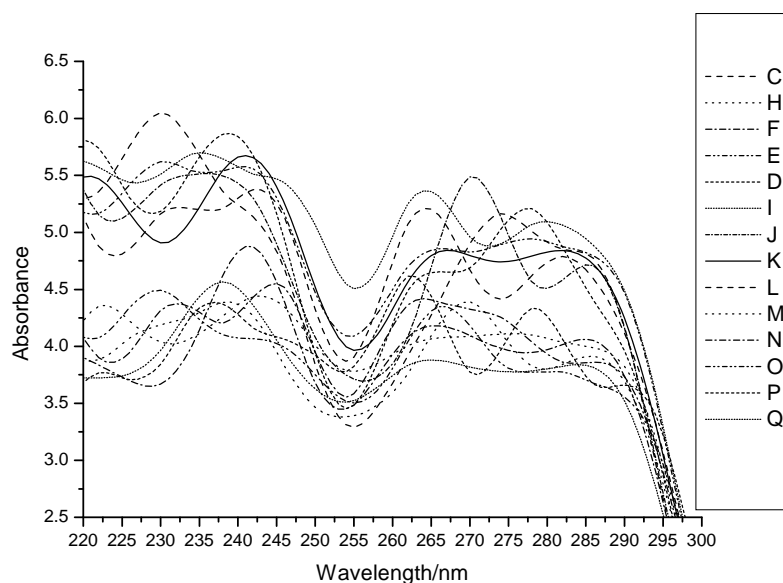


**Figure 4.** The reconstruction signals of part different samples.

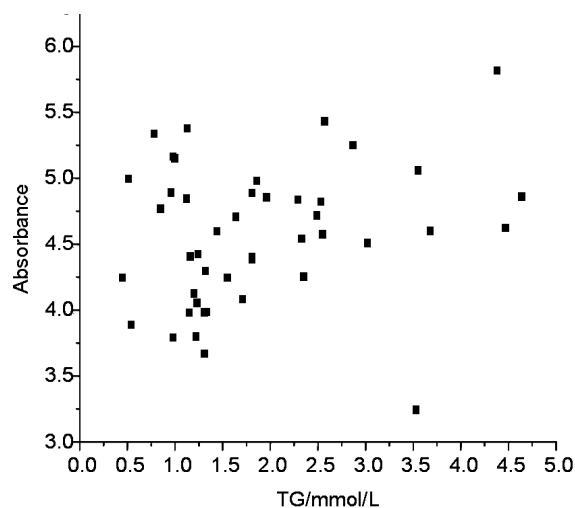


**Figure 5.** The relationship between absorbance of 278nm and blood fat content

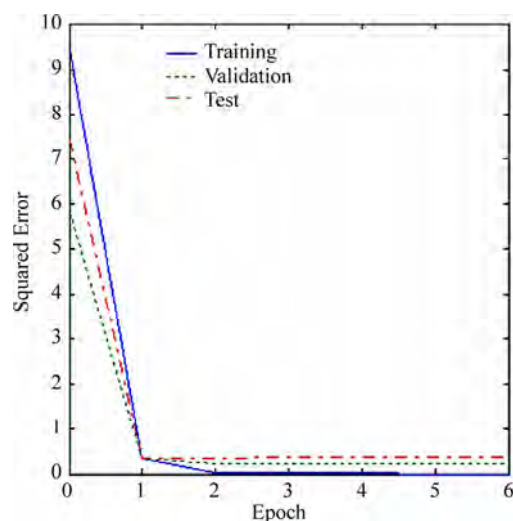


**Figure 6.** Error training curves.

**Figure 6** shows the network training error curves, where the abscissa being the training number and longitudinal coordinate corresponding to MSE. The validation error is basic agreement with testing error's trend, indicating the samples division is reasonable. Network training first stop at step 6, which is because that the testing error becoming larger. Training errors is relatively satisfying from the training curve error.

**Figure 7** is the regression analysis result of network output blood fat content. The correlation coefficient between predicted blood fat content output A and objectives T reaches 0.928, it can be regarded as a better prediction. It also shows that the blood fat content information is implicit in absorption spectrum and neural network provides an effective means to access spectral information.

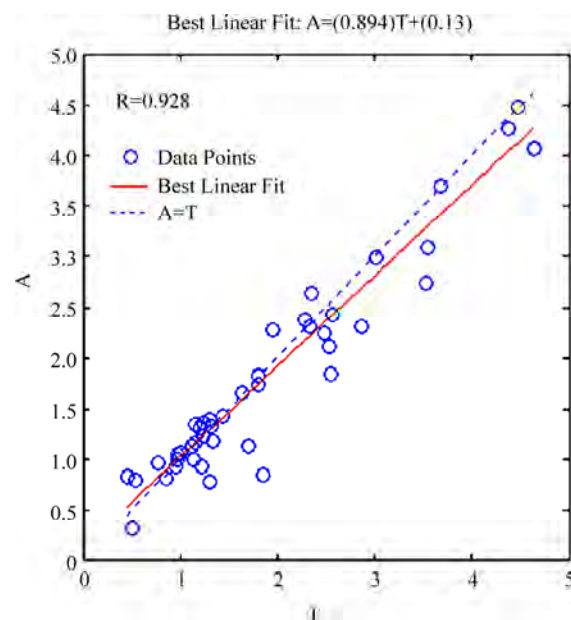


**Figure 7.** Regression analysis result of network output (A) blood fat content.

## 5. CONCLUSIONS

Db4 wavelet has preferable transformation character when it is used to analyze absorption spectra of blood. The signals of reconstruction are obviously improved in the noise serious wave band, reflecting some useful information.

The ultraviolet absorption spectrum of serum is complex. There is more absorption peak from 200 to 300nm, showing that there is a complex ultraviolet absorption phenomenon in blood group macromolecules. The absorption spectrum is the synthesis result of blood fat and other components spectrum, and the information is contained at each wavelength. Therefore, blood fat content and other information are contained in the spectral distribution, which is the basis of blood testing based on spectra analysis. The absorption peaks of different samples are displaced to some degrees.

There is no significant correlation between absorbance at 278nm and blood fat concentration. Based on the evident correlation between serum absorption spectrum and blood fat concentration in the wave band of 265 to 282nm, a neural network model was built to forecast the blood fat concentration, resulting a relatively good prediction.

## 6. ACKNOWLEDGEMENTS

This study was supported by research funds from the National Natural Science Foundation of China (NO.10172043), the Scientific Research and Innovation Fund (NO.1008905704), the Science Foundation of Hohai University (NO. 2008430311), and the International Science and Technology Cooperation Program (NO. BZ2008060).

## REFERENCES

- [1] Z. Shun, (2004) Nanjing Daly.
- [2] L. X. Wang, Z. M. Zhao, H. B. Yao, *et al.*, (2002) Infrared absorption spectrum analysis and its application to blood, *Spectroscopy and Spectral Analysis*, **22**(6), 980–982.
- [3] Z. M. Zhao, Y. M. Chen, and X. L. Yu, (2003) Characteristic analysis and application of blood fluorescence spectra, *Spectroscopy and Spectral Analysis*, **23**(5), 922–925.
- [4] Z. M. Zhao, L. F. Guo, X. L. Yu, *et al.*, (2005) Analysis and application of excitation fluorescence intensity of blood, *Spectroscopy and Spectral Analysis*, **25**(12), 2056–2060.
- [5] X. F. Lan, J. G. Liu, Y. Liu, *et al.*, (2006) Spectroscopy research on cholesterol in hypercholesterolemia serum, *Spectroscopy and Spectral Analysis*, **26**(13), 467–470.
- [6] C. Q. Yu, F. G. Liu, Y. Gu, *et al.*, (2004) Laser induced fluorescence spectra of human skin and blood, *Chin. J. Laser. Med. Surg.*, **13**, 41–444.
- [7] J. D. Li, J. H. Ding, M. Wu, *et al.*, (2006) Diagnosis of hepatocirrhosis by fluorescence spectrum of serum, *APPLIED LASER*, **24**(2), 112–114.
- [8] J. W. Men, R. E. Zheng, Y. D. Zhang, *et al.*, (2003) Cancer detection by serum fluorescence analysis: A pectroscopic study, *Chin. J. Laser. Med. Surg.*, **1**(1), 43–47.
- [9] X. H. Ge, Y. L. Zhao, F. Q. Zhang, *et al.*, (2007) Effect of cancer cells on the spectra of serums, *Spectroscopy and Spectral Analysis*, **24**(7), 841–843.
- [10] X. F. Shi, J. Ma, W. Z. Mao, *et al.*, (2006) Applying partial least squares discriminant analysis on autofluorescence spectra to identify gastric cancer, *Spectroscopy and Spectral Analysis*, **26**(2), 295–298.
- [11] D. Rohleder, G. Kocherscheidt, and K. Gerber, (2005) Comparison of mid-infrared and Raman spectroscopy in the quantitative analysis of serum, *J. Biomedical Optics*, **10**(3), 1–10.
- [12] Runger and M. Thomas, (2007) How different wavelengths of the ultraviolet spectrum contribute to skin carcinogenesis: The role of cellular damage responses, *J. Invest Dermatol*, **127**(9), 2103–2105.
- [13] G. C. Tang, (1989) Pulsed and CW laser fluorescence from cancerous, normal and chemically treated normal human heart and lung tissues, *Applied Optics*, **28**(12), 2337–2343.
- [14] S. Rochkind, M. Nissan, M. Alon, *et al.*, (2001) Effects of laser irradiation on the spinal cord for the regeneration of crushed peripheral nerve in rats, *Laser in Surgery Medicine*, **28**(3), 216–219.
- [15] M. Gniadecka, H. C. Wulf, O. F. Nielsen, *et al.*, (1997) Distinctive molecular abnormalities in benign and malignant skin lesion: Studies by Raman spectroscopy, *Photochem Photobiol*, **66**, 418–423.
- [16] S. P. Qin, J. H. Ding, and J. D. Li, (2006) Research on fluorescence spectra of liver pathological serum of mice with wavelet transforms method, *Journal of Optoelectronics Laser*, **17**(5), 634–637.
- [17] Y. T. Wang and Y. C. Li, (2006) Application of wavelet threshold denoising method in the fluorescence analysis of pesticides, *Journal of Applied Optics*, **27**(3), 192–194.
- [18] D. T. Li, C. J. Zhang, and J. Wang, Application of wavelet transform to infrared analysis, *Spectroscopy and Spectral Analysis*, **26**(11), 2024–2026.
- [19] Y. F. Tang, Z. Y. Zhang, G. Q. Fan, *et al.*, (2005) Identification of official rhubarb samples based on IR spectra and neural networks, *Spectroscopy and Spectral Analysis*, **25**(5), 715–278.
- [20] G. H. Wu, C. Y. He, and R. Chen, (2002) Application of artificial neural network to simultaneous spectro-fluorimetric determination of phenol and resorcinol, *Spectroscopy and Spectral Analysis*, **22**(5), 813–815.
- [21] Y. Z. Han, Y. X. Zhang, S. J. Chang, *et al.*, (2005) Recognition for the nonlinear fluorescence spectra based on optimal wavelet transform and artificial neural network, *Journal of Optoelectronics and Laser*, **16**(6), 719–721.
- [22] Z. M. Zhao, Y. J. Xin, L. X. Wang, *et al.*, (2008) Measurement and analysis of absorption spectrum of human blood, *Spectroscopy and Spectral Analysis*, **28**(1), 138–140.
- [23] J. E. Meng, (2002) Face recognition with radial function (RBF) neural networks, *IEEE Transaction on Neural Network*, **13**(3), 15–17.

# ECG arrhythmia classification based on logistic model tree

V. Mahesh<sup>1</sup>, A. Kandaswamy<sup>2</sup>, C. Vimal<sup>2</sup>, B. Sathish<sup>2</sup>

<sup>1</sup>Department of Information Technology, PSG College of Technology, Coimbatore, India; <sup>2</sup>Department of Bio-Medical Engineering, PSG College of Technology, Coimbatore, India.

Email: [vm@ity.psgtech.ac.in](mailto:vm@ity.psgtech.ac.in); [hod@bme.psgtech.ac.in](mailto:hod@bme.psgtech.ac.in); [vimalfu@gmail.com](mailto:vimalfu@gmail.com); [satfrd@gmail.com](mailto:satfrd@gmail.com)

Received 6 May 2008; revised 25 May 2009; accepted 9 June 2009.

## ABSTRACT

This paper presents a diagnostic system for classification of cardiac arrhythmia from ECG data, using Logistic Model Tree (LMT) classifier. Clinically useful information in the ECG is found in the intervals and amplitudes of the characteristic waves. Any abnormality in the wave shape and duration of the wave features of the ECG is considered as arrhythmia. The amplitude and duration of the characteristic waves of the ECG can be more accurately obtained using Discrete Wavelet Transform (DWT) analysis. Further, the non-linear behavior of the cardiac system is well characterized by Heart Rate Variability (HRV). Hence, DWT and HRV techniques have been employed to extract a set of linear (time and frequency domain) and non-linear characteristic features from the ECG signals. These features are used as input to the LMT classifier to classify 11 different arrhythmias. The results obtained indicate an impressive prediction accuracy of 98%, validating the choice and combined use of the current popular techniques (DWT and HRV) for cardiac arrhythmia classification. The system can be deployed for practical use after validation by experts.

**Keywords:** ECG; Arrhythmia; Wavelet Transform; HRV Analysis; Feature Extraction

## 1. INTRODUCTION

Electrocardiography is a commonly used, non-invasive procedure for recording electrical changes in the heart. The record, which is called an electrocardiogram (ECG or EKG), shows the series of waves that relate to the electrical impulses which occur during each beat of the heart. The information present in the ECG characteristic wave peaks and time intervals between them are impor-

tant. The waves in a normal record are named P, Q, R, S, and T and follow in alphabetical order. Any abnormal change in the shape and variation of time intervals is considered as arrhythmia.

Detection of abnormal ECG signals is a critical step in administering aid to patients. Arrhythmias can occur in a healthy heart and be of minimal consequence. They may also indicate a serious problem and lead to heart disease, stroke or sudden cardiac death. Cardiac arrhythmia is one of the major causes of sudden death. To detect the presence of arrhythmia, patients are hooked to cardiac monitors in hospitals. This requires continuous monitoring by the physicians. Visual inspection is tedious and physician dependent. Computer programs have been developed to help in this visual analysis by providing condensed printouts. This again requires meticulous study by the physician to identify arrhythmia. To cater to large number of patients, to eliminate subjective inaccuracies and to aid the physician in the diagnosis several methods for automated arrhythmia detection have been developed in the past few decades to attempt simplify the monitoring task and improve diagnostic efficiencies.

In pursuit of arrhythmia detection and classification work, many computer techniques have been developed. Notably, Palreddy *et al.* employed a multiple-classifier architecture composed of Self Organizing Maps (SOM) and Learning Vector Quantization (LMQ) to classify premature ventricular contraction (PVC) beats and the non-PVC beats [1]. Babak Mohammadzadeh-Asl *et al.* used both linear and non-linear parameter extracted from heart rate signals with multilayer feed forward neural networks to classify only five types of arrhythmias [2]. J. Lee *et al.* proposed a wavelet based approach along with Linear Discriminant Analysis (LDA) for classifying only five types of arrhythmias using multilayer perceptron classifier [3]. Chazal *et al.* has proposed a method for automatic classification of heartbeats using ECG morphology, heartbeat interval features and RR intervals to discriminate only five different beat types [4]. Dingfie *et al.* classified only six arrhythmias using autoregressive



modeling and Generalized Linear Model (GLM) [5]. Linh *et al.* selected the Hermite Function Expansion as the feature extraction method to represent the QRS complex. They proposed a fuzzy neural network where Hermite coefficients served as the features to classify only seven different types of arrhythmias [6]. Kannathal *et al.* used three non-linear parameters as inputs to the proposed ANF classifier for classification of only ten different types of arrhythmias [7]. Kadbi *et al.* used wavelet parameters along with RR interval and Form Factor as inputs to an ANN classifier to discriminate only ten different arrhythmias [8].

In clinical domains, one has to face the problem of developing classifiers that are able to deal with nonlinear discrimination between classes, incomplete or ambiguous input patterns, and suppression of false alarms. It is necessary to develop new detection schemes with a high level of accuracy, or equivalently, low false-positive and false-negative statistics, for them to be useful in practical applications. In this direction a new approach based on Logistic Model Tree classifier is presented in this paper. LMT is a recent addition to decision trees that replace the terminal nodes of a decision tree with logistic regression functions. This has the advantage of producing decision trees that are more comprehensible, have higher accuracy, and have higher fidelity than previous decision tree extraction algorithms [9].

## 2. DATA SOURCE AND CONTENT

ECG data for use in this classification work has been collected from the MIT-BIH arrhythmia database as published in Physionet, a site dedicated to data for various diseases and their study [10]. The database contains 48 recordings, each containing two 30-min ECG lead signals (denoted A and B). In 45 recordings, lead A is modified-lead II and for the other three is lead V5. Lead B is lead V1 for 40 recordings and is either lead II, V2, V4 or V5 for the other recordings. Twenty-three records, numbered from 100 to 124 with some numbers missing, serve as a representative sample of routine clinical recordings and the remaining twenty-five records, numbered from 200 to 234 again with some numbers missing, contain complex ventricular and supraventricular arrhythmias. In this work, ECG signals from Modified Lead II (MLII) leads are chosen. Prior to recording, the ECG signals in these records have been sampled at a frequency of 360Hz and preprocessed to remove noise due to power-line interference, muscle tremors, spikes etc. This database was selected because it contains a variety of beat types. Another reason for considering this database was its use in other studies and thus comparison of results can be performed. One minute segments of each beat type were extracted from the records for further processing. This work focused on several important arrhythmia types such as Paced beat (P), Atrial prema-

ture beat (A), Right bundle branch block beat (R), Left bundle branch block beat (L), Ventricular escape beat (E), Ventricular flutter wave (!), premature ventricular contraction (V), Fusion of ventricular and normal beat (F), Fusion of paced (f), Blocked Atrial Premature Beat (x) and the Normal beat segment (Normal). The number of segments extracted for each type from the database records is given in **Table 1**.

## 3. FEATURE EXTRACTION

The main objective of the feature extraction process is to derive a set of parameters that best characterize the signal. These parameters, in other words, should contain maximum information about the signal. Hence the selection of these parameters is an important criterion to be considered for proper classification. Arrhythmia classification, therefore, involves determination of several characteristic features of the ECG signal. This work explores a combination of linear (time and frequency domain) and non-linear characteristic features of the ECG signal. The Discrete Wavelet Transform has been used to obtain the amplitude and duration of the characteristic waves of the ECG from which a set of time-domain parameters are derived. The DWT is also used to obtain the RR interval time series. Heart Rate Variability (HRV) helps in understanding the non linear behavior of the cardiac system. Using the RR series a set of non linear parameters are also derived.

### 3.1. Time-Domain Analysis

For each of the segments extracted from the records, the characteristic points P, Q, R, S and T are obtained using Discrete Wavelet Transform.

#### 3.1.1. Discrete Wavelet Transform (DWT)

The wavelet transform is a convolution of the wavelet function  $\psi(t)$  with the signal  $x(t)$ . Orthonormal dyadic discrete wavelets are associated with scaling functions

**Table 1.** Arrhythmia types classified in proposed method.

Type of Arrhythmia	No of Segments Extracted
Normal	459
P	105
A	123
R	99
L	108
E	18
!	24
V	290
F	16
f	27
x	12



$\phi(t)$ . The scaling function can be convolved with the signal to produce approximation coefficients  $A$ . The wavelet transform of the signal  $x(t)$  can be written as:

$$T_{m,n} = \int_{-\infty}^{\infty} x(t) \Psi_{m,n}(t) dt \quad (1)$$

By choosing an orthonormal wavelet basis,  $\Psi_{m,n}(t)$ , one can reconstruct the original signal [11]. The approximation coefficients of the signal at scale  $m$  and location  $n$  can be represented by:

$$A_{m,n} = \int_{-\infty}^{\infty} x(t) \phi_{m,n}(t) dt \quad (2)$$

### 3.1.2. DWT Decomposition

Discrete Wavelet Transform involves decomposition of a signal by wavelet filter banks. DWT uses two filters, a low pass filter (LPF) and a high pass filter (HPF) to decompose the signal into different scales. The output coefficients of the LPF are called approximations while the output coefficients of the HPF are called details. The approximations of the signal are what define its identity while the details only imparts nuance [12].

The DWT decomposition of an input signal  $x[n]$  is schematically shown in the **Figure 1** below. Each stage consists of two digital filters and two downsamplers to produce the digitized signal. The first filter,  $g[n]$  is a high-pass filter, and the second,  $h[n]$  is a low-pass filter. The downsampled outputs of the first high pass filter and low-pass filter provide the detail  $D_1$  and the approxima-

tion  $A_1$  respectively. The first approximation  $A_1$  is decomposed again and this process is continued. The decomposition of the signal into different frequency bands is simply obtained by successive highpass and lowpass filtering of the time domain signal. The signal decomposition can be mathematically expressed as follows:

$$y_{hi}[k] = \sum x[n].g[2k-n] \quad (3)$$

$$y_{lo}[k] = \sum x[n].h[2k-n] \quad (4)$$

The characteristic points P, Q, R, S and T are obtained at different decomposition levels as shown in **Figure 2**.

- Segment selection
- 8-level wavelet decomposition using Daubechies 6 wavelet functions
- Detection of R peak at level 4 using adaptive threshold value (related to the maximum and mean values of the signal)
- Determination of R-R interval using R-R distance
- Detection of Q, S points as local minimum points at level 0, before and after R wave
- Elimination of the QRS complex from the signal to obtain other parameters
- Detection of T wave at level 6 and 7 for finding QT distance
- Detection of P wave at level 6 and 7 for finding P-R and P-P distance

From the values obtained the following five time-domain parameters have been calculated:

Feature	Meaning	Formula
P-P	Mean of P-P interval durations.	$T_{PP} = P_{i+1} - P_i, i=1 \dots N-1$
R-R	Mean of R-R interval durations.	$T_{RR} = R_{i+1} - R_i, i=1 \dots N-1$
P-R	The time duration between successive P and R waves in each beat.	$T_{PR} = R - P_{on-set}$
QRS Duration	The time duration from the beginning of the Q wave to the end of the S wave.	$T_{QRS} = T_S - T_Q$
QT Interval Duration	It is the time from the beginning of the Q-wave to the end of the T-wave	$T_{QT} = T_{off-set} - Q$

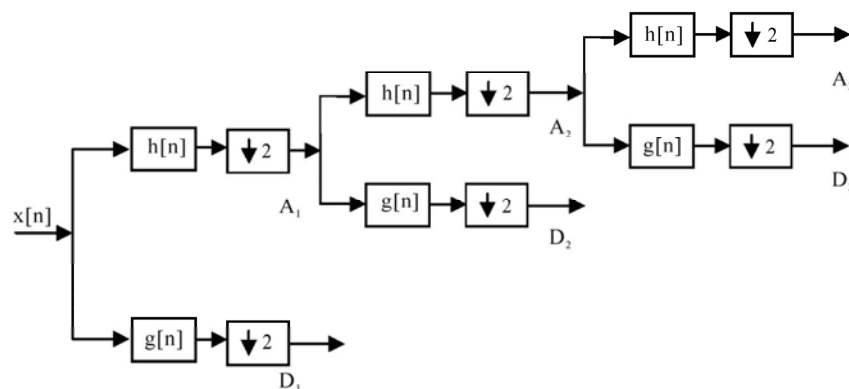


**Figure 1.** DWT decomposition.

### 3.2. Frequency Domain Analysis

Time-domain methods are computationally simple but lack the ability to discriminate between sympathetic and parasympathetic contributions of HRV. Spectral analysis is the most popular linear technique used in the analysis of HRV signals [13]. Spectral power in the high frequency (HF) (0.15–0.4 Hz) band reflects respiratory sinus arrhythmia (RSA) and thus cardiac vagal activity. Low frequency (LF) (0.04–0.15Hz) power is related to baroreceptor control and is mediated by both vagal and sympathetic systems [14]. Hence, the frequency domain parameter LF/HF, which is the ratio between LF and HF band powers, is obtained for each segment.

### 3.3. Non-Linear Analysis

The cardiovascular system is a complex non-linear system and is characterized by many complex estimators. In this classification work the following parameters have been derived from the RR-interval time series obtained using DWT.

#### 3.3.1. Spectral Entropy

The power spectral density (PSD) of a signal is the distribution of power as a function of frequency. This PSD can be obtained using Fourier transform. The normalization of this PSD yields the probability density function (PDF) [15]. This PDF has a value in the range

$$0 \leq p_f \leq 1 \quad f = 1, 2, \dots, n \quad (5)$$

$$\sum_{f=1}^n p_f = 1 \quad (6)$$

The spectral entropy  $H$  which describes the complexity of the heart rate variability (HRV) signal is obtained using Eq.(7).

$$H = - \sum_f p_f \left[ \frac{1}{p_f} \right] \quad (7)$$

Here  $p_f$  is the probability density function at  $f$ . The spec

tral entropy  $H$  calculated for each segment is used as one of the classifying parameters [16].

#### 3.3.2. Detrended Fluctuation Analysis (DFA)

The Detrended Fluctuation Analysis (DFA) is used to quantify the fractal scaling properties of short time R-R interval signals. This technique is a modification of the root-mean square analysis of random walks applied to nonstationary signals [17]. The root-mean-square fluctuation of an integrated and detrended time series is measured at different observation windows and plotted against the size of the observation window on a log-log scale. First, the R-R time series (of total length  $N$ ) is integrated using the equation:

$$y(k) = \sum_{i=1}^k (RR(i) - RR_{avg}) \quad (8)$$

where  $y(k)$  is the  $k$ th value of the integrated series,  $RR(i)$  is the  $i$ th inter beat interval and  $RR_{avg}$  is the average inter beat interval over the entire series [18]. Then, the integrated time series is divided into windows of equal length,  $n$ . In each window of length  $n$ , a least squares line is fitted to the R-R interval data (representing the trend in that window). The 'y' coordinate of the straight line segments are denoted by  $y_n(k)$ . Next, we detrend the integrated time series,  $y_n(k)$  in each window. The root mean-square fluctuation of this integrated and detrended series is calculated using Eq.(9) for each segment.

$$F(n) = \sqrt{\frac{1}{N} \sum_{k=1}^N [y(k) - y_n(k)]^2} \quad (9)$$

## 4. LOGISTIC MODEL TREES CLASSIFIER

Logistic Model Trees are a combination of a tree structure and logistic regression functions to produce a single decision tree [19,20,21,22]. The decision tree structure has the logistic regression functions at the leaves. The leaf node has two child nodes which is branched right

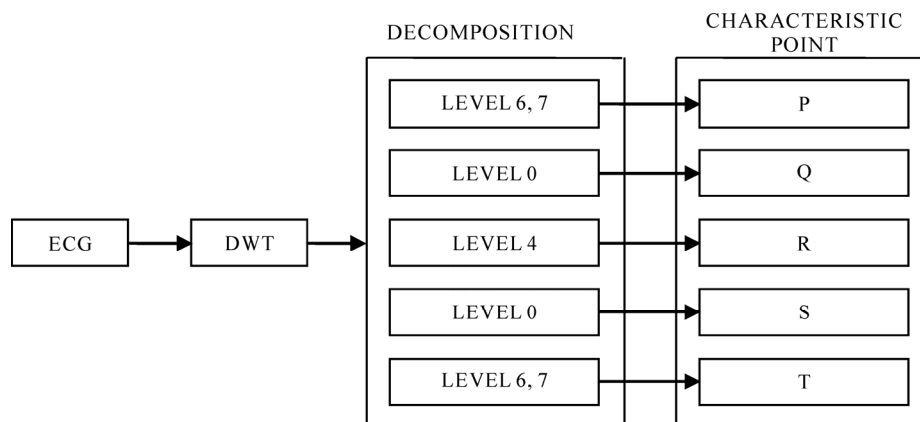


**Figure 2.** Characteristic points extraction from ECG signal at various decomposition levels.

and left depending on the threshold. If the value of the attribute is smaller than the threshold it is sorted to left branch and value of attribute greater than the threshold it is sorted to right branch as shown in **Figure 3**.

The threshold is usually fixed by Logit Boost method [19]. Logit Boost uses an ensemble of functions  $F_K$  to predict classes  $1, \dots, K$  using  $M$  “weak learners”.

$$F_k(x) = \sum_{m=1}^K f_{mk}(x) \quad (10)$$

Steps followed for developing the LMT classifier:

- The linear regression function is fitted using the Logitboost method to build a logistic model. The Logitboost method uses 5 examples for the cross validation to determine the best number of iterations to run, when fitting the logistic regression function at a node of the decision tree
- The logistic model is built using all data.
- The split of the data at the root is constructed using the threshold.
- This splitting is continued till some stopping

criterion is met. Here the stopping criterion is 5 examples, since it helps in cross validation for logitboost method.

- Once the tree has been build it is pruned using CART-based pruning [19].

Reasons for choosing the Logistic Model Tree classifier:

- Logistic Regression is very good at detecting linear relationships and then combining those relationships into an equation that provides the odds of the dependent variable reaching a particular outcome, when the various independent variables are fed into the resulting equation.
- Logistic Regression models are widely used and they are considered robust and not prone to over fitting the data.
- These models can be built with high level of accuracy using little data preparation.
- Logistic Model Trees give explicit class probability estimates rather than just a classification.

The classification task, depicted in **Figure 4**, involves the following steps:

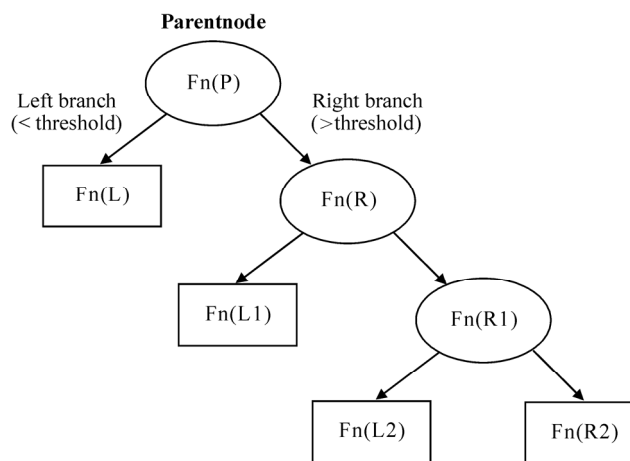


**Figure 3.** Tree structure of logistic model tree (LMT).

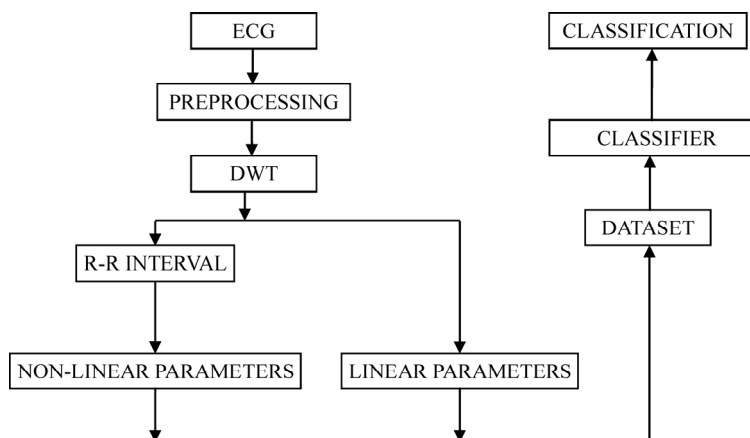


**Figure 4.** Block diagram of the proposed method.

- One minute segments of each beat type are extracted from ECG records in the database.
- Each segment is then decomposed using DWT into various levels for extracting linear time-domain parameters.
- The different nonlinear parameters are calculated using their respective formula.
- Both linear and non-linear parameters for all the segments are combined and a dataset is formed.
- 75% of the dataset, called training set, is used for training the classifier.
- The remaining 25% of the dataset, called test set, is used for testing the classifier.

For the evaluation of the proposed classifier, a total of 1281 segments, extracted from the MIT BIH arrhythmia database records were used. Five time-domain, one frequency domain and two non-linear parameters were derived from these segments. These eight parameters along with the corresponding output class (type of arrhythmia) forms a feature vector. Thus 1281 feature vectors comprise the dataset. 75% of each type from this dataset was used as the train dataset and the remaining 25% as the test dataset. The output obtained from the Logistic Model Tree was used to calculate the accuracy of each type of beat using **Eq.(11)**.

$$\text{Accuracy} = \frac{\text{Number of beats correctly classified}}{\text{Total number of beats}} \quad (11)$$

## 5. RESULTS AND DISCUSSIONS

The objective of any clinical research is to find the relationship between results and presence of any disease.

The experimental results are presented in **Table 2**.

**Table 2.** Performance of the proposed method.

Type of Arrhythmia	No of Segments Extracted	No of Segments for Training	No of Segments for Testing	Correctly Classified	Accuracy %
Normal	459	353	106	102	96.22
P	105	74	31	29	93.54
A	123	95	28	26	92.85
R	99	74	25	25	100
L	108	77	31	31	100
E	18	13	5	5	100
!	24	18	6	6	100
V	290	219	71	70	98.6
F	16	12	4	4	100
F	27	19	8	8	100
X	12	7	5	5	100
					<b>Average=98.29</b>

**Table 3.** Performance comparison of different ECG arrhythmia classifiers.

Work Reference	Types	Accuracy (%)	Feature Extraction Method	Classifier
Palreddy [1]	2	98.58%	LVQ	SOM
Babak [2]	5	99.38%	HRV	NN
Lee [3]	5	99.48%	WT	LDA/MLP
Chazal[4]	5	96.87%	ECG Morphology/ Interval	LDA
Dingfie [5]	6	93.2%	AR Modeling	GLM
Linh [6]	7	96%	HER	FNN
Kannathal [7]	10	94.64%	HRV	ANN
Kadbi [8]	10	90%	WT	Cascade ANN
<b>Proposed Method</b>	<b>11</b>	<b>98.29%</b>	<b>DWT/HRV</b>	<b>LMT</b>

**Table 3** shows the performance comparison of the different ECG arrhythmia classifiers. The proposed method shows comparable performance even when 11 different types of arrhythmias have been considered.

## 6. CONCLUSIONS

In this paper, the effectiveness of the Logistic Model Tree classifier for arrhythmia classification has been demonstrated. The Logistic Model Tree classifier was fed by the combination of linear and non-linear parameters derived from ECG data using DWT and HRV. The results indicate that the proposed method employing the LMT classifier with linear and nonlinear parameters is effective for classification of cardiac arrhythmias with an acceptably high accuracy. Compared to other approaches in the literature cited, the proposed method exploits the power of HRV and DWT techniques in discriminating 11 different arrhythmia types. Parameters derived from ECG features and HRV analysis can therefore be used as a reliable indicator of different types of arrhythmias. The proposed system, after validation by experts, can serve as a diagnostic tool and aid the physician in the detection and classification of cardiac arrhythmias.

## REFERENCES

- [1] S. Palreddy, Y. H. Hu, V. Mani, and W. J. Tompkins (1997) A multipleclassifier architecture for ECG beat classification, *IEEE Workshop on Neural Network for Signal Processing*, 172–181.
- [2] B. Mohammadzadeh-Asl and S. K. Setarehdan, (2006) Neural network based arrhythmia classification using heart rate variability signal, *Proceedings of the EUSIPCO*.
- [3] J. Lee, K. L. Park, M. H. Song, and K. J. Lee, (2005) Arrhythmia classification with reduced features by linear discriminant analysis, *IEEE EMBS 2005, 27th Annual International Conference, Engineering in Medicine and Biology Society*, 1142–1144.
- [4] P. Chazal, M. O'Dwyer, and R. B. Reilly, (2004) Automatic classification of heartbeats using ECG morphology and heartbeat interval features, *IEEE Trans. Biomedical Engineering*, **51**(7), 1196–1206.
- [5] G. Dingfei, N. Srinivasan, and S. Krishnan, (2002) Cardiac arrhythmia classification using autoregressive modeling, *BioMedical Engineering OnLine*, 1–5.
- [6] T. H. Linh, S. Osowski, and M. Stodolski, (2003) On-line heart beat recognition using hermite polynomials and neuro-fuzzy network, *IEEE Trans. Instrumentation and Measurement*, **52**(4), 1224–1231.
- [7] N. Kannathal, S. K. Puthusserypady, C. M. Lim, U. R. Acharya, and S. Laxminarayan, (2005) Cardiac state diagnosis using adaptive neuro-fuzzy technique, *Proceedings of the IEEE Engineering in Medicine and Biology 27th Annual Conference Shanghai, China*.
- [8] M. H. Kadbi, J. Hashemi, H. R. Mohseni and A. Maghsoudi, (2006) Classification of ECG arrhythmias based on statistical and time-frequency features, *3rd International Conference on Advances in Medical, Signal and Information Processing, MEDSIP*.
- [9] D. Dancey, Z. A. Bandar, and D. McLean, (2007) Logistic model tree extraction from artificial neural networks, *IEEE Trans on Systems, Man and Cybernetics*, **37**(4), 794–802.
- [10] <http://www.physionet.org/physiobank/database/mitdb/>.
- [11] S. Z. Mahmoodabadi, A. Ahmadian, M. D. Abolhasani, M. Eslami, and J. H. Bidgoli, (2005) ECG feature extraction based on multiresolution wavelet transform, in *Proc. IEEE Engineering in Medicine and Biology*, 3902–3905.
- [12] E. M. Tamil, N. H. Kamarudin, R. Salleh, M. Yamani Idna Idris, M. N. Noorzaily, and A. M. Tamil, (2008) Heartbeat electrocardiogram (ECG) signal feature extraction using discrete wavelet transforms (DWT), in *Proceedings of CSPA*, 1112–1117.
- [13] D. N. Dutt and S. M. Krishnan, (2000) Computer processing of heart rate variability signals for detection of patient status in cardiac care units, *Current Science*, **78**(7), 864–868.
- [14] Task force of the European society of cardiology and the North American society of pacing and electrophysiology (1996), Heart rate variability—standards of measurements, physiological interpretation, and clinical use, *European Heart Journal*, **17**, 354–381.
- [15] S. I. Niwas, R. S. S. Kumari, and V. Sadasivam, (2005) Artificial neural network based automatic cardiac abnormalities classification, *Proceeding of the Sixth International Conference on Computational Intelligence and Multimedia Application*.
- [16] U. R. Acharya, A. Kumar, P. S. Bhat, C. M. Lim, S. S. Iyengar, N. Kannathal, and S. Krishnan, (2004) Classification of cardiac abnormalities using heart rate signals, *medical, Biological Engineering and Computing*, **42**, 288–293.
- [17] H. Kun, C. I. Plamen, C. Zhi, C. Pedro, and H. E. Stanley, (2001) Effect of trends on detrended fluctuation analysis, *Physical Review E*, **64**, 011114.
- [18] R. U. Acharya, C. M. Lim, and P. Joseph, (2002) Heart rate variability analysis using correlation dimension and detrended fluctuation analysis, *ITBM–RBM*, **23**(6), 333–339.
- [19] N. Landwehr, M. Hall, and E. Frank, (2005) Logistic model trees, *Machine Learning*, **59**(1/2), 161–205.
- [20] D. W. Hosmer and S. Lemeshow, (2000) *Applied logistic regression*, 2nd Edition, Wiley-Interscience, New York.
- [21] J. Friedman, T. Hastie, and R. Tibshirani, (2000) Additive logistic regression: A statistical view of boosting, *Annals of Statistics*, **32**(2), 337–374.
- [22] Z. H. Zhou, Y. Jiang, and S. F. Chen, (2003) Extracting symbolic rules from trained neural network ensembles, *Artificial Intelligence Communication*, **16**(1), 2–15.



# A MCMC strategy for group-specific 16S rRNA probe design

Yi-Bo Wu<sup>1\*</sup>, Li-Rong Yan<sup>2\*</sup>, Hui Liu<sup>1</sup>, Han-Chang Sun<sup>1</sup>, Hong-Wei Xie<sup>1§</sup>

<sup>1</sup>Department of Automatic Control, College of Mechatronics and Automation, National University of Defense Technology, Changsha, Hunan, China; <sup>2</sup>Department of Information, Wuhan General Hospital of Guangzhou Command, Wuhan, Hubei, China; \*These authors contributed equally to this work; §Corresponding author.  
Email: [wybok@hotmail.com](mailto:wybok@hotmail.com)

Received 17 April 2008; revised 6 July 2009; accepted 17 July 2009.

## ABSTRACT

**Revealing biodiversity in microbial communities is essential in metagenomics researches. With thousands of sequenced 16S rRNA gene available, and advancements in oligonucleotide microarray technology, the detection of microorganisms in microbial communities consisting of hundreds of species may be possible. Many of the existing strategies developed for oligonucleotide probe design are dependent on the result of global multiple sequences alignment, which is a time-consuming task. We present a novel program named OligoSampling that uses MCMC method to design group-specific oligonucleotide probes. The probes generated by OligoSampling are group specific with weak cross-hybridization potentials. Furthermore a high coverage of target sequences can be obtained. Our method does not need to globally align target sequences. Locally aligning target sequences iteratively based on a Gibbs sampling strategy has the same effect as globally aligning sequences in the process of seeking group-specific probes. OligoSampling provides more flexibility and speed than other software programs based on global multiple sequences alignment.**

**Keywords:** 16S Rrna; Probe Design; MCMC

## 1. INTRODUCTION

Metagenomics is a new field combining molecular biology and genetics in an attempt to reveal the vast scope of biodiversity in a wide range of environment, as well as new functional capacities of individual cells and communities, and the complex evolutionary relationships between them [1,2,3,4]. Apparently, revealing biodiversity in microbial communities is the first step [1,5]. The

vast majority of microbial diversity had been missed by cultivation-based methods [2]. The analysis of 16S rRNA gene sequences is the most common approach to determine microbial diversity [6].

Oligonucleotide microarrays now afford an idea tool for identifying sequence variants (even single-base-pair variant) in 16S rRNA gene copies of diverse microorganisms simultaneously in a single assay [7,8,9,10]. Many 16S rRNA-based oligonucleotide microarrays have been designed to detect multiple pathogens simultaneously [11, 12,13,14,15]. Such technology has the potential to revolutionize clinical diagnostics [15,16,17,18,19,20,21,22,23].

A critical issue for oligonucleotide microarray design is to find appropriate oligonucleotide probes specific to their target sequences. To improve efficiency in probe design, many softwares or databases have been developed. Kaderali *et al.* proposed a combination of suffix trees and dynamic programming based alignment algorithms to compute melting temperature ( $T_m$ ), and presented an efficient algorithm to select probes with high specificity in detecting the target [24]. Loy *et al.* built a comprehensive database containing more than 700 published rRNA-targeted oligonucleotide probe sequences with supporting bibliographic and biological annotation [25]. Kumar *et al.* provided a software package ARB to evaluate sequence alignments and oligonucleotide probes with respect to three-dimensional structure of ribosomal RNA [26]. DeSantis *et al.* proposed an alignment compression algorithm, NAST (Nearest Alignment Space Termination), to find Operational Taxonomic Units (OTUs) for automated design of effective probes [27,28].

Global multiple sequences alignment plays an important role in comprehensive analysis of group-specific oligonucleotide probe for those methods mentioned above. It is a challenge for personal computer to align a large amount of sequences. Here we present a novel program named OligoSampling that uses MCMC method to design group-specific oligonucleo-

tide probes. OligoSampling does not need to globally align target sequences. This MCMC method is more flexible and efficient.

## 2. RESULTS

### 2.1. Algorithm Overview

**Figure 1** summarizes the global overview of the OligoSampling algorithm. We assume that we are given a set of  $N$  sequences  $S = \{S_1, \dots, S_N\}$  and that those  $N$  sequences are divided into  $m$  group. We seek a group-specific oligonucleotide probe for each group. For a particular probe of specified width  $W$  segments in probe binding sites within each sequence are mutually similar. Conversely we seek within each sequence mutually similar segments. The segments can be regarded as

binding sites for a particular probe. If the probe is specific to group **A**, segments within sequences in group **A** are more mutually similar. And to avoid cross-hybridization, there need to be more sequence variants between segments within sequences of group **A** and segments within sequences in any other group. In the process seeking mutually similar segments, patterns shared by multiple sequences in each group are obtained.

The algorithm maintains an evolving data structures. The data structure is a set of positions  $a_k$ , for  $k$  from 1 to  $N$ . For a particular set of positions  $a_k$  we obtain the pattern descriptions of mutually similar segments in each group  $i$  from 1 to  $m$ , in the form of a probabilistic model of base pair frequencies for each position  $j$  from 1 to  $W$ , and consisting of the variables  $q_{i,j,1}, \dots, q_{i,j,4}$ .

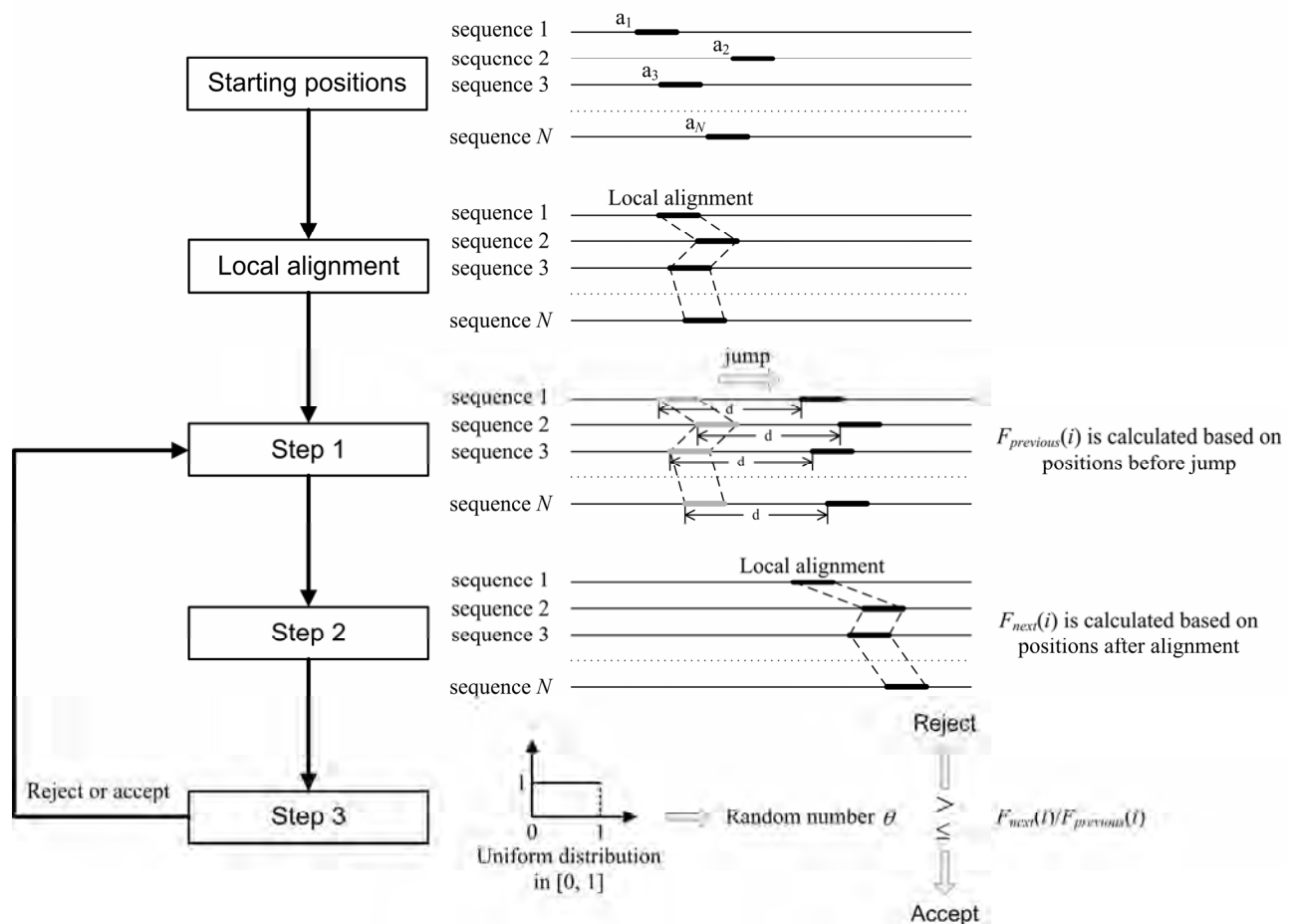


**Figure 1.** Algorithm overview: The algorithm is initialized by choosing starting positions  $a_k$ , for  $k$  from 1 to  $N$ , within the various sequences. A Gibbs sampling-based local multiple alignment algorithm [29] is applied to update  $a_k$ . After an identical jump for each position  $a_k$ , the Gibbs sampling-based local multiple alignment algorithm [29] is applied again to update  $a_k$ . An objective function defined to evaluate sensitivity and specificity of probes is calculated based on positions  $a_k$  before jump and after alignment respectively. The ratio of objective values is compared to a random number  $\theta$  uniformly distributed in  $[0, 1]$ . The result of comparison determine whether the update of  $a_k$  are rejected or not. Then go back to step 1 and start a new iteration loop.

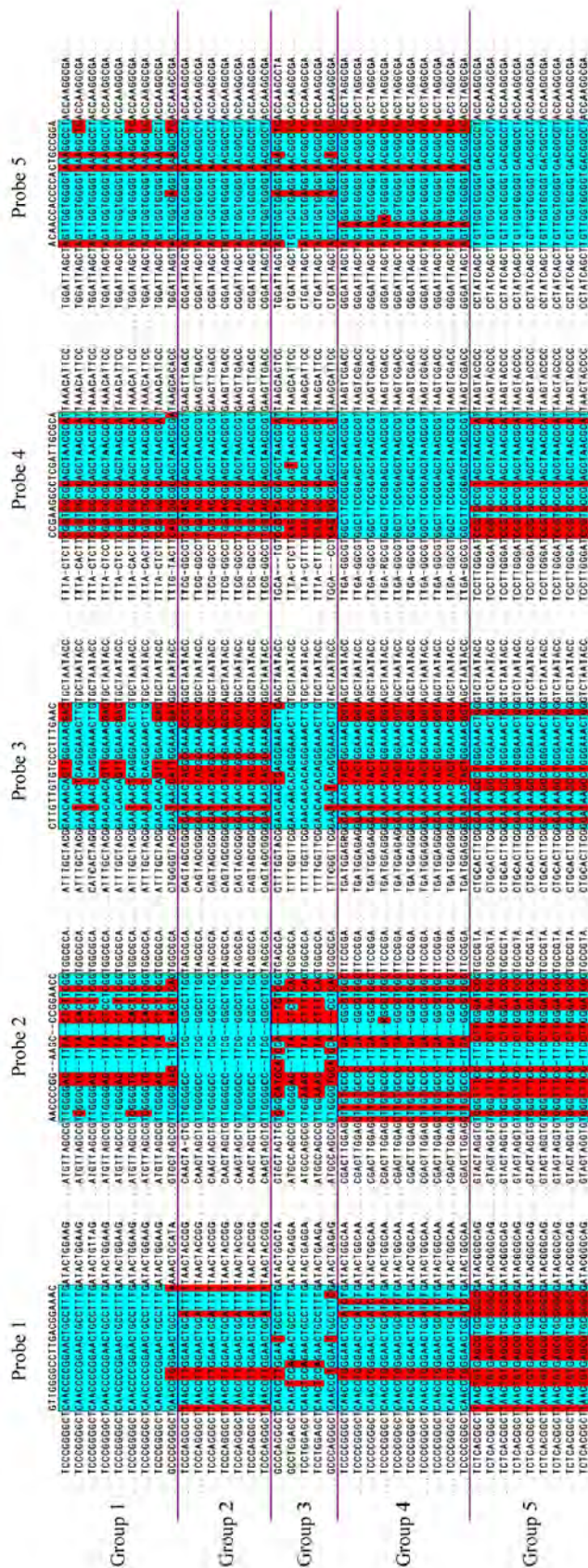


**Figure 2.** Group-specific probe for each species: OligoSampling find a group-specific oligonucleotide probe for each cluster of target sequences (probe  $i$  is specific to group  $i$ , for  $i$  from 1 to 5). Target sequences have been globally aligned. Base pairs on blue background are perfect match. Base pairs on red background are mismatch.



In the process of seeking group-specific probe for group  $i$  the algorithm is initialized by choosing starting positions  $a_k^{(0)}$  within the various sequences. A Gibbs sampling-based local multiple alignment algorithm [29] is applied to update  $a_k^{(0)}$  to  $a_k^{(1)}$ . After alignment the algorithm then proceeds through many iterations to execute the following three steps:

1) Jump step. Draw a sample  $d$  from a normal distribution. Positions  $a_k^{(1)}$  are updated to  $a_k^{(2)} = a_k^{(1)} + d$ .

2) Local multiple alignment step. Gibbs sampling-based local multiple alignment algorithm is applied re-

garding positions  $a_k^{(2)}$  as initial starting point. Positions  $a_k^{(2)}$  are updated to  $a_k^{(3)}$ .

Rejection step. We define an objective function (Eq.1). Based on positions  $a_k^{(1)}$  and  $a_k^{(3)}$ , the objective function  $F_{previous}(i)$  and  $F_{next}(i)$  are calculated respectively. We generate a random number  $\theta$  uniformly distributed in  $[0, 1]$ . If  $\theta \leq F_{next}(i)/F_{previous}(i)$ , we accept  $a_k^{(3)}$ . Otherwise, positions resume to  $a_k^{(1)}$ . Then, go back to step 1.

$$F(i) = -\sum_{j=1}^W \sum_{k=1}^4 \omega_j q_{i,j,k} \log(q_{i,j,k}) + \min_{\substack{1 \leq \alpha \leq m \\ \alpha \neq i}} \sum_{j=1}^W \sum_{k=1}^4 \omega_j q_{\alpha,j,k} \log\left(\frac{q_{\alpha,j,k}}{q_{i,j,k}}\right) \quad (1)$$

In the objective function sensitivity of the probe is measured by entropy, and specificity is measured by Kullback-Leibler divergence. By selecting a set of  $a_k$  that maximizes the objective function, the algorithm finds the most group-specific oligonucleotide probe for group  $i$ .

## 2.2. Design Group-Specific Oligonucleotide Probes for 5 Bacterial Species

To examine the performance of OligoSampling on group-specific probe design, we select 5 bacteria species (*Afpia* sp., *Bordetella pertussis*, *Brucella* sp., *Escherichia coli* O157:H7, and *Mycobacterium tuberculosis*) with a total of 40 sequences. For OligoSampling, the input dataset is 5 clusters of homologous sequences. The objective of this algorithm is to find a group-specific oligonucleotide probe for each cluster. As shown in Figure 2, the probes generated by OligoSampling are group specific with weak cross-hybridization potentials. OligoSampling also obtains a high coverage of target sequences.

## 3. DISCUSSION

The secondary structure model of 16S rRNA consists of a conserved core that is interspersed with a number of variable areas. 16S rRNA evolves slowly and is often not very convenient to resolve bacterial strains at the species level. Therefore, multiple copies of 16S rRNA gene in different species share high sequence similarity. In jump step each aligned position  $a_k$  is updated by jumping a same distance in the same direction. Convergence will be achieved rapidly in the following alignment due to high sequence similarity between sequences (Figure 3). In the process of updating positions  $a_k$ , Gibbs sampling-based local multiple alignment algorithm is applied to keep sequences locally aligned. And then, sensitivity and specificity of probe is evaluated based on entropy and Kullback-Leibler divergence. This process is functionally equivalent to oligonucleotide probe design based on global multiple sequences alignment, but has

less calculation amount.

Through the iterative algorithm mentioned above, different initializations sometimes lead to different local optimal solutions. Therefore, searches beginning with multiple initializations have more possibility to achieve global optimal solution. Searches beginning with different initializations are mutually independent and can be executed in parallel. It is convenient to parallelize this algorithm.

Gibbs sampling-based local multiple alignment algorithm is sensitive to starting positions  $a_k$ . Appropriate starting positions  $a_k$  can quicken convergence speed.

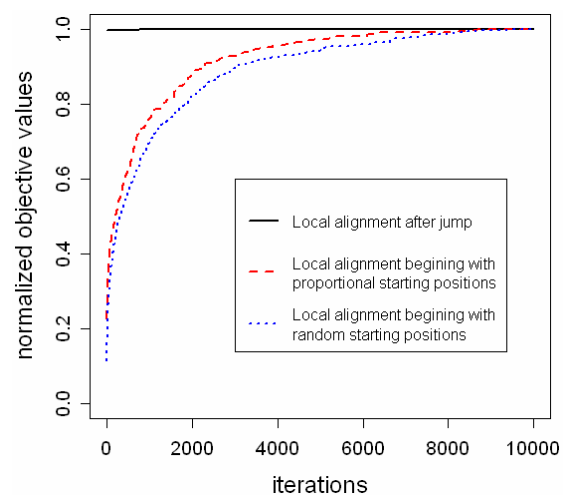


**Figure 3.** Convergence of local alignment: Optimal objective values converge in 10000 iterations under three conditions: after jump, beginning with starting positions proportional to sequence length, and beginning with random starting positions. To make the comparison of convergence speed independent of initialization, ten alignment procedures beginning with different sets of starting positions are executed under each condition. Average optimal objective values in iterations 1 to 10000 were normalized to that in last iteration.

Sets of target sequences are highly similar to each other. We choose initial starting positions by letting the distance from 5' termini to initial starting position in each target sequence be proportional to sequence length. As shown in **Figure 3**, Local alignment beginning with proportional starting positions can achieve faster convergence speed than that beginning with random starting positions. In this method, the algorithm is initialized by choosing a random proportion. And the proportion is used to find starting position in each target sequence.

It is noted that if a probe can match well with several segments in a 16S rRNA, local multiple alignment can not analyze this situation comprehensively. We have analyzed the possibility that a probe matches well with several segments in a 16S rRNA. At present, the Ribosomal Database Project [30] (RDP) has collected around 280,952 16S rRNA sequences in bacteria superkingdom. Among the 280,952 16S rRNA sequences we picked out a 16S rRNA sequence and chose a segment in this 16S rRNA randomly. And then in this 16S rRNA sequence another segment which is most similar to the original segment was found. Mismatches of the two segments were counted. The procedure mentioned above was iterated 10,000 times. As shown in **Figure 4**, there is little possibility that a probe can match well with several segments in a 16S rRNA.

The problem of group-specific probe selection is further complicated as all probes must work under the same hybridization condition. To ensure the closer optimum

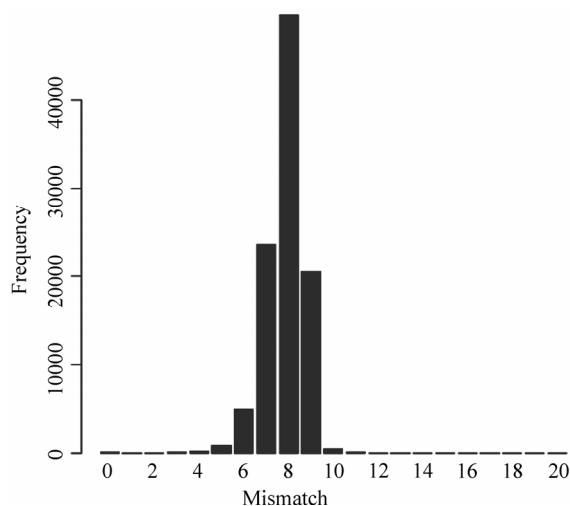


**Figure 4.** Mismatch in similar segments: Among 280,952 16S rRNA sequences in bacteria superkingdom collected by RDP, we picked out a 16S rRNA sequence and chose a segment in this 16S rRNA randomly. And then in this 16S rRNA sequence another segment which is most similar to the original segment was found. Mismatches of the two segments were counted. The procedure mentioned above was iterated 100,000 times.

hybridization condition in one chip including all oligos, probe lengths must be variable. By adjusting probe lengths (increase or decrease base-pairs in 5' and 3' ends), probe whose melting temperatures ( $T_m$ ) are closer to a predefined optimum hybridization condition will be generated. As shown in **Table 1**, probe lengths are selected based on a predefined melting temperature. Melting temperatures of all probes can be close enough to work well under the same hybridization condition.

## 4. CONCLUSIONS

OligoSampling provides an efficient alternative for group-specific oligonucleotide probe design. Using this method we do not need to globally align target sequences. Locally aligning target sequences iteratively based on a Gibbs sampling strategy has the same effect as globally aligning sequences in the process of seeking group-specific probes. OligoSampling provides more flexibility and speed than other software programs based on global multiple sequences alignment. Furthermore, search for multiple local optimal solutions beginning with multiple initializations can improve the effect of this algorithm in group-specific probe design. This algorithm can be parallelized conveniently.

## 5. METHODS

### 5.1. A Gibbs Sampling Strategy for Local Multiple Alignment

Lawrence *et al.* have described a Gibbs sampling algorithm for local multiple alignment of protein sequences [29]. We applied Lawrence's method to locally align target sequences.

Pattern shared by multiple sequences is described in the form of a probabilistic model of base pair frequencies for each position  $i$  from 1 to  $W$ , and consisting of the variables  $q_{i,1}, \dots, q_{i,4}$ . This pattern description is accompanied by an analogous probabilistic description of the "background frequencies"  $p_1, \dots, p_4$  with which base pairs occur in sites not described by the pattern.

Through many iterations to execute two steps of the Gibbs sampler an objective function (**Eq.2**) evaluating the alignment is maximized. In the study, the two steps of the Gibbs sampler were executed to locally align target sequences.

$$F = \sum_{i=1}^w \sum_{j=1}^4 c_{i,j} \log \frac{q_{i,j}}{p_j} \quad (2)$$

First step, one of the  $N$  sequences,  $z$ , is chosen in specified order. The pattern description  $q_{i,j}$  and background frequencies  $p_j$  are calculated, as described in **Eq.3**, from the current positions  $a_k$  in all sequences excluding  $z$ .



**Table 1.** Adjust probe lengths according to a predefined optimum hybridization condition (70°C).

Original probe	$T_m$	Adjusted probe	$T_m$
3'-GTTGGGGCCTTGACGGAAC-5'	74.98	3'-GGGGCCTTGACGGA-5'	71.07
3'-AACCCCGGAAGCCCGGAACC-5'	80.38	3'-CCGGAAGCCCGGA-5'	70.93
3'-CTTGTTGTGTCCCTTTGAAC-5'	66.40	3'-CCTTGTTGTGTCCCTTTGAAC-5'	70.05
3'-CCGAAGGCCTCGATTGCGCA-5'	78.59	3'-GAAGGCCTCGATTGCGC-5'	70.69
3'-ACAACCACCCCACTGCCGGA-5'	82.37	3'-ACCACCCCACTGCCG-5'	71.66

$$q_{i,j} = \frac{c_{i,j} + b_j}{N - 1 + B} \quad (3)$$

For the  $i$ th position of the pattern we have  $N - 1$  observed nucleotides, because sequence  $z$  has been excluded; let  $c_{i,j}$  be the count of nucleotide  $j$  in this position. These  $c_{i,j}$  are supplemented with nucleotide-dependent “pseudocounts”  $b_j$  to yield pattern probabilities.  $B$  is the sum of the  $b_j$ .

Second step, the probability  $Q_x$  of generating segment  $x$  in position  $a_z$  according to the current pattern description  $q_{i,j}$  are calculated, as are the probability  $P_x$  of generating this segment by the background probabilities  $p_j$ . The weight  $A_x = Q_x / P_x$  is assigned to current segment  $x$ . And then draw a sample  $d$  from a normal distribution. Positions  $a_z$  are updated to  $a_z + d$ . In the updated position weight  $A'_x$  is calculated in the same way. We generate a random number  $\theta$  uniformly distributed in  $[0, 1]$ . If  $\theta \leq A'_x / A_x$ , we accept the update of positions  $a_z$ . Otherwise, we reject the update. Then go back to first step.

## 5.2. Selection of Weight Set in Sensitivity and Specificity Evaluation

Pozhitkov *et al.* examined the effects of single-base pair mismatch (all possible types and positions) on signal intensities of hybridization through a series of calibration experiments [31]. The results of experiments indicated that the most optimal discrimination of mismatch from perfect match probe-target duplexes is provided with the mismatch in the middle of the duplex. To suppress non-specific binding of probe to target, the position of the mismatch should be moved from the 5' or 3' termini to the center of the probe. Therefore, in evaluation of sensitivity and specificity of group-specific oligonucleotide probes the weight coefficients  $\omega_j$  (in **Eq.1**) should dependent on the signal intensity values of mismatches in different positions. Based on normalized signal intensity values of mismatch duplexes at position

1 to 20 provided by Pozhitkov *et al.*, the weight coefficients  $\omega_j$  are assigned. Position in the middle has the highest weight.

## 3. ACKNOWLEDGEMENTS

This work was supported by a grant from the National Natural Science Foundation of China (No. 30800253). The authors thank anonymous referees and the associate editor for many helpful comments.

## REFERENCES

- [1] S. R. Gill, M. Pop, R. T. Deboy, P. B. Eckburg, P. J. Turnbaugh, B. S. Samuel, J. I. Gordon, D. A. Relman, C. M. Fraser-Liggett, and K. E. Nelson, (2006) Metagenomic analysis of the human distal gut microbiome, *Science*, **312**, 1355–1359.
- [2] E. Pennisi, (2007) Metagenomics, massive microbial sequence project proposed, *Science*, **315**, 1781.
- [3] A. Jurkowski, A. H. Reid, and J. B. Labov, (2007) Metagenomics: A call for bringing a new science into the classroom (while it's still new), *CBE Life Sci. Educ.*, **6**, 260–265.
- [4] P. J. Turnbaugh, R. E. Ley, M. Hamady, C. M. Fraser-Liggett, R. Knight, and J. I. Gordon, (2007) The human microbiome project, *Nature*, **449**, 804–810.
- [5] P. B. Eckburg, E. M. Bik, C. N. Bernstein, E. Purdom, L. Dethlefsen, M. Sargent, S. R. Gill, K. E. Nelson, and D. A. Relman, (2005) Diversity of the human intestinal microbial flora, *Science*, **308**, 1635–1638.
- [6] S. C. Lau and W. T. Liu, (2007) Recent advances in molecular techniques for the detection of phylogenetic markers and functional genes in microbial communities, *FEMS Microbiol Lett.*, **275**, 183–190.
- [7] S. P. Fodor, J. L. Read, M. C. Pirrung, L. Stryer, A. T. Lu, and D. Solas, (1991) Light-directed, spatially addressable parallel chemical synthesis, *Science*, **251**, 767–773.
- [8] S. P. Fodor, R. P. Rava, X. C. Huang, A. C. Pease, C. P. Holmes, and C. L. Adams, (1993) Multiplexed biochemical assays with biological chips, *Nature*, **364**, 555–556.
- [9] A. C. Pease, D. Solas, E. J. Sullivan, M. T. Cronin, C. P. Holmes, and S. P. Fodor, (1994) Light-generated oligonucleotide arrays for rapid DNA sequence analysis, *Proc. Natl. Acad. Sci., USA*, **91**, 5022–5026.
- [10] R. W. Ye, T. Wang, L. Bedzyk, and K. M. Croker, (2001) Applications of DNA microarrays in microbial systems, *J. Microbiol Methods*, **47**, 257–272.
- [11] A. E. Warsen, M. J. Krug, S. LaFrentz, D. R. Stanek, F. J.

- Loge, and D. R. Call, (2004) Simultaneous discrimination between 15 fish pathogens by using 16S ribosomal DNA PCR and DNA microarrays, *Appl. Environ. Microbiol.*, **70**, 4216–4221.
- [12] D. Z. Jin, S. Y. Wen, S. H. Chen, F. Lin, and S. Q. Wang, (2006) Detection and identification of intestinal pathogens in clinical specimens using DNA microarrays, *Mol Cell Probes*, **20**, 337–347.
- [13] D. Harmsen, C. Singer, J. Rothganger, T. Tonjum, G. S. de Hoog, H. Shah, J. Albert, and M. Frosch, (2001) Diagnostics of neisseriaceae and moraxellaceae by ribosomal DNA sequencing: Ribosomal differentiation of medical microorganisms, *J. Clin. Microbiol.*, **39**, 936–942.
- [14] C. P. Sun, J. C. Liao, Y. H. Zhang, V. Gau, M. Mastali, J. T. Babbitt, W. S. Grundfest, B. M. Churchill, E. R. McCabe, and D. A. Haake, (2005) Rapid, species-specific detection of uropathogen 16S rDNA and rRNA at ambient temperature by dot-blot hybridization and an electrochemical sensor array, *Mol. Genet. Metab.*, **84**, 90–99.
- [15] J. K. Loy, F. E. Dewhirst, W. Weber, P. F. Frelie, T. L. Garbar, S. I. Tasca, and J. W. Templeton, (1996) Molecular phylogeny and in situ detection of the etiologic agent of necrotizing hepatopancreatitis in shrimp, *Appl. Environ. Microbiol.*, **62**, 3439–3445.
- [16] B. X. Hong, L. F. Jiang, Y. S. Hu, D. Y. Fang, and H. Y. Guo, (2004) Application of oligonucleotide array technology for the rapid detection of pathogenic bacteria of foodborne infections, *J. Microbiol Methods*, **58**, 403–411.
- [17] W. Deng, D. Xi, H. Mao, and M. Wanapat, (2007) The use of molecular techniques based on ribosomal RNA and DNA for rumen microbial ecosystem studies: A review, *Mol. Biol. Rep.*
- [18] G. Taroncher-Oldenburg and B. B. Ward, (2007) Oligonucleotide microarrays for the study of coastal microbial communities, *Methods Mol. Biol.*, **353**, 301–315.
- [19] C. R. Kuske, S. M. Barns, C. C. Grow, L. Merrill, and J. Dunbar, (2006) Environmental survey for four pathogenic bacteria and closely related species using phylogenetic and functional genes, *J. Forensic. Sci.*, **51**, 548–558.
- [20] D. R. Call, (2005) Challenges and opportunities for pathogen detection using DNA microarrays, *Crit. Rev. Microbiol.*, **31**, 91–99.
- [21] T. Mohammadi, P. H. Savelkoul, R. N. Pietersz, and H. W. Reesink, (2006) Applications of real-time PCR in the screening of platelet concentrates for bacterial contamination, *Expert Rev. Mol. Diagn.*, **6**, 865–872.
- [22] L. Bodrossy and A. Sessitsch, (2004) Oligonucleotide microarrays in microbial diagnostics, *Curr. Opin. Microbiol.*, **7**, 245–254.
- [23] K. Lemarchand, L. Masson, and R. Brousseau, (2004) Molecular biology and DNA microarray technology for microbial quality monitoring of water, *Crit. Rev. Microbiol.*, **30**, 145–172.
- [24] L. Kaderali and A. Schliep, (2002) Selecting signature oligonucleotides to identify organisms using DNA arrays, *Bioinformatics*, **18**, 1340–1349.
- [25] A. Loy, M. Horn, and M. Wagner, (2003) ProbeBase: An online resource for rRNA-targeted oligonucleotide probes, *Nucleic. Acids. Res.*, **31**, 514–516.
- [26] Y. Kumar, R. Westram, P. Kipfer, H. Meier, and W. Ludwig, (2006) Evaluation of sequence alignments and oligonucleotide probes with respect to three-dimensional structure of ribosomal RNA using ARB software package, *BMC Bioinformatics*, **7**, 240.
- [27] T. Z. DeSantis, I. Dubosarskiy, S. R. Murray, and G. L. Andersen, (2003) Comprehensive aligned sequence construction for automated design of effective probes (CASCADE-P) using 16S Rdna, *Bioinformatics*, **19**, 1461–1468.
- [28] T. Z. DeSantis, P. Hugenholtz, K. Keller, E. L. Brodie, N. Larsen, Y. M. Piceno, R. Phan, and G. L. Andersen, (2006) NAST: A multiple sequence alignment server for comparative analysis of 16S rRNA genes, *Nucleic. Acids. Res.*, **34**, 394–399.
- [29] C. E. Lawrence, S. F. Altschul, M. S. Boguski, J. S. Liu, A. F. Neuwald, and J. C. Wootton, (1993) Detecting subtle sequence signals: A gibbs sampling strategy for multiple alignment, *Science*, **262**, 208–214.
- [30] B. L. Maidak, J. R. Cole, T. G. Lilburn, C. T. Parker, P. R. Saxman, R. J. Farris, G. M. Garrity, G. J. Olsen, T. M. Schmidt, and J. M. Tiedje, (2001) The RDP-II (Ribosomal Database Project), *Nucleic. Acids. Res.*, **29**, 173–174.
- [31] A. Pozhitkov, P. A. Noble, T. Domazet-Lošo, A. W. Nolte, R. Sonnenberg, P. Staehler, M. Beier, and D. Tautz, (2006) Tests of rRNA hybridization to microarrays suggest that hybridization characteristics of oligonucleotide probes for species discrimination cannot be predicted, *Nucleic. Acids. Res.*, **34**, 66.

# Inhomogeneous material property assignment and orientation definition of transverse isotropy of femur

Hai-Sheng Yang<sup>1,2</sup>, Tong-Tong Guo<sup>1</sup>, Jian-Huang Wu<sup>2</sup>, Xin Ma<sup>2,3</sup>

<sup>1</sup>Biomechanics Laboratory, Department of Mathematics and Natural Science, Harbin Institute of Technology Shenzhen Graduate School, Shenzhen, China; <sup>2</sup>Shenzhen Institute of Advanced Integration Technology, Chinese Academy of Sciences/The Chinese University of Hong Kong, Shenzhen, China; <sup>3</sup>Harbin Institute of Technology, Harbin, China.  
Email: [xin.ma@siat.ac.cn](mailto:xin.ma@siat.ac.cn)

Received 28 April 2009; revised 10 June 2009; accepted 12 June 2009.

## ABSTRACT

The finite element method has been increasingly adopted to study the biomechanical behavior of biologic structures. Once the finite element mesh has been generated from CT data set, the assignment of bone tissue's material properties to each element is a fundamental step in the generation of individualized or subject-specific finite element models. The aim of this work is to simulate the inhomogeneous and anisotropic material properties of femur using the finite element method. A program is developed to read a CT data set as well as the finite element mesh generated from it, and to assign to each element of the mesh the material properties derived from the bone tissue density at the element location. Moreover, for cancellous bone in femoral neck and cortical bone in femoral stem, the principal orientations of transverse isotropy were defined based on the trabecular structures and the haversian system respectively.

**Keywords:** Finite Element; Material Property; Inhomogeneous; Transverse Isotropy; Femur

## 1. INTRODUCTION

The determination of the mechanical stresses in human bones is of great importance in both research and clinical practice. Since the stresses in bones cannot be measured non-invasively in vivo, an effective way to estimate them is through the finite element (FE) analysis which is widely used in academic research and clinical applications, such as the theory of bone remodeling [1], the design of prosthesis [2] and the evaluation of fracture risk [3]. In early period the methods used to get bone geometry and mechanical properties were inaccurate and sometimes highly invasive and destructive. It is well known

that CT images can provide fairly accurate quantitative information on bone geometry based on high contrast between the bone tissue and the soft tissue around [4,5]. Moreover, it has been demonstrated that CT numbers are almost linearly correlated with apparent density of biologic tissues [6]. Good empirical relationships have been established experimentally between density and mechanical properties of bone tissues [7,8].

In early studies, if a generic bone model was constructed, then the mechanical properties of the different bone tissues were usually derived from average values reported in published experimental studies [9]. For an individualized or subject-specific model, however, mechanical properties should be derived from CT data. It has been shown that the stress distribution of a bone is strongly related to the mechanical properties distribution in the bone tissue [10], and the mechanical properties of bone have been showed to depend on the subject, anatomic location, orientation, biological processes and time. Hence, it is important to find an effective method to properly map the material properties derived from CT data into finite element models.

The CT data can be regarded as a three-dimensional scalar field (related to the tissue density) sampled over a regular grid. If the finite element mesh is generated starting from the same data, the mesh and the density distribution are perfectly registered in space. The only problem is how to account for this inhomogeneous distribution of material properties into the FE model. Many approaches were proposed in literature to perform this task [11,12,13,14,15,16,17,18,19]. However, these algorithms only simulated the inhomogeneity of bone, and the isotropic material property assignment was adopted without considering the orientation of material. Since the bone material is widely recognized as being anisotropic rather than isotropic [8,20], the FE simulation of inhomogeneity and isotropy cannot reflect the actual characteristics of bone structure. The aim of this study is to simulate the inhomogeneous and anisotropic material

properties of femur with finite element method.

## 2. MATERIALS AND METHODS

### 2.1. CT Data

The CT dataset of a man's femur is obtained from the public database which is created by VAKHUM project (<http://www.ulb.ac.be/project/vakhum/index.html>). The use of the data is free for academic purposes. The CT data are in standard DICOM formats. The slice thickness is 1mm in the epiphysis and 3mm in the diaphysis.

### 2.2. Finite Element Mesh

The finite element mesh of the right femur (**Figure 1**) generated from the corresponding CT dataset above is also obtained from the VAKHUM project. It is in a Patran Neutral file format. The mesh is made of linear hexahedral elements and is generated using the HEXAR (Cray Research, USA) automatic mesh generator that implements a grid-based meshing algorithm. The model mesh is spatially registered with the CT dataset. The complete finite element mesh consisted of 9,294 nodes and 7,934 elements.

### 2.3. The Procedure of Material Property Assignment

#### 2.3.1. Calculation of the Average CT Number ( $\overline{HU}$ )

For each element of the mesh, an average  $HU$  value is calculated with a numerical integration as follows [17]:

$$\begin{aligned}\overline{HU}_n &= \frac{\int_{V_n} HU(x, y, z) dV}{\int_{V_n} dV} \\ &= \frac{\int_{V'_n} HU(r, s, t) \det J(r, s, t) dV'}{V_n}\end{aligned}\quad (1)$$

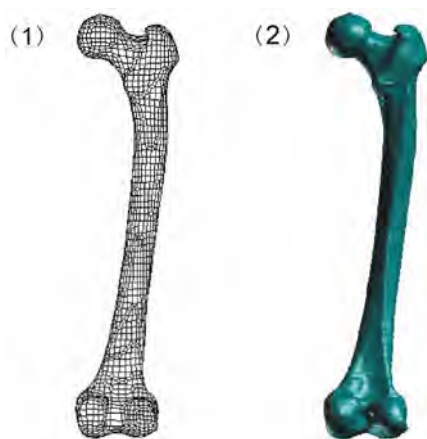


**Figure 1.** (1) The finite element mesh of femur (2) The geometrical model of femur.

where  $V_n$  indicates the volume of the element  $n$ ,  $(x, y, z)$  are the co-ordinates in the CT reference system,  $(r, s, t)$  are the local co-ordinates in the element reference system, and  $J$  represents the Jacobian of the transformation. The integrals in (1) are evaluated numerically, and the order of the numerical integration can be chosen by us. The value of  $HU(x, y, z)$  in a generic point of the CT domain is determined by a tri-linear interpolation between the eight adjacent grid points' values.

#### 2.3.2. Calibration of the CT Dataset and Simulation of the Inhomogeneity

CT numbers are dependent on many factors related to the specific exam. It is assumed that the relationship between CT numbers and apparent density is linear. A calibration phantom with bone-equivalent (solution of hydroxyapatite) insertions of different densities, embedded in a water-equivalent resin-based plastic (The European Spine Phantom, [21]) was used to obtain the parameters of the linear regression. The calibration equation is then:

$$\overline{\rho}_n = \alpha + \beta \overline{HU}_n \quad (2)$$

where  $\overline{\rho}_n$  is the average density assigned to the element  $n$  of the mesh,  $\overline{HU}_n$  is the average CT number and  $\alpha$  and  $\beta$  are the coefficients provided by calibration.

Referenced values for calibration are selected for approximate calibration from [16]: Radiographic and apparent density of water (0 HU, 1 g/cm<sup>3</sup>); Average radiographic density in the cortical region and the apparent density value for cortical bone (1840 HU, 1.73 g/cm<sup>3</sup>).

With the steps above, each element of the mesh is assigned different apparent density. Therefore, this procedure makes the simulation of inhomogeneity of femoral material come true.

#### 2.3.3 The Density-Modulus Relationship and the Simulation of Anisotropy

Various empirical models of the relationship between Young's modulus and the apparent bone density can be found in the literatures [7,8]. The relations are generally reported:

$$\overline{E}_n = a + b \overline{\rho}_n^c \quad (3)$$

where  $\overline{E}_n$  is the average Young's modulus assigned to the element  $n$  of the mesh,  $\overline{\rho}_n$  is its apparent density and  $a$ ,  $b$  and  $c$  are the coefficients.

In most of these works [11,12,13,14,15,16,17,18,19], the isotropic material property assignment was adopted without considering the direction of material property as its simplicity. Many previous studies had clearly demonstrated the anisotropic behavior of bone, and the determination of bone material properties as a function of

direction is the essential requirement [22]. The axial direction is defined according to the Haversian osteons of the cortical bone and according to the spatial main direction of the trabecular structures of cancellous bone. The relationship between bone material properties and apparent density is given by [8]:

- Cortical bone:

$$\begin{aligned} E_1 = E_2 &= 2314\rho^{1.57}, \quad E_3 = 2065\rho^{3.09}, \\ \nu_{12} &= 0.58, \quad \nu_{13} = \nu_{23} = 0.32, \\ G_{12} &= E_1 / 2(1 + \nu_{12}), \quad G_{13} = G_{23} = 3300; \end{aligned} \quad (4)$$

- Cancellous bone:

$$\begin{aligned} E_1 = E_2 &= 1157\rho^{1.78}, \quad E_3 = 1094\rho^{1.64}, \\ \nu_{12} &= 0.58, \quad \nu_{13} = \nu_{23} = 0.32, \\ G_{12} &= E_1 / 2(1 + \nu_{12}), \quad G_{13} = G_{23} = 110; \end{aligned} \quad (5)$$

where  $E$  is the Young's modulus (MPa),  $G$  the shear modulus (MPa),  $\rho$  is the apparent density ( $\text{g/cm}^3$ ),  $\nu$  the Poisson's ratio. All parameters are set in elemental Cartesian coordinate system of Patran (MSC, USA).

This procedure may, theoretically, lead to a different material card (Mat) for each element of the mesh, which may result in computational problems with those codes that can handle a limited number of materials. We can reduce the number of materials by choosing a  $\Delta E$  threshold. Then the maximum computed value of the elastic modulus,  $E_{\max}$  is assigned to the material Mat-1. All the elements with  $E \geq (E_{\max} - \Delta E)$  are assigned the material Mat-1. Mat-2 is characterized by the maximum  $E$  of the remaining elements and so on until the whole set of the model material is defined. In this paper, the threshold  $\Delta E$  is taken as 50 MPa.

A program was developed to read the original data including CT data, finite element mesh data and some parameters and then to implement the procedure described above. In this way, each element is assigned different density, elastic modulus and Poisson's ratio. At last, a finite element mesh provided with the assigned material properties is written out in a Patran Neutral file format.

Every element of the finite element model has its own element coordinate system used to determine the material's principal axis of this element. As the element coordinate systems vary from element to element, the principal material orientations need to be defined so as to

coincide with the structure of bone.

As we know, bone structure is customarily recognized as confirming to 'Wolff's law' which is essentially the observation that bone changes its external shape and internal architecture in response to stresses acting on it. Thus, the structure of bone (or material orientation) strongly coincides with the principal stress track. The directions of the femoral neck and stem can be approximately regarded as stress track in femur.

Femoral bone can be recognized as transversely isotropic material. According to the cortical bone structure in femoral stem and cancellous bone structure in femoral neck, the principal material orientation of cancellous bone is defined by the direction of the trabecular structures and the principal material orientation of cortical bone by the direction of the Haversian system.

### 3. RESULTS

#### 3.1. Material Properties Distribution

This material assignment procedure produces 165 different material cards. The distribution of the material properties in femur are shown in **Figure 2**. The maximum and minimum values for apparent density and elastic modulus are listed in **Table 1**. The maximum values are corresponding to the Mat-1 and the minimum to Mat-165 as a result of the definition in the program. The numbers of elements for each material property card are showed in **Figure 3**.

#### 3.2. The FE Simulation of Transversely Isotropic Material Property

**Figure 2** only showed the inhomogeneous distribution of material properties. After separating the femoral stem and neck, the principal material orientations for elements in neck and stem are defined respectively. **Figure 4** illustrates the vector form of the principal orientations in femoral neck. **Figure 5** presents the vector form of the principal orientations in femoral stem.

### 4. DISCUSSION

As is well-known, it is of significance to explore the biomechanical behavior of bone. FE analysis has been adopted by many researchers based on CT data that can provide useful information on the geometrical topology

**Table 1.** Material properties of femur (the unit for density is  $\text{g/cm}^3$ , and for elastic modulus is MPa).

Material properties	Maximum	Minimum
$\rho$	1.787	0.686
$E_1$ ( $E_2$ )	5755.799	591.512
$E_3$	12410.846	1026.157



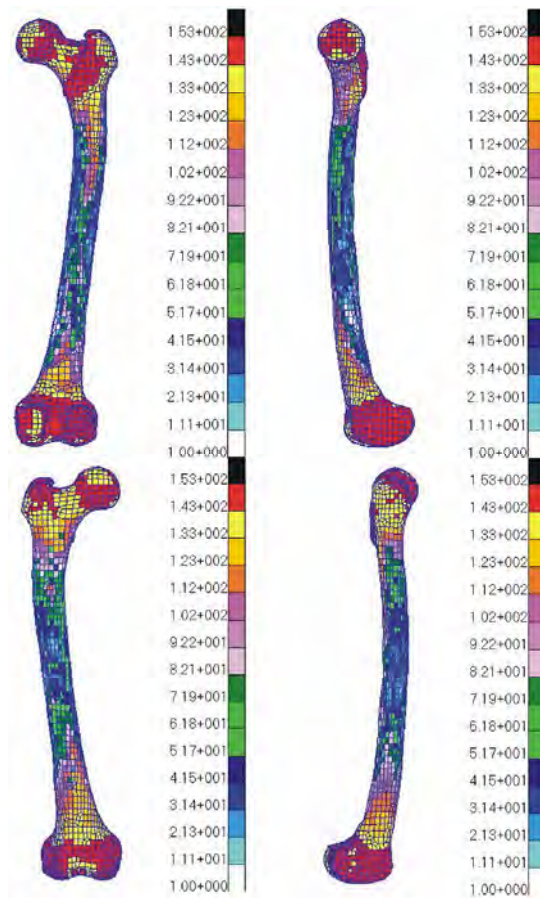


**Figure 2.** Right femur with different material properties mapped on it, observed from different angles of view.

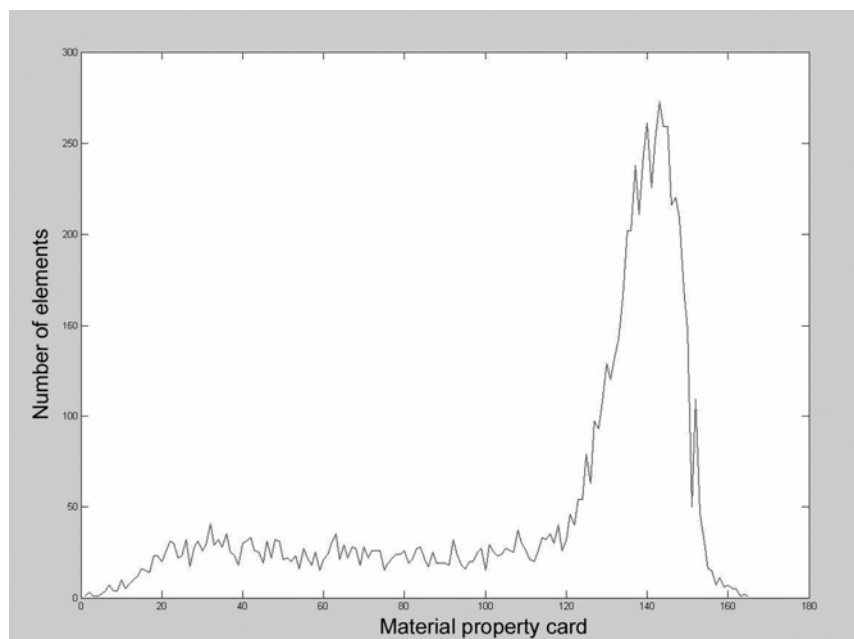


**Figure 3.** The number of elements for each material property card.

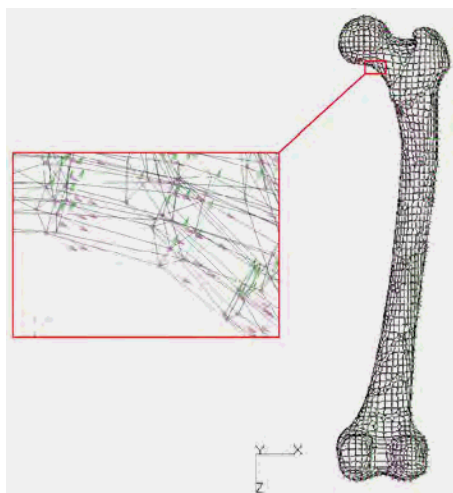


**Figure 4.** The principal material orientations in femoral neck showed in vector form (the purple arrows).

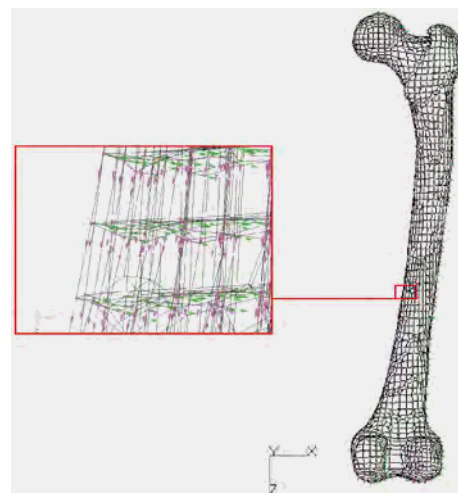


**Figure 5.** The principal material orientations in femoral stem showed in vector form (the purple arrows).

and material properties of bone. However, how to construct accurate FE models that reflect the real material properties of bone remains a problem. This work is aimed to simulate the inhomogeneity and anisotropy of the femur in order to make the FE material model more accurate.

Different algorithms are adopted to assign material properties into elements of the mesh model [17]. Most of these algorithms are based on the assumption that the variability of the CT numbers within the volume of each element can be neglected. All differences rely on how the average value of each element is computed.

Some simple methods are introduced to assign to each element the value by averaging the CT numbers of the CT sampling grids which are nearest to corresponding nodes of element or by averaging the CT numbers of the eight CT sampling points surrounding the element centroid [10,15]. These methods may produce inaccurate results when the element size is significantly larger than the spacing of the CT sampling grid.

A second approach that can avoid those shortcomings determines all CT sampling points that fall inside the element volume and assigns to the element the average of these values [16]. However, this method may not produce satisfactory results when the elements are of comparable dimension or smaller than the voxel size.

An advanced method adopted in our study estimates the average CT numbers by numerical integration over the element volume [17]. In this case, the dimension of the finite element is not influent on the accuracy of the average CT number estimation since the calculation of CT numbers takes into account the spatial distribution of the CT number in the eight surrounding CT lattice vertices.

As the relationship between density and Young's modulus is power law, different results will be produced when firstly averaging on each element the HU field and then calculating the element Young's modulus, or, on the contrary, averaging Young's modulus derived from HU value. It has been demonstrated that the latter can achieve more accurate results [18]. In the present work, CT number over each element volume is averaged first and then the Young's modulus is calculated with the experiential relationships. However, it has no influences on the FE simulation of anisotropy.

As we know, inner of the femur is marrow cavity that contains marrow or air. However, the mesh model in this study does not take into account the endosteal surface. Thus, the elements that belong to marrow cavity are assigned density and elastic modulus as well.

FE simulation of complete anisotropy of femoral bone is impossible at present. Thus, femoral material is simplified as being transversely isotropic in this study. It has been demonstrated that the structure of femur is highly variable, especially to cancellous bone. Thus, a clear and exact definition of the principal axes of transversely isotropy is impossible. In this study, we only separated the femoral neck and stem. Then, the principal orientations of neck were defined on the basis of the direction of trabecular structure and the principal orientations of stem on the basis of the direction of harversian system. As the structure of femur (or material orientation) coincides with the track of principal stress, the orientation definition based on pass of stress is reasonable.

Muscle, as well as bone, is one of the most important parts of the biologic body. Musculoskeletal loading influences the stresses and strains within the human bone and thereby affects the processes of bone modeling and

remodeling. Therefore, three-dimensional FEA for muscle is also of great importance. Assignment of the material properties to muscle FE mesh using the method in this paper may encounter some difficulties as the muscle belong to soft tissue that do not have steady shape. Thus, further research may be focused on the assignment of muscle material property.

Although the inhomogeneous and transversely isotropic material properties simulated in this work are theoretically close to that of real femur, experimental validation need be performed in the future.

## 5. ACKNOWLEDGEMENTS

This work was supported by National Natural Science Foundation of China (No. 30700165 and No. 60803108).

## REFERENCES

- [1] P. R. Fernandes, J. Folgado, C. Jacobs, and V. Pellegrini, (2002) A contact model with ingrowth control for bone remodelling around cementless stems, *Journal of Biomechanics*, **35**, 167–176.
- [2] P. Kowalczyk, (2001) Design optimization of cementless femoral hip prostheses using finite element analysis, *Journal of Biomechanical Engineering*, **123**, 396–402.
- [3] J. H. Keyak, (2001) Improved prediction of proximal femoral fracture load using nonlinear finite element models, *Medical Engineering & Physics*, **23**, 165–173.
- [4] M. Viceconti, L. Bellingeri, L. Cristofolini, and A. Toni, (1998) A comparative study on different methods of automatic mesh generation of human femurs, *Medical Engineering & Physics*, **20**, 1–10.
- [5] M. Lengersfeld, J. Schmitt, P. Alter, J. Kaminsky, and R. Leppeck, (1998) Comparison of geometry-based and CT voxel-based finite element modelling and experimental validation, *Medical Engineering & Physics*, **20**, 515–522.
- [6] J. Y. Rho, M. C. Hobatho, and R. B. Ashman, (1995) Relations of mechanical properties to density and CT numbers in human bone, *Medical Engineering & Physics*, **17**, 347–355.
- [7] D. R. Carter and W. C. Hayes, (1977) The compressive behaviour of bone as a two-phase porous structure, *The Journal of Bone and Joint Surgery, American Volume*, **59**, 954–962.
- [8] D. C. Wirtz, N. Schiffers, T. Pandorf, K. Radermacher, D. Weichert, and R. Forst, (2000) Critical evaluation of known bone material properties to realize anisotropic FE-simulation of the proximal femur, *Journal of Biomechanics*, **33**, 1325–1330.
- [9] M. C. Hobatho, R. Darmana, P. Pastor, J. J. Barrau, S. Laroze, and J. P. Morucci, (1991) Development of a three-dimensional finite element model of a human tibia using experimental modal analysis, *Journal of Biomechanics*, **24**, 371–383.
- [10] B. Merz, P. Niederer, R. Muller, and P. Rueggsegger, (1996) Automated finite element analysis of excised human femora based on precision-QCT, *Journal of Biomechanical Engineering*, **118**, 387–390.
- [11] J. H. Keyak and S. A. Rossi, (2000) Prediction of femoral fracture load using finite element models: An examination of stress- and strain-based failure theories, *Journal of Biomechanics*, **33**, 209–214.
- [12] D. D. Cody, F. J. Hou, G. W. Divine, and D. P. Fyhrie, (2000) Femoral structure and stiffness in patients with femoral neck fracture, *Journal of Orthopaedic Research: Official Publication of the Orthopaedic Research Society*, **18**, 443–448.
- [13] R. L. Austman, J. S. Milner, D. W. Holdsworth, and C. E. Dunning, (2008) The effect of the density-modulus relationship selected to apply material properties in a finite element model of long bone, *Journal of Biomechanics*, **41**, 3171–3176.
- [14] M. Dalstra, R. Huiskes, and L. van Erning, (1995) Development and validation of a three-dimensional finite element model of the pelvic bone, *Journal of Biomechanical Engineering*, **117**, 272–278.
- [15] P. M. Cattaneo, M. Dalstra, and L. H. Frich, (2001) A three-dimensional finite element model from computed tomography data: A semi-automated method, *Proceedings of the Institution of Mechanical Engineers, Part H, Journal of Engineering in Medicine*, **215**, 203–213.
- [16] C. Zannoni, R. Mantovani, and M. Viceconti, (1998) Material properties assignment to finite element models of bone structures: A new method, *Medical Engineering & Physics*, **20**, 735–740.
- [17] F. Taddei, A. Pancanti, and M. Viceconti, (2004) An improved method for the automatic mapping of computed tomography numbers onto finite element models, *Medical Engineering & Physics*, **26**, 61–69.
- [18] F. Taddei, E. Schileo, B. Helgason, L. Cristofolini, and M. Viceconti, (2007) The material mapping strategy influences the accuracy of CT-based finite element models of bones: an evaluation against experimental measurements, *Medical Engineering & Physics*, **29**, 973–979.
- [19] B. Helgason, F. Taddei, H. Pálsson, E. Schileo, L. Cristofolini, M. Viceconti, and S. Brynjólfsson, (2008) A modified method for assigning material properties to FE models of bones, *Medical Engineering & Physics*, **30**, 444–453.
- [20] R. B. Ashman, S. C. Cowin, W. C. Van Buskirk, and J. C. Rice, (1984) A continuous wave technique for the measurement of the elastic properties of cortical bone, *Journal of Biomechanics*, **17**, 349–361.
- [21] W. A. Kalender, (1992) A phantom for standardization and quality control in spinal bone mineral measurements by QCT and DXA: Design considerations and specifications, *Medical Physics*, **19**, 583–586.
- [22] D. Besdo and M. Handel, (1998) Numerical treatment of bone as anisotropic material, *Biomedical Technology*, **39**, 293–298.

# Unsupervised human height estimation from a single image

Ye-Peng Guan<sup>1,2</sup>

<sup>1</sup>School of Communication and Information Engineering, Shanghai University, Shanghai, China; <sup>2</sup>Key Laboratory of Advanced Displays and System Application, Ministry of Education, Shanghai, China.  
Email: [ypguan@shu.edu.cn](mailto:ypguan@shu.edu.cn)

Received 15 May 2008; revised 16 June 2009; accepted 17 June 2009.

## ABSTRACT

**The single image containing only a human face not previously addressed in the literature is employed to estimate body height. The human face especially the facial vertical distribution possesses some important information which strongly correlates with the stature. The vertical proportions keep up relative constancy during the human growth. Only a few facial features such as the eyes, the lip and the chin are necessary to extract. The metric stature is estimated according to the statistical measurement sets and the facial vertical golden proportion. The estimated stature is tested with some individuals with only a single facial image. The performance of the proposed method is compared with some similar methods, which shows the proposal performs better. The experimental results highlight that the developed method estimates stature with high accuracy.**

**Keywords:** Human Height Estimation; Golden Proportion; Facial Proportion; Feature Extraction; Projection Model

## 1. INTRODUCTION

Human height estimation has many important applications such as soft-biometrics and human tracking [1]. In the first case, the stature can be used to rule out the possibility that a particular person is the same person from the surveillance cameras [2,3]. In the latter case, it can be exploited to distinguish among a small set of tracked people in the scene [1,4,5,6,7]. The stature, therefore, may become a very useful identification feature. In the cases with two or more images, the stature estimation by stereo matching is computationally expensive and there exists ambiguity being resident in the stereo correspondence, which is not overcome efficiently so far [8,9,10]. In the case of only one image available, the stature

measurement from single image has to be performed. Many single view based approaches are proposed based on some geometric structures or models [1,2,3,4,5,6,7,11,12,13,14,15,16]. In [1,2,3,4,5,6,7,12,13,14,15,16], plane metrology algorithms based on vanishing points and lines are developed to measure distances or lengths on the planar surfaces parallel to the reference plane. Any slight inaccuracy in measuring vanishing points will result in large errors [2,17]. Reference points defining the top and bottom of the object should be clear and unambiguous. Besides, reference objects must be in the same plane as the target object. Moreover, the full body of the user must be visible in measuring the stature. In [11], BenAbdelkader and Yacoob incorporated some certain statistical properties of human anthropometry into the stature estimation. It would be difficult to obtain the stature when some anthropometric values such as acromion and trapezius (or neck) are not available. Besides, if the whole body and/or the facial plane are at an angle with respect to the camera, the weak perspective assumption cannot be exploited.

Although many single view based approaches have been proposed, there exist some problems in the literature. In order to improve both validation and automation of the procedure, we have developed an approach to estimating the stature with the following advantages. 1) The used image contains only the human face not previously addressed in the literature. The human face especially the facial vertical distribution owns some important information which strongly correlates with the stature [18]. The facial vertical proportion used is based on the golden proportion [19,20]. A number of investigators have commented on the relative constancy of the facial vertical proportions during the human growth [21]. 2) Only a few facial features are necessary to extract, and the procedure is processed automatically by image analysis operators. 3) The extracted facial features and the facial vertical proportions are used together to estimate the stature. The estimated result is tested with some individuals with only a facial image, showing high esti-



mation accuracy, which validates the developed approach to be objective, and can be taken as an automated tool for estimating the stature. The potential applications of this work include biometric diagnoses, user authentication, smart video surveillance, human-machine interface, human tracking, athletic sports analysis, virtual reality, and so on.

The rest of the paper is organized as follows: Section 2 describes the facial proportions used for estimating the stature. Section 3 discusses the face detection and the facial features extraction. Section 4 describes the stature estimation based on a calibrated camera. Experimental results and evaluation of the performance are given in Section 5 and followed by some conclusions and future works in Section 6.

## 2. FACIAL PROPORTIONS

All living organisms including humans are encoded to develop and confirm to a certain proportion [20]. The human face especially the facial vertical proportion owns some important information which correlates with the stature [18]. The facial vertical proportions include

the golden proportion [19,20] and the facial thirds method [22,23]. The facial golden proportion is approximately the ratio of 1.618 to 1 as shown in **Figure 1**. It states that the human face may be divided into a golden proportion distribution by drawing horizontal lines through the forehead hairline, the nose, and the chin, or through the eyes, the lip, and the chin.

The facial thirds method states that the face may be divided into roughly equal a third by drawing horizontal lines through the forehead hairline, the eyebrows, the base of the nose, and the edge of the chin as shown in **Figure 2**. Besides, the distance between the lip and the chin is double the distance between the base of the nose and the lip [22,23].

The golden proportion and the facial thirds are similar to each other. The former specifies a larger number of proportions than the latter. They used some different features so that they cannot be directly compared [19]. By experiments it shows that the accuracy of stature estimated by the golden proportion is more consistent with the ground-truth data than that of by the facial thirds.

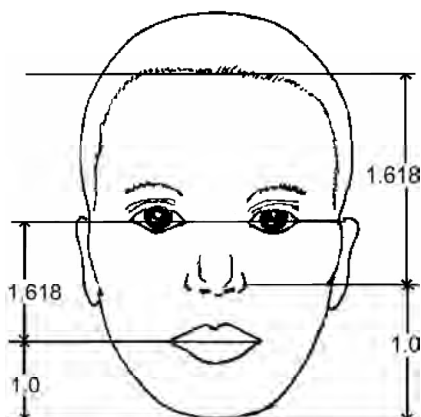


**Figure 1.** Facial vertical golden proportion



**Figure 2.** Facial vertical thirds proportion

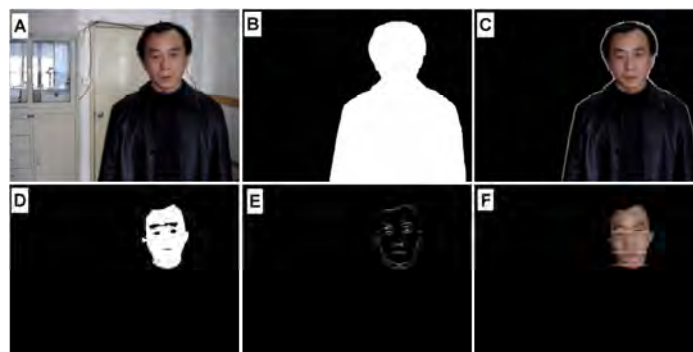


**Figure 3.** Face detection and facial features extraction results. A: original image. B: extracted binary foreground. C: extracted foreground object. D: extracted binary blob. E: resulting image from horizontal edge detection. F: horizontal locations of the eyes, the lip and chin lines.



### 3. FOREGROUND DETECTION AND FACIAL FEATURE EXTRACTION

Robust and efficient extraction of foreground object from image sequences is a key operation. Many algorithms have been developed [24,25,26]. The algorithm proposed in [26] is employed to extract foreground blob as shown in **Figure 3B**. After extracting the foreground objects, accurate facial features extraction is important for reliable estimation of the stature. A number of methods have been developed for extracting facial features [27,28,29]. Among the facial features such as the eyes, nose, lip, chin, and so on, the eyes are one of the most important facial features [30,31]. Since effective automatic location and tracking of a person's forehead hair-line is difficult, we select the eyes, lip, and the chin as the facial features used in the study.

The first step consists of locating the facial region to remove irrelevant information. Human skin color, though differs widely from person to person, is distributed over a very small area on a  $C_b C_r$  plane [32,33]. This model is robust against different types of skin, such as those of people from Europe, Asia and Africa. The skin tone pixels are detected using the  $C_b$  and  $C_r$  components. Let the thresholds be chosen as  $[C_{b1}, C_{b2}]$  and  $[C_{r1}, C_{r2}]$ , a pixel is classified to skin tone if the values  $[C_b, C_r]$  fall within the thresholds. Each pixel in the  $C_b$  and  $C_r$  layer which does not meet the range  $[C_b, C_r]$  is set to zero. In some cases, the obtained mask has concavities or spikes as shown in **Figure 3D**, which affects the facial features location. We use the algorithm in [34] to process this problem.

There are many fairly long horizontal edges near the facial features. In order to make the edge detector behaves more stable, we transform the intensity of the image into a second derivate and then horizontally project it to determine the horizontal positions of facial features [34] (seen from **Figure 3E**). The positions of peaks in the horizontal projection curve correspond with the horizontal facial features including the eyes, nose and lip. Horizontal transition is stronger at the lip than at the eyes in some cases. The lip can be detected in hue/saturation color space [35]. We detect the peak with a maximal value above the lip as the horizontal position of eyes. In the meantime, the chin is automatically located between the lip and the neck. The horizontal location of the eyes, lip and chin is given in **Figure 3F**.

### 4. STATURE ESTIMATION

Stature estimation is discussed here to highlight the use of the extracted facial features. Assume the person stands or walks on a plane and a camera is calibrated with respect to this plane. We compute 3D position of the extracted facial features according to the golden proportion. Since the facial vertical proportions keep

relative constant during the human growth [21], the 3D position of the extracted facial features can be determined if a certain length or distance is known.

More detailed metric description of the head and face was recognized quite early. Major U.S. surveys, those in which large numbers of measurements have been made on samples of a thousand or more individuals, have been carried out on military personnel [18]. The measurement device could provide a sensitivity of less than 0.01 mm in each axis, and the accuracy with the order of 0.1 mm could be achieved [36]. Shiang [18] has made extensive 3D statistical work of human head and face also. According to the measurement sets the metric stature can be estimated based on the calibrated camera.

The camera model used is a central projection. Effect such as radial distortion can be removed and is not detrimental to the method. The camera perspective projection model can be represented by a  $3 \times 4$  matrix  $M$ . The image coordinates  $(u_i, v_i)$  of a point  $P_i$  expressed in a homogenous coordinate system are given as follows:

$$s_i \begin{bmatrix} u_i \\ v_i \\ 1 \end{bmatrix} = \begin{bmatrix} m_{11} & m_{12} & m_{13} & m_{14} \\ m_{21} & m_{22} & m_{23} & m_{24} \\ m_{31} & m_{32} & m_{33} & m_{34} \end{bmatrix} \begin{bmatrix} X_i \\ Y_i \\ Z_i \\ 1 \end{bmatrix} \quad (1)$$

When estimating the stature, we assume that depth difference among the eyes, lip and the chin is negligible. For simplifying computation, assume that the 3D coordinates of the chin point  $(u_1, v_1)$  is  $(X, Y, Z)$  whose horizontal line intersects with the vertical line through the center of the eyes. The coordinates of the lip point  $(u_2, v_2)$  is  $(X, Y, Z+h)$  whose horizontal line intersects with the same vertical line as above. According to the golden proportion the coordinates of the center of the eyes point  $(u_3, v_3)$  is  $(X, Y, Z+2.618h)$ . If  $h$ , the height between the chin and the lip is known, (1) can be used to infer the 3D coordinate of the chin point. Expending the  $(X, Y, Z)$  gives as follows:

$$A \begin{bmatrix} X \\ Y \\ Z \end{bmatrix} = B \quad (2)$$

where,

$$A = \begin{bmatrix} u_1 m_{31} - m_{11} & u_1 m_{32} - m_{12} & u_1 m_{33} - m_{13} \\ v_1 m_{31} - m_{21} & v_1 m_{32} - m_{22} & v_1 m_{33} - m_{23} \\ u_2 m_{31} - m_{11} & u_2 m_{32} - m_{12} & u_2 m_{33} - m_{13} \\ v_2 m_{31} - m_{21} & v_2 m_{32} - m_{22} & v_2 m_{33} - m_{23} \\ u_3 m_{31} - m_{11} & u_3 m_{32} - m_{12} & u_3 m_{33} - m_{13} \\ v_3 m_{31} - m_{21} & v_3 m_{32} - m_{22} & v_3 m_{33} - m_{23} \end{bmatrix} \quad (3)$$

$$B = \begin{bmatrix} m_{14} - u_1 m_{34} \\ m_{24} - v_1 m_{34} \\ m_{14} - u_2 m_{34} - (u_2 m_{33} - m_{13})h \\ m_{24} - v_2 m_{34} - (v_2 m_{33} - m_{23})h \\ m_{14} - u_3 m_{34} - 2.618(u_3 m_{33} - m_{13})h \\ m_{24} - v_3 m_{34} - 2.618(v_3 m_{33} - m_{23})h \end{bmatrix} \quad (4)$$

From (2), the linear least-squares solution is given by

$$[X, Y, Z]^T = (A^T A)^{-1} A^T B \quad (5)$$

Once person's head-top point ( $u_4, v_4$ ) are known, we can rearrange (2) to estimate the stature as (6) using the coordinates ( $X, Y$ ). It is found that (6) as a function of  $v_4$  can get a more stable estimation of the stature.

$$H = \frac{m_{24} - v_4 m_{34} - (v_4 m_{31} - m_{21})X - (v_4 m_{32} - m_{22})Y}{v_4 m_{33} - m_{23}} \quad (6)$$

## 5. EXPERIMENTAL RESULTS

To evaluate the performance of the proposed method, we have done experiments with some individuals. The experiments are performed with a CCD camera which produces 640×480 pixels image sequences. The camera is mounted overhead which look down at an oblique angle to capture human face. In the experiment, the parameters of skin segmentation are fixed for all images as follows:  $C_{b1}=83$ ,  $C_{b2}=127$ ,  $C_{r1}=140$ ,  $C_{r2}=175$ . The parameter  $h$  used in (4) is selected as 44.96 mm.

The experimental setup includes a wall screen with a maximum size of 2.4 m × 4 m which is parted into 2×4 intended panels pointing by the users. The users' position is about 2 m~4.5 m away from the screen and the user can walk freely in the experimental room. The room size is about 3 m×5 m. The experiment is performed as

following way. We capture the pointing person as she/he is pointing at the intended panel. We extract the pointing user's face and estimate his stature. **Figure 4(a)** gives some input video images as a user pointing at the panels. The tested user's face is shown in some light blue pixels superimposed on the original images. The estimated stature (unit: mm) is given in the image also. **Figure 4(b)** shows the stature as the user pointing at the panels at different locations. The symbol in the legend refers to some different statures: the real human height (real H), the thirds proportion based estimated height (thirds based H), and the golden proportion based estimated height (the proposed H).

The standard derivation  $\sigma$  of the estimated stature by the proposal is 6.744 mm, and the maximal deviation from the real height is 17.80 mm which is accurate within  $3\sigma$ . Correspondingly, the  $\sigma$  of the thirds based estimated height is 10.4188 mm, while the maximal deviation from the real height is 36.9 mm which is out of  $3\sigma$ . The proposed method outperforms the thirds based method in estimating the stature.

The deviation is due to the fact that relative error increase with the distance between the camera and the user since the pixel size is proportional to the view angle, which means smaller resolution from a larger distance. In the experiment a pixel difference corresponds to about 5.26 mm resolution ambiguity from the distance of 3 m. Besides, inaccurate camera calibration affects the measurement results. Another factor is human gesture. Human gesture involves periodic up-and-down displacement. Some other factors such as occlusion, and face orientation may affect the estimation result. This problem can be avoided by using multiple cameras and a camera with the best view is used to estimate the stature.

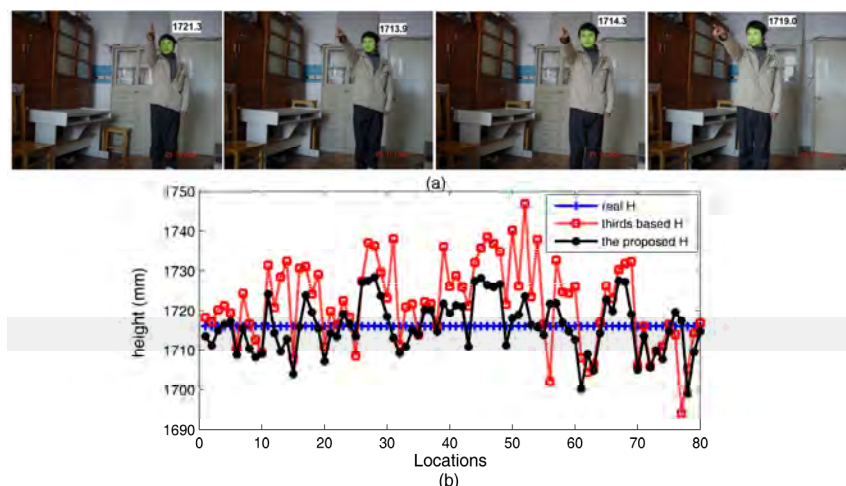


**Figure 4.** Height results. (a) The person pointing at the panels and the extracted face shown in light blue pixels superimposed on the original images. The estimated height is given based on the proposal also. (b) Heights at different locations.

**Table 1.** Height estimation results.

Algorithm	Tested object											
	1			2			3			4		
	AM	$\sigma$	MD	AM	$\sigma$	MD	AM	$\sigma$	MD	AM	$\sigma$	MD
Kim <sup>[7]</sup>	1817.2	5.12	10.77	1708.2	8.56	15.34	1668.5	6.45	15.36	1653.6	6.75	15.75
Wang <sup>[12]</sup>	1820.4	7.35	20.65	1722.4	10.56	26.74	1685.4	8.34	23.74	1664.5	9.26	26.51
Lee <sup>[15]</sup>	1818.5	6.45	17.34	1720.6	9.78	22.58	1682.8	7.67	22.46	1663.7	8.78	25.12
<b>Proposed</b>	<b>1813.6</b>	<b>4.89</b>	<b>8.90</b>	<b>1715.4</b>	<b>8.78</b>	<b>15.56</b>	<b>1672.3</b>	<b>6.16</b>	<b>15.13</b>	<b>1647.3</b>	<b>6.69</b>	<b>14.90</b>

We hope to discuss it in the future. The processing speed of the proposal is roughly 15frames/s for a single object and frontal face in the scene.

To verify the effectiveness of the mentioned approach, we have performed experiments with some moving individuals. The performance of the proposal for four tested individuals with known stature is compared with that of some similar methods [7,12,15] shown in **Table 1**. **Table 1** summarizes the average measurement (AM) stature, the standard derivation ( $\sigma$ ), and the maximal derivation (MD) for each tested object. It is clearly seen that the developed approach performs better.

## 6. CONCLUSIONS AND FUTURE WORKS

We have developed unsupervised single view based method for robust and real-time estimating the stature. The image contains only a face or upper body little discussed in the literature. Only a few facial features such as the eyes, lip and chin are necessary to extract. The metric stature is estimated according to the statistical measurement sets and the facial vertical golden proportion. The estimated stature is tested with some individuals with only a facial image, showing high accuracy, which validates the proposal to be objective, and can be taken as an automated tool for estimating the stature. Extension to un-calibrated scenario case would be developed in the future.

## 7. ACKNOWLEDGEMENTS

This work in part is supported by the National Natural Science Foundation of China (Grant No. 60872117).

## REFERENCES

- [1] C. Ben-Abdelkader, R. Cutler, and L. S. Davis, (2002) Person identification using automatic height and stride estimation, Proceedings of 16th International Conference on Pattern Recognition, **4**, 377–380.
- [2] A. Criminisi, (2002) Single-view metrology: Algorithms and applications, Proceedings of 24th DAGM Symposium on Pattern Recognition, 224–239.
- [3] N. Saitoh, K. Kurosawa, and K. Kuroki, (1999) A study on height measurement from a single view, Proceedings of International Conference on Image Processing, **3**, 523–526.
- [4] A. Bovyryn and K. Rodyushkin, (2005) Human height prediction and roads estimation for advanced video surveillance systems, Proceedings of IEEE Conference on Advanced Video and Signal-Based Surveillance, 219–223.
- [5] C. S. Madden and M. Piccardi, (2005) Height measurement as a session-based biometric, Proceedings of Image and Vision Computing New Zealand, 282–286.
- [6] D. De Angelis, R. Sala, A. Cantatore, P. Poppa, M. Dufour, M. Grandi, and C. Cattaneo, (2007) New method for height estimation of subjects represented in photographs taken from video surveillance systems, International Journal of Legal Medicine, **121(6)**, 489–492.
- [7] D. Kim, J. Lee, H. -S. Yoon, and E. -Y. Cha, (2007) A non-cooperative user authentication system in robot environments, IEEE Trans. Consumer Electronics, **53(2)**: 804–811.
- [8] L. Zhang, (2006) Fast stereo matching algorithm for intermediate view reconstruction of stereoscopic television images, IEEE Trans. Circuits and Systems for Video Technology, **16(10)**, 1259–1270.
- [9] F. Remondino, S. F. El-Hakim, A. Gruen, and L. Zhang, (2008) Turning images into 3-D models, IEEE Signal Processing Magazine, **25(4)**, 55–65.
- [10] W. Xiong, H. S. Chung, and J. Jia, (2009) Fractional stereo matching using expectation-maximization, IEEE Trans. Pattern Analysis and Machine Intelligence, **31(3)**, 428–443.
- [11] C. Ben Abdelkader and Y. Yacoub, (2008) Statistical body height estimation from a single image, Proceedings of 8th IEEE International Conference on Automatic Face and Gesture Recognition, 1–7.
- [12] R. Wang and F. P. Ferrie, (2008) Self-calibration and metric reconstruction from single images, Proceeding of International Archives of the Photogrammetry, Remote Sensing and Spatial Information Sciences, 639–644.
- [13] L. Fengjun, Z. Tao, and R. Nevatia, (2002) Self-calibration of a camera from video of a walking human, Proceedings of 16th International Conference on Pattern Recognition, **1**, 562–567.
- [14] Y. Kida, S. Kagami, T. Nakata, M. Kouchi, and H. Mizoguchi, (2004) Human finding and body property estimation by using floor segmentation and 3D labeling, Proceedings of IEEE International Conference on Systems, Man and Cybernetics, **3**, 2924–2929.
- [15] S. -H. Lee and J. -S. Choi, (2007) A single-view based framework for robust estimation of height and position of moving people, Proceedings of Pacific-Rim Symposium on Image and Video Technology, 562–574.

- [16] E. Jeges, I. Kispal, and Z. Hornak, (2008) Measuring human height using calibrated cameras, *Proceedings of Conference on Human System Interactions*, 755–760.
- [17] A. Criminisi, I. Reid, and A. Zisserman, (1999) Single view metrology, *Proceedings of 7th International Conference on Computer Vision*, 434–442.
- [18] T. -Y. Shiang, (1999) A statistical approach to data analysis and 3-D geometric description of the human head and face, *Proceedings of the National Science Council, Republic of China, Part B, Life Sciences*, **23**(1), 19–26.
- [19] H. Gunes and M. Piccardi, (2006) Assessing facial beauty through proportion analysis by image processing and supervised learning, *International Journal of Human-Computer Studies*, **64**(12), 1184–1199.
- [20] Y. Jefferson, (2004) Facial beauty: Establishing a universal standard, *International Journal of Orthodontics*, **15**(1), 9–22.
- [21] C. E. Nasjleti and C. J. Kowalski, (1975) Stability of upper face height-total face height ratio with increasing age, *Journal of Dental Research*, **54**(6), 12–41.
- [22] H. L. Obwegeser and L. J. Marentette, (1986) Profile planning based on alterations in the positions of the bases of the facial thirds, *Journal of Oral and Maxillofacial Surgery*, **44**(4), 302–311.
- [23] C. Sforza, A. Laino, R. D'Alessio, C. Dellavia, G. Grandi, and V. F. Ferrario, (2007) Three-dimensional facial morphometry of attractive children and normal children in the deciduous and early mixed dentition, *The Angle Orthodontist*, **77**(6), 1025–33.
- [24] R. Li, S. Yu, and X. Yang, (2007) Efficient spatio-temporal segmentation for extracting moving objects in video sequences, *IEEE Trans. Consumer Electronics*, **53**(3), 1161–1167.
- [25] S. Youn, J. -H. Ahn, and K. Park, (2008) Entrance detection of a moving object using intensity average variation of subtraction images, *Proceedings of International Conference on Smart Manufacturing Application*, 459–464.
- [26] Y. P. Guan, (2008) Wavelet multi-scale transform based foreground segmentation and shadow elimination, *The Open Signal Processing Journal*, **1**(6), 1–6.
- [27] K. Sridharan and V. Govindaraju, (2005) A sampling based approach to facial feature extraction, *Proceedings of 4th IEEE Workshop on Automatic Identification Advanced Technologies*, 51–56.
- [28] F. Song, D. Zhang, D. Mei, and Z. Guo, (2007) A multiple maximum scatter difference discriminant criterion for facial feature extraction, *IEEE Trans. Systems, Man, and Cybernetics, Part B*, **37**(6), 1599–1606.
- [29] Y. He, (2009) Real-time nonlinear facial feature extraction using Cholesky decomposition and QR decomposition for face recognition, *Proceedings of International Conference on Electronic Computer Technology*, 306–310.
- [30] P. J. Phillips, H. Moon, S. A. Rizvi, and P. J. Rauss, (2000) The feret evaluation methodology for face-recognition algorithms, *IEEE Trans. Pattern Analysis and Machine Intelligence*, **22**(10), 1090–1104.
- [31] A. M. Martinez, (2002) Recognizing imprecisely localized partially occluded and expression variant faces from a single sample per class, *IEEE Trans. Pattern Analysis and Machine Intelligence*, **24**(6), 748–763.
- [32] H. Wang and S. F. Chang, (1997) A highly efficient system for automatic face region detection in MPEG videos, *IEEE Trans. Circuit System Video Technology*, **7**(4), 615–628.
- [33] C. Garcia and G. Tziritas, (1999) Face detection using quantized skin colour regions merging and wavelet packet analysis, *IEEE Trans. Multimedia*, **1**(3), 264–277.
- [34] Y. Guan, (2007) Robust eye detection from facial image based on multi-cue facial information, *Proceedings of IEEE International Conference on Control and Automation*, 1775–1778.
- [35] G. Chetty and M. Wagner, (2004) Automated lip feature extraction for liveness verification in audio-video authentication, *Proceedings of Image and Vision Computing*, 17–22.
- [36] J. F. Annis and C. C. Gordon, (1988) The development and validation of an automated headboard device for measurement of three-dimensional coordinates of the head and face, *Tech. Report*, <http://oai.dtic.mil/oai/oai>.



# Design of occlusion pressure testing system for infusion pump

Peng Zhang<sup>1</sup>, Shu-Yi Wang<sup>1</sup>, Chuan-Yi Yu<sup>1</sup>, Min-Yan Zhang<sup>1</sup>

<sup>1</sup>School of Medical Instrument and Food Engineering, University of Shanghai for Science and Technology, Shanghai, China.  
Email: [zhangpeng3722@163.com](mailto:zhangpeng3722@163.com)

Received 23 June 2008; revised 16 July 2009; accepted 28 July 2009.

## ABSTRACT

**Reliability of medical devices such as infusion pumps is extremely important because these devices are being used in patients who are in critical condition. Occlusion pressure, as an important parameter of infusion pumps, should be detected when an occlusion occurred. However, infusion pumps' occlusion pressure could not be tested and the performance of these pumps is not known to us. In order to test the occlusion pressure of infusion pump, a testing system has been put forward according to standards of IEC 60601-2-24:1998/ GB 9706.27-2005. The system is comprised of sensor, acquisition card, three-way tap and so on; this system is controlled by a PC. At the same time, sampling rate could be changed if necessary and test time could be recorded. And then the characteristics of this system were studied, such as linear, effects of pump rates and different pumps. The system remained linear in a given environment. The higher is the pump rate, the faster is the time to reach occlusion condition. The testing system has been proved to be effective in testing the occlusion pressure of infusion pumps and the accuracy error of pressure is content the demand of  $\pm 1\%$  of range.**

**Keywords:** Infusion Pump; Occlusion Pressure; Testing System

## 1. INTRODUCTION

Infusion pumps have been widely used in clinical practice, such as in intravenous infusion therapy to infuse fluids, medication or nutrients into patient's circulatory system and can produce quite high but controlled pressure so as to inject controlled amount of fluids, however, pressure values are different regarding to different pumps.

Nowadays, most infusion pumps have an occlusion pressure preset threshold, once the pressure of tubing, connecting to patients, exceeds the preset limit, the alarm of occurring occlusion will be active. Some infusion pumps adopt a method of speed administration, in this case, if fluid rate is zero during a certain time and the alarm of occlusion will be active. However, on the one hand, the pressure values of vascular are different regarding to different persons and the same person at different time. When an occlusion occurs along the delivery path, medication will not be delivered to patient but the pressure does not reach the preset pressure and the alarm will not be active. In this case, the pump can not only continue to operate normally, but it can display erroneous values about the infusion rate and accumulated volume. This incorrect record for the patient could lead to an improper analysis, which will cause injury to patient. The higher is occlusion pressure, the more serious is the injury, so the test of occlusion pressure is crucial to pumps [1]. On the other hand, the inaccurate infusion rates of infusion pumps could be generated if the pumps are not checked up after a long time usage. At last, some infusion pumps could be used to detect tissue extravagation [2]. At this moment, infusion pumps must be periodically tested to determine whether they are functioning properly [3,4].

A testing system of infusion pump occlusion pressure is designed to test an infusion pump and determine whether the pump is operating correctly.

At present, there are several products commercial available in market; mostly they are designed by foreigners, such as IDA-4 Plus Infusion Pump Analyzer, Infutest Solo Infusion Pump Analyzer and so on. The former is designed by Fluke, it has a function of PCA (Patient Controlled Analgesia) Pumps Bolus measurement and testing four pumps at the same time; the latter is designed by Datrend Systems Inc. and there are other corporations to design infusion pump analyzers (tester) [5,6]. Though these devices have well performances, the price is high accordingly. At the same time, some of these devices are not designed rationally; one device is



ruined for its first using, so we designed this simple but good performance testing system. But the most important point is that these devices are not designed followed the IEC 60601-2-24:1998 standard, so they can be not be used to test other infusion pumps and so on.

During our previous work, we have found that, if fluid speed is low in syringe pumps, in the curve of time-pressure, there exists and smooth phase liking a part of round and pressure values should be the in this phase. On this condition, we adopted a different method and got an elementary result, but this method was not satisfactory and would be ameliorated.

## 2. METHODS AND APPARATUS

### 2.1. Description of Apparatus

According to the standards of IEC 60601-2-24:1998 and GB 9706.27-2005, a test system is designed which is shown in **Figure 1**. This system is applied to infusion pumps, volumetric infusion pumps and syringe pumps [7,8].

The testing system can be divided into three parts according to their different functions.

Part 1: In this part, the aim is designed to provide infusion pumps to be tested; and infusion pumps provide the driving force for occlusion pressure. The administration set, which is medical tubing in this system, sets to 1 m.

Part 2: The aim is designed to simulate the occlusion in patient and collect the fluids. Occlusion is realized through the turning of three-way tap and then the signal of sensor is transmitted to the acquisition card. At the beginning of test, when the three-way tap is opened, fluids will be collected in the collecting vessel; if three-way tap is closed, occlusion pressure will be generated following the rigid tubing and then the pressure signal is transmitted to the pressure transducer. At the end of test, fluids will be collected in the collecting vessel.

Part 3: In this part, the interface between PC, running under Windows XP and sensor was realized through an RS-232 connection. The sampling rate is controlled by PC and software, which is basing on Visual C++ 6.0 platform. The signal, coming from sensor, is obtained by acquisition card, and then is transmitted to computer. After the further dealing and calculation of signals, the dealt signals could be displayed on monitor in the form of wave.

### 2.2. Measurements

The test is carried out using a test solution of ISO class III water for medical use, under normal condition ( $20^{\circ}\text{C} \pm 2^{\circ}\text{C}$ ,  $65\% \pm 5\% \text{RH}$  (Relative humidity)). There are several steps to implement this apparatus [7,8]:

First: Connect all the joints and check the testing system. The rigid tubing between three-way tap and sensor should fill with water in advance. If the occlusion alarm threshold can be selected, set it to minimum. Then, set the appropriate pump rate and volume, then start it.

Second: Open the three-way tap (stopcock) and let fluids flows into the collecting vessel. Close the three-way tap (stopcock) when the internal liquid flow becomes steady and test the occlusion pressure alarm threshold, this threshold will be registered by computer, then collect fluids, which generated by the expand of medical tubing.

Third: If the occlusion alarm threshold can be selected, repeat the test with the occlusion pressure set to maximum.

Pressure sensor is an important part in testing system, and the accuracy and precision of sensor are influenced by actual environment, such as temperature, relatively humidity. So to ensure the accuracy of the testing result, pressure calibration of the testing system is necessary before testing infusion pumps.

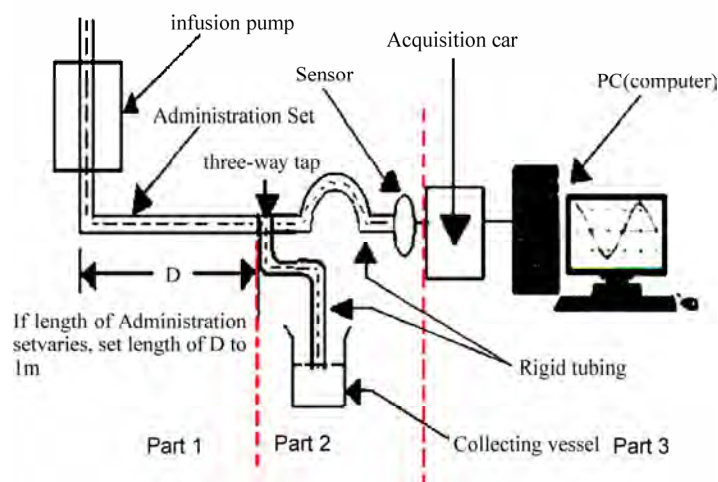


**Figure 1.** Structure of infusion pumps testing system.

**Table 1.** Relation between calibrator value and computer display value.

Calibrator display(KPa)	10.10	19.99	29.96	40.01	50.01	60.02	70.01	79.99	89.98	99.98
Computer display(V)	2.7309	2.9733	3.2176	3.4636	3.7087	3.9555	4.2012	4.4464	4.6906	4.9373
Results of expression(KPa)	10.13	19.99	29.92	39.96	49.95	60.01	70.01	80	89.96	99.99
error	0.03	0	0.04	0.05	0.06	0.01	0	0.01	0.02	0.01

Regarding to the Infusion Pump Analyzers mentioned before, the occlusion pressures are recorded once the pressure level is highest, at the same time the elapsed time is recorded [5,6]. In this testing system, the occlusion pressure and elapsed time are recorded, meanwhile, the delayed time, between the pressure reaches to the alarm threshold of infusion pump and the pump is not active, is recorded. The delayed time is also an important parameter though it is zero in some pumps. The real-time pressure wave could be displayed in monitor and could be reviewed and analyzed.

### 3. RESULTS

In this testing system, pressure calibrator of Fluke-718 30G was used, it can be used to calibrate pressure sensor and this testing system, its accuracy is  $\pm 0.05\%$  of range and resolution is 0.01KPa [9]. The performance of pressure sensor, under the same environment is summarized in **Table 1**. The unit of calibrator is KPa and computer display is V (voltage), computer display is the value of pressure signal, which has been magnified and filtered.

From the data results above, we can see that if the value of calibrator increases about 10KPa, the value of computer display increases about 0.24V correspondingly, so the performance of pressure sensor shows well linear.

Based on the relationship between calibrator value and computer display value, a line could be drawn. The relation between the display of computer and pressure calibrator is almost linear. The expressions were calculated with least squares approximation and they are:  $y = 40.732x - 101.11$  and  $y = -0.0392x^2 + 41.033x - 101.66$ , respectively. The sign  $x$  is computer display which is obtained from acquisition card and the sign  $y$  is the value of calibrator. Since the model is almost linear, the primary output is proportional to the input signal, so the first expression is enough in this system. In our testing system, the range of pressure is 0-200KPa and the accuracy of testing system is  $\pm 1\%$ , so the error is allowed basing on the linear expression.

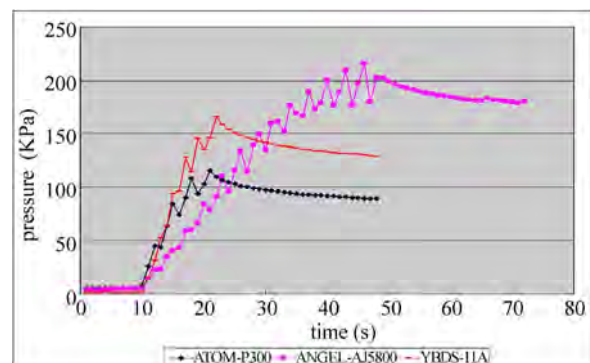
Three different infusion pumps (ANGEL-AJ5800, YBDS-11A, and ATOM-P300) were tested under the infusion rate of 250ml/h and sampling rate was 1Hz. The performance of infusion pumps is shown in **Figure 2**.

### 4. DISCUSSION AND CONCLUSIONS

The lines in **Figure 2** are test results of the pumps and these tests were implemented under normal environment. From these results, firstly, a peak pressure (occlusion pressure) can be found, peak pressure of ATOM-P300 infusion pump, ANGEL-AJ5800 infusion pump and YBDS-11A infusion pump was 114.80KPa, 215.80KPa, and 165.1KPa respectively. Secondly, occlusion time (the time from occlusion to occlusion alarm) was 12s, 38s and 12s, respectively.

The different occlusion pressures between infusions pumps could be seen from the test results. ATOM-P300 infusion pump has a pressure sensor and the precision is high; ANGEL-AJ5800 infusion pump has a higher occlusion pressure value. Pressure of YBDS-11A is neither high nor low. In order to ensure the safety of patients, low occlusion pressure and occlusion time are necessary and pressure sensor is the better choice in fusion pumps. The occlusion pressure of usual infusion pumps is about 100KPa, and some new made infusion pumps is about 7PSI (48.265KPa) or even more lower. Occlusion pressure alarm of ATOM-P300 infusion pump is lower than YBDS-11A infusion pump and ANGEL-AJ5800, ATOM-P300 infusion pump can prevent patient from hurting much sooner than the latter if an occlusion happens.

The sensor is influenced by environment, especially by temperature. In order to ensure the accuracy of the

**Figure 2.** Relation between time and pressure of different pumps.

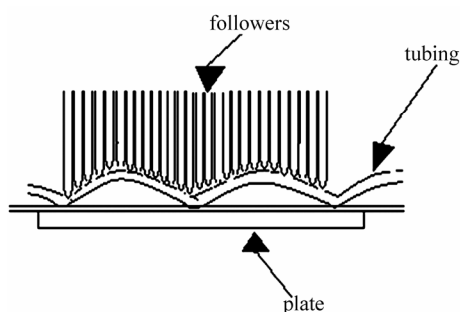


**Figure 3.** Structure of infusion pump.

test, calibration process should be implemented before performance, even in stable environment, calibration should be operated periodically.

Most infusion pumps are peristaltic, so the pressure is not stable. After a higher (lower) value, there is a lower (higher) value, as shown in **Figure 2**. That is determined by the structure of infusion pump, shown in **Figure 3**, so it is natural for the unstable pressure value.

We have mentioned that pressure curve of syringe pump is different to infusion pump; it is also determined by their structure.

In this study the infusion pump testing system is designed and its focus is detection of occlusion pressure. The results of infusion pump automatic detection system have verified that this method is efficient in different type of infusion pumps. The future research is concerned with these following topics.

1) Software should be perfect. The essential function could be achieved in present software, but many accessional functions should be achieved in the future. The

friendly interface is necessary and the manual operation should be decrease to ensure the accuracy of the testing system.

2) Although the occlusion pressures of infusion pumps were recorded, the delayed time should be recorded by testing system automatically, through analyzing the obtained data results.

3) The system is influenced by environment, such as temperature, relative humidity, so more tests should be implemented to come to a much better relation between system and environment, which can be a reference for further tests.

## REFERENCES

- [1] B. Pope and Z. Liu, (2008) Syringe pump steady state detection system, Europe: Patent 193,003,9A2.
- [2] H. Hwan-ing, L. Suan-ling, and Sian-wei T. Shani, (2002) Infusion technology: A cause for alarm, *Paediatric Anaesthesia*, **12**, 780–785.
- [3] L. Wilson, T. H. Burdick, and S. Chen, (1999) Automatic Infusion Pump Tester, U.S. Patent 5,943,633.
- [4] L. Strunin, (1983) Modern infusion pumps: Are they accurate, *Canadian Anaesthetists' Society Journal*, **30**, 655–659.
- [5] IDA-4 Plus Infusion Pump Analyzer Operators Manual.
- [6] Infutest Solo Infusion Pump Analyzer Operating Manual.
- [7] IEC 60601-2-24:1998, Medical electrical equipment-Part 2-24: Particular requirements for the safety of infusion pumps and controllers.
- [8] GB 9706.27-2005, Medical electrical equipment-Part 2-24: Particular requirements for the safety of infusion pumps and controllers.
- [9] Pressure Calibrator 718 Product.

# Design and development of a new biomedical/open surgical instrument

Zheng Li

University of Bridgeport, Bridgeport, USA  
Email: [zhengli@bridgeport.edu](mailto:zhengli@bridgeport.edu)

Received 19 May 2009; revised 30 May 2009; accepted 1 June 2009.

## ABSTRACT

This article introduces a new biomedical / open surgical instrument to assist surgeon in applying surgical clips to patient's body tissue and blood vessel during surgical processes. The new clip delivery system is designed to better the clip's distal advance through internal clip channel, jaw guiding track, and all other transition areas to keep surgical clip from accidental shooting out during clip's distal move into jaws. Currently the clip distal move in normal surgical instrument is usually driven by compression springs and some complains of clip accidental drop-off were recorded in surgical procedures. Because higher request of dimensional tolerance and better component surface quality are needed in case the compression springs are used as driven force, a little dimensional deviation or less qualified part surface produced from manufacturing processes will potentially cause surgical clip device malfunction or misfiring of the clips. It is clearly known that the jaws can seriously sever or damage patient's blood vessel or body tissue if there is no clip inside the jaws due to accidental clip drop-off, when surgeons close instrument handles. The improved internal system design in this new open surgical instrument can prevent clip from accidental drop-off because of well guided and controlled clip distal move through internal clip channel and track. Besides the operational force to fully form clip is lower than existing surgical clip devices due to better mechanical advantage in this new instrument design. In addition to the above, manufacturing and product cost can be decreased since lower requirement of dimensional tolerance and surface quality of instrumental parts is allowed in this new surgical instrument design. This new instrumental prototype is build upon the analysis of computer aided modeling

and simulation to prove its good mechanical advantage, feasible function, reliable performance. The preliminary results of instrument firing force from both computer aided modeling and prototype testing are very close to each other, and preliminary prototype testing shows no accidental clip drop-off in this new biomedical / surgical clip instrument.

**Keywords:** Blood Vessel; Body Tissue; Ligation; Computational Modeling; Mechanical Advantage

## 1. INTRODUCTION

It is critical for surgeons to apply surgical clip instrument to the severed organs, blood vessels and body tissues to stop bleeding in surgical procedure [1,2,3]. The surgical clip instrument jaws should be put around patent blood vessel or body tissue and clips can be closed to secure the vessel and tissue to prevent them from bleeding when surgeon bring instrument handles together. Next surgical clip will be automatically driven into instrument jaws through internal clip channel when surgeons release instrument handles.

The surgical devices to apply clips onto blood vessel and body tissue have been developed for many years [4, 5,6]. It includes single clip and multiple clip applications [7,8,9]. Next clip can be loaded into instrument after firing each clip in single clip applications and multiple clips can be sequentially applied to the vessel or tissue in multiple clip applications. The surgical clip devices usually have two handles, a master body, a clip loading and crimping assembly, clip driving mechanism and some other functioning components such as clip pusher and jaws. The improvement for better clip advancement and lower cost instrument is continued to develop more reliable, better functional and cost-effective clip instruments to support surgeons in their surgical processes.

Some complains were previously recorded from clinic fields showing several incidents of accidental clip shooting out from jaws while clip was driven into jaws



in clip instruments using compression springs as driving force. These incidents showed that the closed jaws will potentially sever or damage blood vessel or body tissue if there is no clip in jaws. The accidental clip drop-off is mainly caused by improper control of dimensional tolerance when manufacture the instrumental components. The surgical instruments in which surgical clips were driven by compression spring require higher dimensional tolerance control and better surface quality during component manufacturing and this will lead a low volume and high cost instrumental production, otherwise the clips will drop-off or shooting out if dimensional tolerance are too loose or clips will jam or not move by spring force if dimensions are too tight.

This new instrument design has different clip delivery system compared with current clip instruments. The distal movement of clip pusher driven by instrument handles gradually advances clip from clip magazine, through clip channel and transition area between clip channel and jaws, and finally form clip after clip being driven into guide track in jaws. The clip pusher returns proximally to its original start position when surgeons release instrument handles and then readily picks up next clip. Since the internal clip delivery can be easily and well controlled through simple lever-linkage driving system in this new design, the accurate dimensional tolerance control and higher surface quality are not required during production and manufacturing processes of instrumental components. This can lead cost-effective machining process, increase production volume, and reduce production cost. The preliminary prototype testing also indicates that there is no accidental clip shooting out in this new instrument design and operational force to fully form clip is lower than current surgical clip instruments.

This new instrumental prototype testing has been conducted on dogs including vascular occlusion, ligating for tubular ducts, and applying surgical clip to animal tissue. In vitro and in vivo studies were conducted to investigate the clip holding force, degradation rate, and tissue reactivity for clips of titanium material. The clips were applied across excised canine cystic ducts by this new instrument and both axial and transverse pull-off forces have been recorded and measured. In the next phase, the titanium clips were implanted subcutaneously into the animals and the remaining strength within the clips has been measured after 1, 3, 5, 7, 9, 11, 13, or 21 days. The preliminary results show that the clips applied by this new surgical instrument function properly.

The preliminary testing results also indicated that there is no clip shooting out in this surgical instrument design and the operating force to fully form the clip is between 3.16 lbf and 3.30 lbf which are lower than 4 lbf in existing surgical instrument.

## 2. ANALYSIS OF NEW SURGICAL CLIP INSTRUMENT

The prototype, instrument front and rear portion views of this new surgical instrument are indicated in **Figure 1-3**. First the instrument will be put around patient blood vessel or body tissue. When surgeons start and gradually close instrument handles, clip driven by clip pusher advances distally from clip magazine through internal track and channel into jaws and finally secured blood vessel or body tissue. The instrument jaws can be open as surgeons release instrument handles, and clip pusher and driving bar return to its original start positions. Compared with current instrument that clip delivery is driven by compression spring, the clip being loaded into jaws is well guided and controlled in this new instrument design. The driving bar linked to instrument handles at pivot point moves distally to drive clip pusher that advances clip steadily into jaws as surgeons gradually close surgical instrument handles. Such a stable clip linear motion in this new design can be easily and well controlled by surgeons to prevent clip from accidentally shooting out from instrument. The preliminary prototype testing of

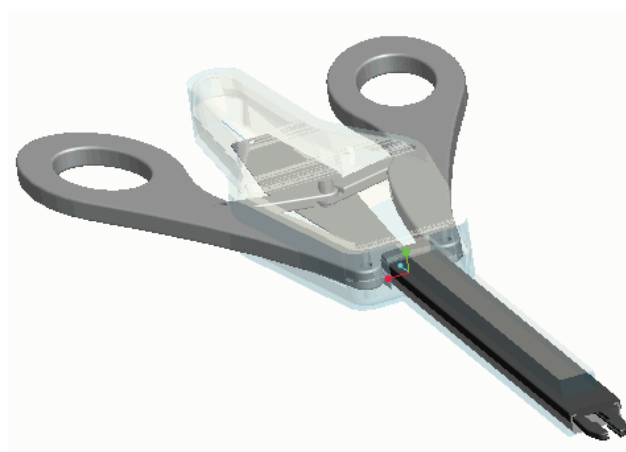


**Figure 1.** Prototype of new surgical instrument.

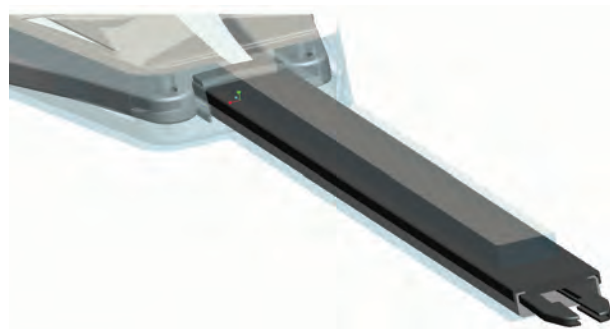


**Figure 2.** Front portion view of new surgical instrument.



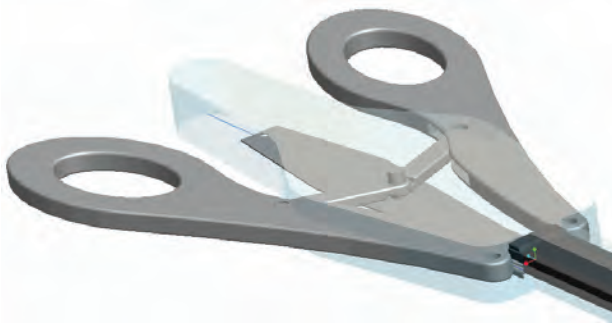


**Figure 3.** Rear portion view of new surgical instrument.

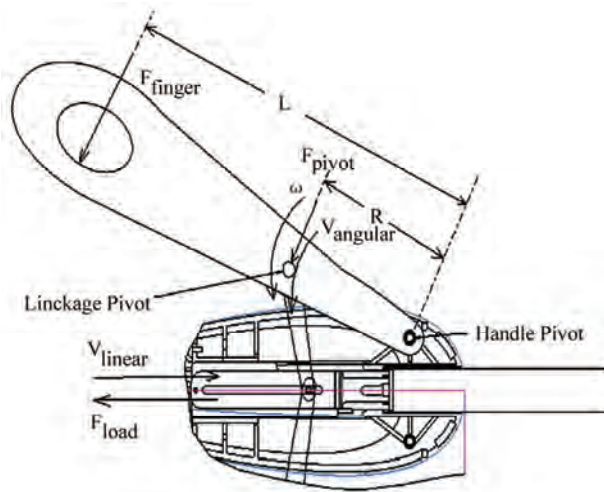


**Figure 4.** Force analysis diagram in instrument.

this new design indicated its proper and reliable performances with no clip shooting out and lower operational force than usual to form surgical clips.

### 3. COMPUTATIONAL MODELING AND ANALYSIS

Referring **Figure 4**, the energy balance and force equations in this new surgical instrument design can be derived as follows.

$$F_{load} * V_{linear} = T * \omega \quad (1)$$

Because torque  $T = F_{pivot} * R$ ,

$$T * \omega = F_{pivot} * R * \omega = F_{pivot} * V_{angular} \quad (2)$$

Then

$$F_{load} * V_{linear} = F_{pivot} * V_{angular} \quad (3)$$

$$F_{load} = (V_{angular} / V_{linear}) * F_{pivot} = (VR) * F_{pivot} \quad (4)$$

Referring the force diagram of this instrument handle in **Figure 4**:

$$F_{finger} * L = F_{pivot} * R \quad (5)$$

The different  $F_{finger}$  can be determined with different combination of  $L$  and  $R$ . The computational simulation

can find the optimized values of  $L$  and  $R$  to reduce the operational force to fully form clip. The computer aided solution suggested  $L = 4.85$  inch and  $R = 2.20$  inch for best instrument performance.

Based on **Eq.5**,

$$F_{finger} * 4.85 = F_{pivot} * 2.20$$

$$F_{pivot} = 2.20 * F_{finger}$$

Referring **Eq.4**,

$$F_{load} = (VR) * F_{pivot} = (VR) * 2.20 * F_{finger} \quad (6)$$

The velocity ratio of  $(V_{angular} / V_{linear})$  can be determined by computer aided simulation targeting optimized instrument performance, and simulation results are shown in **Figure 5**.

The mechanical advantage of this new instrument can be found when surgical clip is fully formed:

$$\text{Mechanical advantage} = (VR) * 2.20 \quad (7)$$

$$= (.04940 / .03548) * .20 = 3.063$$

This result shows that, if 20 lbf forces are required to fully form the surgical clip, the operational force that surgeon needed is 3.265 lbf that is lower than normal spec of 4 lbf and this will benefit surgeons in their surgical procedure. Also, both computational simulation and prototype testing results are very close which verify and prove the credibility of this new instrument design and research methodology.

### 4. CONCLUSIONS

The prototype of this new surgical clip instrument has been proved to have feasible function and better performance based on instrumental functional study, computer aided modeling and solution, and preliminary prototype testing. This new instrument design has several

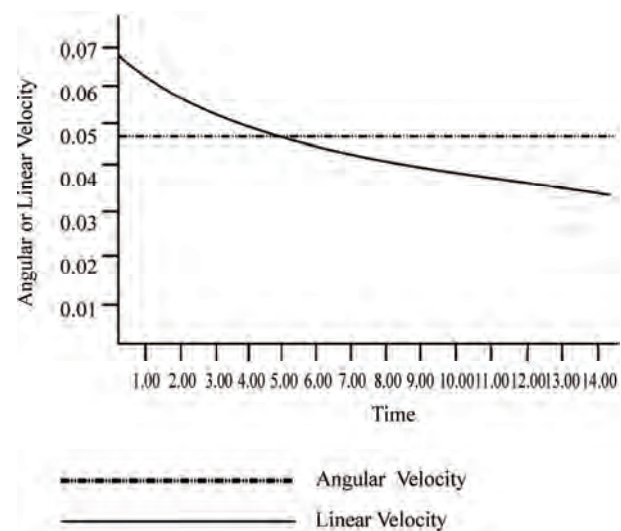


**Figure 5.** Linear and angular velocity vs. time phase in operating the instrument.

major advantages compared with some current surgical clip devices including: the clip's distal move can be properly guided and controlled to prevent patient's blood vessel and body tissue from damage that caused by accidental clip shooting out during surgical processes, operational force to form clip is lower than usual surgical clip instruments, instrument production and product cost can be decreased since loose dimensional tolerance and low surface quality of instrumental components are allowed in this new design. The prototype testing has been conducted in lab and the preliminary result has shown the potential improvement over some current instruments including reliable performance without accidental clip drop-off, reduced operational force to form clip, and lower product cost. While the prototype this new instrument is being sent to fields for more clinical trials and evaluations, further analysis and improvement will be conducted including adding support to enhance jaw pair structure to prevent jaws from twisting when unexpected torque load exerted to the instrument due to improper usage in surgical procedure, adding enhancing structure to prevent jaws from accidental close when unanticipated side load exerted to instrument jaws, simplifying the instrument design to further reduce the product cost.

## REFERENCES

- [1] H. J. Lin, W. C. Lo, Y. C. Cheng, and C. L. Peng, (2007) Endoscopic hemoclip versus triclep placement in patients with high risk peptic ulcer bleeding, *Journal of Gastroenterol*, **102**, 539–543.
- [2] D. Chan, J. Bishoff, I. Ratner, L. Kavoussi, and T. Jarrett, (2000) Endovascular gastrointestinal stapler device malfunction during laparoscopic nephrectomy: Early recognition and management, *Journal of Urology*, **164**(2), 319–321.
- [3] J. Hermiller, C. Simonton, T. Hinohara, and D. Lee, (2005) Clinical experience with a circumferential clip-based vascular closure device in diagnostic catheterization, *Journal of Invasive Cardiology*, **17**, 154–157.
- [4] J. Piatt, B. Starly, E. Faerber, and W. Sun, (2006) Application of computer-aided design methods in craniofacial reconstructive surgery using a commercial image-guidance system, *Journal of Neurosurgery*, **104**(1 Suppl), 64–67.
- [5] A. W. Cheng, P. W. Chiu, P. C. Chan, and S. H. Lam, (2004) Endoscopic hemostasis for bleeding gastric stromal tumors by application of hemoclip, *Journal of Laparoendoscopic & Advanced Surgical Techniques*, **14**, 169–171.
- [6] B. Starly, Z. Fang, W. Sun, and W. Regli, (2005) Three-dimensional reconstruction for medical-CAD modeling, *Journal of Computer-Aided Design and Application*, **2**(1–4), 431–438.
- [7] P. Evans, B. Starly, and W. Sun, (2006) Computer-aided tissue engineering for design and evaluation of lumbar-spine arthroplasty, *Journal of Computer-Aided Design and Application*, **3**(6), 771–778.
- [8] W. Sun, B. Starly, J. Nam, and A. Darling, (2005) Bio-CAD modeling and its application in computer-aided tissue engineering, *Computer-Aided Design*, **37**(11), 1097–1114.
- [9] F. C. Chu and B. C. Chang, (2005) Automatic visual tracking control system using embedded computers, *Proceeding of the 2005 IEEE International Conference on Mechatronics*, July 10–12, 2005.

## APPENDIX

### Nomenclature

T – inch-lbf, torque on pivot point of handle  
 $F_{load}$  – lbf, force required to close jaws to form clip  
 L – inch, distance between handle pivot point and surgeon's finger position  
 $F_{pivot}$  – lbf, load on linkage pivot  
 $\omega$  – degree per second, angular speed of handle at pivot point

$F_{finger}$  – lbf, load on surgeon's finger  
 $V_{linear}$  – inch per second, linear distal moving velocity of instrument drive bar  
 (VR) – velocity ratio  
 R – inch, distance between handle pivot and linkage pivot

# Wavelet based detection of ventricular arrhythmias with neural network classifier

Sankara Subramanian Arumugam<sup>1</sup>, Gurusamy Gurusamy<sup>2</sup>, Selvakumar Gopalasamy<sup>3</sup>

<sup>1</sup>Department of Electrical and Electronics Engineering, NPA Centenary Polytechnic College, Kothagiri, Tamilnadu, India;

<sup>2</sup>Department of Electrical and Electronics Engineering, Bannariamman Institute of Technology, Sathyamangalam, Tamilnadu, India;

<sup>3</sup>Department of Electrical Sciences, Vinayaka Mission's Kirupananda Variyar Engineering College, Salem, Tamilnadu, India.

Email: [sankar\\_aru@yahoo.com](mailto:sankar_aru@yahoo.com); [ngselva\\_kumar@yahoo.com](mailto:ngselva_kumar@yahoo.com)

Received 29 August 2009; revised 10 September 2009; accepted 15 September 2009.

## ABSTRACT

**This paper presents an algorithm based on the wavelet decomposition, for feature extraction from the Electrocardiogram (ECG) signal and recognition of three types of Ventricular Arrhythmias using neural networks. A set of Discrete Wavelet Transform (DWT) coefficients, which contain the maximum information about the arrhythmias, is selected from the wavelet decomposition. These coefficients are fed to the feed forward neural network which classifies the arrhythmias. The algorithm is applied on the ECG registrations from the MIT-BIH arrhythmia and malignant ventricular arrhythmia databases. We applied Daubechies 4 wavelet in our algorithm. The wavelet decomposition enabled us to perform the task efficiently and produced reliable results.**

**Keywords:** Daubechies 4 Wavelet; ECG; Feed Forward Neural Network; Ventricular Arrhythmias; Wavelet Decomposition

## 1. INTRODUCTION

The cardiac disorders which are life threatening are the ventricular arrhythmias such as Ventricular Tachycardia (VT), Ventricular Fibrillation (VFIB) and Ventricular Flutter (VFL). The classification of ECG into these different pathological disease categories is a complex task.

Successful classification is achieved by finding the characteristic shapes of the ECG that discriminate effectively between the required diagnostic categories. Conventionally, a typical heart beat is identified from the ECG and the component waves of the QRS, T and P waves are characterized using measurements such as magnitude, duration and area (**Figure 1**).

In an arrhythmia monitoring system or a defibrillator, it is important that the algorithm for detecting ECG ab-

normalities should be reliable. The patient will be losing a chance of treatment if the system is not able to detect the arrhythmia. Also a false positive detection will initiate a defibrillator to give improper therapeutic intervention. Both situations are linked with the patient's life.

An algorithm based on Wavelet Transform is quite efficient for the detection of ventricular arrhythmias compared to the Discrete Fourier Transform (DFT) since it permits analyzing a discrete time signal using frequency components. The DWT has been used for analyzing, decomposing and compressing the ECG signals [1].

The wavelet transforms make possible, the decomposition of a signal into a set of different signals of restricted frequency bands. Wavelet processing can be considered as a set of band pass filters [2]. Moreover, the discrete wavelet transform corresponds to a multiresolution analysis [3] which can reduce the redundancy of each filtered signal so that the processing algorithm can be applied effectively to a small data subset of the original signal [4,5,6,7,8,9].

A classification scheme is developed in which a feed forward neural network is used as a classification tool depending on the distinctive frequency bands of each arrhythmia. The Back Propagation (BP) algorithm allows experiential acquisition of input/output mapping

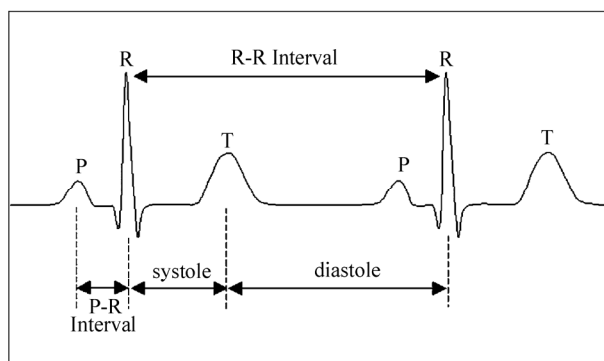


**Figure 1.** Normal ECG waveform.

knowledge within multi-layer networks [10]. BP performs the gradient descent search to reduce the mean square error between the actual output of the network and the desired output through the adjustment of the weights. It is highly accurate for most classification problems because of the property of the generalized data rule. In the traditional BP training, the weights are adapted using a recursive algorithm starting at the output nodes and working back to the first hidden layer.

In our study, an algorithm is implemented to detect and classify Ventricular Tachycardia (VT), Ventricular Fibrillation (VFIB) and Ventricular Flutter (VFL) using wavelet decomposition and neural classification.

The ECG registrations from MIT-BIH arrhythmia and malignant ventricular arrhythmia databases are used here. The analysis is done using Daubechies 4 wavelet.

## 2. VENTRICULAR ARRHYTHMIA

Arrhythmias are the abnormal rhythms of the heart. They cause the heart to pump the blood less effectively. Most cardiac arrhythmias are temporary and benign. The ventricular arrhythmias are life threatening and need treatment. Such ventricular arrhythmias are Ventricular Tachycardia, Supraventricular Tachycardia, Ventricular Fibrillation and Ventricular Flutter.

VT is a difficult clinical problem for the physicians (Figure 2). Its evaluation and treatment are complicated because it often occurs in life-threatening situations that dictate rapid diagnosis and treatment. Ventricular tachycardia is defined as three or more beats of ventricular origin in succession at a rate greater than 100 beats/minute. There are no normal-looking QRS complexes. Because ventricular tachycardia originates in the ventricle, the QRS complexes on the electrocardiogram are widened ( $>0.12$  seconds). Ventricular tachycardia has the potential of degrading to the more serious ventricular fibrillation.

VFIB is a condition in which the heart's electrical activity becomes disordered (Figure 3). During Ventricular

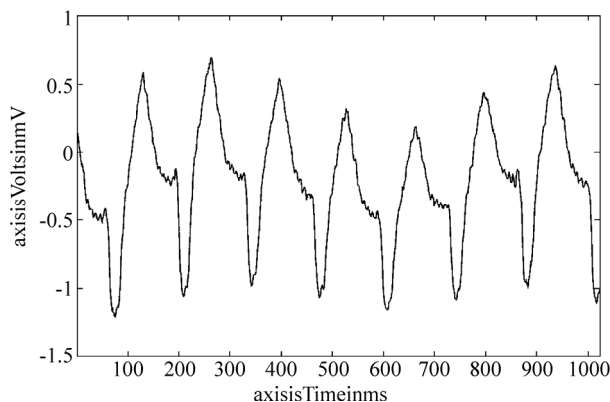


Figure 2. ECG waveform with VT.

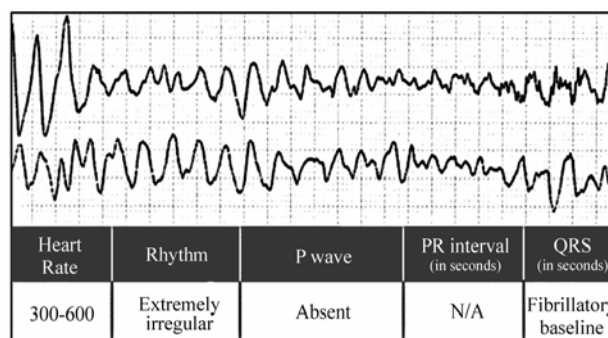


Figure 3. Ventricular fibrillation.

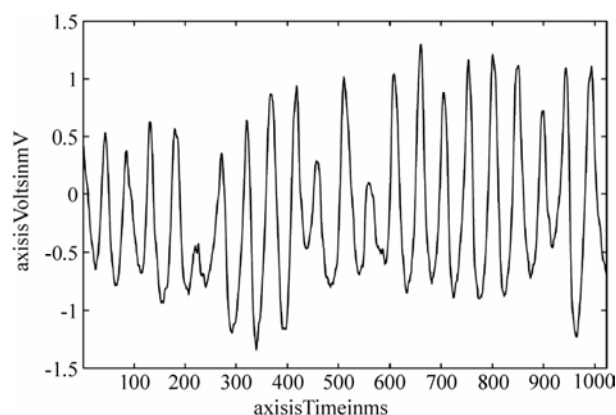


Figure 4. Ventricular flutter.

fibrillation, the heart's ventricles contract in a rapid and unsynchronized way. It is a medical emergency. If this condition continues for more than a few seconds, blood circulation will cease, as evidenced by lack of pulse, blood pressure and respiration, and death will occur [11].

VFL is a tachyarrhythmia characterized by a high ventricular rate with a regular rhythm (Figure 4). The ECG shows large sine wave-like complexes that oscillate in a regular pattern. There is no visible P wave. QRS complex and T wave are merged in regularly occurring undulatory waves with a frequency between 180 and 250 beats per minute. In severe cardiac or systemic disease states, ventricular tachycardia can progress to ventricular flutter, then to ventricular fibrillation.

## 3. COMPARISON OF EXISTING ALGORITHMS

Computer based detection and classification algorithms can achieve good reliability, high degree of accuracy and offer the potential of affordable mass screening for cardiac abnormalities.

Till now, many linear techniques for the detection of ventricular arrhythmias have been developed, such as the probability density function method [12], rate and irregularity analysis, analysis of peaks in the short-term



autocorrelation function [13], sequential hypothesis testing algorithm [14], correlation waveform analysis, four fast template matching algorithms, VF-filter method [15, 16], spectral analysis [17], and time-frequency analysis [18]. However, these methods exhibit disadvantages, some being too difficult to implement and compute for automated external defibrillators (AED's) and implantable cardioverter defibrillators (ICD's), and some only successful in limited cases. For example, the linear techniques [13,18] using the features of amplitude or frequency have shown their limits, since the amplitude of ECG signal decreases as the VFIB duration increases, and the frequency distribution changes with prolonged VFIB duration.

The VF filter method relies on approximating the VFIB signal as a sinusoidal waveform. The method is equivalent to using a bandpass filter, the central frequency of which is the mean signal frequency. The spectral analysis technique relies on the fact that the VFIB frequency contents are concentrated in the bandwidth 4-7Hz [13]. The increased power in this band of frequencies is the major indication of the presence of VFIB. The above spectral analysis technique is applied to stationary signals. However, abrupt changes in the non-stationary ECG signal are spread over the whole frequency range. Important time varying statistical characteristics are lost once the signal has been Fourier transformed.

In recent years time-frequency analysis techniques have proved to be useful in experimental and clinical cardiology. These techniques are needed to fully describe and characterize the various ventricular arrhythmias and facilitate the development of new detection schemes with high correct detection rate, or equivalently, with low false-positive and false-negative performance statistics. The wavelet transforms make possible, the decomposition of a signal into a set of different signals of restricted frequency bands. Wavelet processing can be considered as a set of band pass filters [15]. Moreover, the discrete wavelet transform corresponds to a multi-resolution analysis [12] which can reduce the redundancy of each filtered signal so that the processing algorithm can be applied effectively to a small data subset of the original signal.

A classification scheme is developed in which a feed forward neural network is used as a classification tool depending on the distinctive frequency bands of each arrhythmia. The algorithm is applied to ECG signals with ventricular arrhythmia disorders.

#### 4. WAVELET DECOMPOSITION

The wavelet transform is a mathematical tool for decomposing a signal into a set of orthogonal waveforms localized both in time and frequency domains. The de-

composition produces coefficients, which are functions of the scale (of the wavelet function) and position (shift across the signal).

A wavelet which is limited in time and frequency is called "mother wavelet". Scaling and translation of the mother wavelet gives a family of basis functions called "daughter wavelets".

The wavelet transform of a time signal at any scale is the convolution of the signal and a time-scaled daughter wavelet. Scaling and translation of the mother wavelet is a mechanism by which the transform adapts to the spectral and temporal changes in the signal being analyzed.

The continuous wavelet transform for the signal  $x(t)$  is defined as:

$$W(a, b) = \frac{1}{\sqrt{|a|}} \int_{-\infty}^{\infty} x(t) \psi^* \left( \frac{t-b}{a} \right) dt \quad (1)$$

where  $a$  and  $b$  are the dilation (scaling) and translation parameters, respectively. A wide variety of functions can be chosen as mother wavelet  $\psi$ , provided  $\psi(t) \in L^2$  and

$$\int_{-\infty}^{\infty} \psi(t) dt = 0 \quad (2)$$

The DWT makes possible the decomposition of ECG at various scales into its time-frequency components. In DWT two filters, a Low Pass Filter (LPF) and a High Pass Filter (HPF) are used for the decomposition of ECG at different scales. Each filtered signal is down sampled to reduce the length of the component signals by a factor of two. The output coefficients of LPF are called the Approximation while the output coefficients of HPF are called the Detail. The approximation signal can be sent again to the LPF and HPF of the next level for second level of decomposition; thus we can decompose the signal into its different components at different scale levels.

**Figure 5** shows the decomposition process of a signal into many levels. The details of all levels and the approximation of the last level are saved so that the original signal could be reconstructed by the complementary filters. The reconstructed signals at each level are represented by the notations D1, D2, D3 and so on.

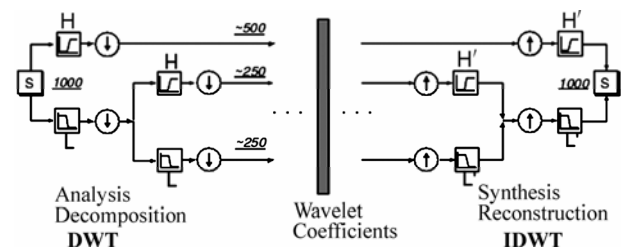


**Figure 5.** Wavelet decomposition and reconstruction.



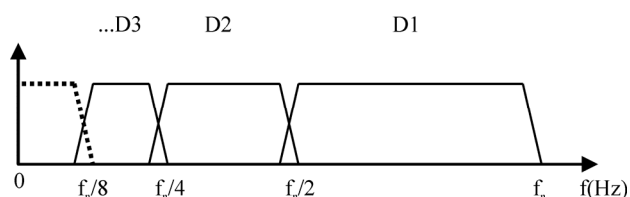


**Figure 6.** Ideal frequency bands for the various details.

**Figure 6** shows the ideal frequency bands for a sampling frequency of 360 samples/second. Depending on the scaling function and the mother wavelet, the actual frequency bands and consequent frequency selectivity of the details are slightly different.

## 5. METHODOLOGY

In this section we present the algorithm which efficiently detects and classifies the various ventricular arrhythmias using wavelet decomposition and neural classification.

### 5.1. Description of the Algorithm

The algorithm first decomposes the ECG signals using wavelet transform. The decomposed signals are fed to the feed forward neural network. The wavelet theory is used as a time-frequency representation technique to provide a method for enhancing the detection of life threatening arrhythmias. It reveals some interesting characteristic features such as low frequency band (0-5 Hz) for VFL, two distinct frequency bands (2-5, 6-8 Hz) for VT, and a broad band (2-10 Hz) for VFIB.

A classification scheme is developed in which a neural network is used as a classification tool depending on the above distinctive frequency bands of each arrhythmia.

The algorithm is applied to ECG signals obtained from patients suffering from the arrhythmias, mentioned above.

### 5.2. ECG Analysis Using Wavelet Decomposition

To quantify the differences between the various arrhythmias with the help of the wavelet transform, the densities for different frequency bands are compared. The wavelet transform is performed using Daubechies 4 wavelet since it provides better sensitivity [19].

The algorithm computes the volume underneath the 3D plots of the square modulus of the wavelet transform for several regions of the time-frequency plane. The time-frequency plane is divided into seven bands ranging from 0 to 15 Hz. For sinus rhythm the energy is calculated within the time intervals  $T_1$  and  $T_2$  integrated over the whole frequency axis. The time interval  $T_1$  is determined by the region of QRS complex, and the time interval  $T_2$  is determined by the region of the T-wave.

As the wavelet transform is very sensitive to abrupt changes in the time direction, the energy parameter over the given time intervals attains relatively large values for normal subjects. This parameter is referred to as  $T_v$  and it defines the sum of the energy parameters computed within the intervals  $T_1$  and  $T_2$ . Although the signals of VFL and VT exhibit a QRS-complex, the parameter value  $T_2$  for these signals remains relatively small, owing to the absence of abrupt changes in the region of the T-wave. Therefore, the value of  $T_v$  will still be smaller than that of the normal subjects.

The 2D and 3D wavelet transform contours of Normal Sinus Rhythm (NSR), VT and VFL are shown in **Figure 7**.

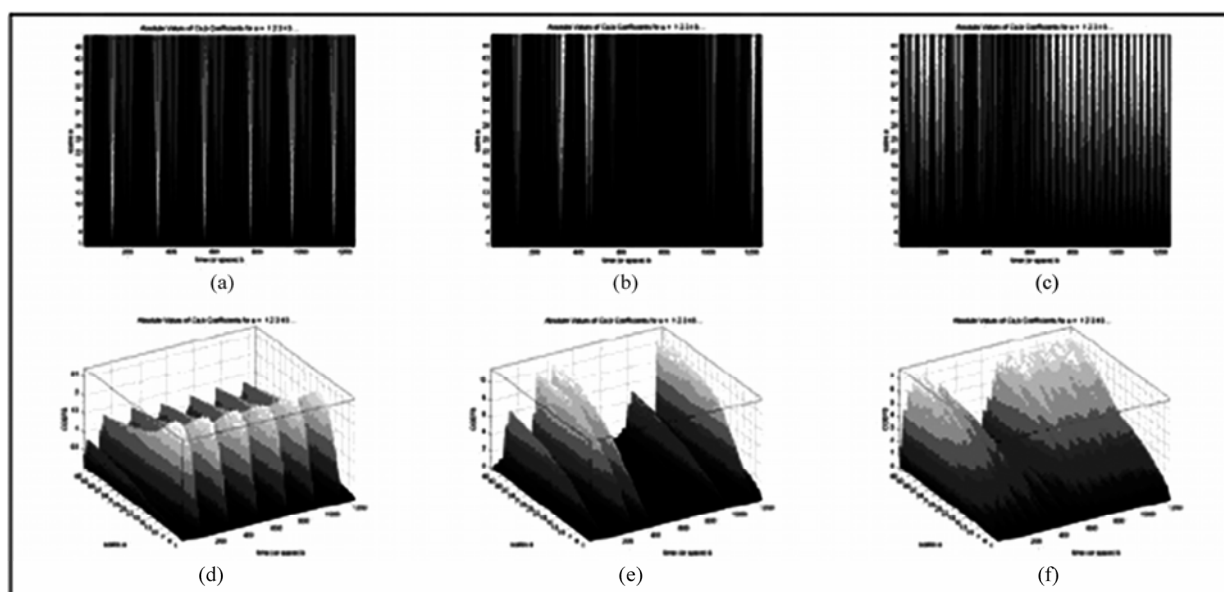


**Figure 7.** (a) 2D wavelet of NSR, (b) 2D wavelet of VT, (c) 2D wavelet of VFL, (d) 3D wavelet of NSR, (e) 3D wavelet of VT and (f) 3D wavelet of VFL.

### 5.3. Classification of Ventricular Arrhythmias Using Neural Network

There are quite lot of network topologies with powerful learning strategies which exist to solve nonlinear problems [20,21,22,23]. For the classification of Ventricular Arrhythmias, back propagation with momentum is used to train the feed forward neural network [24].

A multilayer feed forward neural network with one layer of hidden (Z) units is used for this problem. The output (Y) units have weights  $w_{jk}$  and the hidden units have weights  $v_{jk}$ . During the training phase, each output neuron compares its computed activation  $y_k$  with its target value  $d_k$  to determine the associated Error (E) by using (3) for the pattern with that neuron.

$$E = \sum_{k=1}^m (d_k - y_k)^2 \quad (3)$$

The weights and biases of the Artificial Neural Network (ANN) are adjusted to minimize the least-square error. The minimization problem is solved by gradient technique, the partial derivatives of E with respect to weights and biases are calculated using the generalized delta rule. This is achieved by the back propagation of the error.

When using momentum, the neural network is proceeding not in the direction of the gradient, but in the direction of the combination of the current gradient and the previous direction of weight correction. Convergence is sometimes faster if a momentum term is added to the weight update formula. In the back propagation with momentum, the weights for the training step  $t+1$  are based on the weights at training steps  $t$  and  $t-1$ . The weight update formulae for back propagation with momentum are given by (4)

$$\begin{aligned} w_{jk}(t+1) &= w_{jk}(t) + \alpha \delta_k z_j + \mu [w_{jk}(t) - w_{jk}(t-1)] \\ v_{ij}(t+1) &= v_{ij}(t) + \alpha \delta_j x_i + \mu [v_{ij}(t) - v_{ij}(t-1)] \end{aligned} \quad (4)$$

where the learning factor  $\alpha$  and momentum parameter  $\mu$  are constrained to be in the range 0 to 1, exclusive of the end points. The weights and biases are initialized to some random values and updated in each iteration until the network has settled down to a minimum.

The classification of the VT, VFIB and VFL arrhythmia is carried out using a Back-propagation neural network whose input is the energy level calculated by the wavelet transform as described above, the output is a three bit pattern, in which 100 corresponds to VFL, and 010 corresponds to VT, and 001 corresponds to VFIB.

The network has three layers: The input, the output and one hidden layer. The input layer has seven nodes representing the seven different frequency bands from 0-15 Hz. The output layer has three nodes that represent the three different types of arrhythmia signals VFL, VT

and VFIB. The hidden layer consists of six nodes for effective size of the network and acceptable efficiency. The learning rate and the momentum term are chosen to be 0.7 and 0.3 respectively.

### 5.4. Data

The MIT-BIH arrhythmia and malignant ventricular arrhythmia databases were used for the analysis [25]. The VT episodes from the records 200, 203, 205, 207, 208, 210, 213, 214, 215, 217, 221, 223, 233, 106 etc were taken from the MIT-BIH arrhythmia database. VFIB and VFL episodes were from MIT-BIH malignant ventricular arrhythmia database from the records 418 – 430, 602, 605, 607, 609, 610, 611, 612, 614, 615 and cu01 – cu35. The data files from arrhythmia database and malignant ventricular arrhythmia database were sampled at 360 samples / second.

## 6. RESULTS AND CONCLUSIONS

Twenty-five signals of VT, ten signals of VFL and five signals of VFIB are used for training. The learning process took approximately 1000 iterations to converge with classification error of 0.001. Thirty signals of VT, fifteen signals of VFL and four signals of VFIB are selected as test set. For decomposition of ECG signal Daubechies 4 wavelet is used.

In medical statistics, few parameters are important to evaluate the performance of the algorithm. These parameters are sensitivity (Se) and positive predictivity (+P) which can be computed using (5) and (6).

$$Se = \frac{TP}{TP + FN} \quad (5)$$

$$+P = \frac{TP}{TP + FP} \quad (6)$$

where TP is True Positive, FP is False Positive and FN is False Negative.

Classification results of testing data sets using Feed Forward Neural Network with BP are shown in **Table 1**. Sensitivity and Positive predictivity for the various ventricular arrhythmias are shown in **Table 2**. The results show that the BP algorithm is reliable in the classification of all the three types of ventricular arrhythmias.

**Table 1.** A comparison between the actual and detected ventricular arrhythmias in terms of the number of patterns.

Actual Ventricular Arrhythmia	Detected Ventricular Arrhythmia			Total
	VT	VFL	VFIB	
VT	30	0	0	30
VFL	1	13	1	15
VFIB	0	0	4	4

**Table 2.** Sensitivity and positive predictivity for the testing set.

Ventricular Arrhythmia	TP	FP	FN	Positive Predictivity (%)	Sensitivity (%)
VT	30	1	0	96.77	100
VFL	13	0	2	100	86.67
VFIB	4	1	0	80	100

**Table 1** shows that the BP network misclassified the proper arrhythmia in some cases, one VFL case was classified as VFIB, this is because the energy level in the frequency bands is high and common between VFL and VFIB. The algorithm is able to classify VT and VFIB with 100% sensitivity. The positive predictivity for VFL episodes is 100%. The algorithm is reliable by providing the overall sensitivity of 95.56% and the overall positive predictivity of 92.26%. The algorithm can be validated using more number of ECG samples.

## REFERENCES

- [1] K. Anant, F. Dowla, and G. Rodrigue, (1995) Vector quantization of ECG wavelet coefficients, *IEEE Signal Processing Letters*, **2**(7).
- [2] M. Vetterli, (1992) Wavelets and filter banks: Theory and design, *IEEE Transactions on Signal Processing*, 2207–2232.
- [3] R. M. Rao and A. S. Bopardikar, (1998) Wavelet transforms: Introduction to theory and applications, Addison Wesley Longman.
- [4] L. Khadra, A. S. Al-Fahoum, and H. Al-Nashash, (1997) Detection of life threatening cardiac arrhythmia using the wavelet transformation, *Med. Biol. Eng. Comput.*, **35**, 626–632.
- [5] P. S. Addison, J. N. Watson, G. R. Clegg, M. Holzer, F. Sterz, and C. E. Robertson, (2000) Evaluating arrhythmias in ECG signals using wavelet transforms, *IEEE Engineering in Medicine and Biology Magazine*, **19**, 104–109.
- [6] H. A. N. Dinh, D. K. Kumar, N. D. Pah, and P. Burton, (2001) Wavelets for QRS detection, *Proceedings of the 23<sup>rd</sup> Annual Conference, IEEE EMS, Istanbul, Turkey*, 35–38.
- [7] S. Kadambe, R. Murray, and G. F. Boudreaux-Bartels, (1999) Wavelet transform based QRS complex detector, *IEEE Transaction on Biomedical Engineering*, **46**(7), 838–848.
- [8] I. Romero, L. Serrano, and Ayesta, (2001) ECG frequency domain features extraction: A new characteristic for arrhythmias classification, *Conference of the IEEE Engineering in Medicine and Biology Society*.
- [9] S. M. Szilagyi and L. Szilagyi, (2000) Wavelet transform and neural network based adaptive filtering for QRS detection, *Proceedings of World Congress on Medical Physics and Biomedical Engineering, Chicago, USA*.
- [10] D. E. Rumelhart, G. E. Hinton, and R. J. Williams, (1986) Learning representations by back-propagation errors, *Nature*.
- [11] V. X. Afonso and W. J. Tompkins, (1995) Detecting ventricular fibrillation, *IEEE Eng. Boil.*, 152–159.
- [12] A. Langer, M. S. Heilman, and M. M. Mower, (1976) Considerations in the development of the automatic implantable defibrillator, *Medical Instrumentation*, **10**(3), 163–167.
- [13] S. Chen, N. V. Thakor, and M. M. Mover, Ventricular fibrillation detection by a regression test on the autocorrelation function, *Med. Biol. Eng. Comput.*, **25**(3), 241–249.
- [14] S. W. Chen, P. W. Clarkson, and Q. Fan, (1996) A robust detection algorithm for cardiac arrhythmia classification, *IEEE Transactions on Biomedical Engineering*, **43**, 1120–1125.
- [15] R. H. Clayton, A. Murray, and R. W. F. Campbell, (1994) Recognition of ventricular fibrillation using neural networks, *Med. Bio. Eng. Comp.*, **32**, 217–220.
- [16] S. Kuo and R. Dillman, (1978) Computer detection of ventricular fibrillation, *Computer Cardiology*, 347–349.
- [17] S. Barro, R. Ruiz, D. Cabello, and J. Mira, (1989) Algorithmic sequential decision-making in the frequency domain for life threatening ventricular arrhythmias and imitative artifacts: A diagnostic system, *Journal on Biomedical Engineering*, **11**(4), 320–328.
- [18] V. X. Afonso, W. J. Tompkins, T. Q. Nguyen, and S. Luo, (1999) ECG beat detection using filter banks, *IEEE Transactions on Biomedical Engineering*, **46**(2), 192–202.
- [19] G. Selvakumar, B. K. Bhoopathy, and R. B. Chidhambara, (2007) Wavelet decomposition for detection and classification of critical ECG arrhythmias, *Proc. of the 8th WSEAS Int. Conf. on Mathematics And Computers in Biology and Chemistry, Vancouver, Canada*.
- [20] G. Bortalan and J. L. Willems, (1993) Diagnostic ECG classification based on neural networks, *Journal of Electrocardiology*, **26**, 75–79.
- [21] Z. Dokur, T. Olmez, and E. Yazgan, (1997) Detection of ECG waveforms by neural networks, *Journal on Medical Engineering and Physics*, **19**(8), 738–741.
- [22] L. Edenbrandt, B. Heden, and O. Pahlm, (1993) Neural networks for analysis of ECG complexes, *Journal of Electrocardiology*, **26**, 74.
- [23] R. Silipo and C. Marchesi, (1998) Artificial neural networks for automatic ECG analysis, *IEEE Trans. on Signal Processing*, **46**.
- [24] A. S. Al-Fahoum and I. Howitt, (1999) Combined wavelet transformation and radial basis neural networks for classifying life threatening cardiac arrhythmias, *Med. Biol. Eng. Comput.*, **37**, 566–573.
- [25] MIT-BIH (<http://www.physionet.org>)

# Contrast enhancement methods in sodium MR imaging: a new emerging technique

Rakesh Sharma<sup>1</sup>, Avdhesh Sharma<sup>2</sup>, Soonjo Kwon<sup>3</sup>, Ross Booth<sup>3</sup>

<sup>1</sup>Department of Medicine, Columbia University, New York, USA; <sup>2</sup>Image Processing Lab, Department of Electrical Engineering, Maharana Pratap A&T University, Udaipur Rajasthan, India; <sup>3</sup>Biological Engineering, Utah State University, Logan, USA.  
Email: [rs2010@columbia.edu](mailto:rs2010@columbia.edu); [soonjo.kwon@usu.edu](mailto:soonjo.kwon@usu.edu)

Received 23 August 2008; revised 20 July 2009; accepted 25 July 2009.

## ABSTRACT

**Background:** In the last decade, sodium magnetic resonance imaging was investigated for its potential as a functional cardiac imaging tool for ischemia. Later interest was developed in contrast enhancement for intracellular sodium. Little success was reported to suppress extracellular sodium resulting in the intracellular sodium MRI image acquisition using quantum filters or sodium transition states as contrast properties. Now its clinical application is expanding as a new challenge in brain and other cancer tumors. **Contrast enhancement:** We highlight the physical principles of sodium MRI in three different pulse sequences using filters (single quantum, multiple quantum, and triple quantum) meant for sodium contrast enhancement. The optimization of scan parameters, i.e. times of echo delay (TE), inversion recovery (TI) periods, and utility of Dysprosium (DyPPP) shift contrast agents, enhances contrast in sodium MRI images. Inversion recovery pulse sequence without any shift reagent measures the intracellular sodium concentration to evaluate ischemia, apoptosis and membrane integrity. Membrane integrity loss, apoptosis and malignancy are results of growth factor loss and poor epithelial capability related with MRI visible intracellular sodium concentration. **Applications and limitations:** The sodium MR imaging technical advances reduced scan time to distinguish intracellular and extracellular sodium signals in malignant tumors by use of quantum filter techniques to generate 3D sodium images without shift reagents. We observed the association of malignancy with increased TSC, and reduced apoptosis and epithelial growth factor in breast cancer cells. The validity is still in question. **Conclusion:** Different modified sodium MRI

pulse sequences are research tools of sodium contrast enhancement in brain, cardiac and tumor imaging. The optimized MRI scan parameters in quantum filter techniques generate contrast in intracellular sodium MR images without using invasive contrast shift agents. Still, validity and clinical utility are in question.

**Keywords:** Sodium MRI; Double Quantum; Inversion Recovery; Contrast Enhancement; Cancer

## 1. BACKGROUND

Sodium-23 (Na-23) nuclei are in abundance in the body but exhibit poor magnetic resonance sensitivity and serve as sodium MRI clinical imaging modalities. The sodium Na-23 nucleus is detectable by MRI due to its 3/2 spin existing as -3/2, -1/2, 0, 1/2, 3/2 (5 states). Physical nature of sodium-23 with spin = 3/2 is suitable to have a nonvanishing magnetic moment and Larmor frequency = 11.26 MHz and exhibits four transition states with five different energy levels in the static magnetic field. MR detection sensitivity is very low (9.3 %) at in vivo concentration (approximately 0.05 %).

Sodium is abundant (100 %) in living body tissue in 3/2 spin state. The sodium ion is the predominant cation in the extracellular fluid (139 mmol/L), while its intracellular concentration is very low (in the order of 8-10 mmol/L), mainly bound with glycosides and proteins. The role of increased intracellular sodium due to concerted efflux through Na<sup>+</sup>/K<sup>+</sup> ATP-ase intrinsic action, angiogenesis, and cell proliferation was described in ischemia, hypoxia, arrhythmia, myocardial edema, and tumors [1]. The sodium concentration is sensitive to disease as an indicator of cellular and metabolic integrity. Na-23 concentration in tissues is present in the order of tens of millimoles. The low sodium concentration results in low signal-to-noise ratio of <sup>23</sup>Na MR imaging in long imaging times and/or poor spatial resolution. Therefore, it needs the use of shift reagents or pulse sequences with



filters such as single-, double-, triple-, and multiple quantum (SQ, DQ, TQ and MQ) filters to enhance the sodium contrast [2].

Evidence of sodium transfer rates across the blood-brain barrier dates back to its use in MRI [3] followed by the use of spin echo pulse sequence for experimental sodium imaging with first surface coil [4]. Soon after it, in vivo clinical sodium imaging at clinical 1.5 T scanners was first described using multislice spin echo pulse sequences [5]. Later developments were made at high magnetic field MRI scanners using ultrashort echo time sequences and hardware improvements that permitted better spatial resolution with shorter imaging times and better quantitative measurements of tissue sodium concentration without use of shift reagents [6].

This paper describes the phases and roles of quantum filters in pulse sequence design to generate intracellular/extracellular sodium contrast, high signal-to-noise ratio, and high resolution in magnetic resonance sodium images by triple-quantum filter and double inversion recovery pulse sequence without using paramagnetic shift reagents. Triple quantum filter was evaluated as a superior method for high signal-to-noise ratio but needs a long acquisition time [7]. Other available multiple-quantum, single-, and double quantum filter tomographic magnetic resonance pulse sequences generate intracellular sodium images with high signal-to-noise ratio but need paramagnetic shift reagents as contrast agents.

### 1.1. Nature of Sodium MR Signal

At high field magnetic resonance application, the applied phase-cycled radio frequency pulses at set time intervals cause an alignment of nuclei populations within the sample, resulting in a measurable signal in the transverse plane. Optimized times of echo delay (TE) in single-, double-, triple quantum filters; optimized times of inversion times (TI) for inversion recovery pulse sequence; and application of a multiple quantum filter after injection of paramagnetic shift contrast reagents detected the distinct intracellular sodium signal to obtain a sodium weighted image. As a result, two sodium MRI signals are achieved with distinct MRI signal intensities to measure sodium intracellular and extracellular concentrations in the tissue. The MR signal intensity is related with tissue sodium content as follows: The MR signal intensity of Na-23 is:

$$\text{MR sensitivity} = \% \text{ Na-23/H-1} \cdot C(\text{Na-23}) \cdot A \cdot \gamma \cdot S^2 + S,$$

where % Na-23/H-1 is sodium abundance, C (Na-23) is tissue concentration, A is MR scanner intrinsic parameter,  $\gamma$  is Gyromagnetic Ratio and S is nuclear spin.

Due to the Gyromagnetic Ratio of Na-23 = 11.25 MHz/T relative MR sensitivity is lesser. Moreover, sensitivity is further decreased due to less sodium content in the tissue: about 1/1000th MR sensitivity of proton, so it needs use of high magnetic field imaging scanner and

data acquisition techniques with contrast enhancement mechanisms, such as MQ, SQ, DQ and TQ. Sodium concentration is higher in blood than that in myocardium and other tissues. This high sodium density in blood contributes to tissue contrast in sodium MR imaging. However, a very small amount of Na-23 is MR visible in free ionic extracellular form due to poor sensitivity. Other intracellular forms of invisible sodium are mainly bound to proteins and phospholipids in the tissue, so intracellular sodium MRI visualization needs quantum filters.

### 1.2. Quadruple Interactions and Sodium MR Signal

Sodium signal is conventionally represented as quadruple interactions between Na-23 and its molecular environment. In sodium nuclei, magnetic resonance excitation and subsequent transition of electrons to different energy levels of nuclear spins produce single-, double-, triple-, and multiple quantum sodium transition MR signals as said earlier. These different quantum transitions can be filtered by use of specific SQ, DQ, TQ and MQ pulse sequence techniques by use of selective phases in pulse sequence design as described later. These techniques also produce spectral patterns reflecting the percentage of invisible intracellular sodium. These sodium spectra are iterated superimposed positions of different spectra and represent simulated signals from intracellular sodium in the cytoplasm including interstitium, mitochondria, intravascular space, and so on. However, this invisible “intracellular” Na-23 results from the presence of a broad frequency peak (T2, very short component). It masks the corresponding frequency peak. Another contributory factor to intracellular Na-23 MR invisibility is long correlation times for short and long T2 components. For the heart, the correlation time is in the range of  $10^{-12}$  to  $10^{-9}$  seconds. As a result, intracellular sodium is invisible. The double quantum pulse technique (instead of single quantum pulse technique) selects only double quantum transitions of sodium. These double quantum transitions allow sodium to be more ordered with long correlation time. These pulse sequence techniques visualize the intracellular sodium.

### 1.3. Nature of Sodium Nuclei and MRI Properties

The Larmor frequencies of sodium in extracellular and intracellular sodium populations are the same because they have the same resonant frequencies. Therefore, three different approaches are used in distinguishing these two types of sodium nuclei. These include different relaxation times between intracellular and extracellular sodium, the use of paramagnetic shift reagents, and the use of special multi-quantum pulse sequences.



## 1.4. Sodium Relaxation Times

Based on the observation that tissue transverse relaxation time for the intracellular space is smaller than that of extracellular space, intracellular space can be imaged by shortening the spin-echo time. Intracellular sodium signal intensity proportionally increases due to intracellular space. Sodium transverse relaxation time (T2) is biexponential in nature, while sodium is bound with negatively charged macromolecules – mainly proteins or metabolites. Perhaps the longitudinal relaxation time (T1) also behaves as biexponential.

### 1.4.1. Paramagnetic Shift Reagents

Paramagnetic shift reagents are chelates of paramagnetic lanthanide ions with anionic complexes. These substances don't cross the intact cell membranes. These reagents interact with extracellular sodium and introduce a frequency shift in the resonance frequency of extracellular sodium. This shift allows the advantage of producing two separate spectral peaks arising from intracellular and extracellular sodium. Common lanthanide ions used as paramagnetic shift reagents are  $\text{Dy}^{3+}$  (Dysprosium),  $\text{Tm}^{3+}$  (Thulium),  $\text{Gd}^{3+}$  (Gadolinium),  $\text{PPP}^{5-}$  (Triphosphosphate), and  $\text{TTHA}^{6-}$  (Tetraethylene Triaminehexa acetic acid). These reagents bind with intracellular calcium and cause physiological disturbances and, in some cases, toxicity, so their use is limited. To overcome such problems, several approaches were recently developed based on the modification of pulse sequences and hardware improvements as described in the following section.

## 1.5. Quantum Filters

These are MR pulse sequences that allow direct observation of multiple quantum transitions. These filters usually are constructed by phase cycling manipulations. The general pulse sequence scheme is  $90^\circ\text{-}t/2\text{-}180^\circ\text{-}t/2\text{-}90^\circ\text{-}\pi\text{-}90^\circ\text{-acquire}$ , where  $t$  is creation time and  $\pi$  is evolution time by use of pulsed field gradients. Characteristically, these filters are sensitive to variations in phase cycles up to  $5^\circ$  and magnetic field inhomogeneity. The filter can be single-, double-, triple-, or multiple quantum and allow single, double-, triple-, and multiple quantum transitions. In the following sections, we introduce readers to our strategy of quantum filters used in sodium MRI pulse sequence design.

### 1.5.1. Single Quantum Pulse Sequence

Due to its multiple spin state transitions, an alternative MR single quantum approach is used to measure intracellular Na content based on the interaction of Na poly-anions and their resultant effects on nuclear spin transitions. Spin 3/2 nuclei (such as Na-23) have a nonvanishing quadrupole moment, allowing interaction with electrostatic field gradients. The pulse sequence is a spin echo sequence.

## 1.6. Multiple Quantum Pulse Sequence for Origin of Double- and Triple Quantum

For intracellular sodium, using only multiple-quantum (MQ) NMR requires paramagnetic shift reagents (SRs) that have distinct disadvantages including: toxicity, possible drug interaction, expanded space, and impermeability to the blood brain barrier. It is known that the correlation time,  $t_c$  of the time variations of the electrostatic field gradients in spin 3/2 nuclei satisfies the relation if  $\omega L t_c \gg 1$ , where  $\omega L$  is the Larmor frequency. These nuclei can display biexponential relaxation and MQ spin transitions do occur in the nuclei and these transitions are detected by specific pulse sequences called multiple- quantum filters.

A phase-cycled RF pulse sequence applied over a slice-select axis selects both echo and anti-echo signals of spin undergoing multiple-quantum spin transitions at resonating Larmor frequency. The RF pulse has both a flip angle and a phase angle. The phase angles are cycled using multiple-quantum transition filter and simultaneously produce an output signal proportional to the sum of echo and anti-echo signals of MQ coherence. It includes the evolution period with a flip angle of  $180^\circ$  to refocus the RF pulse to avoid inhomogeneity-induced amplitude deterioration. This output signal is measured by induction current in the RF coil during the realignment process and is used in tomographic MQ transition  $^{23}\text{Na}$  MRI images.

The pulse sequence comprises: a preparation period of length  $t_p$  extending from time  $t_0$ , an evolution period of length  $t_e$  and a detection period of length  $t_d$ . The RF pulse sequence manipulates the selected nuclei to exhibit them with single quantum coherence. During the evolution period, the pulse sequence implements a MQ filter which isolates the coherence (e.g. double- or triple quantum) and simultaneously selects both echo and anti-echo signals corresponding to the coherence by; a) an evolution period first flip angle RF pulse timewise centered at  $t_p$  which converts the selected nuclei from single-quantum coherence to the selected multiple- quantum coherence; b) an evolution period of second  $90^\circ$  flip angle RF timewise centered at  $t_p+t_e$ , converts the selected nuclei from multi-quantum to single-quantum coherence. Therefore, during the detection period, selected nuclei exhibit single quantum coherence to generate a single quantum signal.

The resultant collective phase angle of evolution period RF pulse =  $\Phi_E = \Phi_3 - 2\Phi_4 + \Phi_5$ , where  $\Phi_E$  is collective radio frequency phase during evolution time, and  $\Phi_4$  &  $\Phi_5$  are phases of  $90^\circ$  RF pulses. A further preparation period of  $90^\circ$  flip angle radio frequency slice-selecting pulse, a preparation  $180^\circ$  flip angle refocusing pulse, and a detection period  $180^\circ$  flip angle radio frequency are applied – centered at  $t_0$ ,  $\frac{1}{2} t_p$  and  $t_p+t_e+1/2 t_d$ , respectively. The preparatory  $90^\circ$  flip angle RF pulse selects a

slab of sample perpendicular to a slice-selection axis as shown in **Figure 1**. The preparatory  $90^\circ$  flip angle slice-selection RF pulse has phase angle  $\Phi_1$ , the preparatory  $180^\circ$  Rf refocusing pulse has  $\Phi_2$ , and detection period  $180^\circ$  flip angle RF pulse has phase angle  $\Phi_P$  of the RF pulses during preparation time (evolution period  $90^\circ$  flip angle RF phase  $\Phi_3$ ) as described earlier(8). The phase angle is  $\Phi_P = \Phi_1 - 2\Phi_2 + \Phi_3$  and the output signal will be  $\Phi = \Phi_{P-m} \Phi_{E+} \Phi_{5+2} \Phi_{6+} \Phi_R$ , where  $m$  is the integer of magnetization,  $\Phi$  is the phase of detected signal, and  $\Phi_R$  is the phase of receiver.

For double quantum filtered images,  $m=+2$ , and for triple quantum filtered images,  $m=+3$ . The phases will be  $\Phi_1 = (n/2)\pi$ ,  $\Phi_2 = [n/2 + \text{int}(n/4)]\pi$ ,  $\Phi_3 = (n/2)\pi$ ,  $\Phi_4 = \Phi_5 = \Phi_6 = 0$  and  $\Phi_R = n\pi$  for double quantum filter; and phases will be  $\Phi_1 = (n/3)\pi$ ,  $\Phi_2 = [n/3 + \text{int}(n/6)]\pi$ ,  $\Phi_3 = (n/3 + 1/2)\pi$ ,  $\Phi_4 = 0$ ,  $\Phi_5 = (1/6)\pi$ ,  $\Phi_6 = 0$  and  $\Phi_R = [n + \text{int}(n/6)]\pi$  for triple quantum filter, where  $n/6$  is integer part of the variable  $n/6$ . The variable  $n$  is positive integer of  $0 \dots N-1$ .  $N$  is a multiple of 8 and 12 for double- and triple quantum filters respectively.

The magnetic gradient pulse sequence is also applied along with the RF pulse sequence for positional information in the data. A slice-select gradient pulse, first and second phase encoding gradient pulse, and read-out gradient pulse are applied along read-axis after detection period  $180^\circ$  RF refocusing pulse during output signal observed as shown in **Figure 1**. The read-out pulse area before time  $t_p + t_e + t_d$  is equal to the area of read-out gradient pulse. These gradient pulses exhibit simultaneous synchrony with RF pulses.

### 1.6.1. Inversion Recovery Pulse Sequence

The inversion recovery technique can suppress the extracellular sodium nuclei with specific ranges of the lon-

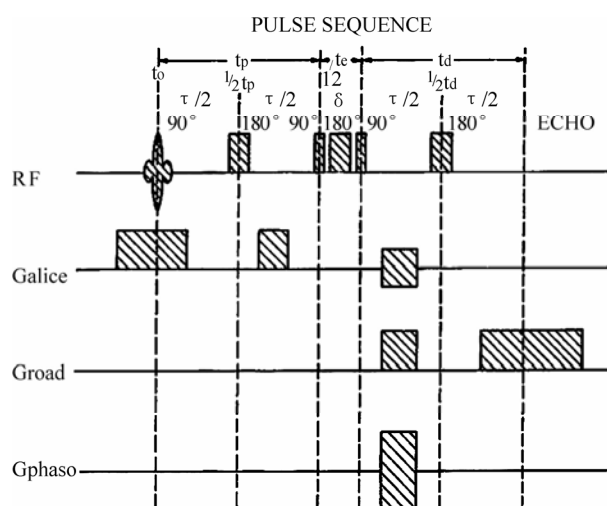


**Figure 1.** The figure illustrates a series of radiofrequency pulses and a synchronized series of magnetic gradient pulses for phase cycled evolution period  $180^\circ$  flip angle refocusing pulse.

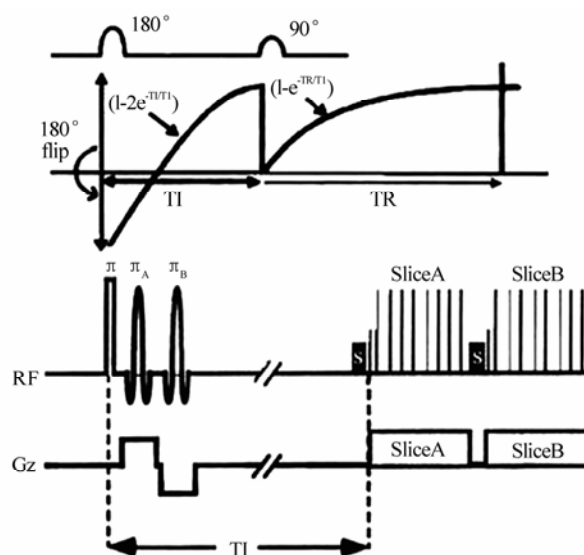


**Figure 2.** A scheme of inversion recovery pulse sequence is presented. On top, one cycle of IR with two recovery curves is shown for a single slice. First,  $180^\circ$  pulse is flipping the magnetization  $M_z$  for first recovery followed by  $90^\circ$  pulse for FID and second recovery within TR period. At bottom, the application of two inversion pulses  $\pi_A$  and  $\pi_B$  is shown for slices A and B with simultaneous application of RF and gradient pulses.

gitudinal relaxation time,  $T_1$  using fast spin-echo pulse sequence. The sequence has two sets of slice selective inversion pulse trains (long recovery period  $TI_1$  for extracellular sodium and short recovery period  $TI_2$  for intracellular sodium nuclei). The first inversion pulse is played during a long recovery period  $TI_1$ , during which extracellular sodium magnetization recovers just past its null point while longitudinal magnetizations of intracellular sodium nuclei are almost fully restored. The second set of inversion pulse is played during short recovery period  $TI_2$ , when intracellular Na nuclei magnetizations reach their null points following  $TI_2$  interval and become  $180^\circ$  out-of-phase. After inversion pulses, a fast spin-echo acquisition sequence is applied to achieve magnetization in z-direction ( $M_z$ ) as following:

$$M_z = M_0 [(1 - 2e^{-T_{1e}/T_{1e}} + e^{-T_R/T_{1e}})(1 - 2e^{-T_{1i}/T_{1i}})] \quad (1)$$

where 'e' represents extracellular sodium nuclei and 'i' represents intracellular sodium nuclei.  $M_0$  is initial longitudinal magnetization,  $TI_1$  &  $TI_2$  are long and short inversion times, and  $T_{1e}$  &  $T_{1i}$  are longitudinal relaxation times of extracellular and intracellular sodium nuclei, respectively.

The relaxation time for intracellular Na nuclei varies from 5-10 milliseconds (for Na bound to large molecules or dispersed in highly order environment) to 51 milliseconds (for extracellular sodium nuclei in free solution). Based on 3D projection reconstruction imaging pulse sequence, echo time TE as short as 0.1 ms can be

achieved. This captures the more rapid decay of short  $T_2$  sodium components in the NMR signal so as to further improve the signal to noise (SNR).

As shown in **Figure 2**, radio frequency pulse at  $180^\circ$  is followed by a  $90^\circ$  pulse for slice excitation utilizing echo-train length with any option of selective or non-selective, single or composite, sinc, sech or tyco pulse as needed. So, inversion pulses are played out during inversion  $TI_1$  and  $TI_2$  periods for both types of sodium nuclei. Data acquired includes projection reconstruction with slice selection or without slice selection using spin-echo or gradient echo. Thus, inversion/acquisition periods are played out for several slices per repetition of fast spin echo (FSE) sequence exhibiting two distinct null points for both sodium nuclei populations.

## 2. MRI PHYSICS OF CONTRAST ENHANCEMENT BY INVERSION RECOVERY AND TWO NULL POINTS

After first  $180^\circ$  RF pulse flips the magnetization from  $M_z \rightarrow M_{-z}$ , the two different inversion times ( $TI_1$  and  $TI_2$ ) for two sodium populations exhibit two null points and growth of longitudinal magnetizations. In this sequence, soon after  $TI$ , a  $90^\circ$  RF pulse is applied to flip the longitudinal magnetization into the x-y plane for the  $T_1$  growth curve within repetition time  $TR$ . At this point, frequency induction decay (FID) is measured when the longitudinal magnetization is flipped into the x-y plane. Thereafter  $180^\circ$  RF pulses are repeatedly applied. The magnetization signal 'S' may be measured as:  $[S] \propto M_0(1 - e^{-TI/T_1})(1 - e^{-TR/T_1})$ , as  $T_1$  recovery curves for both  $180^\circ$  and  $90^\circ$  degree pulses applied.

The intracellular and extracellular populations of nuclei have different longitudinal relaxation times, so they generate intracellular/extracellular sodium contrast. To set the IR pulse sequence to suppress the contribution of sodium nuclei with specific ranges of  $T_1$ , the inversion time  $TI_1$  or  $TI_2$  is set as  $(\ln 2)(T_{1ex})$ , where  $T_{1ex}$  is the composite longitudinal relaxation time. This inversion time then determines the time between the  $180^\circ$  and  $90^\circ$  pulses in the IR pulse sequence.

### 2.1. Projection Reconstruction Methods

First, projection reconstruction was proposed based upon Fourier transformation of the FID (free induction decay) signals [9].

Now, these FID signals are obtained by rotating a magnetic field gradient with back-projection to determine the spin-density function or enhanced contrast. So far, this technique has been used only for animal hearts. These signals can be gated to heart rate to reduce the motion artifact. Signals are reconstructed from 12 projections. Each projection is obtained from an average of 320 FID signals. For image matrix  $64 \times 64$  total data acquisition, time is approximately 15 minutes.

### 2.2. Three-Dimensional Fourier Techniques

In this technique, phase-encoding is made in two orthogonal directions, and a fixed gradient is applied in a third direction of read-out gradient [10]. The pulse-encoding steps are applied, typically 40 steps along each phase-encoding direction. As a result two echo signals with different spin-echo times are generated and added in a coherent manner to enhance contrast. This phenomenon also improves the signal-to-noise ratio. This technique is used for the human brain. In cardiac sodium imaging the utility of this technique is limited to animal heart experiments. Typically short  $TR = 100$  ms is used to get data in 3 hours, including different spin echoes summation. The application of greater sodium signal in the left anterior descending artery was observed in occlusion, followed by re-perfusion of circumflex in the coronary artery after ischemia.

### 2.3. Hybrid Spin Echo Techniques

The spin-spin  $T_2$  relaxation time of intracellular sodium is shorter than that of the extracellular sodium compartment, so it is difficult to observe it to create contrast, and it needs a hybrid spin-echo pulse sequence. In the hybrid approach, both projection-reconstruction and Fourier encoding schemes are used at the same time. Fourier analysis does slice selection in one direction while another projection-reconstruction is performed in two other orthogonal directions. This technique is good for clinical MR scanners with gradient refocused sequence with modified head coil to generate echo time as short as 2.8 msec [11].

### 2.4. Surface Coil Techniques and Coil Sensitivity

Sodium imaging at short  $T_2$  relaxation times can be performed by use of a customized radio-frequency coil focused on the region-of-interest to improve the signal-to-noise ratio. The pulse sequence is applied with optimizing the minimum saturation time of preamplifier and duration of 90-degree RF pulse. This effect minimizes the magnetic homogeneity influence over the free induction image and the short  $T_2$  can be imaged. This technique is relatively better than others for human cardiac sodium imaging on clinical scanners. First, using different transmitter gains optimizes the gain for  $90^\circ$  pulse, and different transmitter gains at increased and decreased gain values yields  $^{23}\text{Na}$  images at different flip angles of  $45^\circ$ ,  $90^\circ$ , and  $135^\circ$  with matrix sizes  $32 \times 32 \times 32$  points. Nonlinear least squares fit of the pixels intensities in all three images determines the B1 field strength (for 5% maximum intensity on image) as a function of the related  $[\text{Na}]$  image intensities in response to the local RF coils for receive and transmit sensitivities [13].

The image signal intensity depends on coil transmit and coil receive sensitivity as:

$$I_k = R_k M_{0k} |\sin(\Phi_k)| \quad (2)$$

where  $I_k$  is the signal intensity of the  $k_{th}$  pixel,  $R_k$  is a sensitivity at the coil center, and  $M_{0k}$  is the equilibrium magnetization. The flip angle  $\Phi_k$  is a function of the transmitter gain setting (TG) as:

$$\Phi_k = (CR_k)10^{TG/20} \quad (3)$$

$(C \cdot R_k)$  and  $M_{0k}$  were each fitted with a single parameter for each pixel. The constant 'C' is independent of spatial position and receives sensitivity. It is also directly proportional to the transmit field distribution for the coil [13]. After normalization, the product  $(C \cdot R_k)$  yields the relative sensitivity  $R_k$  for the  $k_{th}$  pixel. The  $B_1$  (expressed as  $B_1/2$ ) depends on reference transmit power,  $TG_{ref}$ :

$$\frac{\gamma B_{1k}}{2\pi} = (CR_k)10^{TG_{ref}/20} / (t_p (2\pi)) \quad (4)$$

where  $t_p$  is the pulse duration.

Local field  $B_1$  and longitudinal relaxation time  $T_1$  determine the correction factors for saturation for each pixel  $k$ ,  $SF_k$  as follows:

$$SF_k = \frac{[-e^{-TR/T_1}] \sin(t_p \frac{\gamma B_{1k}}{2\pi})}{[1 - e^{-TR/T_1} \cos(t_p \frac{\gamma B_{1k}}{2\pi})]} \quad (5)$$

where  $B_{1k}$  is the  $B_1$  field in the respective ROI and is the gyromagnetic ratio for  $[Na]_i$  using the pulse time  $t_p=0.4$  msec, and the  $TR=120$  msec [13].

## 2.5. Rotating Frame Techniques

Conventionally, sodium imaging can be done using the rotating frame technique based on superimposing a magnetic field gradient on the excitation field  $B_1$ . As a result, during this excitation period, spatial localization and spatial encoding may be performed very fast to generate sodium contrast. In this process, loss of MR signal intensities is also minimized. In an isolated perfused rabbit heart, sodium-rotating frame imaging experiment was completed in 12 msec in a  $128 \times 128$ -image matrix with a clinical 1.5 T scanner [12].

### 2.5.1. Use of Contrast Agents

Different shift agents such as dysprosium or Tm (DOTP) contrast agents increase the sensitivity and specificity of sodium MRI by shifting intracellular sodium magnetization away from extracellular sodium magnetization (exhibited well as shifted peaks). Dextran-magnetite increases the contrast between tumor and surrounding soft tissue sodium images. Normal reticulo-endothelial cells take up a greater amount of magnetic particles than tumor cells do, which supports the potential for tumor so-

dium imaging by contrast agents. However, a major role of sodium imaging seems to distinguish myocardial ischemia.

**Techniques used for sodium *in vivo* MRI:** Several approaches have been used. Despite little success, these techniques are gaining interest in physiological MR imaging using intracellular sodium. Some landmark techniques have been described for image generation.

### 2.5.2. Spectrally Weighted Twisted Projection Imaging

The 3D sodium MRI imaging can be made faster by reducing the  $T_2$  signal attenuation effects. This is implemented by 3D twisted projection imaging. At high spatial frequencies, the sample density is reduced, and as a result the reduced readout time is achieved. This leads to decreased  $T_2$  signal attenuation, which translates into improved signal-to-noise ratio (SNR) without a loss of resolution [14].

### 2.5.3. Biexponential Relaxation Effect and Sodium Concentration Mapping

Dual-frequency RF coils with identical  $B_1$  field distributions at the two different observation frequencies provide sodium and proton mapping. These optimize both dual frequencies in dual quadrature RF coils. Sodium and proton channels are decoupled to make dual-quadrature birdcage configurations. The fourth harmonic of sodium frequency happens to be very close to proton frequency. This is suitable for echo-planar imaging and metabolite quantification [15].

### 2.5.4. 3-D Triple Quantum-Filtered Twisted Projection Na-23 Imaging

A new approach was developed based on a three pulse, six-step, coherence transfer filter (with fast twisted projection imaging sequence) to generate spatial maps of the TQ signal. In principle, three pulse coherence filter leads to TQ sodium images. In these images, the image intensity depends on the spatial variation of the flip angle. This image intensity is lesser than the flip angle chosen in the four pulse TQ filter. This technique allows the generation of RF inhomogeneity corrected TQ sodium images after TQ signal variation. The pulse sequence of TQ filtering is based on spherical tensor operators or a density matrix. It consists of three non-selective RF pulses, and sometimes a fourth RF pulse between the three first and the second pulses, to refocus the main magnetic field inhomogeneities [16]. In this pulse sequence, RF induces different flip angles as  $\theta_{30}$ ,  $2\theta_{30}$ ,  $\theta_{150}$ ,  $\theta_0$ ,... flip angles where the phase stepped up through the values  $30^\circ$ ,  $90^\circ$ ,  $150^\circ$ , and so on. The second pulse is intended for the B inhomogeneities refocusing and is absent in the case referred to as "three pulse". The preparation time is the period between two phases and evolution time is the period between  $\theta_{150}$  and  $\theta_0$ .



## 2.6. Simultaneous Quadruple and Double Quantum Na-23 MR Imaging

Na-23 is a quadruple nucleus with biexponential relaxation or non-vanishing quadruple coupling. Both properties contribute to generate Na-23 multiple-quantum (MQ) coherence [17]. The Multiple Quantum Filter pulse sequence can be represented as **Eq.6**:

$$(\theta_1, \varphi_1) - t_p/2 - (\theta_2, \varphi_2) - t_p/2 - (\theta_3, \varphi_3) - t_E - (\theta_4, \varphi_4) - \text{Acq}(T, \varphi_R), \quad (6)$$

where refocused preparation time,  $\varphi_p$  and non-refocused evolution time,  $\varphi_E$  may be represented as **Eq.7**:

$$\varphi_P = \varphi_1 - 2\varphi_2 + \varphi_3; \varphi_E = -\varphi_3 + \varphi_4 \quad (7)$$

where  $\varphi_{1-4}$  denote the phase of each RF pulse with flip angle  $\theta_{1-4}$ ,  $\varphi_R$  is receiver phase, and  $T$  is acquisition time, each  $\theta_1 = \pi/2$  and  $\theta_2 = \pi$ .

This sequence is good for detecting well-defined and ordered structures in biological tissues. Both quadruple-order and double-quantum signals can be generated simultaneously by the same RF sequence without any loss in signal amplitude. In addition, the acquired MQ signals can be readily decomposed into their second – and third – rank components, i.e. into quadruple order and biexponential relaxation components. This allows reduction of the scan time to acquire MQ signals of different coherence orders and ranks, which should prove useful for in vivo studies.

## 2.7. Double Spin-Echo Imaging and Transverse Relaxation Time

This approach of imaging is good for myocardial water content analysis based upon the calculation of transverse relaxation time from dual-quantum spin-echo MRI [18]. Right and left ventricles can be assessed for quantification of myocardial edema. The transverse relaxation times ( $T_2$ ) of ventricles can be calculated from the signal intensities within multiple regions of interest over myocardium as shown in **Eq.8**:

$$T_2 = [(TE_2 - TE_1) / \ln(I_1/I_2)], \quad (8)$$

where  $TE_1$  is first echo time,  $TE_2$  is second echo time, and  $I_1$  &  $I_2$  are image amplitudes of first & second spin echoes.

## 2.8. Double-Quantum-Filtered Na-23 MR Spectroscopy

The extracellular EC-Na and intracellular IC-Na contents are better visualized by multiple-quantum-filter spectra acquired in the absence of chemical shift or relaxation reagents. The intracellular IC-Na sensitivity can be enhanced by double-quantum-filter (DQF) Na-23 NMR to measure the detection of  $\text{Na}^+$  motion anisotropy with the presence of residual quadruple splitting (19). However, the application of this technique is limited to the experimental heart studies using the pulse sequence:

$90^\circ - \tau/2 - 180^\circ - \tau/2 - \theta - t_1 - \theta - t_{\text{Acq}}$ , where  $\tau$  denotes the creation time and  $t_1$  is evolution time,  $\theta$  is RF flip angle.

The magnetization  $M(\tau, t, \theta)$  for the MQF Na-23 NMR signal, when the quadruple splitting factor ( $\omega_Q$ ) is zero, is given by **Eq.9**:

$$M(\tau, t, \theta) = \alpha M_0 [\exp(-\tau/T_{2s}) - \exp(-\tau/T_{2f})] \times [\exp(-t/T_{2s}^*) - \exp(-t/T_{2f}^*)] \times \sin^2\theta (1 - 3\cos^2\theta) \quad (9)$$

where  $\alpha$  is a factor which depends on the degree of quantum coherence,  $M_0$  is equilibrium magnetization,  $T_{2f}$  &  $T_{2s}$  are fast & slow transverse relaxation times, and  $T_{2f}^*$  &  $T_{2s}^*$  are the corresponding inhomogeneity-broadened times. An important implication for this technique is the possibility of measuring intracellular sodium concentration in animal hearts with the DQF spectrum in the absence of shift or relaxation reagents. Significant attenuation of the DQF spectrum derived from extracellular  $\text{Na}^+$  allows to differentiate the NMR spectrum from intracellular  $\text{Na}^+$ .

## 2.9. Double Quantum Filtering and Spin-Quantum Coherence

Conventionally, the double-quantum filtering method for sodium imaging is completed in a four-step phase-cycling scheme. In this process, the radio-frequency pulses generate single-quantum coherence. Its phase appears similar to the phase of a double-quantum coherence signal in the pulse sequence. Consequently, the intersequence stimulated echo passes through the double-quantum filtration in the phase cycling scheme and gradient pulses in the DQ pulse sequence, so the single-quantum coherence is an unwanted component in this pulse sequence. It is eliminated by the use of spoiling RF pulses followed by dephasing gradient pulses incorporated into the DQ filtering pulse sequence. These spoiling pulses disperse the pulse transition and eliminate the magnetization components of the intersequence stimulated echo in the DQ pulse sequence [20]. Another good way to eliminate single quantum coherence is to increase the repetition time TR. Moreover, a low signal level of DQ coherence also demands many signal averaging at short TR to keep short scan time and not a longer TR.

## 2.10. Chemical Shift Selective Acquisition of Multiple Quantum-Filtered Na-23

In cardiac imaging, MQ signals over a wide off-resonance bandwidth is a problem which causes interference between echo and anti-echo. It is due to a resonance off-set insensitive to the flip angle of the creation RF pulse; usually the second  $\pi/2$  pulse. Off-resonance effects are applied to eliminate the MQ signal in the presence of a chemical shift. It suppresses the MQ signal over a wide range of off-resonance bandwidth [21]. Existing tech-



niques for chemical-shift-selective acquisition of SQ signals can be combined with MQ off-resonance effects to enhance the selectivity of chemical shift.

### 2.11. Double Quantum Filtering and Elimination of Intersequence Stimulated Echo

In cardiac sodium imaging the 'intersequence stimulated echo' is an unwanted component because the phase of this echo has the same properties as that of the double-quantum (DQ) signal. Using a partition method and computer simulation can eliminate the magnetization components of the intersequence stimulated echo [22]. The DQ filter pulse sequence with non-refocused preparation time ( $\tau_P$ ) and evolution time ( $\tau_E$ ) may be expressed as:  $(\theta_1, \varphi_1) - \tau_P - (\theta_2, \varphi_2) - \tau_E - (\theta_3, \varphi_3) - \text{Acq}(t_2, \varphi_R)$ , where  $\varphi_n$  denotes the phase angle of each RF pulse with the flip angle  $\varphi_n$ ;  $t_2$  is acquisition or detection time and  $\varphi_R$  is receiver phase.

### 2.12. Multiple Quantum Filters of Arbitrary Phases of Na-23 Nuclei

These Triple Quantum filtered data acquisition, uses the pulse sequence with arbitrary phase values:  $90^\circ_{(\theta_1)} - t/2 - 180^\circ_{(\theta_2)} - t/2 - 90^\circ_{(\theta_3)} - \delta - 90^\circ_{(\theta_4)} - \text{acq}_{(\theta_5)}(T)$ , where  $\delta$  is evolution time,  $t$  is the acquisition time,  $\theta_1, \theta_2, \theta_3, \theta_4$ , and  $\theta_5$  are the phase values. Multiple-quantum-filtered (MQF) Na-23 NMR spectroscopy may provide increased sensitivity in detecting IC Na and thus offers the possibility of monitoring changes in IC Na content without SR. The amplitude of the MQF spectrum is determined by several factors such as transverse relaxation times, creation times, and the amount of Na that exhibits MQ coherence. By the behavior of relaxation and greater IC-Na MQ coherence, it is possible to have MQF spectrum with intracellular sodium to measure IC-Na content [23].

### 2.13. Spiral Cardiac Respiratory Gate Multi-Shot Functional MRI as Possibility

Physiological fluctuations (possibly by sodium) are known to be a major contribution to noise in fMRI data. Cardiac noise adds noise to both the magnitude and phase of the image in regions localized near vessels and ventricles. Another factor, respiratory motion, has both global changes in the phase of image and localized variations in the image magnitude, particularly near ventricles. Recently, an empirical model was used to capture the observed features of physiological noise in fMRI data to reduce intracellular ionic noise in fMRI data using a 3-D cylindrical-stack spiral pulse sequence [24]. Briefly, spiral waveforms of sequence were applied on the x and y gradients. The waveforms were designed get low slew rate limited except for the first few points, and

their maximum amplitude was 0.75 G/cm to give a 3.8 x 3.8 mm nominal in-plane resolution. Six interleaves were measured by adjusting the spiral waveforms (multiplying the x and y gradients by coefficients of a rotation matrix) to effectively rotate the k-space trajectory in the  $k_x - k_y$  plane. At the end of each TR interval, crusher gradients were used to minimize spillover of the FID signal into subsequent intervals. Their amplitudes were set to generate about  $3\pi$  dephasing over each voxel dimension of covered volume of interest. It results in a "stacked spirals" k-space acquisition scheme. With the spiral acquisition, all gradient moments,  $M_n(t)$ , can be shown as Eq.10:

$$M_n(t) = \int G_{(t)} t_n dt \quad (10)$$

with  $t = 0$  at the center of the RF pulse, are zero at the center of k-space ( $t = t_c$ ).

The zero<sup>th</sup> [ $M_0(t)$ ] and first [ $M_1(t)$ ] order moments of the slab select null at gradient at  $t = t_c$  by using two additional gradient phases after the slice selection lobe. Furthermore, the magnetization were nulled at  $t = \text{TR}$  i.e.,  $M_0(t)$  for the phase encode gradient and  $M_0(t)$  and  $M_1(t)$  for the spiral waveforms. These spiral waveforms are made of trapezoid waveforms at amplitude with minimum gradient moments. In addition, a phase encoding scheme is inverted and quadratic RF phase modulation is performed to minimize stimulated echoes. Additional gradient pulses can minimize stimulated echoes after acquisition. Another good practice to decrease the scan time is inserting extra 'dummy views' to avoid extra acquisitions when the physiological phase corresponds to the view far away from the actual view to acquire, although these 'dummy views' reduce fMRI temporal resolution and lead to improper assessment of functional activity & physiological variance. Cardiac ordering shows greater utility due to shorter cardiac periods. It can reduce inter-image variance by using k-space post-processing techniques and may enhance sodium contrast. This technique is very promising but longer scan times are required.

## 3. CLINICAL SODIUM MRI TRIALS

Sodium MRI can be used in anatomical imaging applications in brain, tumors and cardiac cycle (25-29). Special attention was focused on achieving intracellular sodium images. Triple Quantum filter in spin echo acquisition mode and inversion recovery methods are considered useful for it without using shift contrast agents. However, the triple-quantum filtered technique requires a very long repetition time. Inversion recovery technique suffers from poor nulling and poor suppression of extracellular or intracellular sodium population (30-31). Moreover, for imaging applications with the resolutions of 64 or 128 pixels, physiological noise corrupt even better regions without variation. These are referred to as 'ghosts', and may be shifted away from the area of in-

terest or avoided by using the 'view ordering' technique. It was done by sorting the views for which physiological period  $T = T_0$  ( $\alpha = 1$ ) 'low frequency sort mode' or  $T = T_0 \times N/2$  'high frequency sort mode', where  $\alpha = N/2$ ,  $N$ =total number of views). For cardiac sodium MRI data acquisition in real time, the physiological phase and corresponding view are obtained again and again till all views are expended. Physiological ghosts, phase variation is cause of further inter-image fluctuations in cardiac MRI time course and affect activation related changes in the acquired signal.

**Intracellular sodium concentration measurement:** Several attempts to measure the intracellular sodium concentration including sodium flame photometry and ion electrodes in serum; ratiometric, electrom beam CT, atomic force (AFM) spectroscopy in tumors; and sodium MRS in myocardium suggested the role of ATP energy and  $\text{Na}^+/\text{K}^+$  pump in ischemia & tumor apoptosis. Therapies that alter tumor ion homeostasis or affect/destroy tumor cell membrane integrity are likely to generate changes that are observable with  $^{23}\text{Na}$  MR imaging and sodium concentration measurements [29,31]. For different methods, the concentration of intracellular sodium can be measured based on NMR peak areas by subtraction or magnetization ratio and intracellular/extracellular volumes as following:

For MQ method,

$$[Na]_{i(MQ)} = \left\{ 1 - \frac{[y]M_{M0(x)}}{[x]M_{M0(y)}} \right\} \left\{ V_R / V_{in} \right\} [Na]_R \sim M_{0,vM(x)} \quad (11)$$

where  $[x]$  and  $[y]$  denote the corresponding tissue and standard phantom intracellular sodium concentrations.  $K$  is a constant equal to  $M_{M0,v(y)}/[y]$ .  $V_R/V_{in}$  is the ratio of reference and intracellular volumes in tissue.

For DQ method,

$$[Na]_{i+}^{DQ} = \{(A_{in}/A_{ref}) - (\text{intercept})\} / (\text{slope}) \quad (12)$$

where  $A_{in}$  and  $A_{ref}$  represent areas under tissue and phantom intracellular sodium peaks.

For SQ method,

$$IC[Na] = \{A_{in}/A_{out}\} \{V_{out}/V_{in}\} \{EC[Na]\} \quad (13)$$

$A_{in}$  and  $A_{out}$  are areas of the SQ  $^{23}\text{Na}$  NMR peaks for IC and EC spaces;  $EC[Na]$  is extracellular Na concentration.

With these measurements, changes can be observed much earlier than with the effects of anatomic remodeling.  $^1\text{H}$  MR imaging FLAIR sequence, use of MR contrast agents, and T2-weighted imaging along with  $^{23}\text{Na}$  MR imaging may improve tumor visualization of a necrotic core or proliferating zones by multiparametric analysis methods. Other approaches of enhancement of 3D  $^{23}\text{Na}$  images signal-to noise ratio depend on receivers and coils and the twisted-projection imaging pulse sequence [32].

The sodium concentration may be measured by placing a phantom next to tumor or animal during MR imaging. The mean sodium concentration per kilogram wet body weight in the region of interest will be:

$$[Na]_k = \frac{\frac{I_k}{R_k SF_k} - b}{aD} \quad (13)$$

The coefficients  $a$  and  $b$  were calculated from the sodium concentrations  $C_1$  and  $C_2$  and signal intensities  $I_1$  and  $I_2$  of the two phantoms as

$$a = \frac{\frac{I_2}{R_2 SF_2} - \frac{I_1}{R_1 SF_1}}{C_2 - C_1} \quad (14)$$

and

$$b = \frac{I_2}{R_2 SF_2} - aC_2 \quad (15)$$

where  $R_1$  and  $R_2$  are sensitivity factors.

In the following section, we describe our experiments in support of increased sodium in malignancy and association with apoptosis in breast tumors and epithelial growth factor in breast isolated cancer cells. For simplicity, we introduce readers to the biochemical basis of increased sodium in tumor cells. The low sodium-hydrogen exchange kinetics by slow sodium-hydrogen transporter is center point. In malignant tumor cells, acidic pH enhances the intracellular sodium that impairs both the sodium-hydrogen transporter ability and  $\text{Na}^+/\text{K}^+$  pump resulting in reduced  $[\text{Na}^+/\text{K}^+]$  ATPase enzyme to release sodium (high intracellular sodium concentration inside cells) from mitochondrial oxidation which also triggers cells to slow down apoptosis or other associated epithelial growth factors [high intracellular Na with low apoptosis and EGF]. The low concentration of intracellular sodium is sensitive to any malignancy change and serves as a diagnostic rapid MRI imaging assay to test drugs.

### 3.1. Chemosensitivity Rapid Assays Using Sodium MRI

Very limited studies reported the value of intracellular sodium in a chemosensitivity assessment by cell proliferation and apoptosis in prostate and breast tumors. However, its applications are expanding to glioma, cartilage, and liver [32,33]. A technical advance was reported using an inversion recovery pulse sequence and optimization of inversion times to achieve intracellular sodium images in less time. Its application was applied in textotere chemosensitivity response to PC 3-induced mouse prostate and MCF 7-induced rat breast tumors as shown in **Figure 3**. The enhanced contrast of increased intracellular sodium MRI signal was correlated with histopathology characterization of tumor tissues [34,35,

Lesion Type (% high power field)	IR Sodium MRI signal Intensity	Lesion Type (% high power field)	IR sodium MRI signal Intensity
<b>A. Pre-Malignant Lesions:</b> (mA.U.)		<b>C. Malignant Carcinoma</b> (mA.U.)	
a. Intraductal Proliferation(8-10)	11.5	h. Papillary Carcinoma(25)	13.5
b. Ductal Hyperplasia(12-14)	8.8	i. Invasive Cribriform Carcinoma(25)	12.8
c. Atypical Ductal Hyperplasia(40)	10.6	j. Invasive Comedo Carcinoma(25)	11.5
d. Cell Proliferation and Apoptosis(>50)	6.2	k. Invasive Tubular Carcinoma(25)	13.8
<b>B. Malignant Lesions:</b>		<b>D. Adenocarcinoma:</b>	
e. Ductal Microcapillary carcinoma(12)	14.2	l. Metastasis(25-30)	9.5
f. Cribriform Ductal Carcinoma(40)	12.8	M. Lymph Node Invasion(10-20)	12.5
g. Ductal Comedocarcinoma(30)	12.2		

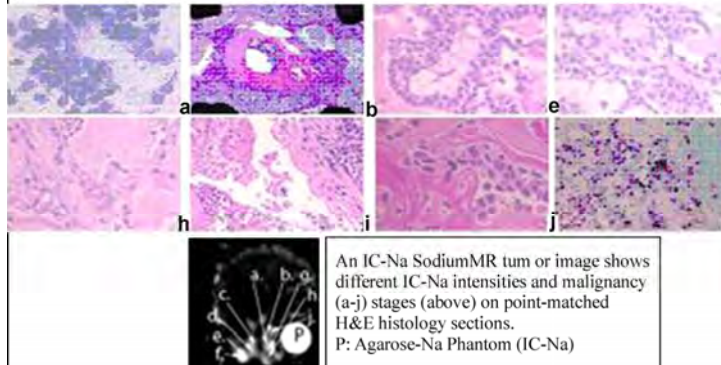


**Figure 3.** Inversion recovery pulse sequence using optimized inversion time generated high resolution intracellular sodium images of tumor (right on the phantom image) in each panel. On right, a tumor image is enlarged to show regional heterogeneity of MCF 7 induced breast tumor in rat. P represents image of agarose-sodium phantom and alphabets at different points indicate different stages of tumor growing cells to correlate with histology as shown in table to highlight the accuracy of sodium MR signal intensity and tumor pathology staging [36].

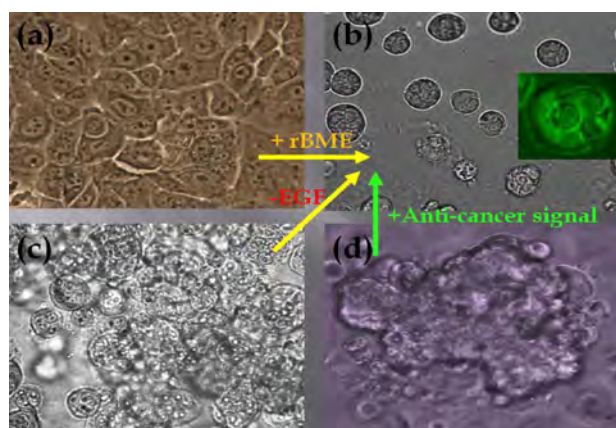


**Figure 4.** A Comparison between normal and malignant human breast epithelial cells (grown in a 2D monolayer and 3D culture matrix) shows a role of EGF in luminal structure formation. Normal human breast epithelial (NHBE) cells (grown in the 3D culture matrix) form a luminal structure of normal phenotype. (a) Normal human breast epithelial cells in monolayer without rBME (2D monolayer) with normal EGF, (b) NHBE cells in rBME (3D matrix) with reduced EGF, (c) NHBE cells in rBME (3D) with normal EGF, (d) Malignant human breast epithelial cells (HTB-132 obtained from ATCC) in rBME (3D) with reduced EGF. Notice the role of FGF and the rBME matrix used in association with malignant characteristic of cells.

36]. However, the exact cause of increased TSC is not known. In another set of breast cancer culture cells, we observed the reduced EGF in tissues sensitive to sodium ion homeostasis and metabolic integrity.

### 3.2. Correlation between Intracellular Sodium Signal and Malignancy

Elevated TSC in breast lesions measured by non-invasive  $^{23}\text{Na}$  MRI appears to be an indicator at the cellular level associated with malignancy. This  $\text{Na-}^{23}$  MRI method may have potential to improve the specificity of breast MRI with only a modest increase in scan time per patient [37]. Several physiological and biochemical changes associated with proliferating malignant tumors may cause an increase in total tissue sodium concentration (TSC) as a result of impaired sodium-hydrogen transporter and  $[\text{Na}/\text{K}]$  pump activity resulting in reduced EGF (**Figure 5**).

Normal and malignant epithelial ductal cells were grown on a reconstituted basement membrane extract (rBME). In the event of the correct signaling from growth factor and extra-cellular matrix proteins, isolated human breast epithelial (HBE) cells formed their original phenotype *in vivo*. HBE cells in the absence of reconstituted basement membrane extract (rBME) failed to assemble organized structures, and arrested growth when

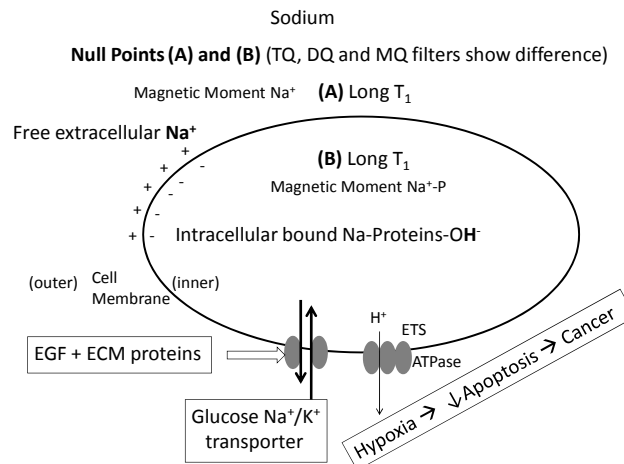


**Figure 5.** This schematic description represents the origin of intracellular sodium across the membrane and different null points of sodium inside and outside generate contrast due to different longitudinal relaxation constants as basis of sodium MRI. The increased intracellular sodium leakage out of cells is associated with hypoxia and apoptosis in cancer. EGF: Epidermal Growth Factor, ECM: Extracellular matrix, and ETS: Electron Transport System.

they reached confluence. HBE cells on-top of rBME could display an acinar structure with a dead luminal space in the absence of epidermal growth factors (EGF) (**Figure 4(b)**). This simulated the ductal structures of breast epithelial cells found *in vivo*. Under the same condition, carcinoma cells exhibited colony overgrowth, luminal filling, and loss of intracellular sodium (**Figure 4(d)**). These changes eventually reduce the resistance against apoptosis and enhance the cell proliferation resulting in severe morphological deformities visible by microscopy and imaging as earlier reported elsewhere [37]. It was observed that EGF disrupted the formation of luminal structures of HBE either in monolayer or in 3 dimensional cell cultures with rBME. It may be attributed with the possibility if luminal structures bound with sodium get free by the disruption after adding EGF. When EGF was reduced or removed from the cultures, normal phenotypes (e.g. luminal structure and uniformed size) of human breast epithelial cell were obtained. With the variation of the time to reduce EGF, we could generate different sizes of luminal structure of HBE

### 3.3. Limitations of Sodium Contrast and Sensitivity

Due to high concentrations of extracellular sodium, its suppression by using inversion recovery pulses makes it difficult to get absolute intracellular sodium images. However, intracellular sodium images may be indicators of edema, interstitial space, cell proliferation, malignancy, and hypoxia as criteria to divide tumor dormancy, slow-growing, and fast growing regions. Newer techniques without the use of shift reagents using high reso-

lution RF coils generate  $3\text{D}^{23}\text{Na}$  images with high signal-to noise ratio in less than 15 minutes, permitting use of combined  $^{23}\text{Na}$  and  $^1\text{H}$  MR imaging protocols with total examination times of about 45 minutes. Moreover, sodium imaging in myocardium and cardiac ischemia is well investigated as a clinical tool.

## 4. CONCLUSIONS

A present state-of-art for sodium MR imaging is presented with a focus on quantum filters in pulse sequences and their variants in order to acquire intracellular sodium images with hands-on software pulse sequence design and MRI physics principles. Triple quantum filtering scheme and non-invasive inversion recovery fast spin-echo pulse sequences are described for distinct intracellular sodium MR images. Our experiments on breast tumors and isolated culture cells indicated the association of malignancy with increased intracellular sodium and reduced apoptosis and reduced EGF in cells with possibility of other growth factors involved.

## 5. ACKNOWLEDGEMENTS

The present work was supported by the grant GIA 0086 funded by Aventis Pharmaceutical Company Inc. for design and development of sodium MRI technique. Partly the work was presented at workshop ISMRM: Minimization of data acquisition with maximum outcome in 2002. The study for the normal and malignant breast epithelial cell culture was supported by NIH (1 R21 CA 131798-01A1).

## REFERENCES

- [1] I. L. Cameron, N. K. Smith, T. B. Pool, and R. L. Sparks,



- (1980) Intracellular concentration of sodium and other elements as related to mutagenesis and oncogenesis in vivo, *Cancer Res.*, **40**(5), 1493–500.
- [2] A. Amidsen and M. Schou, (1968) Lithium and the transfer rate of sodium across the blood-brain barrier, *Psychopharmacologia*, **12**(3), 236–238.
  - [3] B. J. Carroll, L. Steven, R. A. Pope, and B. Davies, (1969) Sodium transfer from plasma to CSF in severe depressive illness, *Arch. Gen. Psychiatry*, **21**(1), 77–81.
  - [4] M. E. Moseley, W. M. Chew, M. C. Nishimura, T. L. Richards, J. Murphy-Boesch, G. B. Young, T. M. Marschner, L. H. Pitts, and T. L. James, (1985) In vivo sodium-23 magnetic resonance surface coil imaging: Observing experimental cerebral ischemia in the rat, *Magn. Reson. Imaging*, **3**(4), 383–387.
  - [5] W. H. Perman, P. A. Turski, L. W., Houston, G. H. Glover, and C. E. Hayes, (1986) Methodology of in vivo human sodium MR imaging at 1.5 T, *Radiology*, **160**(3), 811–820.
  - [6] S. S. Winkler, D. M. Thomasson, K. Sherwood, and W. H. Perman, (1989) Regional T2 and sodium concentration estimates in the normal human brain by sodium-23 MR imaging at 1.5 T, *J. Comput. Assist. Tomogr.*, **13**(4), 561–566.
  - [7] J. M. Dizon, J. S. Tauskela, D. Wise, D. Burkoff, P. J. Cannon, and J. Katz, (1996) Evaluation of triple-quantum-filtered <sup>23</sup>Na NMR in monitoring of Intracellular Na content in the perfused rat heart: comparison of intra- and extracellular transverse relaxation and spectral amplitudes, *Magn. Reson. Med.*, **35**(3), 336–345.
  - [8] K. J. Jung and J. Katz, (1996) Chemical-shift-selective acquisition of multiple-quantum-filtered <sup>23</sup>Na signal, *J. Magn. Reson. B.*, **112**(3), 214–227.
  - [9] P. G. Morris, (1986) Nuclear magnetic resonance imaging in medicine and biology, Clarendon Press, Oxford, England, **123**.
  - [10] S. W. Lee, S. K. Hilal, and Z. H. Cho, (1986) A multinuclear magnetic resonance imaging technique-simultaneous proton and sodium imaging, *Magn. Reson. Imaging*, **4**(4), 343–350.
  - [11] P. J. Cannon, A. A. Maudsley, S. K. Hilal, H. E. Simon, and F. Cassidy, (1986) Sodium nuclear magnetic resonance imaging of myocardial tissue of dogs after coronary artery occlusion and reperfusion, *J. Am. Coll. Cardiol.*, **7**(3), 573–579.
  - [12] C. T. Moonen, S. E. Anderson, and S. Unger, (1987) <sup>23</sup>Na rotating frame imaging in the perfused rabbit heart using separate transmitter and receiver coils, *Magn. Reson. Med.*, **5**(3), 296–301.
  - [13] R. Ouwerkerk, K. B. Bleich, J. S. Gillen, M. G. Pomper, and P. A. Bottomley, (2003) Tissue sodium concentration in human brain tumors as measured with <sup>23</sup>Na MR imaging, *Radiology*, **227**(2), 529–3.
  - [14] F. E. Boada, G. X. Shen, S. Y. Chang, and K. R. Thulborn, (1997) Spectrally weighted twisted projection imaging: reducing T2 signal attenuation effects in fast three-dimensional sodium imaging, *Magn. Reson. Med.*, **38**(6), 1022–1028.
  - [15] I. Hancu, F. E. Boada, and G. X. Shen, (1999) Three-dimensional triple-quantum-filtered (<sup>23</sup>Na) imaging of in vivo human brain, *Magn. Reson. Med.*, **42**(6), 1146–1154.
  - [16] A. Borthakur, I. Hancu, F. E. Boada, G. X. Shen, E. M. Shapiro, and R. Reddy, (1999) In vivo triple quantum filtered twisted projection sodium MRI of human articular cartilage, *J. Magn. Reson.*, **141**(2), 286–290.
  - [17] K. J. Jung, P. J. Cannon, and J. Katz, (1997) Simultaneous acquisition of quadrupolar order and double-quantum <sup>23</sup>Na signals, *J. Magn. Reson.*, **129**(2), 130–133.
  - [18] L. M. Box, D. Hsu, J. Katz, P. Detweiler, S. McLaughlin, T. J. Kolb, and H. M. Spotnitz, (1993) Estimation of myocardial water content using transverse relaxation time from dual spin-echo magnetic resonance imaging, *Magn. Reson. Imaging*, **11**(3), 375–383.
  - [19] G. X. Shen, J. F. Wu, F. E. Boada, and K. R. Thulborn, (1999) Experimentally verified, theoretical design of dual-tuned, low-pass birdcage radiofrequency resonators for magnetic resonance imaging and magnetic resonance spectroscopy of human brain at 3.0 Tesla, *Magn. Reson. Med.*, **41**(2), 68–75.
  - [20] K. J. Jung, J. Katz, L. M. Box, S. K. Hilal, and Z. H. Cho, (1995) Breakthrough of single-quantum coherence and its elimination in double-quantum filtering, *J. Magn. Reson. B.*, **107**(3), 235–241.
  - [21] K. J. Jung, J. S. Tauskela, and J. Katz, (1996) New double-quantum filtering schemes, *J. Magn. Reson. B.*, **112**(2), 103–110.
  - [22] K. J. Jung and J. Katz, (1997) Mathematical analysis of generation and elimination of intersequence stimulated echo in double-quantum filtering, *J. Magn. Reson.*, **124**(1), 232–236.
  - [23] J. S. Tauskela, J. M. Dizon, J. Whang, and J. Katz, (1997) Evaluation of multiple-quantum-filtered <sup>23</sup>Na NMR in monitoring intracellular Na content in the isolated perfused rat heart in the absence of a hemical-shift reagent, *J. Magn. Reson.*, **127**(1), 115–127.
  - [24] V. A. Stenger, S. Peltier, F. E. Boada, and D. C. Noll, (1999) 3D spiral cardiac/respiratory ordered fMRI data acquisition at 3 Tesla, *Magn. Reson. Med.*, **41**(5), 983–991.
  - [25] H. Serrai, A. Borthakur, L. Senhadji, and R. Reddy, (2000) Bansal, N. Time-domain quantification of multiple-quantum-filtered (<sup>23</sup>Na) signal using continuous wavelet transform analysis, *J. Magn. Reson.*, **142**(2), 341–347.
  - [26] J. B. Ra, S. K. Hilal, C. H. Oh, and I. K. Mun, (1988) In vivo magnetic resonance imaging of sodium in the human body, *Magn Reson Med.*, **7**(1), 11–22.
  - [27] S. K. Hilal, A. A. Maudsley, J. B. Ra, H. E. Simon, P. Roschmann, S. Wittekoek, Z. H. Cho, and S. K. Mun, (1985) In vivo NMR imaging of sodium-23 in the human head, *J Comput Assist Tomogr*, **9**(1), 1–7.
  - [28] T. Hashimoto, H. Ikehira, H. Fukuda, A. Yamaura, O. Watanabe, Y. Tateno, R. Tanaka, and H. E. Simon, (1991) In vivo sodium-23 MRI in brain tumors: Evaluation of preliminary clinical experience, *Am J Physiol Imaging*, **6**(2), 74–80.
  - [29] K. L. Allen, A. L. Busza, S. R. Williams, and S. C. Williams (1994) Early changes in cerebral sodium distribution following ischaemia monitored by <sup>23</sup>Na magnetic resonance imaging, *Magn Reson Imaging*, **12**(6), 895–900.
  - [30] R. Sharma and R. P. Kline, (2004) Chemosensitivity assay in mice prostate tumor: Preliminary report of flow

- cytometry, DNA fragmentation, ion ratiometric methods of anti-neoplastic drug monitoring. *Cancer Cell International Cancer Cell International*, **4**(3).
- [31] R. P. Kline, E. X. Wu, D. P. Petrylak, M. Szabolcs, P. O. Alderson, M. L. Weisfeldt, P. Cannon, and J. Katz, (2000) Rapid in vivo monitoring of chemotherapeutic response using weighted sodium magnetic resonance imaging, *Clin Cancer Res.*, **6**(6), 2146–56.
- [32] P. M. Winter, V. Seshan, J. D. Makos, A. D. Sherry, C. R. Malloy, and N. Bansal, (1998) Quantitation of intracellular [Na<sup>+</sup>] in vivo by using TmDOTP5-as an NMR shift reagent and extracellular marker, *J Appl Physiol.* **85**(5), 1806–12.
- [33] P. M. Winter, H. Poptani, and N. Bansal, (2001) Effects of chemotherapy by 1,3-bis(2-chloroethyl)-1-nitrosourea on single-quantum- and triple-quantum-filtered <sup>23</sup>Na and <sup>31</sup>P nuclear magnetic resonance of the subcutaneously implanted 9L glioma, *Cancer Res.*, **61**(5).
- [34] J. M. Colet, N. Bansal, C. R. Malloy, and A. D. Sherry, (1999) Multiple quantum filtered <sup>23</sup>Na NMR spectroscopy of the isolated, perfused rat liver, *Magn Reson Med.* **41**(6), 1127–35.
- [35] R. Sharma, R. P. Kline, E. X. Wu, and J. K. Katz, (2005) Rapid in vivo Taxotere quantitative chemosensitivity response by 4.23 Tesla sodium MRI and histo-immunostaining features in N-Methyl-N-Nitrosourea induced breast tumors in rats, *Cancer Cell International*, **5**, 26.
- [36] R. Sharma, (2008) Extended expression for transverse magnetization using four pulse sequence to construct double quantum filter of arbitrary phases for spin 3/2 sodium nuclei, *International J. Computer Research*, **16**(4), 371–388.
- [37] R. Ouwerkerk, M. A. Jacobs, K. J. Macura, A. C. Wolff, V. Stearns, and S. D. Mezban, N. F. Khouri, D. A. Bluemke, and P. A. Bottomley, (2007) Elevated tissue sodium concentration in malignant breast lesions detected with non-invasive <sup>23</sup>Na MRI, *Breast Cancer Research and Treatment*, **106**(2), 151–60.

# Trends in global warming and evolution of polymerase basic protein 2 family from influenza A virus

Shao-Min Yan<sup>1</sup>, Guang Wu<sup>2</sup>

<sup>1</sup>National Engineering Research Center for Non-food Biorefinery, Guangxi Academy of Sciences, Nanning, China; <sup>2</sup>Computational Mutation Project, DreamSciTech Consulting, Shenzhen, China.  
Email: [hongguanglishibahao@yahoo.com](mailto:hongguanglishibahao@yahoo.com)

Received 9 June 2009; revised 25 June 2009; 29 June 2009.

## ABSTRACT

Both global warming and influenza trouble humans in varying ways, therefore it is important to study the trends in both global warming and evolution of influenza A virus, in particular, proteins from influenza A virus. Recently, we have conducted two studies along this line to determine the trends between global warming and polymerase acidic protein as well as matrix protein 2. Although these two studies reveal some interesting findings, many studies are still in need because at least there are ten different proteins in influenza A virus. In this study, we analyze the trends in global warming and evolution of polymerase basic protein 2 (PB2) from influenza A virus. The PB2 evolution from 1956 to 2008 was defined using the unpredictable portion of amino-acid pair. Then the trend in this evolution was compared with the trend in the global temperature, the temperature in north and south hemispheres, and the temperature in influenza A virus sampling site and species carrying influenza A virus. The results show the similar trends in global warming and in PB2 evolution, which are in good agreement with our previous studies in polymerase acidic protein and matrix protein 2 from influenza A virus.

**Keywords:** Global Warming; Influenza; Virus; Polymerase Basic Protein 2

## 1. INTRODUCTION

Changes in environmental conditions can rapidly shift allele frequencies in populations of species with relatively short generation times [1]. The global warming imposes the new danger not only on environments, but also on humans and various species [2]. As a result we would see the composition of species, such as proteins,

under the influence of global warming although some proteins could be hidden deeply inside cells. Thus, it is important to compare the trends in global warming and protein evolution of interest family in order to see if there are similar trends in both.

Accordingly, we recently conducted two studies to analyze the trend in both global warming and evolution of polymerase acidic protein (PA) [3] and matrix protein 2 [4] from influenza A virus.

It is well known that the evolution of protein family is a process of mutations, and therefore we could represent this evolution if we could represent mutated proteins along the time course. We need to do so because the global warming is the change in temperature over time. However, a mutation in protein is an event of changing one letter to another because amino acids in protein are presented as 20 letters, which are neither scalar data nor vectors, whereas the temperature is a scalar datum.

This means that we need to convert the letter-based proteins into scalar data in order to plot them along the time course to see their evolutionary trend. Since 1999, our group has developed three approaches to convert either a single amino acid or a protein into a scalar datum based on random principle (for review, see [5,6,7,8]). Using our approaches, we can effectively represent a protein family over time, which provides the basis for conducting the study on analyzing the trends in global warming and evolution of proteins of interest.

At this moment, we are particularly interest in the polymerase basic protein 2 (PB2) from influenza A virus, because it is a subunit of RNA-dependent RNA polymerase complex associated with the transcription and replication of the influenza A viral genome [9]. The PB2 subunit interacts with PA in the cytoplasm initially and is subsequently transported as a dimer into the nucleus [10]. The viral RNA polymerase complex is important for the efficient propagation of the virus in the host and for its adaptation to new hosts [11], and considered as a major determinant of the pathogenicity of the 1918 pandemic virus [12].

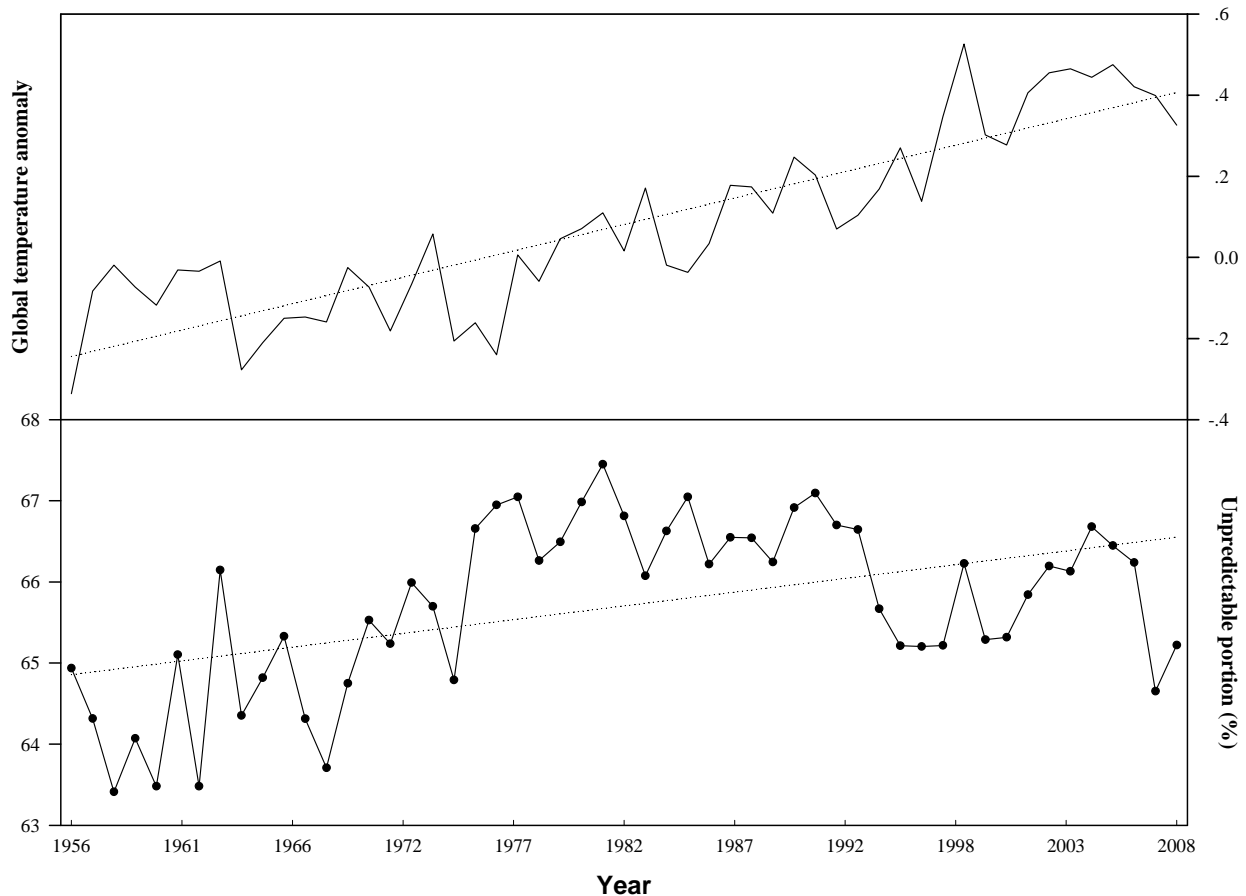


**Figure 1.** Global temperature anomaly ( $^{\circ}\text{C}$ ) and evolution of PB2 proteins from influenza A viruses. The dotted lines and points were regressed lines and the mean of all PB2 proteins at a given year ( $n = 2397$  from 1956 to 2008).

The mutations in PB2 protein can affect the virulence of influenza A virus [13], change RNA binding activity [14,15], and contribute to intra- and inter-host transmission in diverse virus backgrounds [15,16].

The aim of this study is to use the unpredictable portion of amino-acid pair to convert symbolised PB2 proteins into numerical data, and then to analyze the trends in global warming and the evolution of PB2 proteins from influenza A virus, in order to explore the potential impact of global warming on protein evolution.

## 2. MATERIALS AND METHODS

### 2.1. Temperature Data

The global, north and south hemispheric temperature anomalies from 1850 to 2007, whose anomaly is based on the period 1961-1990, were obtained from HadCRUT3v [17,18]. The local temperature from 1956 to 1998 based on  $0.5^{\circ}$  by  $0.5^{\circ}$  latitude and longitude grid-box basis cross globe was obtained from New *et al.* [19].

### 2.2. PB2 Data

A total of 5092 full-length PB2 sequences of influenza A

virus sampled from 1956-2008 was obtained from the influenza virus resources [20]. After excluded identical sequences, 2397 PB2 proteins were used in this study.

### 2.3. Converting PB2 Proteins into Scalar Data

For presenting PB2 protein family along the time course, we need to convert each PB2 protein into a scalar datum, which must differ for different PB2 proteins. Among our three random approaches (for review, see [5,6,7,8]), the simplest one is the amino-acid pair predictability, by which we view if the combination of two adjacent amino acids can be explained by the permutation. For a whole protein, we can determine the percentage of how many amino-acid pairs can be predicted according to the permutation. We have used this method in many studies (for publications in 2008, see [21,22,23,24,25]).

For a PB2 protein, we counted the first and second amino acids as a pair, the second and third amino acids as another pair, until the next to terminal and the terminal amino acids as the last pair. Then, we determined whether an amino-acid pair could be explained by permutation, or predicted by random mechanism in other



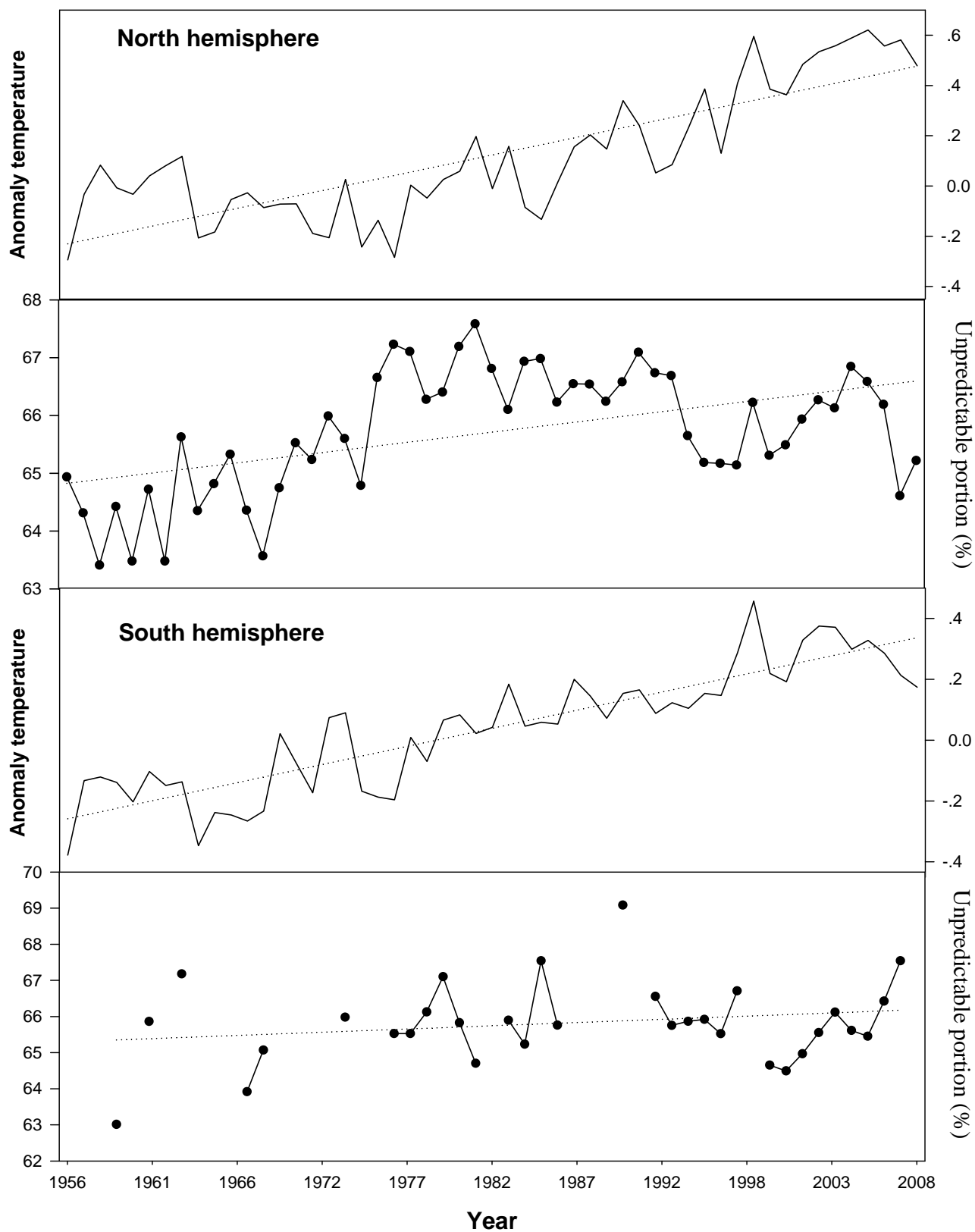


**Figure 2.** Trends in temperature and PB2 evolution grouped according to north ( $n = 2177$ ) and south ( $n = 220$ ) hemispheres. The dotted lines were regressed lines.

words. Finally, we calculated the percentage of how many amino-acid pairs were predictable and unpredictable in a PB2 protein.

For example, a PB2 protein (strain A/Virginia/UR06-0139/2007(H1N1) and accession number ABW40267) was composed of 759 amino acids. There were 53 threonines “T” and 59 arginines “R” in this protein. If the appearance of amino-acid pair TR could be explained by the permutation, it would appear 4 times in the PB2 protein ( $53/759 \times 59/758 = 4.12$ ). Actually there were 4 pairs of TR in it, so the appearance of TR was predictable. By clear contrast, there were 34 asparagines “N” and 28 prolines “P” in this PB2 protein. According to the permutation, the amino-acid pair NP would appear once ( $34/759 \times 28/758 = 1.25$ ) in this protein. However, it appeared 5 times in reality, which was unpredictable. In this way, we classified all of the amino-acid pairs in ABW40267 PB2 protein as predictable and unpredictable.

It is absolutely necessary that the predictable/unpredictable portion is subject to a tiny difference between two PB2 proteins, thus different PB2 proteins should have different values to be distinguishable. In the past, we have tested many proteins to verify this request and

got the positive answer [3,4,5,6,7,8,21,22,23,24,25]. For instance, the predictable and unpredictable portions were 36.49% and 63.51% for ABW40267 PB2 protein. Another human H1N1 influenza A virus was isolated from USA in 2007, its PB2 protein (accession number ABW 40410) had only one amino acid at position 108 different from that of ABW40267 PB2 protein. However, its predictable and unpredictable portions were 36.82% and 63.18%.

In this manner, we converted 2397 letter-symbolized PB2 proteins into 2397 scalar data [26]. As each PB2 protein had its sampling year, we thus had two scalar datasets, the temperature recorded each year and the unpredictable portion of PB2 protein sampled each year. Hence we could plot both datasets along the time course to observe their trends.

### 3. RESULTS AND DISCUSSION

**Figure 1** showed the trends in both global warming and evolution of PB2 proteins, where both trends revealed similar as indicated by their regressed lines. The unpredictable portion of PB2 proteins increased over time, which was similar to that the global temperature increased along the time course.

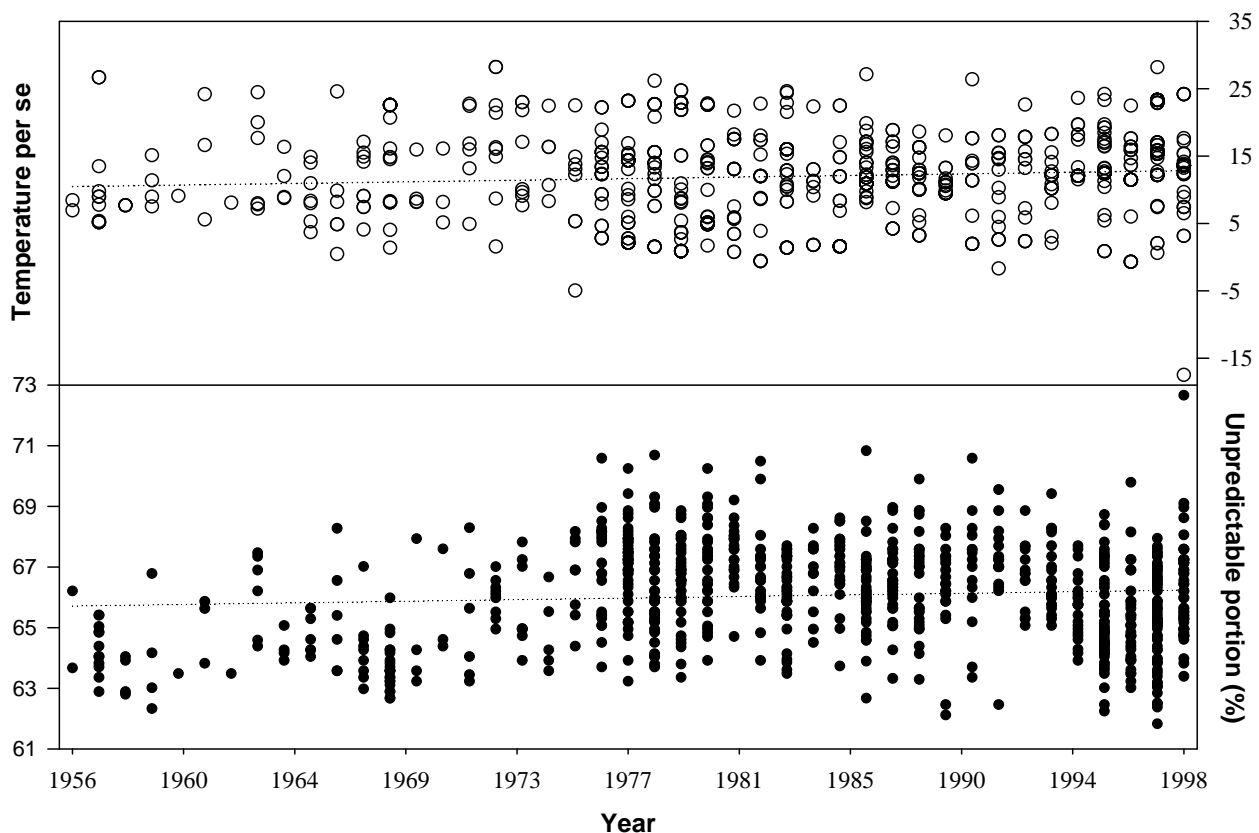


**Figure 3.** Point-to-point temperature versus PB2 proteins ( $n=828$ ) from 1956 to 1998. Each point presented a local temperature ( $^{\circ}\text{C}$ ) at the given year (upper panel), corresponding to the place where a PB2 protein was sampled (lower panel). The dotted lines were regressed lines.

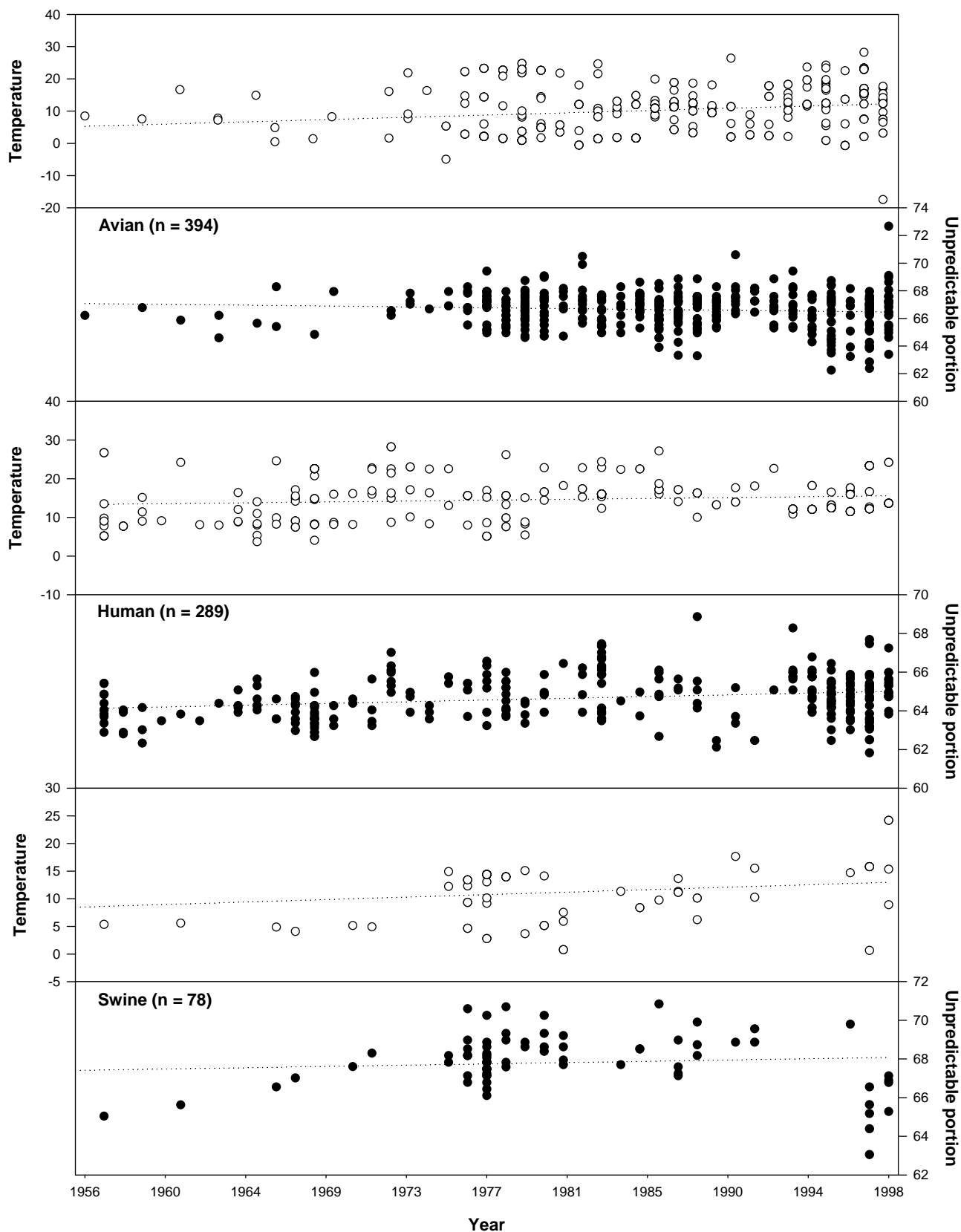


**Figure 4.** Point-to-point temperature (°C) versus PB2 proteins sampled from different species. The dotted lines were regressed lines.

Moreover, the global temperature was generally divided into north and south hemisphere, so we could group PB2 proteins accordingly to see if the trend still held on in such circumstance. As shown in **Figure 2**, the similar trend was clearer in north hemisphere than in south one, which could be explained by the fact that most of PB2 proteins were sampled in north hemisphere.

Actually the data of PB2 proteins in **Figures 1 and 2** were averaged in each year. For example, there were only 2 samples in 1956, but 220 PB2 proteins were sampled in 2007. Another way to analyze the trends is to apply the point-to-point method, that is, we coupled each PB2 protein with the temperature according to its sampling place and year. In other word, we took the temperature measured at each geographical latitude and longitude of the place where a PB2 protein was sampled at the same year to make the comparison.

**Figure 3** displayed 828 point-to-point relationships between temperature and unpredictable portion of PB2 proteins from 1956 to 1998, and their regression indicated the similar trends. The results in **Figure 3** were in consistent with what we found in **Figures 1 and 2**, that is, there were similar trends between global warming and evolution of PB2 proteins.

Because influenza viruses were hosted in different species, we could advance our analysis by the point-to-point relationship between temperature and species, from which the PB2 proteins were sampled. **Figure 4** demonstrated the trends of PB2 evolution with respect to the temperature in three major species. The results suggested that the trends were similar in human and swine, but different in avian.

In this study, we found the similar trends in global warming and the evolution of PB2 proteins from influenza A viruses. This is very suggestive, because this founding indicates that the effect of global warming on many different levels on biological evolution, even the proteins hidden inside cell could be subject to the global warming. This is understandable because all of the biological functions are interconnected from macro level to micro level.

However, can we correlate both trends in this study statistically? At this stage, it would be difficult to determine such correlation because 1) to the best of our knowledge there is no statistical method available to determine the correlation between two lines including a discontinued one in this study; and 2) many statistical books tell that the correlation does not mean the cause-consequence relationship, that is, even we would find the so-called correlation between two trends, we still need to determine if there is any direct or indirect cause-consequence relationship.

On the other hand, we cannot ignore these trends be-

cause we cannot create another earth without global warming but with active influenza virus for comparison over the same time span. As the validation of global warming is done through the comparison along the time course, we would argue that the validation of PB2 evolution should also be done along the time course, i.e. the comparison between any two different time points.

This study demonstrated the changes in the unpredictable portions of PB2 proteins were different in different species. In human and swine, the trends of evolution of PB2 proteins were similar to that of temperature, but not in avian (**Figure 4**). This difference can be due to the fact that the place where avian was sampled would not be the place where the mutation occurred, because migratory birds are common reservoirs responsible for spreading avian influenza viruses [28,29,30,31]. Climate change would almost certainly alter bird migration, influence the avian influenza virus transmission cycle and directly affect virus survival outside the host [32,33]. On the other hand, the human and swine were generally localized, thus the present results indicate the potential impact of global warming on the evolution of influenza A viruses.

Global climate changes affect the functioning of ecosystems, in particular host-pathogen interactions, with major consequences in health ecology [34,35,36]. The results in this study are in good agreement with our previous studies [3,4], thus these results furthermore suggest the general trend in evolution of proteins from influenza A virus. However, much studies are in need because there are still seven other proteins from influenza A virus, which we have yet to study.

#### 4. ACKNOWLEDGEMENTS

This study is supported in part by Guangxi Science Foundation No. 0782003-4, 0991080 and Guangxi Academy of Sciences, project 09YJ17SW07.

#### REFERENCES

- [1] A. A. Hoffmann and Y. Willi, (2008) Detecting genetic responses to environmental change, *Nat. Rev. Genet.*, **9**, 421–432.
- [2] C. D. Thomas, A. Cameron, R. E. Green, M. Bakkenes, L. J. Beaumont, Y. C. Collingham, B. F. Erasmus, M. F. De Siqueira, A. Grainger, L. Hannah, L. Hughes, B. Huntley, A. S. Van Jaarsveld, G. F. Midgley, L. Miles, M. A. Ortega-Huerta, A. T. Peterson, O. L. Phillips, and S. E. Williams, (2004) Extinction risk from climate change, *Nature*, **427**, 145–148.
- [3] G. Wu and S. Yan, (2009) What these trends suggest? *Am. J. Appl. Sci.*, **6**, 1116–1121.
- [4] G. Wu and S. Yan, (2009) Trends in global warming and evolution of matrix protein 2 family from influenza A virus, *Interdiscip. Sci. Comput. Life. Sci.*, (in press).
- [5] G. Wu and S. Yan, (2002) Randomness in the primary structure of protein: methods and implications, *Mol. Biol. Today*, **3**, 55–69.



- [6] G. Wu and S. Yan, (2006) Fate of influenza A virus proteins, *Protein Pept. Lett.*, **13**, 399–406.
- [7] G. Wu and S. Yan, (2006) Mutation trend of hemagglutinin of influenza A virus: A review from computational mutation viewpoint, *Acta Pharmacol. Sin.*, **27**, 513–526.
- [8] G. Wu and S. Yan, (2008) Lecture notes on computational mutation, Nova Science Publishers, New York.
- [9] O. G. Engelhardt and E. Fodor, (2006) Functional association between viral and cellular transcription during influenza virus infection, *Rev. Med. Virol.*, **16**, 329–345.
- [10] J. N. Hemerka, D. Wang, Y. Weng, W. Lu, R. S. Kaushik, J. Jin, A. F. Harmon, and F. Li, (2009) Detection and characterization of influenza A virus PA-PB2 interaction through a bimolecular fluorescence complementation assay, *J. Virol.*, **83**, 3944–3955.
- [11] N. Van Hoeven, C. Pappas, J. A. Belser, T. R. Maines, H. Zeng, A. García-Sastre, R. Sasisekharan, J. M. Katz, and T. M. Tumpey, (2009) Human HA and polymerase subunit PB2 proteins confer transmission of an avian influenza virus through the air, *Proc. Natl. Acad. Sci., U. S. A.*, **106**, 3366–3371.
- [12] T. Watanabe, S. Watanabe, K. Shinya, J. H. Kim, M. Hatta & Y. Kawaoka, (2009) Viral RNA polymerase complex promotes optimal growth of 1918 virus in the lower respiratory tract of ferrets, *Proc. Natl. Acad. Sci. U. S. A.*, **106**, 588–592.
- [13] M. Hatta and Y. Kawaoka, (2002) The continued pandemic threat posed by avian influenza viruses in Hong Kong, *Trends Microbiol.*, **10**, 340–344.
- [14] T. Kuzuhara, D. Kise, H. Yoshida, T. Horita, Y. Murazaki, A. Nishimura, N. Echigo, H. Utsunomiya, and H. Tsuge, (2009) Structural basis of the influenza A virus RNA polymerase PB2 RNA-binding domain containing the pathogenicity-determinant lysine 627 residue, *J. Biol. Chem.*, **284**, 6855–6860.
- [15] J. Steel, A. C. Lowen, L. Pena, M. Angel, A. Solórzano, R. Albrecht, D. R. Perez, A. García-Sastre, and P. Palese, (2009) Live attenuated influenza viruses containing NS1 truncations as vaccine candidates against H5N1 highly pathogenic avian influenza, *J. Virol.*, **83**, 1742–1753.
- [16] Q. M. Le, Y. Sakai-Tagawa, M. Ozawa, M. Ito, and Y. Kawaoka, (2009) Selection of H5N1 influenza virus PB2 during replication in humans, *J. Virol.*, **83**, 5278–5281.
- [17] N. A. Rayner, P. Brohan, D. E. Parker, C. K. Folland, J. J. Kennedy, M. Vanicek, T. Ansell, and S. F. B. Tett, (2006) Improved analyses of changes and uncertainties in marine temperature measured in situ since the mid nineteenth century: The HadSST2 dataset, *J. Clim.*, **19**, 446–469.
- [18] Climatic Research Unit, (2009) <http://www.cru.uea.ac.uk/cru/data/temperature/>.
- [19] M. New, M. Hulme, and P. Jones, (2000) Representing twentieth-century space-time climate variability, Part II: Development of 1901–96 monthly grids of terrestrial surface climate, *J. Clim.*, **13**, 2217–2238.
- [20] Influenza virus resources, (2009) <http://www.ncbi.nlm.nih.gov/genomes/FLU/Database/multiple.cgi>.
- [21] G. Wu and S. Yan, (2008) Prediction of mutations engineered by randomness in H5N1 neuraminidases from influenza A virus, *Amino Acids*, **34**, 81–90.
- [22] G. Wu and S. Yan, (2008) Prediction of mutations initiated by internal power in H3N2 hemagglutinins of influenza A virus from North America, *Int. J. Pept. Res. Ther.*, **14**, 41–51.
- [23] G. Wu and S. Yan, (2008) Prediction of mutation in H3N2 hemagglutinins of influenza A virus from North America based on different datasets, *Protein Pept. Lett.*, **15**, 144–152.
- [24] G. Wu and S. Yan, (2008) Prediction of mutations engineered by randomness in H5N1 hemagglutinins of influenza A virus, *Amino Acid*, **35**, 365–373.
- [25] G. Wu and S. Yan, (2008) Three sampling strategies to predict mutations in H5N1 hemagglutinins from influenza A virus, *Protein Pept. Lett.*, **15**, 731–738.
- [26] Amino-acid pair predictability, (2009) <http://www.dreamscitech.com/Service/rationale.htm>.
- [27] Get Lat Lon, (2009) <http://www.getlatlon.com/>.
- [28] S. Krauss, D. Walker, S. P. Pryor, L. Niles, L. Chenghong, V. S. Hinshaw, and R. G. Webster, (2004) Influenza A viruses of migrating wild aquatic birds in North America, *Vector Borne Zoonotic Dis.*, **4**, 177–189.
- [29] L. Z. Garamszegi and A. P. Møller, (2007) Prevalence of avian influenza and host ecology, *Proc. Biol. Sci.*, **274**, 2003–2012.
- [30] T. P. Weber & N. I. Stilianakis, (2007) Ecologic immunology of avian influenza (H5N1) in migratory birds, *Emerg. Infect. Dis.*, **13**, 1139–1143.
- [31] A. Jahangir, Y. Watanabe, O. Chinen, S. Yamazaki, K. Sakai, M. Okamura, M. Nakamura & K. Takehara, (2008) Surveillance of avian influenza viruses in Northern pintails (*Anas acuta*) in Tohoku District, Japan, *Avian Dis.*, **52**, 49–53.
- [32] M. Gilbert, J. Slingenbergh & X. Xiao, (2008) Climate change and avian influenza, *Rev. Sci. Tech.*, **27**, 459–466.
- [33] Louchart, (2008) Emergence of long distance bird migrations: A new model integrating global climate changes, *Naturwissenschaften*, **95**, 1109–1119.
- [34] S. de La Rocque, J. A. Rioux & J. Slingenbergh, (2008) Climate change: effects on animal disease systems and implications for surveillance and control, *Rev. Sci. Tech.*, **27**, 339–354.
- [35] S. Morand & J. F. Guégan, (2008) How the biodiversity sciences may aid biological tools and ecological engineering to assess the impact of climatic changes, *Rev. Sci. Tech.*, **27**, 355–366.
- [36] E. A. Gould & S. Higgs, (2009) Impact of climate change and other factors on emerging arbovirus diseases, *Trans. R. Soc. Trop. Med. Hyg.*, **103**, 109–121.

# Diabetic diagnose test based on PPG signal and identification system

Hadis Karimipour<sup>1</sup>, Heydar Toossian Shandiz<sup>1</sup>, Edmond Zahedi<sup>2</sup>

<sup>1</sup>School of Electrical Engineering, Shahrood University of Technology, Shahrood, Iran; <sup>2</sup>School of Electrical Engineering, Sharif University of technology, Tehran, Iran.

Email: [h\\_karimipour@yahoo.com](mailto:h_karimipour@yahoo.com); [zahedy@sharif.edu](mailto:zahedy@sharif.edu)

Received 11 May 2009; revised 29 June 2009; accepted 6 July 2009.

## ABSTRACT

In this paper, photoplethysmogram (PPG) signals from two classes consisting of healthy and diabetic subjects have been used to estimate the parameters of Auto-Regressive Moving Average (ARMA) models. The healthy class consists of 70 healthy and the diabetic classes of 70 diabetic patients. The estimated ARMA parameters have then been averaged for each class, leading to a unique representative model per class. The order of the ARMA model has been selected as to achieve the best classification. The resulting model produces a specificity of %91.4 and a sensitivity of, %100. The proposed technique may find applications in determining the diabetic state of a subject based on a non-invasive signal.

**Keywords:** PPG Signal; Diabetic; Identification; ARMA Model

## 1. INTRODUCTION

Diabetes has been recognized as fourth leading cause of death in developed countries. Prediction based on recorded data in health centers worldwide shows that it is reaching epidemic proportions in many developing and newly industrialized nations [1].

When the body has difficulty regulating the amount of glucose in the blood stream Diabetes Mellitus has been occurred. Rising of the blood sugar level which will lead to hyperglycemia or hypoglycemia is due to the glucose accumulates in the bloodstream [2-3]. Glucose level above 150- 160mg/dl for long time poses significant health risk with possible long lasting effect [4]. Easy, low cost and on time recognizing diabetic with simple method and portable technology for the primary care and community-based clinical settings is the main goal of researchers in this area. The PPG technology has been used in a wide range of commercially available medical

devices for measuring oxygen saturation, blood pressure and cardiac output [5]. Due to change in glucose level, the amount of blood volume in the figure changes, this variation can be measured by PPG. When a fixed source of infrared radiation is used, the variation of blood volume act as a phototransistor and the receive signal is changed. This is why we use the PPG signal for recognizing the diabetic. In this work by filtering on photoplethysmography (PPG) signal and estimate ARMA model for healthy and patient, a method for recognizing diabetic is proposed. Field data shows this method work properly.

## 2. METHODOLOGY

Identification systems methods are the best way for finding mathematic description of a black box. **Figure 1** shows such a system in which only input and output terminals are introduced.

If there is no a noise source inside the system or measurement input and output are noise free, the number of unknown parameters in the system can determine the number of required measurements. As the real systems mathematically describe with finite parameter, everybody can determine the model easily. Perturbation in the system parameter and noise in the measurements lead to parameter estimation of the system.

**Figure 2** shows the flow chart of each system identification method. The prior knowledge is used in all part of the model calculation. Based on the prior knowledge the experiment is set up to produce the data. The data have to be as much as informative. The observer adjusts the frequency content and amplitude of the input signals in the system with external input or chose the probability density function (PDF) in the system with unknown input.

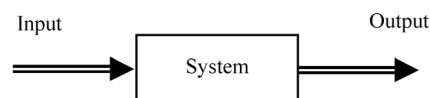


**Figure 1.** A black box system.

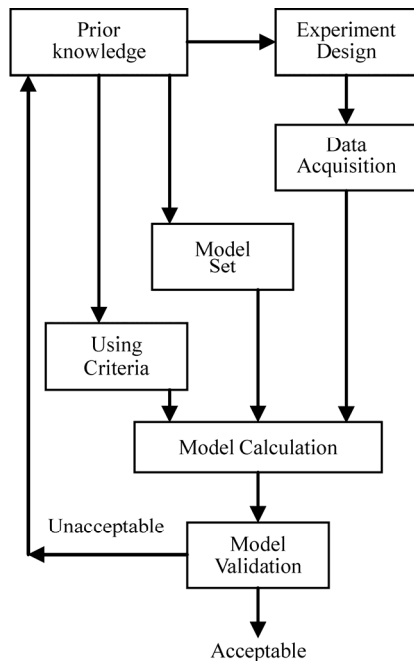


**Figure 2.** System identification flow chart.

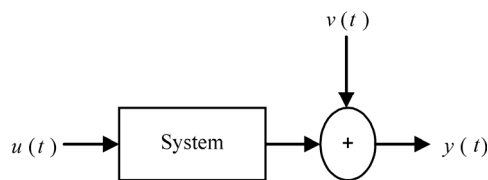


**Figure 3.** Modeling disturbance.

Choosing model set is second step in system identification based on prior knowledge. Different set of model is chosen, by considering number of input and output, linearity or nonlinearity, coupling or uncoupling between inputs and outputs, discrete or continuous in time, frequency domain or time domain, application of calculated model for simulation, simplifying, controlling or inverse engineering.

**Figure 3** shows a linear, time invariant, single input and output (SISO) model in which disturbance in system parameters and noise in measurement are modeled as additive in output [6]. This kind of model set is described as:

$$y(t) = \sum_{k=1}^{n_a} a_k y(t-k) + \sum_{k=0}^{n_b} b_k u(t-k) + v(t) \quad (1)$$

In which  $y(t)$  is output and  $u(t)$  is input,  $v(t)$  is disturbance which is modeled as:

$$v(t) = \sum_{k=0}^{n_c} c_k e(t-k) \quad (2)$$

where,  $e(t)$  is white noise.

The produced data are used to calculate the coefficients  $a_i, b_i$  and  $c_i$  of the model.

Next step is using criteria. Least square mean error (LSE) is used as the positive and negative error is the same and small error becomes smaller and big error become much bigger. The model rewrite as follow:

$$y(t) = \varphi(t)\theta \quad (3)$$

In which data are put in  $\varphi(t)$  and  $\theta$  contain all unknown parameter.

As the data is mixed with the measurement noise only an estimation of  $\theta$  can be calculated. There are many criteria, we chose minimization of error between real output and model output as follow:

$$V(\theta, Z^N) = \frac{1}{N} \sum_{t=1}^N e^2(t) \quad (4)$$

In which  $Z^N$  is input - output measured data and

$$e(t) = y(t) - \varphi(t)\theta \quad (5)$$

Therefore

$$\hat{\theta} = \arg \min_{\theta} V(\theta, Z^N) \quad (6)$$

The last step in model estimation is model validation. If in some sense the output of the model is fitted on the output of the system the estimated model is accepted otherwise the process is repeated again.

Model in **Figure 3**, is called autoregressive moving average extra input (ARMAX). Autoregressive means  $y(t)$  depend on previous amount of it. X stand for external input  $u(t)$  and MA stand for moving average refer to last term in **Figure 3**.

In the following subsections the proposed method is explained.

## 2.1. Model Selection

As there is no exact information about causes which affected PPG signal, ARMA model is used to model healthy and patient. The output of such system called time series. **Figure 4** shows such systems.

In order to modeling the system mathematically equation 1 reduced to 7:

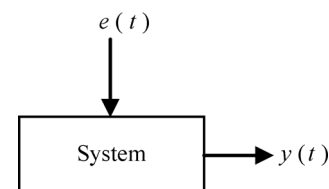


**Figure 4.** Modeling time series.

$$y(t) = \sum_{k=1}^{n_a} a_k y(t-k) + \sum_{k=0}^{n_c} c_k e(t-k) \quad (7)$$

In which  $y(t)$  is PPG signal as output and white noise  $e(t)$  with zero mean and variance  $\lambda$  as input. This is like other time series analysis, such as vocal system, weather system, in which an effect without cause is in our hand.

The process of finding model is as follow:

Each patient and healthy data is used to calculate an ARMA model individually then the average of all models for each group is evaluated as the ARMA model for that category. After testing polynomials with deference dimensions, it was found that the  $n_a=15$  and  $n_c=11$  for patient model's parameter and  $n_a=15$  and  $n_c=10$  for healthy model's parameter, give the best result.

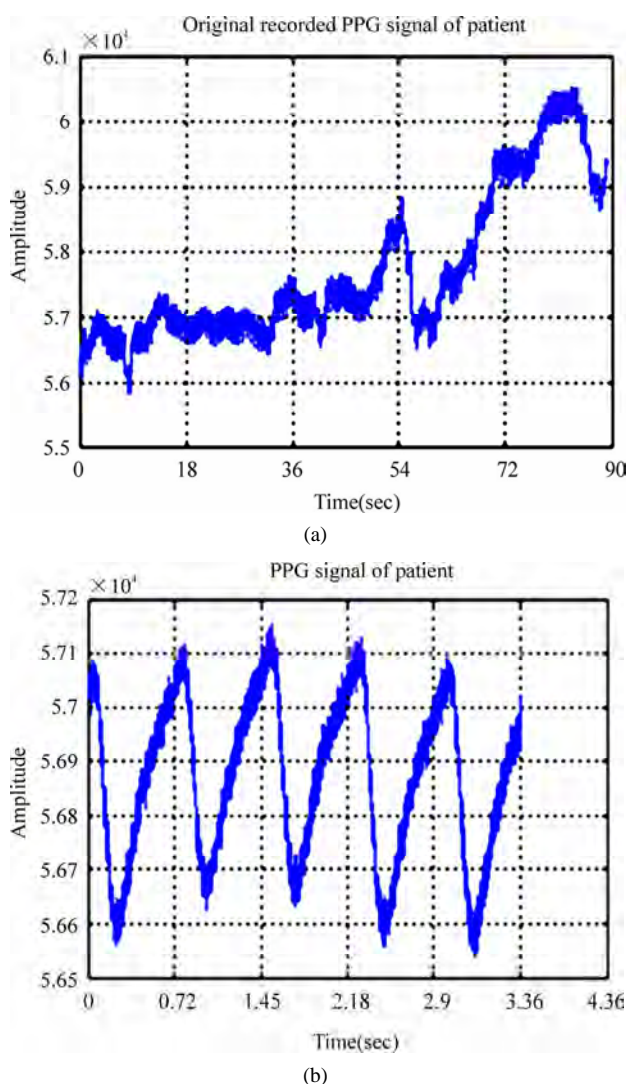


**Figure 5.** (a) recorded PPG signal and (b) one stable part with 1000 sample of it.

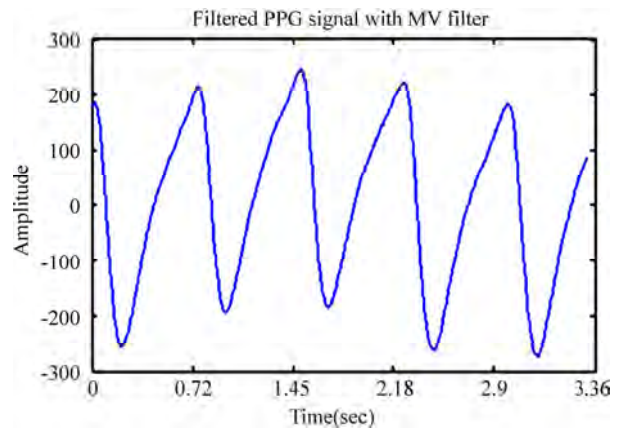


**Figure 6.** Result of applying moving average on healthy PPG signal.

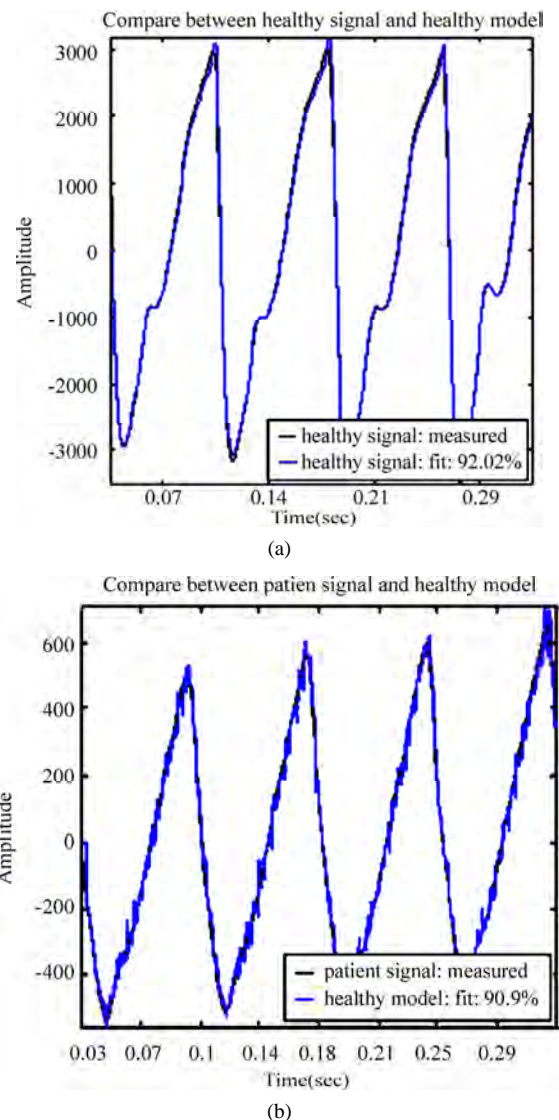
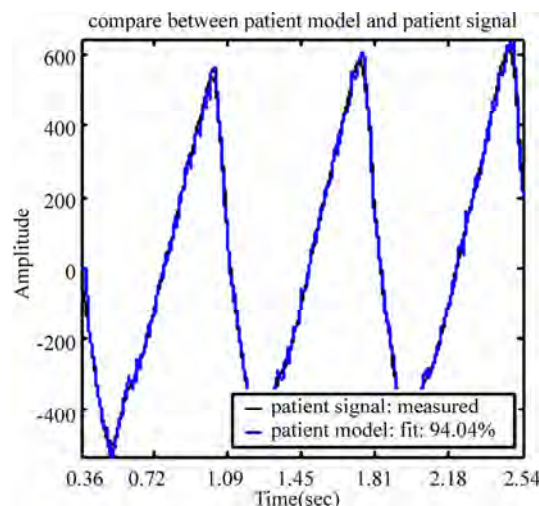
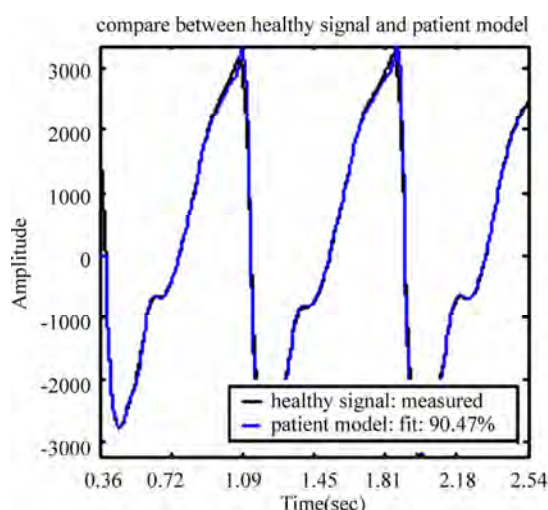


**Figure 7.** Result of applying (a) Patient PPG signal and (b) healthy PPG signal on the healthy model.





(a)



(b)

**Figure 8.** Result of applying (a) Patient PPG signal and (b) healthy PPG signal on the patient model.

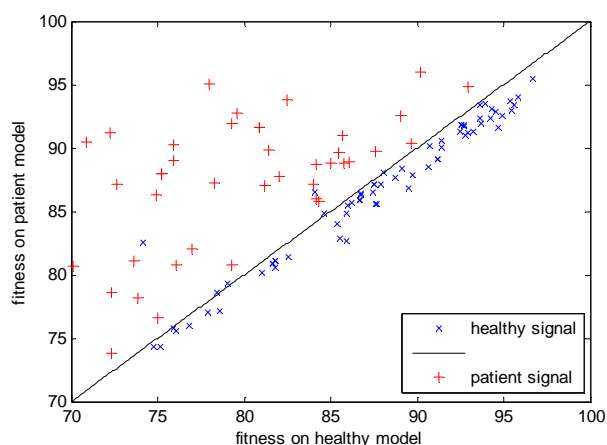


**Figure 9.** Result of applying PPG signal on the patient and healthy model.

## 2.2. Experimental Setup

There are two array groups of PPG signals. Pathologic arrays contain data from all subject tested in the hospital who were diabetic (39-64 years ages). Healthy arrays contain all data from healthy subjects (22-52 years old).

**Figure 1** shows a recorded PPG signal for a diabetic patient.

In each file, the only variable is a (50x24750) which is the raw PPG data:

- Each row is one particular lead.
- First column: subject number: Sb
- Second column: lead number: Ld
- Third column: Age
- Fourth column up to end: raw PPG data
- The length of the files has been limited to 90 sec (sampled at 275 Hz, this gives 24750 sample points)
- The number of rows (records) has been limited to 50 per file to limit file size
- The format of the data is uint32 to save on space.

## 2.3. Criteria and Model Validation

The MATLAB identification toolbox is used to calculate model parameter. The LSE is used as criteria and output matching as model validation.

## 3. PRACTICAL RESULTS

**Figure 5** shows a sample of PPG signal of healthy and patient which is recorded in a hospital.

The additive noise corrupts the PPG signals. Moving average filter is used to remove disturbance from signal.

**Figure 6** shows output of the filter.

**Figure 7** and **8** show the result of applying Healthy and patient PPG signal on estimated model for healthy and patient samples.

There are two areas in **Figure 9**, if data fit on healthy model better than patient model, there is a point under the line (subject is healthy) and inverse .the point on the line shows possibility of wrong classification.

As **Table 1** shows the proposed method can calcify healthy person and patient by 100% and 94%, respectively.

Simulation result shows that, specificity, sensitivity, negative predictive value (NPV) and positive predictive

**Table 1.** Contingency table.

		Data	
		Healthy	Patient
Classification result	Patient Healthy	%94	%0
	Patient Healthy	%6	%100



value (PPV) is % 91.4, % 100, % 100, and % 92.1 respectively.

#### 4. CONCLUSIONS

The proposed technique using non-invasive PPG signals is able to separate healthy subjects from patients using an ARMA model. One potential application of these models could be to estimate the state of diabetes of patients and eventually be used in controlling the amount of insulin needed to be injected to diabetic people.

#### 5. ACKNOWLEDGEMENTS

The authors gratefully acknowledge the PPG signals kindly provided by the Faculty of Engineering and Built Environment, University Kebangsaan Malaysia.

#### REFERENCES

- [1] D. Gan, editor, (2003) Diabetes atlas, 2nd Edition, Brussels: International Diabetes Federation,
- [2] <http://www.eatlas.idf.org/webdata/docs/Atlas%202003-Summary.pdf>.
- [3] H. L. Wee, H. K. Ho, and S. C. Li, (2002) Public awareness of diabetes mellitus in singapore, J .Singapore Med **43**(3), 128–134.
- [4] Cesar Carlos Romanillos Palerm, (2003) Drug infusion control: An extended direct model reference adaptive control strategy, PhD thesis, Rensselaer Polytechnic Institute, Troy, New York.
- [5] V. Carmen Doran, H. Nicolas Hudson, T. Katherine, J. Moorhead, Geoffrey Chase, M. Geoffrey Shaw, and E. Chris Hann, (2004) Derivative weighted active insulin control modelling and clinical trials for ICU patients, Elsevier ju, Medical Engineering & Physics.
- [6] V. K. Jayasree, T. V. Sandhya, and P. Radhakrishnan (2008) Non-invasive studies on age related parameters using a blood volume pulse sensor, Measurment Science Reveiw, **8**(4), Section 2.
- [7] L. Ljung, (1999) System identification: theory for user, Second edition, Prentice Hall.

Call for Papers



IEEE



**The 4<sup>th</sup> International Conference on Bioinformatics and Biomedical Engineering  
(iCBBE 2010)**

June 18-20, 2010

Chengdu, China

The 4<sup>th</sup> International Conference on Bioinformatics and Biomedical Engineering (iCBBE 2010) will be held from June 18<sup>th</sup> to 20<sup>th</sup>, 2010 in Chengdu, China. You are welcome to share your recent advances and achievements in all aspects of bioinformatics and biomedical engineering on the conference. **And all accepted papers in iCBBE 2010 will be published by IEEE and indexed by Ei Compendex and ISTP.**

**Topics**

**Bioinformatics and Computational Biology**

- Protein structure, function and sequence analysis
- Protein interactions, docking and function
- Computational proteomics
- DNA and RNA structure, function and sequence analysis
- Gene regulation, expression, identification and network
- Structural, functional and comparative genomics
- Computer aided drug design
- Data acquisition, analysis and visualization
- Algorithms, software, and tools in Bioinformatics
- Any novel approaches to bioinformatics problems

**Biomedical Engineering**

- Biomedical imaging, image processing & visualization
- Bioelectrical and neural engineering
- Biomechanics and bio-transport
- Methods and biology effects of NMR/CT/ECG technology
- Biomedical devices, sensors and artificial organs
- Biochemical, cellular, molecular and tissue engineering
- Biomedical robotics and mechanics
- Rehabilitation engineering and clinical engineering
- Health monitoring systems and wearable system
- Bio-signal processing and analysis
- Biometric and bio-measurement
- Biomaterial and biomedical optics
- Other topics related to biomedical engineering

**Special Sessions**

Biomedical imaging

Biostatistics and biometry

The information technology in bioinformatics

Environmental pollution & public health

**Sponsors**

IEEE Eng. in Medicine and Biology Society, USA

Gordon Life Science Institute, USA

University of Iowa, USA

Wuhan University, China

Sichuan University, China

Journal of Biomedical Science and Engineering, USA

**Important Dates**

Paper Due: Oct.30, 2009

Acceptance Notification: Dec.31, 2009

Conference: June 18-20, 2010

**Contact Information**

Website: <http://www.icbbe.org/2010/>

E-mail: [submit@icbbe.org](mailto:submit@icbbe.org)

## Journal of Biomedical Science and Engineering (JBiSE)

[www.scirp.org/journal/jbise](http://www.scirp.org/journal/jbise)

JBiSE, an international journal, publishes research and review articles in all important aspects of biology, medicine, engineering, and their intersection. Both experimental and theoretical papers are acceptable provided they report important findings, novel insights, or useful techniques in these areas. All manuscripts must be prepared in English, and are subject to a rigorous and fair peer-review process. Accepted papers will immediately appear online followed by printed in hard copy.

### Subject Coverage

- Bioelectrical and neural engineering
- Bioinformatics and Computational Biology
- Biomedical modeling
- Biomedical imaging, image processing and visualization
- Clinical engineering, wearable and real-time health monitoring systems
- Biomechanics and biotransport
- Software, tools and application in medical engineering
- Biomaterials
- Physiological signal processing
- Biomedical devices, sensors, artificial organs and nano technologies
- NMR/CT/ECG technologies and electromagnetic field simulation
- Structure-based drug design

### Notes for Intending Authors

Submitted papers should not have been previously published nor be currently under consideration for publication elsewhere. Paper submission will be handled electronically through the website. All papers are refereed through a peer review process. For more details about the submissions, please access the website.

### Website and E-Mail

[www.scirp.org/journal/jbise](http://www.scirp.org/journal/jbise)

Email: [jbise@scirp.org](mailto:jbise@scirp.org)



### Editor-in-Chief

**Kuo-Chen Chou**

Gordon Life Science Institute, San Diego, California, USA

### Editorial Board

Prof. Hugo R. Arias	Midwestern University, USA
Prof. Christopher J. Branford-White	London Metropolitan University, UK
Prof. Thomas Casavant	University of Iowa, USA
Prof. Ji Chen	University of Houston, USA
Dr. Aparup Das	National Institute of Malaria Research (ICMR), India
Dr. Sridharan Devarajan	Stanford University, USA
Prof. Fu-Chu He	Chinese Academy of Science, China
Prof. Zeng-Jian Hu	Howard University, USA
Prof. Wolfgang Kainz	Food and Drug Administration, USA
Prof. Sami Khuri	San Jose State University, USA
Prof. Takeshi Kikuchi	Ritsumeikan University, Japan
Prof. Lukasz Kurgan	University of Alberta, Canada
Prof. Zhi-Pei Liang	University of Illinois, USA
Prof. Juan Liu	Wuhan University, China
Prof. Gert Lubec	Medical University of Vienna, Australia
Dr. Patrick Ma	Hong Kong Polytechnic University, Hong Kong (China)
Prof. Kenta Nakai	The University of Tokyo, Japan
Prof. Eddie Ng	Technological University, Singapore
Prof. Gajendra P. S. Raghava	Head Bioinformatics Centre, India
Prof. Qiu-Shi Ren	Shanghai Jiao-Tong University, China
Prof. Mingui Sun	University of Pittsburgh, USA
Prof. Hong-Bin Shen	Shanghai Jiaotong University, China
Prof. Yanmei Tie	Harvard Medical School, USA
Dr. Elif Derya Ubeyli	TOBB University of Economics and Technology, Turkey
Prof. Ching-Sung Wang	Oriental Institute Technology, Taiwan (China)
Dr. Longhui Wang	Huazhong University of Science and Technology, China
Prof. Dong-Qing Wei	Shanghai Jiaotong University, China
Prof. Zhizhou Zhang	Tianjin University of Science and Technology, China
Prof. Jun Zhang	University of Kentucky, USA

ISSN 1937-6871 (Print), 1937-688X (Online)

## TABLE OF CONTENTS

### Volume 2, Number 6, October 2009

<b>Analysis and prediction of exon, intron, intergenic region and splice sites for A. thaliana and C. elegans genomes</b> H. Lin, Q. Z. Li, C. X. Chen.....	367
<b>Directly immobilized DNA sensor for label-free detection of herpes virus</b> P. D. Tam, M. A. Tuan, N. D. Chien.....	374
<b>Development of a low cost fetal heart sound monitoring system for home care application</b> A. K. Mittra, N. K. Choudhar.....	380
<b>Classification with binary gene expressions</b> S. Tuna, M. Niranjana.....	390
<b>Study of blood fat concentration based on serum ultraviolet absorption spectra and neural network</b> W. H. Zhu, Z. M. Zhao, X. Guo, L. X. Wang, H. Chen.....	400
<b>ECG arrhythmia classification based on logistic model tree</b> V. Mahesh, A. Kandaswamy, C. Vimal, B. Sathish.....	405
<b>A MCMC strategy for group-specific 16S rRNA probe design</b> Y. B. Wu, L. R. Yan, H. Liu, H. C. Sun, H. W. Xie.....	412
<b>Inhomogeneous material property assignment and orientation definition of transverse isotropy of femur</b> H. S. Yang, T. T. Guo, J. H. Wu, X. Ma.....	419
<b>Unsupervised human height estimation from a single image</b> Y. P. Guan.....	425
<b>Design of occlusion pressure testing system for infusion pump</b> P. Zhang, S. Y. Wang, C. Y. Yu, M. Y. Zhang.....	431
<b>Design and development of a new biomedical / open surgical instrument</b> Z. Li.....	435
<b>Wavelet based detection of ventricular arrhythmias with neural network classifier</b> A. S. Subramanian, G. Gurusamy, G. Selvakumar.....	439
<b>Contrast enhancement methods in sodium MR Imaging: a new emerging technique</b> R. Sharma, A. Sharma, S. Kwon, R. Booth.....	445
<b>Trends in global warming and evolution of polymerase basic protein 2 family from influenza A virus</b> S. M. Yan, G. Wu.....	458
<b>Diabetic diagnose test based on PPG signal and identification system</b> H. Karimipour, H. T. Shandiz, E. Zahedi.....	465

